Spectroscopy of single photon emitting defects in Gallium Nitride and Diamond

A thesis submitted in fulfilment of the requirement for the degree of Doctor of Philosophy

School of Mathematical and Physical Sciences (MAPS)
University of Technology Sydney

Author
Amanuel Michael Berhane

Research Supervisors
Prof. Igor Aharonovich
Prof. Milos Toth

March 2018

Certificate of original authorship

I, Amanuel Michael Berhane, declare that this thesis titled, 'Spectroscopy of single photon emitting defects in Gallium Nitride and Diamond' has not previously been submitted for a degree nor has it been submitted as part of requirements for a degree except as fully acknowledged within the text.

I also certify that the thesis has been written by me. Any help that I have received in my research work and the preparation of the thesis itself has been acknowledged. In addition, I certify that all information sources and literature used are indicated in the thesis.

Production Note:
Signature of Student: Signature removed prior to publication.

Date: 13/03/2018

Acknowledgements

I, primarily, would like to thank my supervisor Prof. Igor Aharonovich, first, for taking a chance and allow me to undertake my PhD study at your group in the fascinating field of Nanophotonics. I also thank you for your guidance and for being there to help with my academic struggles. I admired and learned a lot from your regular presence as well as prompt, positive replies for many of my questions and requests over the years. The opportunities you provided me with have helped me grow as an experimental scientist, and I am forever grateful for that.

I would also like to extend my sincere thanks to my co-supervisor Prof. Milos Toth. Your invaluable comments and all-around advice are truly motivating. Thank you for all your support throughout my study.

I thank Mrs Katie McBean for accommodating me in the lab from the start and the training you gave me on the different set-ups around MAU. I am also thankful to Mr Geoff McCredie and Mr Herbert Yuan for the technical support as well as the training on different vacuum systems. Thanks are also extended to Dr Mark Lockrey and Dr Angus Gentle for the training and help you gave me during my study.

To my fellow students at MAU, thank you for being a great bunch to study and work with. Particularly, I thank James Bishop and Russell Sandstrom for the shared social life and making my time at UTS enjoyable.

I would like to acknowledge the collaborators with whom we worked with over the years. I am very grateful to Asst. Prof. Dirk Englund at Massachusetts Institute of Technology (MIT) for our fruitful collaboration and hosting me at your lab. I am thankful to Dr Kwang-Yong Jeong, at MIT who measured half of the room temperature spectroscopy data

presented in Chapter 4. We also collected the low-temperature data featured in chapter 4 & 5 together during my visit to MIT. I am also very grateful to Prof. Adam Gali and Dr Zoltán Bodrog at Wigner RCP of the Hungarian Academy of Sciences for carrying out the numerical work presented in chapter 4. Thanks, is also extended to Prof. Hiromitsu Kato at AIST, Japan for providing us with the single crystalline diamond diode which is used to present the work in chapter 7.

To my friends around the globe, thanks for sharing your ideas and experiences: Daniel Taye, thank you for being a pal through thin and thick for so many years. I also thank you for your help with some of the 3D images in this work. Getasew Admasu and Abreham Degarege, our regular meet-ups and your brotherly advice during my PhD study are genuinely appreciated.

To my inspirational wife, Mrs Fasika A. Tekest. Thank you for helping me stay true the cause. Thank you for being patient through all the hurdles and for being the support I ever needed. Everything works out when you are around.

Finally, to my mother Hanna Habtemariam and my late step-father Major Tessema, thank you for your unconditional love. This thesis is dedicated to you both.

Publications

Peer-reviewed publications including one under review that contributed to this work:

1) **A. M. Berhane**, K.-Y. Jeong, Z. Bodrog, S. Fiedler, T. Schröder, N. V. Triviño, T. Palacios, A. Gali, M. Toth, D. Englund, and I. Aharonovich, "Bright Room-Temperature Single-Photon Emission from Defects in Gallium Nitride," Advanced Materials, 1605092, 29 (2017).
2) **A. M. Berhane**, C. Bradac, and I. Aharonovich, "Photoinduced blinking in a solid-state quantum system," Physical Review B **96**, 041203 (2017).
3) **A. M. Berhane**, Kwang-Yong Jeong, Carlo Bradac, Michael Walsh, Dirk Englund, Milos Toth, Igor Aharonovich, "Photophysics of Single Photon Source in Gallium Nitride at the Visible Spectrum" **(under review)**
4) **A. M. Berhane**, S. Choi, H. Kato, T. Makino, N. Mizuochi, S. Yamasaki, and I. Aharonovich, "Electrical excitation of silicon-vacancy centres in single crystal diamond," Applied Physics Letters **106**, 171102 (2015).

Peer-reviewed publications not included in this thesis but contain research contributions during the PhD study:

1) T. T. Tran, C. Zachreson, **A. M. Berhane**, K. Bray, R. G. Sandstrom, L. H. Li, T. Taniguchi, K. Watanabe, I. Aharonovich, and M. Toth, "Quantum Emission from Defects in Single-Crystalline Hexagonal Boron Nitride," Physical Review Applied **5** (2016). This work reports the single photon emission from bulk hexagonal Boron Nitride (hBN). Spectroscopic properties of the emission are studied using photoluminescence (PL) and cathodoluminescence (CL). The fluorescence time trace, as well as time, resolved PL is used to characterise temporal behaviours of

the intensity. The results are vital in introducing hBN for nanophotonic applications.

2) S. Choi, **A. M. Berhane**, A. Gentle, C. Ton-That, M. R. Phillips, and I. Aharonovich, "Electroluminescence from localized defects in zinc oxide: toward electrically driven single photon sources at room temperature," ACS applied materials & interfaces **7**, 5619-5623 (2015). This study reports electrically driven defect fluorescence from Zinc Oxide (ZnO) diodes. Direct evidence of electroluminescence (EL) from the defect is provided by exciting it both by PL and later EL yielding the same spectral properties. The results entail that defects in ZnO can be further investigated to show electrically driven single photon emission.
3) S. Stehlik, L. Ondic, **A. M. Berhane**, I. Aharonovich, H. A. Girard, J.-C. Arnault, and B. Rezek, "Photoluminescence of nanodiamonds influenced by charge transfer from silicon and metal substrates," Diamond and Related Materials (2015).: Here NV centre in a 5 nm detonated nanodiamond is studied by varying the termination as well as the substrate. It is reported that the spectral, as well as lifetime of the NV centre, changes by varying the factors above. This result underpins the effect of surface electrostatics on the optical properties of nanodiamonds.

Table of Contents

List of Tables

List of Figures

Symbolic Notation

Symbol	Meaning	Page
ω	Angular frequency	5
h	Planck's constant	5
g^2	Second-order correlation function	13
τ	Delay time	13
I	Intensity	13
$P_{1,2}$	Probability of counting photons	15
$\eta_{1,2}$	Detection efficiency	15
Δt	Detection time	15
$\hat{n}_{1,2}$	Intensity operator	16
$\hat{a}_i$	Annihilation operator	16
$\hat{a}_i$	Creation operator	16
$\hat{a}_1$	Input field operator	17
$\hat{a}_2$	Vacuum field operator	17
n	Number of photons	17
Δn^2	Photon number variance	17
N	Number of emitters	22
p_j	Probability of emission per time	22
i_j	Discrete intensities	22
r_j	Position of emitters	22
κ_{ij}	Rate coefficients	23
λ	Eigenvalues	24

t_d	Antibunching time constant	25
q	Scaling factor	25
S	Signal counts	26
B	Background counts	26
λ_1	Radiative decay rate	28
λ_2	Non-radiative decay rate	28
a	Scaling factor for bunching	28
V_b	Potential barrier	31
E_f	Fermi energy level	32
E_e	Conduction band energy	32
E_v	Valance band energy	32
$N_{e,v}$	Intrinsic carrier concentration	32
N_d	Electron carrier density	32
N_a	Hole carrier density	32
E_g	Band gap energy	32
q	Charge of electron	32
ρ	Charge density	33
d	Width of depletion region	33
$E_{\max}$	Maximum field	34
ε	Dielectric constant	34
J_{diff}	Diffusion current	34
D	Diffusion constant	34
∇n	Concentration gradient	34
J_f	Forward current	35
J_r	Reverse current	35

V_{ext}	Applied voltage	35
ΔE	Potential step	36
K	Boltzmann constant	36
T	Temperature	36
n_i	Intrinsic concentration	37
$N_{acc(don)}$	Acceptor or donor concentration	37
τ	Lifetime	37
L	Diffusion length	37
R_d	Electron recombination rate	40
c_d	Electron capture cross-section	40
n_e	Electron density	40
f	Number of neutral defects in ground state	40
N_{SPS}	Number of single photon source per unit volume	40
c_u	Hole capture rate	41
n_p	Hole density	41
x	Population of neutral state	41
G_d	Electron generation rate	41
G_u	Hole generation rate	41
e_d	Electron re-emission rate	41
e_u	Hole re-emission rate	41
e_r	Re-emission rate of the neutral defect state	41
R_{SPS}	Recombination rate at single photon source	42
ϕ	Quantum efficiency	42
$\sigma_{d(u)}$	Capture cross-section	42
$\upsilon_{d(u)}$	Group velocity	42
P	Probability density of blinking events	45
$\tau_{On,\mathbf{Off}}$	Characteristic on- and off- blinking times	45

C^0	Neutral defect concentration	56
C^-	Ionized defect concentration	56
C_0	Total defect concentration	56
f	Probability of occupation	56
E_a	Acceptor energy level	56
E_f	Fermi energy level	56
C_v	Concentration of point defects	56
n_v	Number of point defects	56
N	Total number of crystal electrons	56
G_F	Gibbs free energy	56
H_F	Formation enthalpy	56
S_F	Formation entropy	56
W_{n0}	Transition probability	56
S	Huang-Rhys factor	56
E_0	Energy difference	57
n	Excitation vibrionic level	57
a	Offset parameter	59
b	Initial intensity amplitude	59
ϕ	Angle between excitation laser and dipole orientation	59
Γ	Transform limited linewidth	60
a_{ec}	Bohr-radius	70
μ^*	Reduced mass	70
m_e	Mass of electron	70

m_h	Mass of hole	70
ΔE_{ex}	Effective binding energy	70
κ	Semiconductor permittivity	70

List of Abbreviations

Abbreviation	Meaning	Page
SPEs	Single Photon Emitters	xxxix
GaN	Gallium Nitride	xxxix
cw	continuous Wave	xl
ZPL	Zero Phonon Line	xl
FWHM	Full Width at Half Maximum	xl
PL	Photoluminescence	xli
EL	Electroluminescence	xli
CL	Cathodoluminescence	4
PMT	Photomultiplier Tube	6
APDs	Avalanche Photo Diodes	6
HBT	Hanbury-Brown and Twiss	12
SCR	Space Charge Region	31
SPEDs	Single Photon Emitting Diodes	38
LEDs	Light Emitting Diodes	38
PD	Point Defect	55
HPHT	High-Pressure High Temperature	61
CVD	Chemical Vapor Deposition	62
SF	Stacking Fault	65
QW	Quantum Well	69
MOCVD	Metalo-Organic Chemical Vapor Deposition	74
HVPE	Hybrid Vapor Plasma Epitaxy	75
PIC	Photonic Integrated Circuit	84

Abstract

Amanuel Michael Berhane

Spectroscopy of single photon emitting defects in Gallium Nitride and Diamond

A single photon is among the few quantum mechanical systems that are finding applications in myriad fields. The applications include serving as building blocks for the ongoing endeavour to realise faster computers and secure communication technologies. As a result, a variety of platforms are being inspected to generate single photons on-demand. Point defects and complexes in wide bandgap semiconductors such as nitrogen-vacancy (NV) and silicon-vacancy (SiV) centres in diamond, carbon antisite in Silicon Carbide (SiC), etcetera, are shown to be reliable room temperature (RT), single photon emitters (SPEs). Despite reports of several defect based SPEs in diamond and other semiconductors, the exploration continues to find ideal sources for applications. The central part of this work also focuses on the discovery and characterisation of novel SPE in the device fabrication friendly material- Gallium Nitride (GaN).

The other important aspect in the study of SPEs is the method by which emitters are excited. While optical technique via laser excitation is the standard approach, electrically excited single photon generation is highly desirable for large-scale nanophotonic applications. The second part of the work investigates electrically driven fluorescence from SiV ensemble in diamond, whose properties so far, were only investigated using optical excitations. Therefore, the thesis consists of two main parts. First, the discovery as well as study of a new family of SPEs in GaN via optical excitation is covered. The second part features electrically driven characterisation of SiV centre in diamond.

The RT stable, SPEs are discovered in GaN films using a confocal microscope. The emitters are off-resonantly excited using a continuous wave (cw) laser of wavelength 532 nm. The centre of wavelength in the emission spectra spans a wide range of from around 600 nm to 780 nm. Also, a significant portion of the emission comes from the characteristic, narrow zero-phonon lines (ZPLs) with the mean cryogenic and RT Full Width at Half Maximum (FWHM) of around 0.3 nm and 5 nm, respectively. The nature of the defect responsible for the emission is studied experimentally via temperature resolved spectroscopy as well as numerical modelling giving a strong indication that the emitter is a defect localised near cubic inclusions.

Absorption and emission polarisation properties from the SPEs in GaN is studied in detail via polarization-resolved spectroscopy. High degree of linear, emission polarisation is observed with an average visibility of more than 90 %. The absorption polarisation measurement shows that individual emitters may have different dipole orientation. In addition, brightness measurements from several of the SPEs in GaN show the average maximum intensity of around 427 kCounts/s placing the emitters among the brightest reported so far. A three-level model describes the transition kinetics of the SPEs successfully which explains some of the observed properties of the emitters such as photon statistics.

A small number of the SPEs in GaN show unusual photo-induced blinking. This blinking is shown to be due to a permanent change in the transition kinetics of the emitters when exposed to a laser power above a certain threshold. This is evidenced by the change in the transition kinetics observed before and after blinking of SPEs. Combining long-time autocorrelation measurement and photon statistics analysis, numerical values for power-dependent blinking behaviours are determined.

The second major result in this work is the first electrically driven luminescence from the negative charge state of Silicon-Vacancy (SiV^-). The result was directly obtained by measuring photoluminescence (PL) and electroluminescence (EL) spectra from SiV^- ensemble located in PIN diamond diode. The defect was incorporated into the diode via ion implantation. Further characterisation shows that the saturation behaviour under excess carrier injection yields similar results with when the defect is pumped optically by lasers. Finally, charge state switching between the negative and neutral states of the defect was also attempted by using reverse-biased PL elucidating transition dynamics of SiV centres in diamond.

This work, therefore, reports new findings in the spectroscopic studies of defect based single photon emission. Furthermore, it provides detailed photophysical studies which may serve as a benchmark for future investigation of SPEs in GaN for multiple applications. The results provide new platform as well as alternative excitation approach for the application of defect based SPEs in nanophotonics.

1 Introduction

In this chapter, the study of defect based single photon generation is introduced by first highlighting the relevant technological applications. This is followed by a description of the different platforms that are used to generate single photons. Notably, the advantage of using optically active defects in wide bandgap semiconductors as single photon emitters (SPEs) is emphasised. These advantages are further exemplified by a brief review of a famous defect in diamond (i.e. NV centre) and its applications in different fields. By highlighting progress and limitations in the study of defect-based SPEs so far, the motivation for this PhD project and its contribution in moving the field forward is featured. Brief historical background on the study of SPEs is provided to clarify earlier conception of photons as well as illustrate experimental progress made since the first detection. Finally, specific objectives of this PhD work and outline of the thesis are provided.

1.1 Motivation

The dual nature of light, namely wave- and particle-like, is established through multiple experiments since its first theoretical conception[1-4]. This observation has allowed the study of light in terms of its fundamental constituents – photons[5, 6]. Throughout this work, photons are considered as single-mode constituents of a continuous electromagnetic wave of light [5, 7]. As such, various light sources are categorised based on temporal statistics of emitted photons at a detector. Among these sources is SPEs, which are identified by photon coincidence where each photon arriving at a detector is separated by a characteristics time[8]. Ideally, a single photon emitter ejects one photon on average with a variance of zero. In-depth mathematical treatment of photon statistics from different light sources including SPEs is provided in the following chapter. This sub-chapter, on the other hand, focuses on the major applications that motivate the study of single photon emitters.

While a wide variety of applications ranging from bio-markers to quantum metrology are reviewed as potential fields of application for SPEs, the primary drivers are quantum computing and quantum cryptographic technologies[8-10]. The ever-growing need for faster computing devices has now led to exploring alternatives using quantum mechanical objects as bits (qubits), where much quicker processing than possible using classical bits are allowed[11, 12]. This advantage arises because qubits, unlike their classical counterparts, have an additional possibility of existing in a superposed state of two bits forming a third state. Thus, a network of three-bit systems does multiple computations at the same time, which otherwise would be done one at a time using the two-bit systems. This oversimplified statement grants future quantum computers the power to process large data and calculations in much less time than possible today. As a consequence, significant strides towards building the first quantum computers is underway backed by multibillion-dollar funds both from private tech-giants as well as governmental agencies[13].

Among the primary quantum mechanical systems being pursued for application as qubits, single photons travelling in a photonic circuit constitute an important one[11]. Photons, as bosonic particles, don't interact with each other, thus have the advantage of maintaining their superposed state for more extended periods of time. However, because of the non-interactive behaviour, it is also hard to have the quantum mechanical states of two photons interfere to form the third superposed state. By using interferometer with a specific arrangement of 50/50 beam splitters (BSs), two-photon interferences can be achieved. Currently, such systems can be designed on-chip to build photonic logic gates [14, 15]. The single photon, in this case, is introduced by coupling external emitter to the circuit. For a controlled introduction of single photons into the circuit, however, chip-mounted emitters are preferred. Thus, on-demand generation of bright, single photons on a photonic circuit is one of the major challenges to address when building a viable photonic logic gate.

The other application pursued using SPEs is quantum cryptography which promises absolute security while exchanging encoded information. An example of such an unbreakable protocol

is proposed in 1984 by Gilles Brassard and Charles Bennett[8, 13]. In this protocol, a sender encodes a single photon with one of four polarisation directions to exchange message with a receiver. If eavesdropper has been reading some of the polarisation states and re-sends some of their own to mask the trapped states, the number of wrong readings increases at the receiver's end. This is because every reading by the eavesdropper changes the state of the initially sent polarisation directions. Thus, it is impossible for an eavesdropper to crack the key without leaving a trace if the keys are encoded with ideal single photons. However, if pseudo-single photon emitter (sends two or more photons at times) is used to encode the message, an eavesdropper can easily get the same polarisation information as the receiver undetected by splitting some of the bunched photons using BS (without introducing additional error to the communication). Thus, ideal single-photon emitters with photophysical properties such as polarizability are vital for such application.

Consequently, a list of criteria has been set for an ideal SPE to fulfil. This includes[8, 16]:

i. On-demand or deterministic generation of single photons upon excitation.
ii. Single photon emission with zero probability of multiphoton emission.
iii. Photons from the same SPE should be indistinguishable; That is, the single photons should have identical spectral and temporal properties.
iv. Polarizability both in absorption and emission.
v. Bright, photostable emission under different pumping powers.
vi. Allows both electrical and optical excitation.

Thus, different platforms are investigated as potential SPE considering these and other idealist criteria. These platforms include single neutral atoms, single ions, single molecules, quantum dots and defects in wide bandgap semiconductors. This work focuses on the later, mainly because wide bandgap semiconductors [17]:

- are transparent at the visible spectrum.
- host numerous optically active defects.
- allow on-demand excitation of SPEs at room temperature.

- allow on-chip coupling of emitters to photonic components.
- serve as platforms for fabrication of integrated nanophotonic devices.

A benchmark semiconductor for the study of defect based single photon generation is diamond, hosting hundreds of optically active defects[9, 10, 16]. Thus, a number of room temperature stable SPEs have intensively been investigated for nanophotonic applications. Most prominently, the Nitrogen-Vacancy (NV) defect in diamond has attracted interest both for its optical as well as spin properties[18]. The NV-center forms when a substitutional nitrogen atom traps a vacancy at an adjacent lattice site of diamond as shown in Figure 1.1 (a). This centre can be intentionally generated in bulk diamond as well as nanodiamonds via nitrogen impurity incorporation using techniques like chemical vapour deposition (CVD) and ion implantation. Under laser illumination, the NV centre fluoresces giving characteristic spectrum. Two peaks one at 575 nm and 637 nm ZPL are known for this defect corresponding to two charge states of the defect, namely, the Neutral (NV^0) and negative (NV^-) charge states, respectively. The more attractive charge state of the two for application in quantum technology is NV^- (see Figure 1.1 (a&b)) fulfilling most of the outlined criteria for an ideal SPE. For example. NV^- is the only defect in diamond so far to demonstrate electrically triggered single photon emission[19]. The immense interest towards NV^-- centre is, however, on its spin properties. That is, the electronic transition of the centre shows spin dependence, which is manipulated to control spin read-out[18]. Nevertheless, the optical properties of the centre remain essential where, for example, transform-limited linewidth with minimal spectral diffusion is reported with the successful demonstration of two-photon entanglement[20]. Other applications using single photon emission from NV-center include fluorescence bio-imaging[21] and quantum metrology[22, 23].

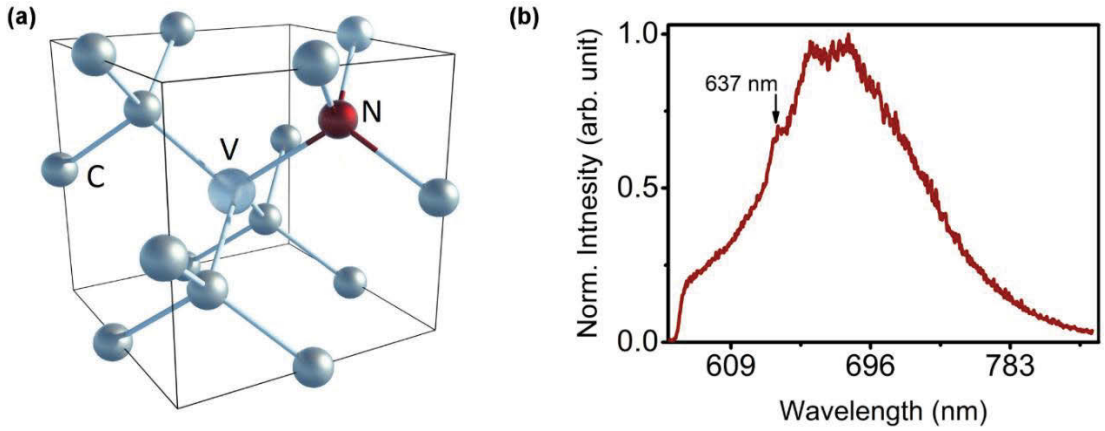

Figure 1.1: (a) Atomic structure of NV centre in the diamond unit cell (b) Spectrum from an NV centre showing fluorescence peak of the NV^- at 637 nm.

While single photon emission from NV and other optically active defects continue to attract interest, difficulties related to diamond processing hinders large-scale nanophotonic device fabrication. As a result, colour centres in other fabrication-friendly, wide bandgap semiconductors are explored with reports of SPEs from materials such as Silicon Carbide (SiC)[24] and Zinc Oxide (ZnO)[25]. The other group of mature semiconductors are III-nitrides ((Indium Nitride (InN), Aluminium Nitride (AlN) and Gallium Nitride (GaN)). III-nitrides are microelectromechanical systems (MEMS) compatible with widespread use in solid-state lighting [26], high-frequency and high-power electronics[27, 28] and laser technologies[29].

The vital role of III-nitrides for the different applications emanates from their direct bandgap with the Al-Ga-In-N system covering the entire visible spectrum as shown in Figure 1.2 [30]. Also, the strong covalent bond of III-nitrides matrix makes them resistant to applications in high temperatures, high illumination or high currents conditions. In particular, gallium nitride (GaN) features advantageous optical and electronic properties such as non-linear second order susceptibility [31], biocompatibility[32] and a direct, wide bandgap[33, 34]. Thus, GaN is increasingly being used as a platform for photonic integrated circuits (PIC)[35, 36] including waveguides[37], microdisk cavities[38-40], and photonic crystals[41-43]. In addition, GaN is the basis of a multi-million dollar efficient lighting industry underpinned by mature

nanofabrication and growth technologies[44, 45]. As a polar material that grows in the wurtzite phase, GaN exhibits spontaneous polarisation [30, 46, 47]. Moreover, due to its symmetry, a strong piezoelectric polarisation is observed in GaN[46]. Thus, electronic and optical property studies of the material typically take the polarity and polarisation properties of GaN into consideration.

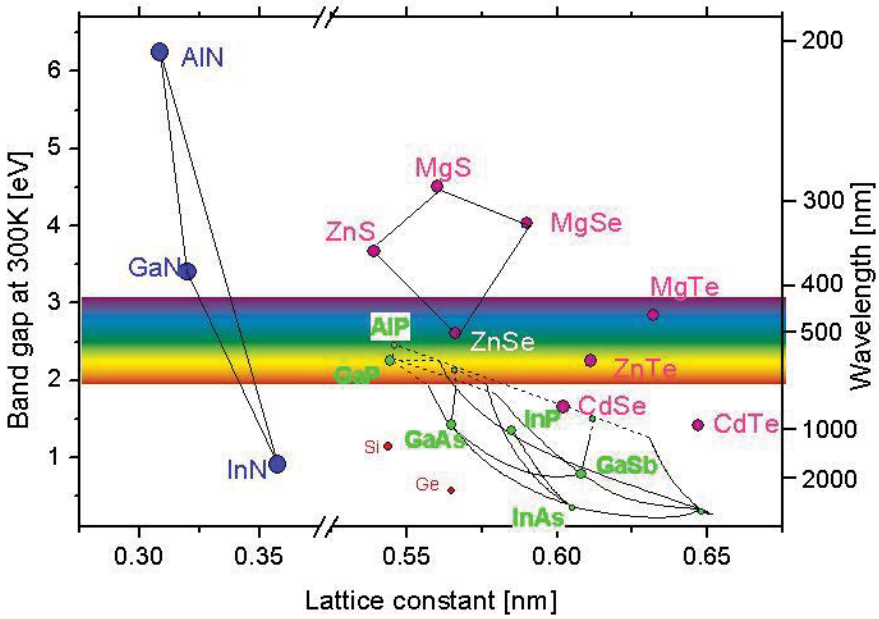

Figure 1.2: The bandgap energies and lattice constants of various direct and indirect bandgap semiconductors including III-nitrides[48].

Commercial GaN films are mostly grown using heteroepitaxial growth methods such as metal-organic chemical vapour deposition (MOCVD)[47, 49]. Due to the high growth temperature requirement, which could reach up to about 1200 ^{o}C, only select few substrates have been used to grow GaN films[30]. These include sapphire (α-Al_2O_3), polytypes of silicon-carbide (SiC) and Silicon (Si). The large lattice mismatch, as well as difference in the linear coefficient of expansion between GaN and the substrates, makes the growth of large, high-quality films difficult. Standard dislocation density in GaN film grown using heteroepitaxial methods is > 10^8 cm^{-2}. High quality (with a dislocation density of about 10^3 cm^{-2}) GaN film can also be grown homoepitaxially on GaN single crystal substrates using high- pressure high-temperature (HPHT) technique[30]. Although such growth technique is

limited to the growth of small surface area films, new fabrication approaches such as hybrid vapour phase epitaxy (HVPE) have been used to grow 3-inch wafers with a film thickness of around 300 - 400 μm[30]. Also, the electronic property of GaN can readily be altered by various doping elements. For example, achieving p-type conductivity in GaN had long been an obstacle to progress in classical optoelectronics. This problem was resolved by successful doping of GaN with Mg-atoms via hydrogen termination leading to the fabrication of the first white LED[50]. The undoped free carrier concentration in GaN can reach up to > 10^{16} cm^{-3}.

Numerous structural and point defects are known to reside in GaN bulk, altering the mechanical, optical and electronic properties of the material[51, 52]. Despite the extensive studies of defects in GaN, experimental reports of defect-related single photon emission have been lacking. In fact, RT single photon emission from III-nitrides have been restricted to few reports of quantum dots (QDs) sources[53-55]. Consequently, the wealth of knowledge behind bulk GaN material, processing and device fabrication has not been fully utilised by the fast-emerging quantum technologies. The primary focus of this thesis is investigating room temperature (RT) stable, defect-related SPEs in GaN films. Furthermore, detailed study of the photophysics of the emitters will also be covered in this work, evaluating the properties for nanophotonic applications. The results constitute essential findings that may allow the fast realisation of integrated devices using the mature platform.

One of the criteria above for applications of SPEs is allowing electrically driven fluorescence. This property is crucial because it allows large-scale, single photon-based technologies to be controlled with existing electronics. Moreover, the underlying recombination mechanism of electroluminescence (EL) is different from that of photoluminescence (PL), allowing a complete study into the transition kinetics of defects. EL has been successfully demonstrated for NV^--centre in diamond by generating electrically driven single photons from PIN diamond diodes[19, 56]. The NV centre can be controlled both optically as well as electrically making it even more attractive centre for applications. As stated, however, diamond hosts several

other defects that can serve as SPE such as Silicon-Vacancy (SiV) whose distinguishing properties have been studied only through optical excitation so far. Thus, the next focus of this thesis is studying the capability of electrically driven fluorescence from Silicon-Vacancy (SiV) centres in the diamond diode. The results will establish the possibility of harnessing unique attributes of the centre via electrical excitation and give the motivation to achieve electrically driven single photon emission with narrow linewidth from SiV.

1.2 Background

The concept of a photon has been best described by considering an electromagnetic field within a perfect resonator or cavity[5]. In such case, depending on the resonator or cavity size, there can only be some allowed discrete spatial modes. A different picture arises when treating time variation of the same allowed modes using classical and quantum harmonic oscillator equations. In the latter case, a mode with the angular frequency, ω, can only be excited by integer multiples of $h\omega$, where h is Planck's constant[5, 8]. Thus, a spatial mode excited into the n^{th} harmonic oscillations will have n number of photons, where n is an eigenvalue of the oscillator number operator. The photons in a single mode are uniformly distributed indicating that they are delocalized in time. In an open optical system, the standing-wave modes for cavity correspond to wave packets travelling along a propagation axis. Similarly, for a single photon propagation, the wave packet function is the product of h and the average of its frequency distribution with some level of localisation[8]. While the theoretical definition of a single photon does not entirely imply a localised state, experimentally a single photon ionises a single current pulse upon hitting a photodetector[5]. Thus, a single photon state can still be analysed by considering a wave of light and discrete detector as will be presented in Chapter 2.

In the 1970s, interference experiments from different groups demonstrated an electromagnetic field that required a quantum mechanical explanation[57]. This observation has served as

evidence for the existence of a photon. Subsequent experiments in the 1980s have confirmed the same results. Grangier, Roger and Aspect carried out correlation experiment using a 50/50 BS in 1986[58]. They proposed that a single photon can only be detected once. Therefore, a single photon entering the BS can either be detected at the reflecting or transmitting the output of the BS but not at both ends at the same time. As a result, they measured coincidence that can only be explained by considering a single photon state (details in Chapter 2). The first photon correlation experiment using two detectors, however, is reported by Hanbury Brown and Twiss (HBT) in 1956[59]. Applying photomultiplier tube (PMT) as the detectors, photocurrents were measured. The results show that current at the two PMTs increases simultaneously. This positive correlation is a characteristic behaviour of photons and is referred to as bunching. In a later experiment, they conducted the measurement by considering individual photon counts instead of just the photocurrent where a reduced positive correlation is observed[60]. This result has significantly helped subsequent experiments that demonstrated the existence of a single photon state.

Today, second-order autocorrelation measurement of single photons is robust coupled with development in detection technologies. Following the first single photon counting using PMTs., McIntyre developed Avalanche Photo Diodes (APDs) in the mid-1960s. This development allowed single photon counting using solid-state detector[8]. The advent of silicon-based APDs enabled high efficiency and low noise single photon counting in the visible spectra with short measurement times. In this work, we use the elegant approach of HBT by correlating coincidence using BS and APDs to detect the excitation of single photons (details described in Chapters 2 & 4).

1.3 Objective

The general aim of this thesis is twofold: First, we study the spectroscopic characteristics of the new defect based SPEs in GaN films. The study is done both by measurements using spectroscopy where wavelength distribution of emission from the SPEs is characterised as

well as time-dependent intensity correlation measurements. The emission properties are investigated systematically both at cryogenic and room temperatures. The second part of the thesis features the first electrical excitation of a well-known stable, colour centre in diamond, namely, Silicon-Vacancy (SiV). The measurement is carried out on confocal microscopy by comparing intensity maps as well as spectral characteristics from PL, EL and Cathodoluminescence (CL) measurements.

Thus, the specific objectives of the thesis are to:

- Investigate defect related SPE in several GaN films grown on different substrates. Also, indicate the possible defect system responsible for the emission via experimental measurements and numerical calculations.
- Study the photophysical properties of the emitters in GaN using measurements such as intensity saturation, polarisation and low-temperature spectroscopy.
- Investigate power dependent blinking behaviours in some of the SPEs in GaN.
- Investigate electroluminescence from SiV center in diamond.

1.4 Organization of the thesis

Following is the organisation of the thesis:

Chapter 1 provides the technological motivation for the study of defect based single photon emission. The contribution of this work in moving the study and application of defect based SPEs is highlighted. A history of the study of single photons as well as the evolution of their experimental detection is also covered. Finally, the general and specific objectives of this thesis are outlined.

Chapter 2 reviews fundamental topics required to cover the excitation and detection of single photon emitters. The theory of single photon emission is covered in this chapter. Also, the basics of optical and electrical excitation of SPEs is also provided. Finally, the different mechanisms of blinking are summarised to frame later discussion on the topic.

Chapter 3 describes defect based fluorescence in wide bandgap semiconductors. It covers the formation of optically active point defects at equilibrium followed by a summary of prior reports of SPE in GaN. Configuration coordinate diagram is used to illustrate the optical transition in defects. In light of the SPE in GaN, the material properties and formation of stacking faults are featured. Finally, diamond material properties, as well as defect-based SPEs in diamond, are summarised. Particularly, a brief discussion on the electronic and structural properties of SiV is provided.

Chapter 4 focuses on the first report of single photon emission (SPE) from various GaN films grown on sapphire and SiC substrates. Spectroscopic and second-order correlation measurements elucidate characteristic behaviours of the SPE. Preliminary evaluation of emitters for applications in quantum technology is also provided. Finally, low-temperature spectroscopy and a numerical model is used to indicate the defect system responsible for the SPE.

Chapter 5 follows from the previous chapter and reports on the photophysics of the SPE in GaN film. This is done via analysis of results from several emitters collected both at cryogenic and room temperature. The results are discussed in the framework of comparing the photophysical properties to established emitters in other semiconductors.

Chapter 6 describes unusual photo-induced blinking behaviour that some of the SPE in GaN showed. By using fluorescence trajectory, second-order correlation and probability distribution analysis, a mechanism responsible for the blinking is proposed. Furthermore, characteristic decay time as well as "on" and "off" times are determined as a function of excitation power.

Chapter 7 features the second main objective of this thesis which is to report the first electrical excitation of SiV centre in diamond. By comparing optical and electrical excitation, direct evidence of electroluminescence from SiV ensembles is provided. Furthermore, the study of charge state switching in SiV is attempted by using reverse-biased photoluminescence.

Chapter 8 concludes the major findings and contributions of the PhD work. In addition, a proposal is included as a future direction to build on the work presented here.

Accordingly, Chapters 1-3 give background into the field of defect based single photon emission. These topics are followed by chapters 4-6, which cover the central contribution of the thesis- discovery and characterisation of SPEs in GaN. Chapter 7 presents electrically driven fluorescence from SiV defect ensemble in the diamond diode. The significant results are summarised, and the broader context of the work is covered in Chapter 8.

2 Fundamentals

This chapter provides the basics behind the major topics of this thesis. First, a mathematical treatment of generation and detection of light in terms of the time distribution of its photons is provided. The review is followed by basic descriptions of the mechanism behind optical excitation of SPE using continuous wave (cw) lasers. One other alternative mechanism of excitation- electrical excitation via excess carrier recombination at single photon emitting defects- is also reviewed. Finally, the causes and mechanism behind single photon fluorescence blinking are featured.

2.1 Photons as basis for quantum mechanical behaviour of light

The standard classical and semiclassical approach to mathematically model the distribution of photons at detectors is through the correlation of intensities [6, 58, 59]. Such formulation fundamentally relies on splitting light path using beam splitters (BS) leading to two detectors from which time distribution of the respective intensities is correlated[58, 61]. This arrangement constitutes an essential part of the HBT set-up[59]. As will be shown below, however, intensity correlation could only describe some sources of light, namely chaotic and coherent light sources, where the continuous electromagnetic field or its magnitude is correlated in time. A comprehensive formulation is obtained using a quantum mechanical approach where operators for intensity (or electric field) are correlated at the two detectors.

Thus, classical and semiclassical formulation of photon statistics of chaotic and coherent light sources is presented underpinned by the second-order correlation of intensities. This approach will help not only obtain characteristic correlation behaviours for chaotic and coherent light sources but also helps appreciate the limitations of the approach in describing single-mode light sources. This treatment is followed by the comprehensive, quantum mechanical approach of second-order correlation of operators which will be shown to yield consistent

results with the classical approach for chaotic and coherent light sources with the additional advantage of rendering the full description of single photon emitters. In the end, the different sources of lights will be demonstrated to show distinct photon correlation behaviours. More importantly, characteristic description of single photon emitters will be covered which is the focus of this work and will be used throughout the result chapters.

2.1.1 Classical and semiclassical approach for the analysis of photon statistics

Chaotic light sources also referred to as thermal light sources are characterised by the emission of photons that are independent of each other resulting in random fluctuation of the electric field and intensity. Examples of chaotic light sources include discharge lamp, filament lamp, light bulb, etcetera where the photons distribution in time is bunched at detectors as illustrated by "comb" diagram in Figure 2.1 (a). By focusing on the average intensity fluctuations from such sources, the second-order correlation is constructed by measuring the time at two detectors with a delay time, τ , introduced on one of the channels. The measurement can be attained by considering an ideal beam splitter where the chaotic light beam is split into the detectors as shown in Figure 2.1 (b). Thus, for a stationary, chaotic source, the average intensity fluctuation is given by the second-order correlation function as [5, 57, 62, 63]:

$$g^2(\tau) = \frac{\langle I(t+\tau)I(t)\rangle}{\langle I(t+\tau)\rangle\langle I(t)\rangle} \tag{2.1}$$

where < > denotes time average, I is the intensity as a function of times, t and $t+\tau$. Under the stationary, chaotic source consideration, the time average and statistics average of photons are the same and designated by the angle brackets. For delay time of zero, i.e. $\tau = 0$, the expression in equation (2.1) reduces to $g^2(\tau = 0) = \frac{\langle [I(t)]^2 \rangle}{\langle I(t)\rangle^2}$ for a lossless beam splitter. Applying Cauchy-Schwartz inequality, where $\langle I(t)\rangle^2 \leq \langle [I(t)]^2 \rangle$, the second order-correlation at zero delay time reduces to

$$g^2(\tau = 0) \geq 1 \tag{2.2}$$

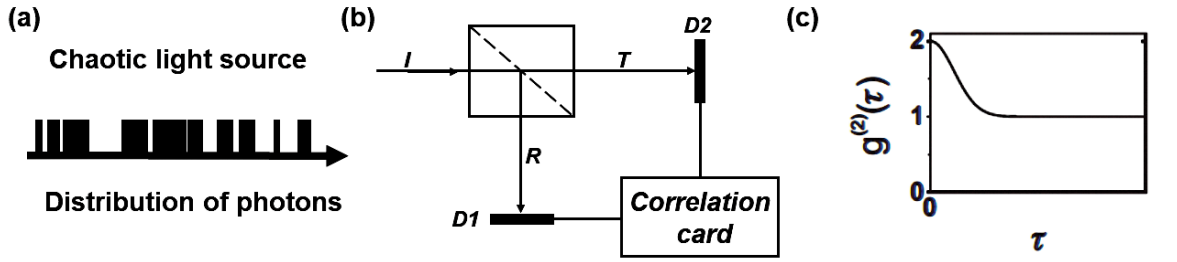

Figure 2.1: (a) Chaotic photon distribution at detectors. (b) beam splitter for photon correlation analysis where an incident beam of light (*I*) is split 50/50 into a transmitted (*T*) and reflected (*R*) beams leading to two detectors D1&D2. (c) shows the autocorrelation results for chaotic light source obtained after intensity fluctuation at the two detectors is correlated in time by introducing delay (τ) in the arrival times in one of the beam paths (*R* or *T*)[64].

This result shows that for a light beam with a fluctuating beam intensity, the $g^2(\tau = 0) > 1$. In fact, for truly chaotic light source where the contribution of individual photons is insignificant compared to a large number of fluctuating photons, it can be shown that $g^2(\tau = 0) = 2$, as depicted in Figure 2.1 (c)[59, 60, 65]. The arrival of photons in groups with the corresponding fluctuation at detectors is referred to as photon bunching.

An ideal laser beam, on the other hand, is a coherent light source with stable intensity, where $\langle I(t)\rangle^2 = \langle [I(t)]^2 \rangle$ indicating that photons in such sources are uncorrelated to each other (Figure 2.2 (a)). In such case, the intensity remains constant along the normal with the autocorrelation function yielding $g^2(\tau = 0) = 1$ as depicted in Figure 2.2 (b).

While the classical model of intensity fluctuation at detectors described the photon statistics from chaotic and coherent sources very well as verified by experiments, a more accurate approach that resembles detection mechanism is required. That is, in real detectors such as photomultiplier tube (PMT) or Avalanche Photodiodes (APDs), the intensity is converted and measured indirectly as photocurrent or photocounts. As such, a semiclassical approach which

considers the electromagnetic field (chaotic and coherent light beam) and quantum mechanical detectors have been demonstrated.

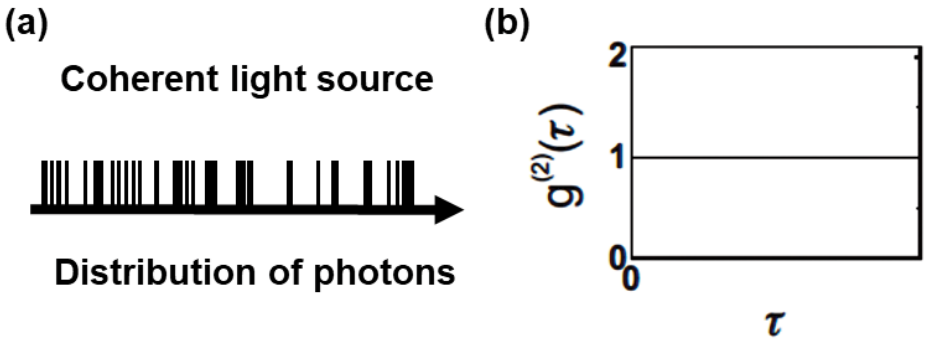

Figure 2.2: (a) Coherent photon distribution at detectors. (b) shows the autocorrelation results for a coherent light source obtained after intensity fluctuation at the two detectors is correlated in time by introducing delay (τ) in the arrival times in one of the beam paths (*R* or *T*)[64].

The discussion presented here is based on [5, 57, 62]. In this model, the probability of counting a photon (P_1) in detection time of Δt is proportional to the average intensity hitting the detector and is given by:

$$P_1 \Delta t = \eta_1 \langle I_1(t) \rangle \Delta t \tag{2.3}$$

where η_1 is the detection efficiency of detector '**D1**'. Now, for the two-detector system with a lossless beam splitter described in Figure 2.1 (b) as well as the introduction of the delay time of, τ, on detector **D1**, the combined photon counting probability is as follows:

$$P_{12}(\tau)\Delta t^2 = \eta_1 \eta_2 \langle I_1(t+\tau) I_2(t) \rangle \Delta t^2 \tag{2.4}$$

Thus, the second-order correlation function, $g^2(\tau)$, is given by dividing the combined probability of detection by individual probabilities as:

$$g^2(\tau) = \frac{P_{12}(\tau)}{P_1 P_2} \tag{2.5}$$

Solving Equation (2.5) at $\tau = 0$, yields

$$g^2(\tau = 0) = \frac{P_{12}(0)}{P_1 P_2} = \frac{\langle I_1(t) I_2(t) \rangle}{\langle I_1(t) \rangle \langle I_2(t) \rangle} \geq 0 \tag{2.6}$$

Therefore, the semiclassical consideration gives the same second-order correlation relation for chaotic and coherent light sources as the classical approach. In a coherent light beam, the photons are uncorrelated (do not fluctuate) with signature $g^2(\tau = 0) = 1$ at $P_{12}(0) = P_1 P_2$. Moreover, the second-order correlation function is also used to identify chaotic light sources which show a positive correlation with $g^2(\tau = 0) > 1$ showing intensity fluctuates at both detectors.

The classical and semiclassical approach to constructing intensity and photon count correlations at detectors assume the wave-like electromagnetic property of light. However, for a full description of the particle-like properties of photons, a quantum mechanical formulation is required. Thus, in the following approach, second-order correlations are constructed considering both a quantum mechanical light beam (single photons) and detectors.

2.1.2 Quantum mechanical approach for the analysis of photon statistics

Consider the same beam splitter as in the classical and semiclassical cases above where the incident beam now is quantised – the coincidence of photon-stream is split into the two detectors as shown in Figure 2.3 (b). The discussion presented here is based on [5, 57, 66, 67] and references therein. In this case, the second-order correlation function is expressed in terms of intensity operators $\hat{n}_1$ and $\hat{n}_2$ with a delay time, τ, as

$$g^2(\tau) = \frac{\langle \hat{n}_1(t)\hat{n}_2(t+\tau)\rangle}{\langle \hat{n}_1(t)\rangle\langle \hat{n}_2(t+\tau)\rangle} = \frac{\langle \hat{a}_1^\dagger(t)\hat{a}_2^\dagger(t+\tau)\hat{a}_2(t+\tau)\hat{a}_1(t)\rangle}{\langle \hat{a}_1^\dagger(t)\hat{a}_1(t)\rangle\langle \hat{a}_2^\dagger(t+\tau)\hat{a}_2(t+\tau)\rangle} \tag{2.7}$$

where $\hat{a}_i$ and $\hat{a}_i^\dagger$ are the electric field annihilation and creation operators, respectively and $\hat{n}_i = \hat{a}_i^\dagger \hat{a}_i$. Also, now the average of the operators is understood as the expectation value, which is the dot product of the operators. As the most important distinction between the second-order correlations of different light sources occurs at zero delay time, $\tau = 0$, further discussion drops the time variable.

Furthermore, the quantum mechanical system allows operators $\hat{a}_1$ and $\hat{a}_2$ be expressed as the linear superposition of input field operators ($\hat{a}_I$) and vacuum field operator ($\hat{a}_V$) (see Figure 2.3 (a)) arriving at the lossless beam splitter. For a choice of phase, it can be shown the superposition is given by

$$\hat{a}_1 = \frac{1}{\sqrt{2}}(\hat{a}_I + \hat{a}_V) \quad , \; \hat{a}_2 = \frac{1}{\sqrt{2}}(\hat{a}_I - \hat{a}_V) \tag{2.8}$$

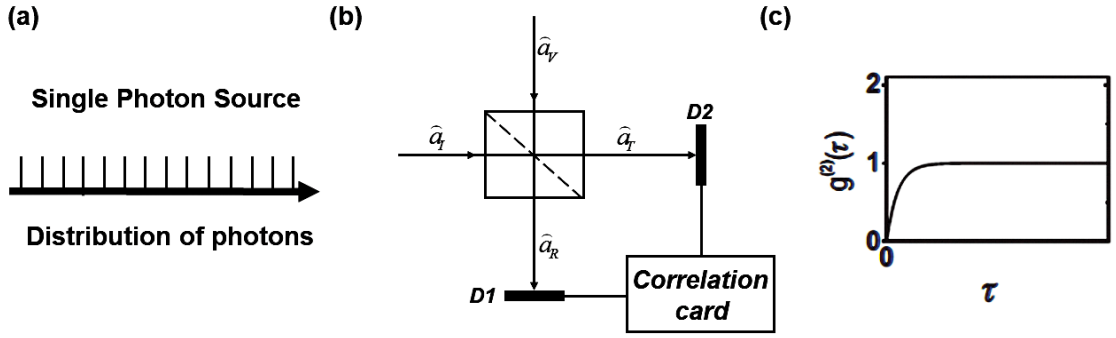

Figure 2.3: Single photon distribution at detectors with a characteristic time spacing. (b) Field operators at a beam splitter (c) Single photon autocorrelation function where the $g^2(\tau = 0) = 0$. This is referred to as photon antibunching[64].

Substituting equation (2.8) in (2.7) and using the additional commuter relation between field operators: $\hat{a}_i \hat{a}_i^\dagger - \hat{a}_i^\dagger \hat{a}_i = 1$, the $g^2(\tau = 0)$ as a function of the number of photons (n) arriving at detectors is expressed as

$$g^2(\tau = 0) = \frac{\langle n(n-1) \rangle}{\langle n \rangle^2} = \frac{\langle n^2 \rangle - \langle n \rangle}{\langle n \rangle^2} \tag{2.9}$$

Using the photon-number variance (Δn^2) given by the relation $(\Delta n)^2 = \langle n^2 \rangle - \langle n \rangle^2$, equation (2.9) further reduces to

$$g^2(\tau = 0) = 1 + \frac{(\Delta n)^2 - \langle n \rangle}{\langle n \rangle^2} \tag{2.10}$$

Considering that a photon-number variance is a whole number, equation (2.10) can be expressed

$$g^2(\tau = 0) \geq 1 - \frac{1}{\langle n \rangle} \text{ for } \langle n \rangle \geq 1 \tag{2.11}$$

Equation (2.11) already shows a new lower limit of 0 for $\langle n \rangle = 1$ that was not indicated when the $g^2(\tau = 0)$ is derived using both classical and semiclassical approaches. Following characteristic $g^2(\tau = 0)$ values are obtained for different light sources.

Chaotic light source: The photon number probability, $P(n)$, of such light source is given by

$$P(n) = \frac{\langle n \rangle^n}{(1 + \langle n \rangle)^{1+n}} \tag{2.12}$$

The variance that follows from this relation is given as

$$(\Delta n)^2 = \langle n \rangle^2 + \langle n \rangle \tag{2.13}$$

where the variance of chaotic states differs from the coherent counterparts by the mean square. Substituting equation (2.17) in (2.10), the reduced second-order correlation function for chaotic light source gives $g^2(\tau = 0) = 2$. Again, this result is consistent with the one obtained using the classical and semiclassical approaches where photons arrive at detectors together at the same time. This is bunching of photons, and it is a natural tendency of photons. Experimentally, SPEs may appear to bunch when the coherence time between individual photons is less than the time resolution of detectors. Such observation entails an important property of the transition kinetics of the SPEs as will be discussed in Chapter 5.

To conclude, in a single photon, coherent and chaotic light sources, the nature of the photon statistics can be deduced comprehensively using the quantum mechanical approach. Coherent and chaotic light sources follow super-Poissonian ($(\Delta n)^2 > \langle n \rangle$) and Poissonian ($(\Delta n)^2 = \langle n \rangle$

), statistics respectively. True single photon emitter with $(\Delta n)^2 = 0$, on the other hand, follow sub-Poissonian photon statistics with $(\Delta n)^2 < \langle n \rangle$, for a time delay of zero; However, depending on the transition kinetics of specific emitters, practical photon statistics of SPE may deviate from sub-Poissonian statistics as will be discussed in subchapter 2.3.

Coherent light source: The statistics for this source can be expressed as a superposition of single states $|n\rangle$ giving a coherent state $|\alpha\rangle$ which is expressed in terms of annihilation operator as $\hat{\alpha}|\alpha\rangle = \alpha|\alpha\rangle$. The conjugate product between the creation and annihilation operator yields the expectation value of the coherent state, $\langle n \rangle$, given by the relation [5]

$$\langle n \rangle = \langle \alpha | \hat{\alpha}^{\dagger} \hat{\alpha} | \alpha \rangle = \langle \alpha | n | \alpha \rangle = |\alpha|^2 \tag{2.14}$$

Similarly, the expectation value of the mean-square coherent state, $\langle n^2 \rangle$, can be shown to yield

$$\langle n^2 \rangle = \langle \alpha | \hat{n}^2 | \alpha \rangle = |\alpha|^4 + |\alpha|^2 = \langle n \rangle^2 + \langle n \rangle \tag{2.15}$$

where the photon-number variance is now

$$(\Delta n)^2 = |\alpha|^2 = \langle n \rangle \tag{2.16}$$

Finally, substituting equation (2.15) in (2.10) gives the second-order correlation function for a coherent state of $g^2(\tau = 0) = 1$. This result is consistent with the one obtained using classical and semiclassical approaches for coherent light sources as discussed before and shown in Figures 2.2.

Single Photon Emitter (SPE): These group of light sources emit individual photons separated by characteristic time as depicted in Figure 2.3 (a). Thus, for single photons, the relation $\hat{n}|n\rangle = 1|n\rangle$ holds where $|n\rangle$ is the single mode number state and eigenvalue of 1. This shows that there is no uncertainty in the photon number of the single photons yielding

variance of zero, (i.e. $\Delta n^2 = 0$) where now equation (2.11) can be reduced to a second-order correlation of the form [5]

$$g^2(\tau = 0) = 1 - \frac{1}{n} \tag{2.17}$$

where $n = 1$, $g^2(\tau = 0) = 0$. This is called antibunching, and it is a purely quantum mechanical phenomenon violating the limit set by the classical and semiclassical approaches before ($g^2(\tau = 0) \geq 1$). Antibunching behaviour of SPE under cw-laser excitation is illustrated by the second-order correlation plot in Figure 2.3 (c).

Single photon emitters from defects in wide bandgap semiconductors are the central subject of this work. Hence, extensive experimental results and discussion will be presented in subsequent chapters. As it will be shown, the theoretical value of $g^2(\tau = 0) = 0$ may not be achieved experimentally due to, for example, background contribution. However, $g^2(\tau = 0) < 0.5$ is still considered to index a single photon emitter because higher photon number ($n \geq 2$) will result in $g^2(\tau = 0) \geq 0.5$. The experimental interpretation of this phenomenon is that a single photon cannot be measured at two detectors with zero delay time.

2.2 Excitation of single photon emitters

The focus of this thesis is the generation and detection of single photon emitters. The standard experimental approach to detecting SPEs is by using the HBT set-up. This method relies on 50:50 beam splitter dividing the incident cascade of single photons into two detectors (avalanche photodiodes) as shown in Figure 2.3 (b). By introducing a time delay at the channel of one of the detectors, histogram of photon coincidence can be built based on arrival time differences at the two detectors. Time-to-amplitude converter (TAC or correlation card) is usually used to register and bin the detection events into the histogram shown in Figure 2.3 (c). The measurement obtained this way can be modelled well by using equation (2.7) where delay time (τ) is much smaller than the average arrival time difference at the two detectors

ensuring small count rates. Under this condition, $g^2(\tau)$ in equation (2.7) corresponds to the joint probability of detecting a photon at t and an immediately preceding photon at $t+\tau$. While the time correlation measurement and HBT set-up will be discussed in more detail in Chapter 4, it is clear the time difference between subsequent photons arriving at the BS affects the histogram constructed when using such measurement.

In an ideal SPE, the generation of individual photons is separated by characteristic time, namely the excited state lifetime [8, 68]. This is the amount of time it takes the excited state to decay back to ground state emitting a photon upon recombination for every pumping cycle. Thus, recombination mechanisms dictate the rate and thus the distribution of the coincidence of photons at detectors. Two major factors that affect recombination mechanism in single photon emitters are a number of energy levels involved in the transition kinetics of the SPE as well as the excitation technique used to stimulate transition. Thus, expressing second-order correlation function ($g^2(\tau)$) in terms of lifetimes not only will it elucidate the transition kinetics but also help determine the rate coefficients involved in the transition. The first part of this section of the thesis, therefore, reviews the analysis of $g^2(\tau)$ when a SPE is under cw - laser excitation. The case of a two- and three-level single photon emitting system are considered to obtain further relation of decay rates. As a result, the distinction in $g^2(\tau)$ function when using a cw- laser excitation will be highlighted.

2.2.1 Continuous-wave (cw)-laser excitation of single photon emitters

Laser excitation of SPEs is normally carried out by focusing the beam via high-resolution objectives. The beam waist of the focused laser is diffraction limited, where for visible lasers the spot size reaching several hundreds of nanometers. Thus, the spot size covers a large area on the sample exciting multiple SPEs that lie within its diameter. In such case, the total fluorescence intensity at a time t from multiple SPEs can be written as the summation of individual intensities expressed as [69-71]

$$I(t) = \sum_{j=1}^{N} i_j(r_j, t) \tag{2.18}$$

where i_j is the intensity from individual emitter j located at r_j and N is the total number of SPEs with the laser spot. Now, let's re-write the normalised second-order correlation function ignoring short time aberration caused by detector dead-time as

$$g^2(\tau) = \frac{\langle I(t)I(t+\tau)\rangle}{\langle I\rangle^2} \tag{2.19}$$

Thus, the numerator in equation (2.19) follows as

$$\langle I(t)I(t+\tau)\rangle = \left\langle \sum_{j=1}^{N} i_j(r_j, t) \sum_{k=1}^{N} i_k(r_k, t+\tau) \right\rangle \tag{2.20}$$

Assuming individual emission events are independent of each other both in amplitude and phase, intensity fluctuation average from the same source ($j = k$) can be separated from those coming from different sources ($j \neq k$) yielding

$$\langle I(t)I(t+\tau)\rangle = N\langle i_j(r_j, t) i_k(r_k, t+\tau)\rangle_{j=k} + N(N-1)\langle i_j(r_j, t) i_k(t+\tau)\rangle_{j\neq k} \tag{2.21}$$

with the average intensity from N emitters written as $\langle I\rangle = N\langle i\rangle$. Now, discrete intensities can be expressed in terms of probability of emission per time ($p_j(t)$) and collection efficiency as a function of the respective location ($\eta_j(r_j)$) as $i_j(r_j, t) = \eta_j(r_j) p_j(t)$ giving

$$\langle I\rangle = N\langle \eta\rangle\langle p\rangle \tag{2.22}$$

Substituting equation (2.21) into (2.22) results in

$$\begin{aligned} \langle I(t)I(t+\tau)\rangle &= N\langle p(t)p(t+\tau)\rangle\langle \eta(r,t)\eta(r',t+\tau)\rangle \\ &\quad + N(N-1)\langle\langle p_j(t)p_k(t+\tau)\rangle\langle \eta_j(r_j)\eta_k(r_k)\rangle\rangle \end{aligned} \tag{2.23}$$

Considering individual emission events are independent, equation (2.23) can further be simplified as

$$= \quad N\langle p(t)p(t+\tau)\rangle\langle \eta(r,t)\eta(r',t+\tau)\rangle + N(N-1)\langle p^2\rangle\langle \eta^2\rangle \tag{2.24}$$

Now the $g^2(\tau)$ can be written as

$$g^2(\tau) = \frac{N(N-1)}{N^2} + \frac{1}{N}\frac{\langle p(t)p(t+\tau)\rangle}{\langle p\rangle^2}\frac{\langle \eta(r,t)\eta(r',t+\tau)\rangle}{\langle \eta\rangle^2} \tag{2.25}$$

Looking at the second term in equation (2.25), it indicates that detection efficiency varies if a particle at position r at time t moves to a new position r' at $t+\tau$. Thus, for a stationary SPE $\langle \eta(r,t)\eta(r',t+\tau)\rangle = \langle \eta\rangle^2$ reducing equation (2.25) to

$$g^2(\tau) = \frac{N(N-1)}{N^2} + \frac{1}{N}\frac{\langle p(t)p(t+\tau)\rangle}{\langle p\rangle^2} \tag{2.26}$$

Thus, the second-order correlation function is now expressed in terms of probability of radiative emission at two different times.

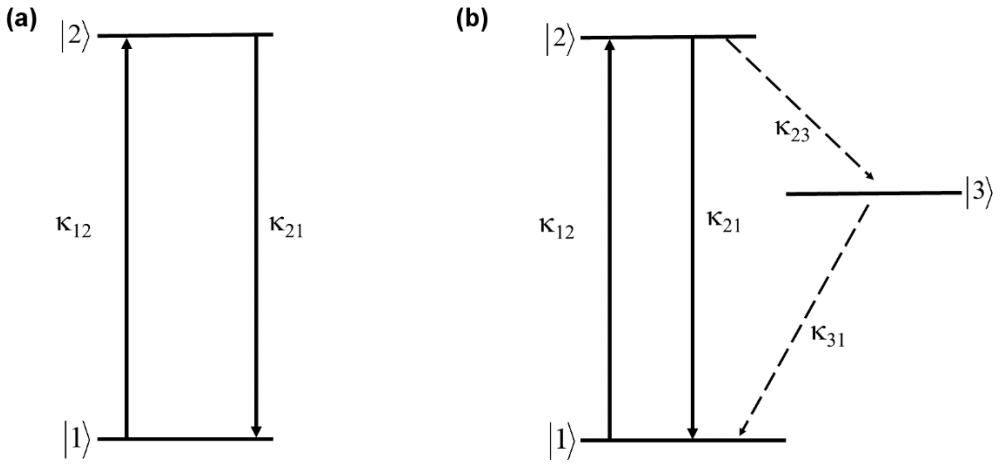

Figure 2.4: Energy level diagrams illustrating transition kinetics with decay paths and corresponding rate coefficients (a) two-level transition kinetics (b) three-level transition kinetics.

Consider now single photon emitters with a two- and three- energy level transition systems as shown in Figure 2.4 (a&b). By looking at the two-level energy diagram in Figure 2.4 (a) first, a particle is pumped from the ground state $|1\rangle$ to the excited state $|2\rangle$ using a cw-laser of a certain power. The particle's transition rate to the excited state is κ_{12}. The excited particle decays back to the ground state radiatively via the rate κ_{21} emitting a photon. Looking closer at this simple transition, the probability of being in state $|2\rangle$ at any time ($p_2(\infty)$) is

proportional to the probability of emission. Thus, detecting a photon at a time t is proportional to $p_2(\infty)$ (i.e. $\alpha p_2(\infty)$) at which time the system is back to the ground state $|1\rangle$. Thus, a subsequent photon emission τ time later depends on the time it took the system to reach the ground state (t). Therefore, the subsequent emission is proportional to $p_2(t,1;\tau)$. The detection of a subsequent photon emission then follows with proportionality $\alpha p_2(t,1;\tau)$. This consideration modified the probability term in equation (2.26) as [69, 72]

$$\frac{\langle p(t)p(t+\tau)\rangle}{\langle p\rangle^2} = \frac{\alpha^2 p_2(\infty)\langle p_2(t,1;\tau)\rangle}{\alpha^2 p_2^2(\infty)} = \frac{\langle p_2(t,1;\tau)\rangle}{p_2(\infty)} \tag{2.27}$$

By going back to the two-level diagram, rate equations can be written for the population dynamics as

$$\frac{dp_1(\tau)}{dt} = -\kappa_{12}p_1(\tau) + \kappa_{21}p_2(\tau) \tag{2.28}$$

$$\frac{dp_2(\tau)}{dt} = \kappa_{12}p_1(\tau) - \kappa_{21}p_2(\tau) \tag{2.29}$$

where $p_1 + p_2 = 1$, indicating there is no additional channel for decay. The rate equations (2.28) and (2.29) are a system of linear differential equations and can be written in matrix form as

$$\frac{d}{dt}\begin{pmatrix} p_1(\tau) \\ p_2(\tau) \end{pmatrix} = \begin{pmatrix} -\kappa_{12} & \kappa_{21} \\ \kappa_{12} & -\kappa_{21} \end{pmatrix}\begin{pmatrix} p_1(\tau) \\ p_2(\tau) \end{pmatrix} \tag{2.30}$$

To solve this equation, eigenvalues, λ, of the matrix A is determined using the relation

$$(A - \lambda I) = 0 \text{ where } A = \begin{pmatrix} -\kappa_{12} & \kappa_{21} \\ \kappa_{12} & -\kappa_{21} \end{pmatrix} \text{ and } \lambda I = \begin{pmatrix} \lambda & 0 \\ 0 & \lambda \end{pmatrix}$$

with I as the identity matrix. Consequently, the two eigenvalues determined are $\lambda_1 = 0$ and $\lambda_2 = k_{12} + \kappa_{21}$ corresponding to eigenvectors of $\begin{pmatrix} a_1 \\ \kappa_{12} a_1 / \kappa_{21} \end{pmatrix}$ and $\begin{pmatrix} -a_2 \\ a_2 \end{pmatrix}$, respectively. Thus, the solution is then written as the linear combination of the exponential as

$$\begin{pmatrix} p_1(\tau) \\ p_2(\tau) \end{pmatrix} = a_1 \begin{pmatrix} 1 \\ \kappa_{12}/\kappa_{21} \end{pmatrix} \exp(0) + a_2 \begin{pmatrix} -1 \\ 1 \end{pmatrix} \exp(-(\kappa_{12} + \kappa_{21})\tau) \tag{2.31}$$

For the initial condition $\begin{pmatrix} p_1(0) \\ p_2(0) \end{pmatrix} = \begin{pmatrix} 1 \\ 0 \end{pmatrix}$, coefficients for the eigenvectors yield

$$a_1 = \frac{\kappa_{21}}{\kappa_{12} + \kappa_{21}} \text{ and } a_2 = \frac{-\kappa_{12}}{\kappa_{12} + \kappa_{21}} \tag{2.32}$$

Thus, giving linear differential equation written as

$$\begin{pmatrix} p_1(\tau) \\ p_2(\tau) \end{pmatrix} = \begin{pmatrix} a_1 & -a_2 \\ \kappa_{12} a_1 / \kappa_{21} & a_2 \end{pmatrix} \begin{pmatrix} \exp(-\lambda_1 \tau) \\ \exp(-\lambda_2 \tau) \end{pmatrix} = \begin{pmatrix} \frac{\kappa_{21}}{\kappa_{12} + \kappa_{21}} & \frac{\kappa_{12}}{\kappa_{12} + \kappa_{21}} \\ \frac{\kappa_{12}}{\kappa_{12} + \kappa_{21}} & \frac{-\kappa_{12}}{\kappa_{12} + \kappa_{21}} \end{pmatrix} \begin{pmatrix} \exp(-\lambda_1 \tau) \\ \exp(-\lambda_2 \tau) \end{pmatrix} \tag{2.33}$$

Solving equation (2.33) by recalling $\lambda_1 = 0$

$$\begin{aligned} \frac{\langle p_2(t,1;\tau) \rangle}{p_2(\infty)} &= \frac{\frac{\kappa_{12}}{\kappa_{12} + \kappa_{21}} \exp(0) - \frac{\kappa_{12}}{\kappa_{12} + \kappa_{21}} \exp(-(\kappa_{12} + \kappa_{21})\tau)}{\frac{\kappa_{12}}{\kappa_{12} + \kappa_{21}}} \\ &= 1 - \exp(-(\kappa_{12} + \kappa_{21})\tau) \end{aligned} \tag{2.34}$$

Hence, the second-order correlation function for a single photon emitter (N=1) in equation (2.26) is re-written to give

$$g^2(\tau) = \frac{N(N-1)}{N^2} + \frac{1}{N}(1 - \exp(-(\kappa_{12} + \kappa_{21})\tau) = 1 - \exp(-\tau / t_d) \tag{2.35}$$

where the antibunching time constant $t_d = 1/\lambda_1 = 1/(\kappa_{12} + \kappa_{21})$. It can also be noted that $g^2(\tau = 0) = 0$. Figure 2.5 (a) illustrates a typical histogram of photon coincidence as a function of delay time built using TAC when recording single photons from ideal emitters with two energy levels. However, due to background contribution, experimental measurements deviate from the ideal case of $g^2(\tau = 0) = 0$ as shown in Figure 2.5 (b). Thus, to account for the background, a scaling factor (ρ) is usually used modifying equation (2.35) to [73]

$$g^2(\tau) = 1 - \rho^2 \exp(-\tau/t_d) \tag{2.36}$$

where $\rho = \frac{S}{S+B}$; S and B are the signal and background counts. The physical origin of this scaling factor will be discussed below for a three-level system.

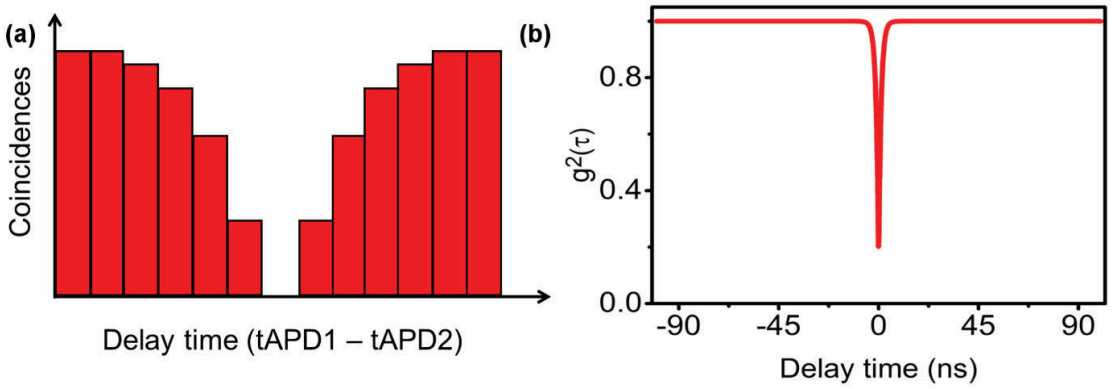

Figure 2.5: (a) Schematics is showing coincidence statistics during a second-order correlation measurement for a single photon emitter. (b) The real second-order function used to fit data with background contribution offsetting $g^2(0)$.

The same approach can be used to derive $g^2(\tau)$ description in terms of radiative and nonradiative lifetimes in the three-energy level of a single photon emitter depicted in Figure 2.4(b). In such systems, the excited state has an alternative decay path to the ground. That is, first via κ_{23} to shelving (triple) state, $|3\rangle$, followed by non-radiative transition via κ_{31} to the

ground state, $|1\rangle$. While the transition from $|3\rangle$ back to $|2\rangle$ could occur, for most practical cases this transition has the same effect as the transition from $|3\rangle$ to $|1\rangle$, hence is neglected in the following derivation. Such system describes single photon emission kinetics in a wide variety of platforms including single molecules[71, 74], quantum dots (QDs)[75, 76] and many defects in wide bandgap semiconductors[24, 77-80].

The full derivation of the three-level system is provided in [69]. Here, brief revision is provided following the same steps as in the case of the two-level system before. Now the matrix form of the rate equation is given by

$$\frac{d}{dt}\begin{pmatrix} p_1(\tau) \\ p_2(\tau) \\ p_3(\tau) \end{pmatrix} = \begin{pmatrix} -\kappa_{12} & -\kappa_{21} & \kappa_{31} \\ \kappa_{12} & -(\kappa_{23}+\kappa_{21}) & 0 \\ 0 & \kappa_{23} & -\kappa_{31} \end{pmatrix} \begin{pmatrix} p_1(\tau) \\ p_2(\tau) \\ p_3(\tau) \end{pmatrix} \tag{2.37}$$

where additional rate coefficients are considered for the shelving state occupation probability, p_3. By using the same approach as the two-level system above, eigenvalues for the matrix of rate coefficients are determined to yield

$$\begin{aligned} \lambda_1 &= \frac{1}{2}(\kappa_{12}+\kappa_{21}+\kappa_{31}+\kappa_{23}+\sqrt{(\kappa_{12}+\kappa_{21}+\kappa_{23}-\kappa_{31})^2-4\kappa_{12}\kappa_{23}}) \\ \lambda_2 &= \frac{1}{2}(\kappa_{12}+\kappa_{21}+\kappa_{31}+\kappa_{23}-\sqrt{(\kappa_{12}+\kappa_{21}+\kappa_{23}-\kappa_{31})^2-4\kappa_{12}\kappa_{23}}) \\ \lambda_3 &= 0 \end{aligned} \tag{2.38}$$

Considering much higher radiative decay rate to the ground state than the nonradiative decay rate via the shelving state (i.e. $\kappa_{21} >> \kappa_{23}+\kappa_{31}$), the eigenvalues further simplify to

$$\begin{aligned} \lambda_1 &= \kappa_{12}+\kappa_{21} \\ \lambda_2 &= \kappa_{31}+\kappa_{23}\kappa_{12}/(\kappa_{12}+\kappa_{21}) \end{aligned} \tag{2.39}$$

Now, the general solution for equation (2.37) in matrix form is given by

$$\begin{pmatrix} p_1(\tau) \\ p_2(\tau) \\ p_3(\tau) \end{pmatrix} = \begin{pmatrix} a_{11} & a_{12} & a_{13} \\ a_{21} & a_{22} & a_{23} \\ a_{31} & \kappa_{31} & a_{33} \end{pmatrix} \begin{pmatrix} \exp(-\lambda_1\tau) \\ \exp(-\lambda_2\tau) \\ \exp(-\lambda_3\tau) \end{pmatrix} \tag{2.40}$$

The equilibrium population of the excited state $|2\rangle$ occur at $t \to \infty$ with eigen coefficients corresponding to the eigenvalue (i.e. a_{13}, a_{23} and a_{33}). Independent of the initial condition, analytical solution for the coefficients yields,

$$\begin{aligned} a_{13} &= \kappa_{21}\kappa_{31} \Big/ (\kappa_{21}\kappa_{31} + \kappa_{12}\kappa_{31} + \kappa_{12}\kappa_{23}) \\ a_{23} &= \kappa_{12}\kappa_{31} \Big/ (\kappa_{21}\kappa_{31} + \kappa_{12}\kappa_{31} + \kappa_{12}\kappa_{23}) \\ a_{33} &= \kappa_{21}\kappa_{23} \Big/ (\kappa_{21}\kappa_{31} + \kappa_{12}\kappa_{31} + \kappa_{12}\kappa_{23}) \end{aligned} \tag{2.41}$$

with $p_2(\infty) = a_{23}$.

Again, the initial condition $\begin{pmatrix} p_1(\tau) \\ p_2(\tau) \\ p_3(\tau) \end{pmatrix} = \begin{pmatrix} 1 \\ 0 \\ 0 \end{pmatrix}$ is considered to solve for the rest of the coefficients yielding

$$\begin{aligned} a_{21} &= \kappa_{12} \Big/ (\kappa_{12} + \kappa_{21}) \\ a_{21} &= \kappa_{12}^2\kappa_{23} \Big/ (\kappa_{21}\kappa_{31} + \kappa_{12}\kappa_{31} + \kappa_{12}\kappa_{23})(\kappa_{12} + \kappa_{21}) \end{aligned} \tag{2.42}$$

The normalisation then yields,

$$\frac{\langle p_2(t,1;\tau)\rangle}{p_2(\infty)} = 1 - (1+a)\exp(-\lambda_1\tau) + a\exp(-\lambda_2\tau) \tag{2.43}$$

Substituting this in equation (2.26) and solving for *N*=1 yields

$$g^2(\tau) = \frac{N(N-1)}{N^2} + \frac{1}{N}((1+a)\exp(-\lambda_1\tau) + a\exp(-\lambda_2\tau))$$
$$= 1-(1+a)\exp(-\lambda_1\tau) + a\exp(-\lambda_2\tau) \quad (2.44)$$

Thus, the second-order correlation function for a three-level system is given by

$$g^2(\tau) = 1-(1+a)\exp(-\lambda_1\tau) + a\exp(-\lambda_2\tau) \quad (2.45)$$

where

$$\lambda_1 = \kappa_{12} + \kappa_{21}$$
$$\lambda_2 = \kappa_{31} + \kappa_{23}\kappa_{12}/(\kappa_{12} + \kappa_{21})$$
$$a = \kappa_{12}\kappa_{23}/[\kappa_{31}(\kappa_{12} + \kappa_{21})]$$

Equation (2.45) describes the second-autocorrelation function of an ideal SPE for a three-level system where at $g^2(\tau=0) = 0$. Experimentally, the normalised $g^2(\tau)$ is obtained from the photon coincidence number, $c(t)$, integrated over a period of T using a time bin width of w as [81, 82]:

$$g^2(\tau) = \frac{c(t)}{R_1 R_2 T w} \quad (2.46)$$

where R_1 and R_2 are the count rates at each detector. This relation is fully correlated and normalised to 1 for large integration periods following Poissonian distribution. In real emitters, however, $g^2(\tau=0)$ value usually deviate from the zero-value indicating the presence of uncorrelated background contribution (ρ) in the coincidence measurement. To correct for this background count, the signal and background counts are measured independently. The corrected second-order autocorrelation function ($g_c^2(\tau)$) is then given by [82]:

$$g_c^2(\tau) = \frac{(g^2(\tau) - (1-\rho^2))}{\rho^2} \quad (2.47)$$

where ρ is the signal to background ratio. The other common cause for $g^2(\tau=0)$ to deviate from zero is impulse response function (IRF) of detectors [81]. This is typically a Gaussian

function with characteristic linewidth, which can be measured independently. The Gaussian function can then be convoluted with equation (2.45) to correct for the IRF.

A clear distinction can be observed in the expressions of $g^2(\tau)$ for a two- and three-level system highlighting the difference in intensity fluctuations as consequence of transition dynamics difference. The radiative decay for both level systems occurs as result of the transition from the excited state, $|2\rangle$, directly down to the ground state, $|1\rangle$ via rate coefficient, κ_{21} as shown in Figure 2.4 (a)&(b). However, for the three-level system a non-radiative decay via the shelving state, $|3\rangle$, gives rise to the second exponential term in equation (2.45) with decay rate, λ_2. The non-radiative decay rate indicates that for a three-level system, the intensity undergoes a "dark" state decreasing the efficiency of single photon emission. Experimentally, this is depicted by a drop in the $g^2(\tau)$ value in the short-time scale of hundreds of ns as shown in Figure 2.6 (a).

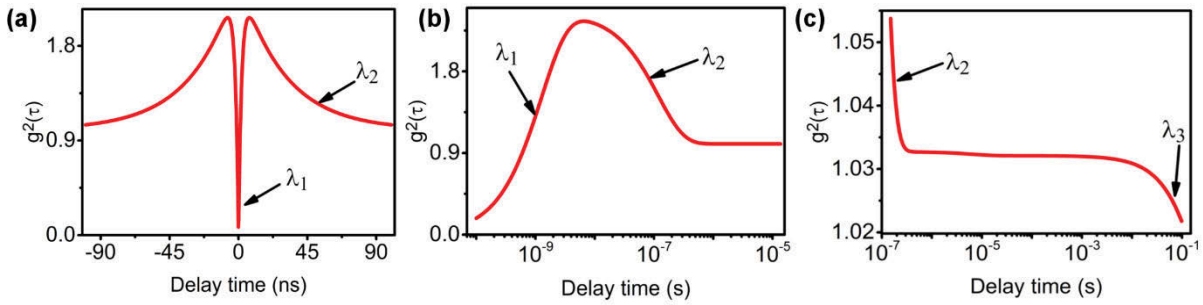

Figure 2.6: Antibunching characteristics of SPE in GaN with a three-level transition. (a) $g^2(\tau)$ vs delay time generated using equation (2.44) by considering a correlation time of up to 100 ns. (b) $g^2(\tau)$ vs delay time generated using equation (2.44) by considering a correlation time of up to 15 μs . The antibunching rate (λ_1) and fast non-radiative decay rate via shelving state (λ_2) are depicted occurring at different time scales. (c) $g^2(\tau)$ vs delay generated using double decay function for long periods of from a few μs to 0.1 ms showing once again the λ_2 and additional long-lived, dark-state with rate λ_3 appearing once again at different time scales.

This is distinct from the $g^2(\tau)$ behaviour of its counterpart two-level SPE shown in Figure 2.5 (b), where $g^2(\tau)$ value remained constant along the normal. If the $g^2(\tau)$ from a three-level SPE is correlated for more extended periods of time (~ up to a few μs), the drop in the $g^2(\tau)$ normalises as shown in Figure 2.6 (b). However, if additional shelving state (4th state) that is weakly coupled to the antibunching is involved in the transition kinetics of the three-level SPE, it will further reduce $g^2(\tau)$ showing a drop in long-timescale (μs to min) as shown in Figure 2.6 (c)[25, 83]. This is a significant relationship and will be used extensively to demonstrate the transition kinetics of the novel single photon emitters in GaN in this thesis.

The basics behind electroluminescence from defects in wide bandgap semiconductor are the focus of the second part of this section. This will be presented to frame the result presented in chapter 7, where SiV centre in diamond showed fluorescence under injection of excess carriers into its vicinity.

2.2.2 Electrical excitation of single photon emitters

The other increasingly explored technique of excitation is electroluminescence, where excess carriers are injected into the single photon emitting systems resulting in radiative recombination [19, 76, 84-87]. This technique is distinct from optical excitation technique using mainly lasers (photoluminescence) discussed above, both in the way the external energy is applied as well as recombination mechanism resulting in the emission of single photons. Such excitation technique allows electrically controlled single photon generation promising the realisation of large-scale integrated quantum devices. Also, using external voltage supply to inject/withdraw current into the SPE reveals fundamental properties such as charge state switching in emitters.

Electrically driven excitation requires incorporation of SPEs in the active region of a device junction where efficient injection of excess carriers will be trapped by the emitters.

Subsequent decay of trapped carriers with characteristic time will result in the emission of single photons. Primary semiconductor junction structures for single photon emission are presented. This is followed by a discussion of excess carrier trap and decay mechanism at single photon sites.

2.2.2.1 PN Junctions: Current and single photon emitting diodes

For electrically driven single photon emission, recombination of excess charge carriers must occur between energy levels of SPE. Thus, incorporation of emitters into classical devices is inevitable to introduce excess carriers into the vicinity of the energy levels. Here, a simplified review of the basics of common semiconductor junctions that are backbones for single photon emitting diodes is covered to understand charge flow and driving forces behind excess carrier injection.

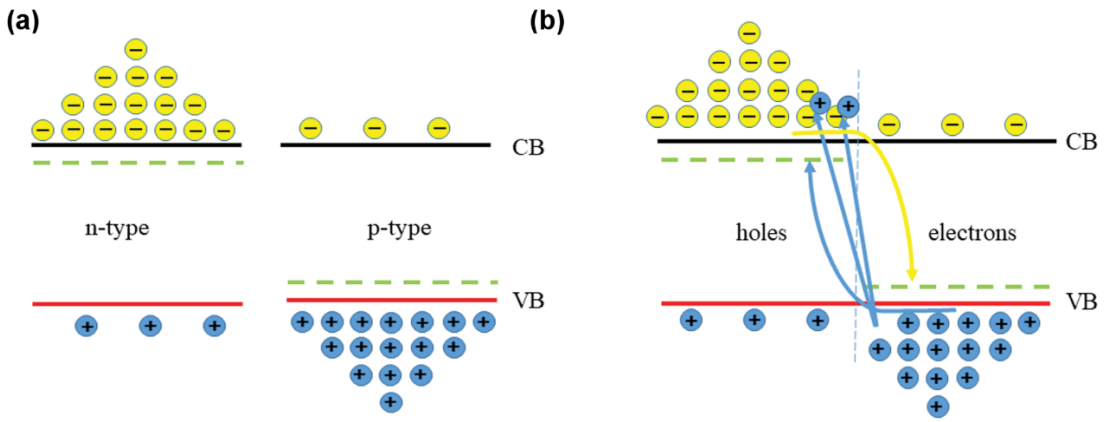

Figure 2.7: Energy band diagrams of two semiconductors that are n- and p-doped.. (a) Before contact majority electrons reside in the conduction band (CB) of the n-doped semiconductors while majority holes reside in the valence band (VB) and p-doped semiconductor. (b) At contact, majority carriers from both sides diffuse into the opposite side to become a minority carrier before they recombine and dissipate.

Consider two semiconductors of the same kind that are doped differently (n-doped & p-doped) and are brought to close contact as shown by the band diagram in Figure 2.7 (a). The dotted line in the respective band diagrams represents the Fermi energy levels of the n-doped (majority carrier electrons) and p-doped (majority carrier holes). Upon contact, however, holes can diffuse to the n-side across the junction leaving behind acceptor-impurities in the

p-side becoming a minority carrier as shown in Figure 2.7 (b)[88, 89]. This will, of course, lower the Fermi energy level of the n-side and raises it on the p-side. The same conclusion can be drawn considering electron-minority flow to the p-side leaving behind donor-impurities in the n-side, but that is intuitive considering holes are the absence of electrons. This diffusion process near the junction will result in recombination of majority carrier to minority carriers resulting in conservation of charge via photon emission as well as momentum.

The diffusion of carriers cannot continue forever, however, due to electric field build up across the junction between the fixed acceptor- and donor-impurities[90, 91]. This inbuilt field will screen charge flow pushing holes to p-side and electrons to n-side. This region, which is devoid of carriers, is referred to as depletion region or the space charge region (SCR). In other words, the minority carrier flow now has to overcome a potential barrier, V_b, due to the built-in electric field. This is expressed as band-bending in the band diagram shown in Figure 2.8, with a potential step indicating the barrier for free carrier movement. Also, at thermal equilibrium, the Fermi level of the system is the same everywhere indicated by the broken black line in the middle.

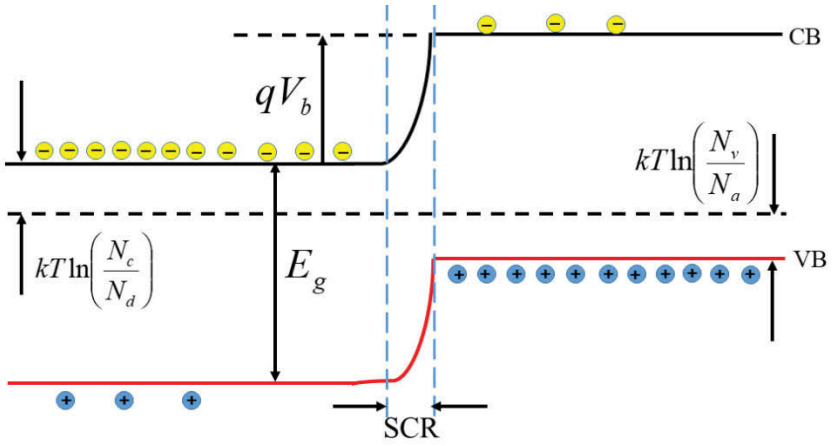

Figure 2.8: The band energy diagram with subsequent band bending when two semiconductors that are n- and p-doped come in contact at equilibrium.

Let's now derive a quantitative description of the built-in potential, V_b, at thermal equilibrium. The difference in energy between of fermi level (E_f) and the conduction (E_c) and valence (E_v) band is given by [89]

$$\begin{aligned} E_c - E_f &= \kappa T \ln\left(\frac{N_c}{N_d}\right) \\ E_f - E_v &= \kappa T \ln\left(\frac{N_v}{N_a}\right) \end{aligned} \tag{2.48}$$

where N_c and N_v are intrinsic carrier concentration and are material dependent parameters. Whereas, N_d and N_a are electron and hole carrier densities, respectively which depend on the doping levels of the n- and p-type semiconductors. κT is the product of the Boltzmann constant and temperature which yields 25 meV at RT. By looking at Figure 2.8, it can easily be seen that

$$\begin{aligned} qV_b &= E_g - (E_c - E_f) - (E_f - E_v) \\ &= E_g - kT\ln\left(\frac{N_c}{N_d}\right) - kT\ln\left(\frac{N_v}{N_a}\right) \\ &= E_g - kT\ln\left(\frac{N_c N_v}{N_d N_a}\right) \end{aligned} \tag{2.49}$$

where q is the charge of the minority carrier under consideration. This approach can be used to determine the width of the SCR to a very good approximation.

Consider a junction formed from close contact of heavily-doped p-side and undoped side. As described for PN-junction before, the excess holes will diffuse to the undoped side, leaving acceptor atoms on the p-side. Once enough holes occupy states on the undoped side and reaches an SCR width, d, the built-in electric field prohibit further charge flow as shown in Figures 2.9 (a).

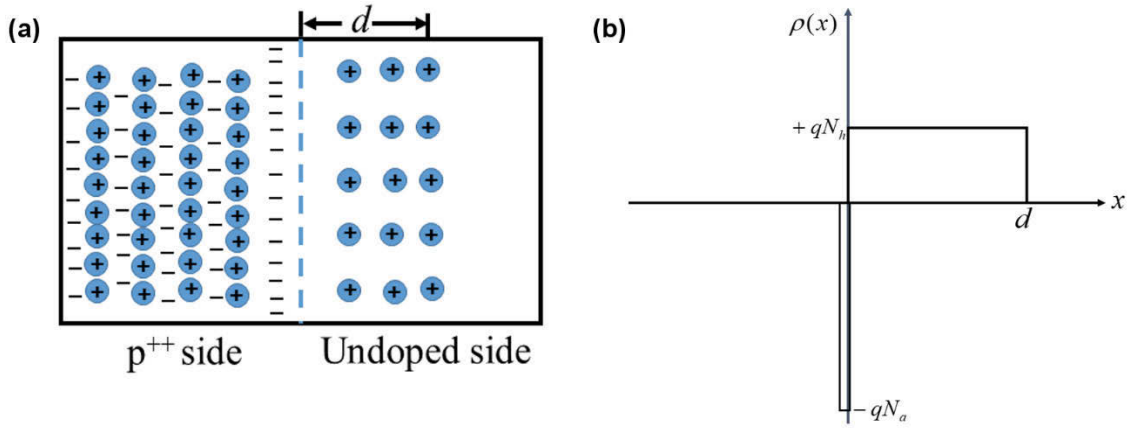

Figure 2.9: (a) Junction between a heavily doped p-type (p^{++}) semiconductor and undoped (intrinsic) semiconductors. (b) Charge density vs. position for the junction in (a)

Now if we calculate the charge density ($\rho(x)$) in SCR on both sides of the junction giving $+qN_h$ on the undoped side and $-qN_a$ on the p-doped side, where N_h is the concentration of holes. This is illustrated by the diagram in Figure 2.9 (b) where SCR is extending more into the undoped side as it requires to accumulate charges for electrostatic field stopping further diffusion and very little in the p-side as it is heavily doped. Thus, the width in the p-doped side is $\frac{N_h}{N_a}d$, where for $N_a >> N_h$ the density approaches Dirac-delta function ($\delta(x)$). Using Gauss's law, the electric field is related to charge density as

$$E(x) = \frac{1}{\varepsilon}\int \rho(x)\, dx \tag{2.50}$$

where ε is the dielectric constant of the semiconductor. Under the $\delta(x)$ -function assumption for the p-doped side, the integral could be written as

$$E(x) = \frac{1}{\varepsilon}\int_0^d qN_h dx \tag{2.51}$$

with the electric field vanishing at the boundaries and beyond the SCR. Thus, the maximum field in the depletion region is given by

$$E_{\max} = \frac{qN_h d}{\varepsilon} \tag{2.52}$$

Assuming the maximum integral electric field is reached at the middle of the SCR, i.e. at $d/2$, the potential drop due to band bending is given by

$$V_b = \frac{E_{\max} d}{2} = \frac{qN_h d^2}{2\varepsilon} \tag{2.53}$$

Thus, the width of the SCR for the simplified junction considered above is given by

$$d = \sqrt{\frac{2\varepsilon V_b}{qN_h}} \tag{2.54}$$

A similar approach can be used to calculate the width of SCR at thermal equilibrium for a PN-junction giving

$$d = \sqrt{\frac{2\varepsilon V_b (N_h + N_a)}{q^2 (N_h N_a)}} \tag{2.55}$$

Now let's look at the currents flowing across the bands as result of carrier diffusion and electric field. Diffusion current is driven by concentration difference of carriers on either side of the PN-junction given by Fick's first law as

$$j_{diff} = -qD\nabla n \tag{2.56}$$

where D and ∇n are the diffusion coefficient and concentration gradient of carriers, respectively. This is a movement of electrons to p-side constituting minority carriers and vice versa for holes. The flow direction of such current is referred to as the forward direction (in relation to diode application), and hence, the more common terminology for the flow of carriers is forward current (j_f).

The other current flow is driven by the electric force on carriers by virtue of the built-in electric field. Such current is referred as drift current and drives carriers in the opposite direction than the forward current. As such, a current due to the built-in electric field is

referred as reverse current (j_r). In the absence of externally applied voltage (V_{ext}), a forward current is equal to the reverse current as illustrated in Figure 2.8. This is given as

$$j_f(V_{ext} = 0) = -j_r(V_{ext} = 0) \tag{2.57}$$

The "$-$" signifies the opposite flow direction of the currents. This means the PN-junction is in dynamic equilibrium where all diffused carriers are compensated by the opposite flowing drift current at all time under no external bias making the total net current vanish.

Now consider the PN-junction under externally applied voltage, where the system is contacted at both ends as depicted by the grey-blocks in Figure 2.10. A positive voltage can be applied contacting the positive terminal to the p-side of the device and the negative to the n-side[89]. In such way, electrons will flow out from the p-side while holes flow into the p-side and on the n-side electrons repel flowing in and out from the region. This will affect the potential step around the junction by lowering it on the p-side due to increased concentration of electrons. It is important to remember the Fermi-energy level is no longer constant at the junction. Also, the decrease in the potential step by ΔE due to the applied voltage means, the equilibrium current flow due to the Boltzmann distribution of carriers (see equation (2.47) & (2.48)), will fall by $e^{-\frac{\Delta E}{KT}}$ giving a net forward current of

$$j_f(V_{ext}) = j_f(V_{ext} = 0)\, e^{-\frac{\Delta E}{KT}} = j_f(V_{ext} = 0)\, e^{-\frac{qV_{ext}}{KT}} \tag{2.58}$$

This is illustrated in Figure 2.10 (a) by using thick arrows to designate the forward currents both electrons (conduction band) and holes (valence band).

For reverse bias, the negative terminal is connected to p-side increasing the potential step around the junction as shown in Figure 2.10 (b). Thus, Boltzmann distribution of carriers at equilibrium is not affected by the reverse bias with all random motion leading to carriers reaching the edge of the potential step will fall to the other side of the junction as illustrated in Figure 2.10 (b) yielding [89]

$$j_r(V_{ext}) = j_R(V_{ext} = 0) = j_r \tag{2.59}$$

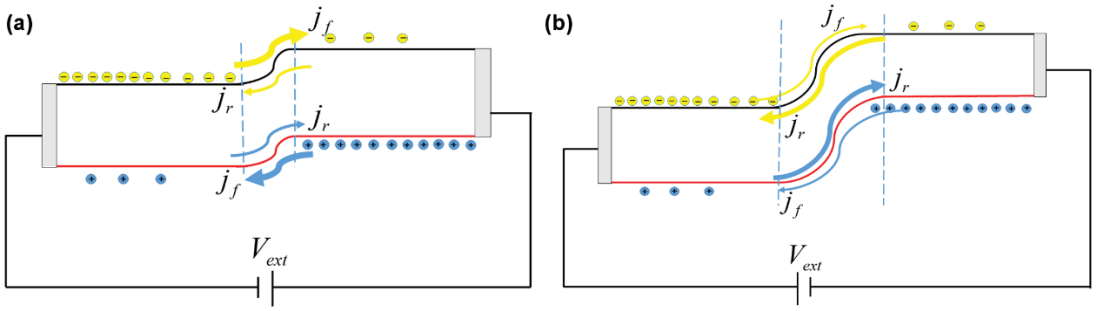

Figure 2.10: The PN-junction under external bias at the contact terminals of the semiconductors. (a) Forward bias where the positive terminal of the external voltage source is connected to p-side of the device while the negative to the n-side. (b) Reverse bias where the negative terminal of the external voltage source is connected to p-side and vice versa.

However, the carrier falls a larger potential step if the device is increasingly reverse biased. Consequently, the high stored energy in the falling electrons transfers into an ionizing more electron-hole pair. This leads to a cascade effect which results in the fast generation of carriers referred as avalanche multiplication. This will be observed by a very sharp increase in the reverse current at given reverse bias leading to a phenomenon known as avalanche breakdown.

The total current in the device is then the difference in the forward and reverse currents of electrons and holes given by

$$j(V_{ext}) = (j_f - j_r)_e + (j_f - j_r)_h = j_{er}(e^{-\frac{qV_{ext}}{KT}} - 1) + j_{hr}(e^{-\frac{qV_{ext}}{KT}} - 1) \tag{2.60}$$

where j_{er} and j_{hr} are the reverse currents for electrons and holes, respectively. Equation (2.60) is commonly referred as the diode equation and characterised by the conventional current-voltage (IV) curve. It can be shown that the reverse current is given by

$$j_{e(h)_r} = \frac{qLn_i^2}{\tau N_{ace(dop)}} \tag{2.61}$$

where n_i is the intrinsic concentration, $N_{ace(don)}$ is acceptor or donor concentration, L is the diffusion length and τ is the lifetime. Thus, modifying the diode equation as

$$j(V_{ext}) = \frac{qLn_i^2}{\tau N_{ace}}(e^{-\frac{qV_{ext}}{KT}} - 1) + \frac{qLn_i^2}{\tau N_{dop}}(e^{-\frac{qV_{ext}}{KT}} - 1) \tag{2.62}$$

While PN-junctions are discussed to obtain insight into semiconductor device properties such as band bending and current flow, various other junction structure can be realised depending on the desired choice of semiconductor, fabrication technique and application. For Single Photon Emitting Diodes (SPED), PIN-diode structures made from diamond and Gallium Arsenide (GaAs) have been demonstrated [19, 56, 84].

2.2.2.2 Single photon emitting diodes (SPEDs) and PIN-junction

Single photon emitting diodes (SPEDs) are characterised by the quantum nature of light they emit indexed by antibunching under HBT measurements [17, 19, 84]. Unlike the classical Light emitting diodes (LEDs) where radiative emission results from multiple electronic transitions from the conduction band to valence band by excess carriers, SPEDs generate single photons via transitions in the isolated electronic transition of an exciton pair[19, 92, 93]. This has been achieved by integrating different SPE platforms in classical LED structures. For instance, by embedding Indium Arsenide (InAs) QDs into the intrinsic layer of GaAs PIN-diode, single photon electroluminescence is demonstrated[84]. A similar structure using PIN-Gallium Nitride (GaN) nanowires is also used to generate electrically driven single photons by inserting Indium Gallium Nitride (InGaN) quantum dot in the intrinsic layer[55]. Nevertheless, EL of single photons from QDs is predominantly carried at cryogenic temperatures.

Defect-based SPEs can be incorporated into classical diode structures and be operated at RT, allowing scalability and integration of quantum devices with existing technologies[19, 56]. It is vital, however, to make sure that the excess carrier injection will result in the SPE site avoiding other recombination channels. Therefore, particular attention is needed while

preparing junctions and recombination active sites for electrically driven single photon emission. One of the few successfully implemented device structure for SPED is PIN junctions where an intrinsic (i) semiconductor is sandwiched between a p- and n-type semiconductors [19, 56, 84, 94].

The band bending process of a PIN junction at equilibrium is schematically shown in Figure 2.11, where the same principle as for a PN-junction applies[95]. A clear distinction in PIN diodes is their sizeable intrinsic layer over which the depletion region (SCR) resides on both ends of the junction (P-I and I-N). There are peculiar properties of PIN diodes due to the large intrinsic layer: First, the excess carriers injected spend more time in the intrinsic layer (long diffusion length) making rectification less in PIN junctions[96]. This is an apparent advantage for applications in photovoltaics and photodetectors where the current is withdrawn from the device before photogenerated excitons recombine. SPEDs also benefit from the long diffusion length in PIN-diodes where the probability of excess carriers being trapped at SPE site increases undergoing single photon transition kinetics. Under low forward bias, the total current is governed by the diode equation for PN-junctions given in equation (2.62).

However, for high-level injection, the intrinsic region is flooded with carriers from the doped sides of the device, with a large built-in electric field increasing conductivity. This can be an added advantage for SPEDs where excess carrier concentration once again increases the probability of charge transition at SPE site. However, if the single photon emitter form agglomerates within the intrinsic layer, the flood of injected carriers will be captured by the cluster leading to unwanted multiple photon emission. This high-injection flooding also means PIN diodes have low reverse recovery time, making the diode hard to switch off. If reverse-biased appropriately, however, excess carriers can be removed from SPE site allowing the study of charge state switching.

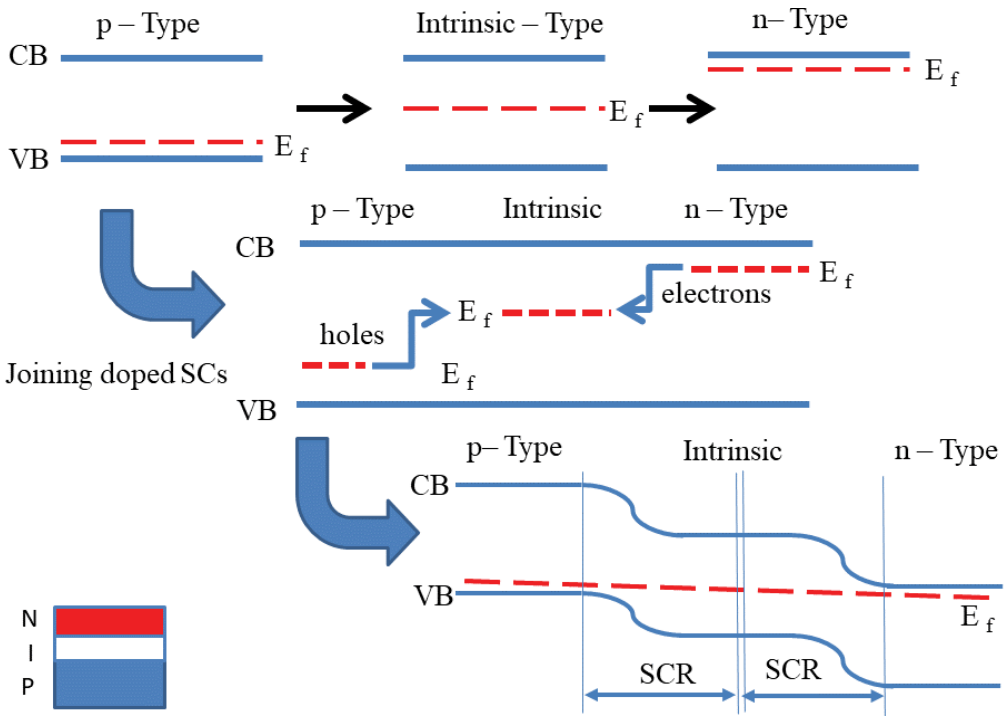

Figure 2.11: Schematic process illustrating band bending via carrier diffusion at equilibrium is illustrated for the PIN structure shown in the inset. The same steps as the PN-junction follower, where now three semiconductors are involved (p-type, intrinsic and n-type).

By now, a clear distinction in optical (using lasers) and electrical (excess carrier injection) pumping of SPE must have been drawn. The former uses sub-bandgap laser directly that drives electron transition in the isolated SPE energy states. In the case of the latter, excess charge carriers are injected via external voltage source involving conduction and valence band of the semiconductor from which subsequent trapping at SPE occurs. Thus, electrically driven transitions for single photon emission has to take into consideration transitions from conduction (valance) band to SPE site which is best described by a modified Shockley-Read-Hall (SRH) recombination via a third state within indirect bandgap semiconductors.

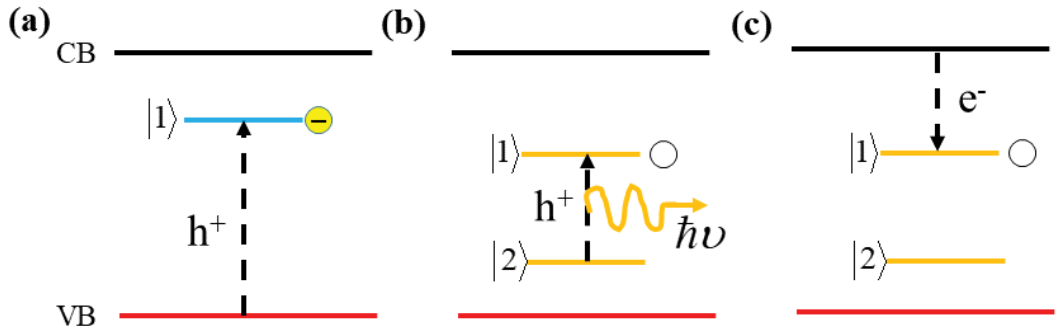

Figure 2.12: Schematic illustration of single photon emission at the charged defect site. (a) a hole is trapped by a defect state that has an electron in its ground state. (b) The successive decay of the trapped state from the excited to the ground state of the decay results in single photon emission switching the charge state to neutral. Subsequent electron trap by the defect switches it back to its negatively charged ground state.

Consider the third state (SPE) in this case is a defect state in an indirect semiconductor that has one electron in its ground state (e.g. negative charge state of Nitrogen-Vacancy in diamond (NV^-)). This naturally attracts excess minority holes crossing the SCR into its excited state altering the charge state as illustrated in Figure 2.12 (a). Thus, relaxation of the trapped hole to the ground state results in characteristic single defect electroluminescence (Figure 2.12 (b)). It is important to note that charge state of the defect is altered into a neutral charge state during the electrically driven single photon emission losing its electron in the ground state via the radiative recombination[93]. Subsequently, the defect returns to its negative charge state by trapping electron from conduction band (Figure 2.12 (c)). This mechanism of electrically driven emission can be treated using SRH model by first considering the rate of electron decay from conduction band to the SPE state given by[89, 93]

$$R_d = c_d \, n_e \, f \, N_{SPS} \tag{2.63}$$

where c_d is the electron capture rate, n_e is the electron density, f is the number of neutral ground states and N_{SPS} is the number of SPE per unit volume. The hole decay rate is expressed in a similar way as

$$R_u = c_u \, n_p (1 - x - f) \, N_{SPS} \tag{2.64}$$

where c_u is the hole capture rate, n_p is the hole density and $(1-x-f)\,N_{SPS}$ is the negative charge state per unit volume with x as the population of the neutral excited state. The re-emission of trapped electrons and holes back to the conduction and valence band from the defect either via thermal and illumination mechanisms can then be expressed as

$$G_d = e_d\,(1-x-f)\,N_{SPS} \tag{2.65}$$

and

$$G_u = e_u\,x\,N_{SPS} \tag{2.66}$$

With e_d and e_u as the re-emission constant for electrons and holes. The rate of hole relaxation from the excited state to the ground state, κ_{21}, with a lifetime τ, is given by

$$k_{21} = {}^{1}\!/_{\tau}\,x\,N_{SPS} \tag{2.67}$$

while the emission of a hole into the excited state (electron trap by the ground state) is given by

$$k_{12} = e_r f\,N_{SPS} \tag{2.68}$$

where e_r is the re-emission constant from ground state to the excited state of the neutral state of the defect via thermal or illumination mechanism. Now the rate of decay from each energy level is given by the sum of all population and depopulation rates from the respective bands or states given by

$$\begin{aligned}
\frac{dn_e}{dt} &= G_d - R_d + G_d^{ext} = e_d(1-x-f)\,N_{SPS} - c_d\,n\,f\,N_{SPS} + G_n^{ext} \\
\frac{dn_h}{dt} &= G_u - R_u + G_u^{ext} = e_u\,x\,N_{SPS} - c_d\,n_h(1-x-f)\,N_{SPS} + G_u^{ext} \\
\frac{d(fN_{SPS})}{dt} &= G_d - R_d + \kappa_{21} - \kappa_{12} = e_d(1-x-f)\,N_{SPS} - c_d\,n\,f\,N_{SPS} \\
&\quad + {}^{xN_{SPS}}\!/_{\tau} - e_r f\,N_{SPS} \\
\frac{d(xN_{SPS})}{dt} &= R_u - G_u + \kappa_{12} - \kappa_{21} = c_u\,n_h(1-x-f)\,N_{SPS} \\
&\quad - e_u\,x\,N + e_r f\,N_{SPS} - {}^{xN_{SPS}}\!/_{\tau}
\end{aligned} \tag{2.69}$$

With G_d^{ext} and G_u^{ext} is the generation of excess carriers (electrons and holes) via external electrical pumping. Local equilibrium of transition between bands and energy states of SPE implies that $\frac{dn_e}{dt} = \frac{dn_h}{dt} = 0$ and $\frac{d(fN_{SPS})}{dt} = \frac{d(xN_{SPS})}{dt} = 0$. Similarly, at local equilibrium the difference in the recombination and generation rates of electrons and holes is equal. i.e., $G_d - R_d = G_u - R_u$. Assuming a vanishing re-emission (generation) rate from the defects, it can be shown from the above analytical steps that the recombination rate at the SPE is given by

$$R_{SPS} = \phi \frac{1}{1/c_d n_e + 1/c_u n_e + \tau} \tag{2.70}$$

Where ϕ is the quantum efficiency, and the capture rates are given by the products of capture cross-sections and group velocities (i.e. $c_{d(u)} = \sigma_{d(u)} v_{d(u)}$). As stated above, for some defects only the neutral charge state of the defect shows electroluminescence. The negative charge state switches to the neutral every time it captures the hole. This is demonstrated experimentally for the NV centre in diamond where only the neutral charge state showed electrically driven single photon emission.

However, this is not always the case where in some defects electrically driven luminescence from the charged state remains a possibility. Another defect in diamond, namely Silicon-Vacancy (SiV) is an example of the negative charge state showing single photon electroluminescence. In this case, the negative charge state of SiV (SiV^-) only has one electronic state in its ground state. When it traps a hole from a valence band, it's energetically favourable to switch to the neutral charge state (SiV^0)[93]. On the other hand, when the SiV^0 traps an electron from conduction band in its excited state, it switches to excited SiV^- which upon relaxation emits a photon as illustrated in Figure 2.13. The experimental results of electrically driven luminescence from SiV constitute part of this thesis and recombination rate discussed above holds for the SiV defect as well.

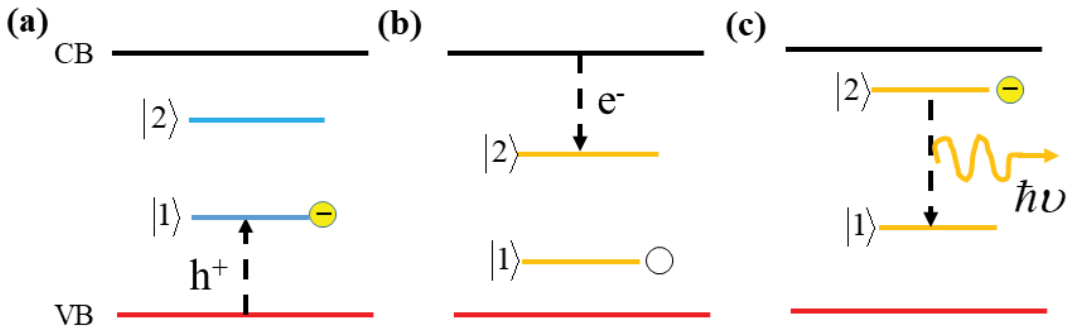

Figure 2.13: Schematic illustration of single photon emission at the charged defect site. (a) a hole is trapped by a defect state that has an electron in its ground state switching to neutral charge state. (b) The neutral charge state then traps an electron in its excited state turning to the excited negative charge state of the defect. (c) Relaxation of the excited negative charge state emits a photon.

Finally, a brief discussion into another excitation mechanism that results in fluorescence of defects via recombination of excess carriers at the SPE site much like the electroluminescence above: cathodoluminescence. This technique relies on the excitation of the semiconductor by exposing it to an electron beam. In such case, a high-energy electron beam ionises the semiconductor generating plenty of carriers in both the conduction and valence band. Subsequent capture of decaying excess carriers at defect sites results in fluorescence. Interestingly, the charge states that showed luminescence when driven electrically show fluorescence under cathodoluminescence as well. For example, NV^0 and SiV^- can be observed under cathodoluminescence measurements with ease while their counter charges states (NV^- and SiV^0) remain in the dark state similar to experimental results using electroluminescence. Although detailed study comparing cathodoluminescence and electroluminescence techniques for SPE system is required, it appears excitation via electrical beam can be used to confirm which charge state of a single photon emitting defect would show fluorescence via excess carrier recombination. This is important because unlike electroluminescence, cathodoluminescence does not require device structure for excess carrier injection. Hence, it can be used as a fast approach to identify defect charge states that will fluoresce upon carrier capture.

2.3 Photon statistics and fluorescence blinking

When considering single photon emitters as building blocks for quantum technologies, one of the primary criteria is fluorescence stability[97]. This is indexed by occurrence statistics of photon events at a given time interval while the SPE is under laser excitation. Considering the two- and three-level transition kinetics described in subsection 2.2.1, the single photon occurrence events follow Poissonian statistics under cw-laser excitation. That is if the fluorescence time trace is measured by binning the histogram in few ms, it remains constant along a specific photon count for as long the measurement lasted. On the contrary, if a certain mechanism disrupts the transition cycle of the excited state of the SPE, the fluorescence time trace will show a sporadic rise and fall in the photon counts within comparable binning time[98]. This is known as photon (fluorescence) blinking/intermittency, and it is a very common phenomenon in many single photon emitting systems including defects in wide bandgap semiconductors[24, 99, 100]. Although fluorescence blinking is easy to index from measurement and is ubiquitous in different single photon emitting systems, the underlying mechanisms of the cause remain far more complicated and manifold leading to a different hypothesis.

Despite the lack of a unified description for the mechanism of transition kinetics disruption, charging and discharging of the SPE is the accepted cause of dark ("off"-) and bright ("on"-) state[92, 101, 102]. That is, an excited SPE will have its charge conserved locally as long as an electron stayed within its energy levels. The eventual radiative decay of the excited state to the ground state leads the SPE to remain in the bright state. In this context, decaying down non-radiatively even via a shelving state, for example in the case of three-level transition kinetics in section 2.2.1, introduces a dark state in the photon statistics. This, however, usually occurs in a much shorter time interval, nanoseconds (ns), rarely affecting some crucial applications. On the other hand, many other mechanisms trap the excited electron for more extended periods of time (ms to min), leaving the SPE charged. This charged SPE remains in the dark state until a mechanism forces an electron to decay down to the ground state

preparing it for subsequent transition cycle. Next, a brief review of some of the relevant models proposed for charging and discharging processes of SPEs will be summarised.

2.3.1 Charging and discharging mechanisms of blinking SPEs

2.3.1.1 Quantum jump and auger ionisation model

The quantum jump model best describes what has been discussed so far as a three-level system with a shelving state ($|3\rangle$) in addition to the ground ($|1\rangle$) and excited state ($|2\rangle$). This is a fast process with the sporadic dark state occurring for every non-radiative decay of the excited state via a shelving state observed both in the blinking of QDs and single molecules[103, 104]. While this is a simplified model, it can be extended to a system with more than one shelving state where the dark transition between these states keeps the SPE in the "off" state for longer periods. This process is illustrated in Figure 2.4 (b). Consistent with the rate model derived considering the three-level transition in subsection 2.2.1., the "on"- and "off"-times in this model are constant, and their probability density ($P_{on.off}$) is given by a single exponential of the form[105]

$$P(\tau_{on}, \tau_{off}) \approx \exp\left(\frac{-\tau}{(\tau_{on}, \tau_{off})}\right) \tag{2.71}$$

where $\tau_{on.}$ and τ_{off} are the characteristic "on"- and "off"-times of blinking.

Another fast charging and discharging model for blinking is the Auger ionisation where unlike a one-photon absorption described before, a two-photon absorption leads to recombination of one-pair and ejection of an electron as illustrated in Figure 2.14 (a)[106, 107]. Until another electron comes into the energy level of the SPE recovering the ground state, the emitter remains charged and in the dark state. The probability densities in this case also are given by the single exponential of the form given in equation (2.71). This model is used to describe fluorescence blinking in defect related SPEs in SiC [24] and diamond[99]. Recently, we observed this mechanism to be responsible for excitation dependent blinking of SPEs in GaN constituting one of the major results in this thesis (Chapter 6)[100].

2.3.1.2 Spatial diffusion model

This model is demonstrated for blinking in QDs which considers wondering away of the excited state via some diffusion process into the crystal lattice leaving the QD SPE charged as depicted in Figure 2.14 (b)[108]. The charged SPE will remain in the dark state until the electron returns to its energy levels. The diffusion time it takes the electron to return, however, varies thus leading to a probability density that's given by a power law of the form

$$P(\tau_{on}, \tau_{off}) \approx \tau_{on,\text{off}}^{-3/2} \tag{2.72}$$

The power law indicates that the "on"- and "off"- times vary for each charging and discharging process following the variation in the diffusion time. It is also important to note that the diffused electron may never return leaving the SPE in a permanent dark state. Such power induced permanent switch-off in emission is referred to as photobleaching.

2.3.1.3 Fluctuating electronic states model

This model starts by considering a trap state for holes near the valence band of QDs as depicted in Figure 2.14 (c)[109]. The conduction band has energy levels ($1P_e$ and $1S_e$ in Figure 2.14 (c)) with a uniform distribution of electronic state. Upon excitation, electron transition from $1S_e$ to $1P_e$ leads to a hole localisation at a trap state as indicated in the Figure 2.14 (c). Subsequent excitation results in emission only when electron transition and hole trap rates are not in resonance. If these transitions are in resonance, however, cyclic process of de-excitation from $1P_e$ to $1S_e$ and auger assisted, the dark transition from trap state to valence band occurs leaving the emitter in the dark state. The probability density of the "on"- and "off"- states are given by the power law in equation (2.72) indicating non-ergodicity in the process.

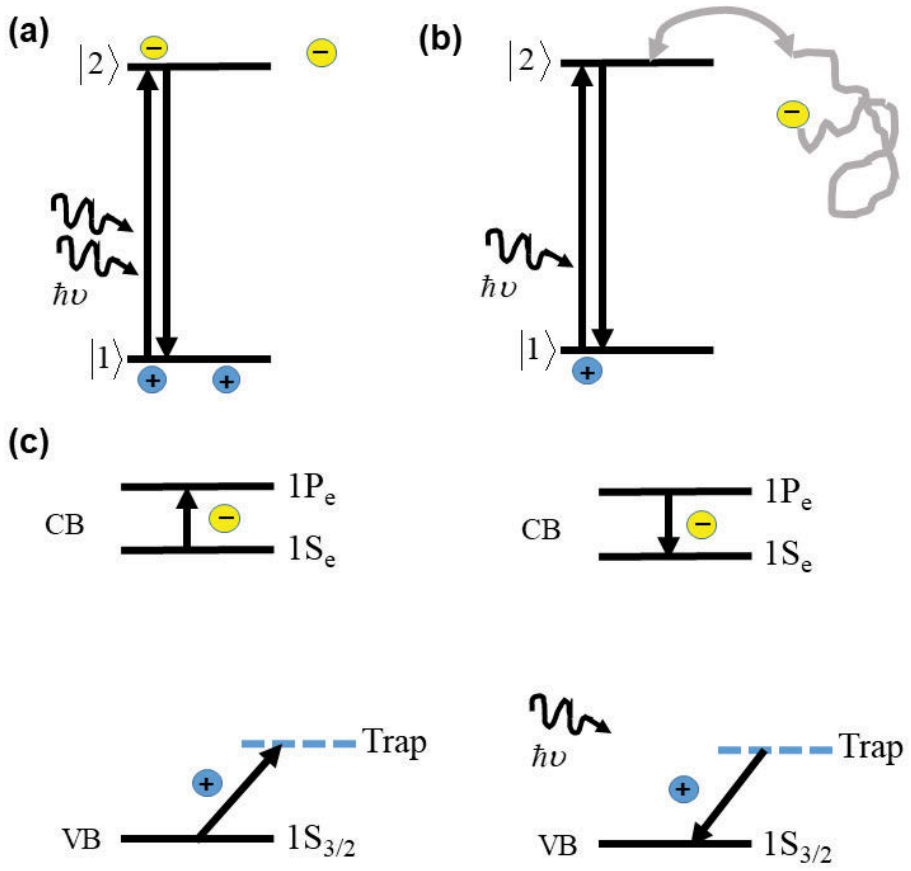

Figure 2.14: Charging and discharging mechanisms in SPE leading to "off" and "on episodes. (a) Auger ionisation model (b) Spatial diffusion models (c) Fluctuating electronic state model.

While these and more models of blinking are primarily proposed for QDs transitions, they are reviewed here in the context of a defect-related single photon blinking in GaN. This is because of the substantial experimental, and theoretical evidence gathered that indicate the SPEs in GaN are strongly affected by a cubic inclusion in the wurtzite GaN. The cubic inclusion acts as s a localised quantum well, where confinement in one dimension occurs. Thus, blinking models although proposed for QDs, they can be applied in the context of cubic inclusion influenced by defect luminescence in GaN. Furthermore, despite the difference in the proposed models, all of them have key, standard features for blinking. Next, the key features are summarised based on reviews in [98, 102, 110].

2.3.2 Key parameters of blinking measurements

I. **Probability density of "on"- and "off"- times:** This parameter is a weighted number of bright and dark event durations as an SPE undergoes fluorescence trajectory over a given measurement time[103, 110]. If the event duration falls exponentially with time, the semi-log plot of the probability density of "on" - (P_{on}) and off- (P_{off}) yield a linear curve. The deterministic probability density gives characteristic times in which the system spends on the bright and dark state[105]. This is especially important in understanding single photon transition dynamics indicating the existence of trap states[24, 99]. Also, determination of the values of "on" and "off" times allows comparison with radiative and non-radiative decay rates giving insight into the intricate nature of transition kinetics of SPEs[100, 111]. However, most other systems such as QDs, single molecules show a power-law probability density indicating the phenomena has no average time characteristics[101, 106, 109, 112]. This complicates the nature of charging and discharging process where more than one physical phenomenon must usually be considered to explain observations.

II. **Excitation light dependent phenomenon:** fluorescence blinking is observed when the SPE is under light illumination where the fate of de-excitation determines whether the emitter fluoresce, or undergoes episodes of "on" and "off" state or even bleach[102]. This feature is common to all blinking behaviours [113]. In fact, some SPEs show excitation power dependent blinking behaviours. That is, below a certain excitation laser power threshold, emitters show stable fluorescence which dramatically changes into blinking emission when the power is increased above the threshold[100]. This phenomena will be discussed in detail in Chapter 6.

III. **Relation to spectral diffusion:** Spectral diffusion is instability in emission frequency (wavelength) of the zero-phonon line (ZPL) in the spectra of an SPE[114]. Spectral diffusion has been linked to a similar phenomenon that causes fluorescence blinking [114-116]. This is easily observed by simultaneously recording the fluorescence time trace and the spectrum, where the dark state duration is seen to correspond to the

disappearance of the ZPL. Conversely, the appearance of ZPL peak is coupled with the bright state duration.

IV. **Relation to local electric fields:** The modulation of the "on" and "off" durations have been linked to fluctuations in local electric fields [116-118]. The modulation is demonstrated by controlling the durations by applying the external electric field thus affecting the local dielectric permittivity. The cause is believed to be similar to that of what causes spectral diffusion, which is charge reshuffling around the SPE.

2.3.3 Blinking measurements and data analysis

2.3.3.1 Photon binning histograms

This analysis technique is directly obtained from fluorescence trajectory where photons are binned into similarly sized histograms building a profile for as long as the measurement lasts [102, 103, 110, 113]. This is limited by the shortest bin size of the photodetector or counter, where dark peaks are distinguished by a sudden fall in intensity. Counting the number of "on" and "off" peaks, the probability density analysis can be constructed[103].

2.3.3.2 Probability density of "on"/ "off" times

Probability density ($P_{on,off}$) can be obtained from the photon-binned histograms by first setting a threshold of photon counts. This is usually 2 or 3 times the background count[103]. All peaks lying above the threshold are counted as "on" events and all peaks below the threshold as "off" events[103, 110]. In multilevel blinking, more than one threshold may be used to distinguish between the different "on" events. Subsequently, by making exponentially spaced time bins and weighting the nearest events, the weighted $P_{on,off}(s^{-1})$ can be obtained. Linear forms of $P_{on,off}$ can be obtained by plotting semi-log (for exponential relations) or log-log (for power-law relations).

2.3.3.3 Second-order autocorrelation ($g^2(\tau)$) analysis

In subchapter 2.1., it is shown that by measuring the photon count fluctuations as a function of delay times at two detectors, the second-order autocorrelation function ($g^2(\tau)$) is used to characterise the nature of the photon source. Recall equation (2.19) where $g^2(\tau)$ is expressed in terms of normalised intensity (I) fluctuations. For single photon emitters, this function at short delay times (0 to 1000 ns) can be used to characterise rates for processes such as photon antibunching and fast non-radiative via shelving states. The former is a result of the radiative decay of a single excited state while the latter corresponds to a fall in intensity ($I(t+\tau)$) as result of reduced photons arriving at detectors. Similarly, the different processes discussed as a mechanism for blinking above cause long-lived dark states (a few μs to min). Thus, the different blinking processes with corresponding characteristic "on" and "off" times will show on the $g^2(\tau)$ function as rates where all significant dark states are indexed by a drop in the signal. By determining the rates for this blinking time, an elegant comparison can be made with the probability density. In this thesis, such approach and analysis techniques will be used to study power induced blinking behaviour of a SPEs in Chapter 6.

This chapter covered the fundamentals behind excitation and generation of single photon emitters. The other relevant background required to understand the results presented in this work is defect fluorescence in wide bandgap semiconductors. The following chapter provides more basics on defect based single photon fluorescence.

3 Defect related luminescence: single photon emission from wide bandgap semiconductors

Wide varieties of nanomaterials including QDs[119-122], single molecules[71, 74, 123], single ions [124, 125] can serve as single photon emitters. Each with own distinguishing materials characteristics, exhibit single photon emission via excitation and relaxation cycles between their energy levels. Furthermore, many of these platforms require a cryogenic operation for on-demand generation of stable, single photons limiting their application. Optically active defects in different wide bandgap semiconductors have the advantage of emitting RT stable single photons [9, 10, 17]. Optical transition in defects can be induced by using light excitation as well as injection of the excess carrier as discussed in the previous chapter. This chapter begins by covering brief description of point defect formation in semiconductors. Optical transitions at defect energy levels that define spectroscopic and associated photophysical properties are then discussed. In this framework, subsequent sections focus on reviewing earlier theoretical as well as experimental works on optically active defects in GaN and diamond when used as SPEs.

3.1 Optical properties of point defects

3.1.1 Equilibrium point defect formation

Pont defects (PD) also referred to as 0-dimensional defects are the simplest forms of defects in crystals[126, 127]. These defects can form by removal or rearrangement of lattice constituting atoms in which case are referred to as intrinsic point defects. Alternatively, point defects may form by intentional or unintentional incorporation of impurity atoms into the crystal lattice during or post crystal growth. Point defects formed this way are referred to as extrinsic point defects. The most common intrinsic defects are vacancies and self-interstitials. The former is formed in the most straightforward case when an atom is removed from the original crystal lattice leaving atomic sized vacant space in the lattice sites while the latter is

formed when constituting atom moves to occupy a lattice site in between a regularly arranged lattice structure. This is referred to as self-interstitial indicating that the re-positioning is carried out by the lattice constituting atom. In case of extrinsic point defects, impurity atoms can occupy an interstitial site (interstitials) or lattice sites (substitutional). The PDs form at thermal equilibrium and their structure may not always be as simple. For example, instead of just one atom being removed from a lattice site or re-positioned into the interstitial site, multiple atoms can carry out these re-configurations forming extended vacancies or interstitials[127]. In crystals that are composed of more than one atom type, some lattice constituting atoms could be positioned in the site of other atoms forming point defects referred to as antisite. Thus, the seemingly simple point defect formation in semiconductors can become far more complicated.

An important manifestation of point defect formation is charge state. When an atom is removed to form a vacancy in semiconductors, for example, charge neutrality in the crystal will be disrupted due to lost charge[127]. Thus, a charge must be added at the vacancy site or a site in the crystal to conserve the total charge in the semiconductor. The existence and type of a charge near a point defect define its charge state. The charge state depends on the Fermi energy level of the semiconductor and thus affects the electronic (optical) property of the semiconductor. Let's re-consider doping, a concept already introduced in subchapter 2.2.2.1, as a process of incorporating extrinsic impurity atoms to the bulk of a semiconductor altering the electronic property. Acceptor dopant with two charge states: neutral concentration, c^0, and ionised state with concentration, c^-, gives a total impurity concentration, $c_{0,}$ where $c_0 = c^0 + c^-$. The ionised state concentration is then given by[127]

$$c^- = c^0(1 - f(E_a, E_f; T)) \tag{3.1}$$

where the term $1 - f(E_a, E_f; T)$ refers to the probability that the electronic energy state, E_a, of the acceptor dopant is not occupied by an electron. Thus, for a semiconductor with Fermi energy level, E_f, at temperature T, the ionised concentration is expressed as

$$c^{-} = c^{0}(1 - \exp(\frac{E_f - E_a}{KT})) \tag{3.2}$$

Similarly, point defects will have a defined electronic state that may or may not be occupied by electrons within the bandgap of the host semiconductor. The concentration of point defects, c_v, which is the ratio of the number of point defects, n_v, to the total number of crystal atoms, N, is given by

$$c_v = \frac{n_v}{N} = \exp(-\frac{G_F}{KT}) \tag{3.3}$$

where G_F is Gibbs free energy of point defect formation. It can be expressed in terms of formation enthalpy, H_F, and formation entropy, S_F, as

$$G_F = H_F - T.S_F \tag{3.4}$$

Now, the concentration of charged point defect, for example, a vacancy within the semiconductor is given by

$$c_v^{-} = c_v \exp(\frac{E_f - E_a}{KT}) \tag{3.5}$$

Therefore, the charge state of point defects depends on the Fermi level and temperature, in addition to the formation energy and entropy[127]. Thus, the spectral properties of a defect are expected to vary among the different charge states.

Furthermore, equilibrium formation of point defects usually refers to a local equilibrium where the Gibbs free energy will be minimum at some locality without requiring absolute minima for the whole crystal. The local equilibrium can break, for example, when the sample is annealed at high temperature or irradiated allowing point defect kinetics such as movement of a localised point defect, generation of new defects as well as the annihilation of interstitials with vacancies.

3.1.2 Electronic states of defects

The introduction of defects not only shifts the Fermi energy level but also perturbs the periodic potential of the semiconductor forming a highly localised electronic state[128]. Depending on the degree of perturbation, the defect electronic states could be shallow or deep levels. Example of shallow defect levels is electronic states created by most dopant elements leading to minor perturbation in the periodic potential of the semiconductor. On the other hand, point defects and defect complexes form deep levels within the band gap of a semiconductor causing significant perturbation on the periodic potential. That is, a vacancy (missing atom) for instance is a strong, local perturbation in the otherwise periodic potential of the semiconductor. The presence of a vacancy, thus, requires the participation of the energy states of neighbouring lattice atoms or attracts impurity atom locally forming electronic states[128].

In case of shallow dopant impurities, the majority of the valence electrons involved in bonding with the host lattice[129]. Excess electrons that didn't involve in the bonding, then, stay in the vicinity of the dopant due to Coulomb interaction with excess positive charges in the nucleus. This forms Coulomb perturbation Hamiltonian that resembles a Hydrogen atom[129]. Thus, the energy levels for a shallow impurity are approximated by Bohr energy levels of Hydrogen in a crystal with reduced mass and binding energy. For deep level defects, however, the perturbation is severed and extends over several lattice constants[129]. Thus, the interaction of several atoms has to be considered in defining the energy levels that lie deep in the band gap of the semiconductor.

Consider point defects formed with defined, local electronic states in the bandgap of a semiconductor. If an optical transition is allowed between the excited electronic states to the ground state, the point defect will emit a characteristic light. Such defects are said to be optically active and referred to as colour centres [72, 127, 128]. These are the basis for the

study of defect based quantum optics and nanophotonics in different wide bandgap semiconductor including GaN and Diamond.

Looking more closely at the transition that leads to the emission of light, two primary processes take place: the absorption and emission of light by the defect. Figure 3.1 shows a configuration coordinate diagram that depicts the ground (E_g) and excited (E_e) vibronic states of a typical defect in the bulk of a semiconductor. Upon absorption of excitation light, a transition from the ground state to the excited state occurs. At absolute zero (T= 0K), only m=0 can be populated where all other phonon related states are expected to disappear[72]. From this ground state, excitation to any one of the vibronic excited states could occur with a probability of [128]

$$W_{n0} = S^n e^{-s} / n! \tag{3.6}$$

where S is the Huang-Rhys (HR) factor, n is the occupied excited vibronic level. The absorption spectrum in such case corresponds to

$$E = E_0 + n\hbar\omega \tag{3.7}$$

where E_0 the energy difference between the ground and excited state and ω the phonon frequency corresponding to the n^{th} vibronic excited state. That is, the most probable transition, also referred to as Franck-Condon, after absorption is from **A** to **B**, where subsequent relaxation to **C** occurs by emitting $n = S = 3$ phonons. A decay down to **D** releases a photon followed by another phonon-assisted ($m = S = 3$) relaxation to the ground state, m=0. On the other hand, a pure electronic transition without phonon involvement could occur between m=0 and n=0. This is termed as a zero-phonon line (ZPL) indicating the absence of phonon involvement in this transition.

Thus, at low-temperature spectral measurement, ZPL is expected to dominate the spectrum surrounded by satellite phonon sidebands (PSB). The PSB transition, both acoustic and optical phonons modes, increases with increasing temperature. In addition, the linewidth or more precisely the Full Width at Half Maximum (FWHM) of a ZPL is narrow showing the

only lifetime limited homogenous broadening. This is, however, usually not achievable in real crystals due to other inhomogeneous broadening mechanisms such as crystal strain and spectral diffusion due to charge fluctuations[72]. Even more common is increased electron-phonon coupling at higher temperatures leading to ZPL broadening.

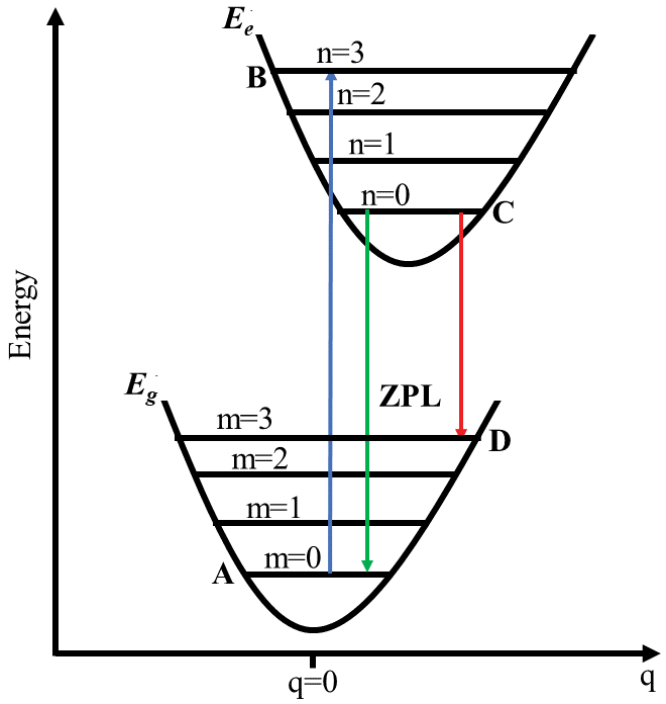

Figure 3.1: A typical configuration coordinate diagram of a defect showing electronic transitions together with vibrational levels.

The Huang-Rhys factor, S, indexes the fraction of emission coming from the ZPL by comparing it to the fraction coming from the phonon-side bands (PSB) at T= 0K as

$$I_{ZPL} = I_{tot} \exp(-S) \tag{3.8}$$

where I_{ZPL} and I_{tot} are the ZPL and total intensities. Looking at Figure 3.1., the phonon-assisted absorption occurs at higher energy than the phonon-assisted emission with symmetrical middle energy value for the ZPL. This is referred as the Stokes shift, and its width is given by

$$E_{abs} - E_{emiss} = 2S\hbar\omega \tag{3.9}$$

where E_{abs} and E_{emiss} are the phonon-assisted absorption and emission energies. The width of the PSB (Δ) can also be expressed in terms of the Huang-Rhys factor as

$$\Delta^2 = 5.6(\hbar\omega)^2 S \tag{3.10}$$

S is calculated from equations (3.8), (3.9) & (3.10) could vary for certain defect systems indicating the presence of non-linear electron-phonon coupling. This leads to energy degeneracy which no longer can be described by the configuration coordinate model. Such phenomenon is also referred to as the Jahn-Teller effect in which the symmetry of phonon-assisted absorption and emission energy around the ZPL also break [128-130].

Another critical factor in the absorption and emission paths is the dipole orientation of the defect system. This entails that optical transitions in the configuration coordinate model depend on the polarisation direction of the excitation and emission[72]. Furthermore, in the Franck-Condon approximation of the model, the absorption and emission are expected to have identical properties following the mirror symmetry around the ZPL described earlier. The polarisation properties are well described by[131, 132]

$$I(\phi) = a + b\cos^2(\phi) \tag{3.11}$$

where a, b and ϕ are offset parameter, initial intensity amplitude and angle between excitation and dipole orientation, respectively. Thus, the maximum ($I_{\max} = I(\phi = 0) = a + b$) and minimum ($I_{\min} = I(\phi = 90^{\circ}) = a$) polarisation directions should be the same for both absorption and emission. However, this is not always the case where the orientation of maximum absorption and emission axis are different subtending a non-zero angle as will be seen in Chapter 5. This non-zero relative orientation of the absorption and emission dipole has recently been expressed in terms of the Stokes shift described in equation (3.9) for SPE, where large misalignment angles gave higher stokes shift values[133]. This is believed to be due to the involvement of the additional electronic state in the absorption and emission mechanisms deviating from the simple two-state configuration coordinate model.

3.2 Single photon emitters in III-nitrides

Defects in III-nitrides ((Indium Nitride (InN), Aluminium Nitride (AlN) and Gallium Nitride (GaN)) have been extensively studied in light of the materials technological importance[51, 52]. Nevertheless, the plethora of optically active defects in III-nitrides remained unavailable for use as single photon emitters. This may be due to difficulty in identifying defect structures responsible for observed fluorescence signatures or challenges of isolating a defect in the GaN matrix to avoid emission from ensembles. As a result, the generation of single photons from III-nitrides was limited to InGaN QDs as wells GaN QDs in nanowires[53-55]. However, QDs operate as good SPEs mainly at cryogenic temperatures and perform poorly at RT.

This thesis reports results of the first bright RT stable, defect based SPEs from GaN films grown on different substrates in Chapter 4. The single photons from GaN hold promising attributes for applications in quantum technologies as can be deducted from the photophysical results featured in Chapter 5. However, the responsible defect(s) in GaN that emits single photons is still not fully known limiting further improvement of single photon properties. These exciting new results and lack of knowledge about the symmetry and structural nature of the SPE, have motivated the following review of two prior theoretical works on isolated defects in GaN and AlN that showed single photon emission[134, 135].

3.2.1 An optically active isolated defect in cubic GaN

First-principle calculations predict the existence of a defect in cubic GaN that can be optically excited and its spin states manipulated using microwaves[134]. The defect is composed of a substitutional oxygen atom at nitrogen site (O_N) and a neighbouring gallium vacancy (V_{Ga}) forming complex $V_{Ga}O_N$. It is shown for energy optimised arrangement of the defect in the 3C-GaN, $V_{Ga}O_N$ shows C_{3v} symmetry. This means upon polarisation dependent measurements; this defect should show high emission visibility and strong dependence on absorption polarisation. Also, it is suggested that high-temperature annealing of the 3C-GaN

leads to the formation of the defect complex ($V_{Ga}O_N$), which is more favourable than the two point defects forming apart from one another ($V_{Ga} + O_N$).

It is shown that the defect can form in either of four different charge states, namely +1, 0, -1 or -2, depending on the position of the Fermi energy level (E_f). For example, in a p-doped 3C-GaN with E_f ranging between 0.20 eV to 0.75 eV, the formation energy of the neutral charge state ($V_{Ga}O_N^0$) is minimal. On the other hand, $V_{Ga}O_N^{-2}$ forms for E_f higher than 1.21 eV. The different charge states of the defect correspond to different spin configurations of the ground state.

Finally, the configuration coordinate diagram for the neutral charge state of the defect is plotted as shown in Figure 3.2 (a). Absorption energy of 1.29 eV, as well as, phonon-assisted emission energy of 1.19 eV is calculated. The ZPL energy is predicted to be at 1.27 eV. These values indicate that efficient excitation and emission of the neutral charge state occurs in the infrared spectral range. This excitation energy is lower than required to excite common defects in diamond such as Nitrogen-Vacancy (NV) centre.

3.2.2 An optically active isolated defect in wurtzite AlN

A similar study on wurtzite AlN demonstrates an isolated defect that can be manipulated optically[135]. This is a defect complex comprising of Aluminum vacancy (V_{Al}) and a substitutional Oxygen at a nitrogen site (O_N) giving $V_{Al}O_N$. Spectroscopic study of these emitters indicates that this defect complex is a deep level acceptor. Like the $V_{Ga}O_N$ in 3C-GaN discussed above, the $V_{Al}O_N$ has C_{3v} symmetry.

Similarly, four stable charge states, +1, 0, -1 and +2, are determined for $V_{Al}O_N$ at different Fermi levels. For Fermi levels ranging between 0.43 eV to 1.02 eV, the neutral charge state ($V_{Al}O_N^0$) of the defect complex is stable indicating that this defect is most likely to be found in p-type AlN. The concentration of this defect is calculated yielding around 5.9 x10^{12} cm^{-3}.

The configuration coordinate diagram of the neutral charge state of the $V_{Al}O_N$ is shown Figure 3.2 (b). As indicated, absorption and emission energy of 0.73 eV and 0.53 eV is calculated with associated Franck-Condon shifts of 0.64 eV and 0.09 eV, respectively. The ZPL energy of $V_{Al}O_N^0$ is estimated to be approximately 0.64 eV. Once again, the spectra from the defect complex $V_{Al}O_N$ in AlN is in the low energy infrared spectral range.

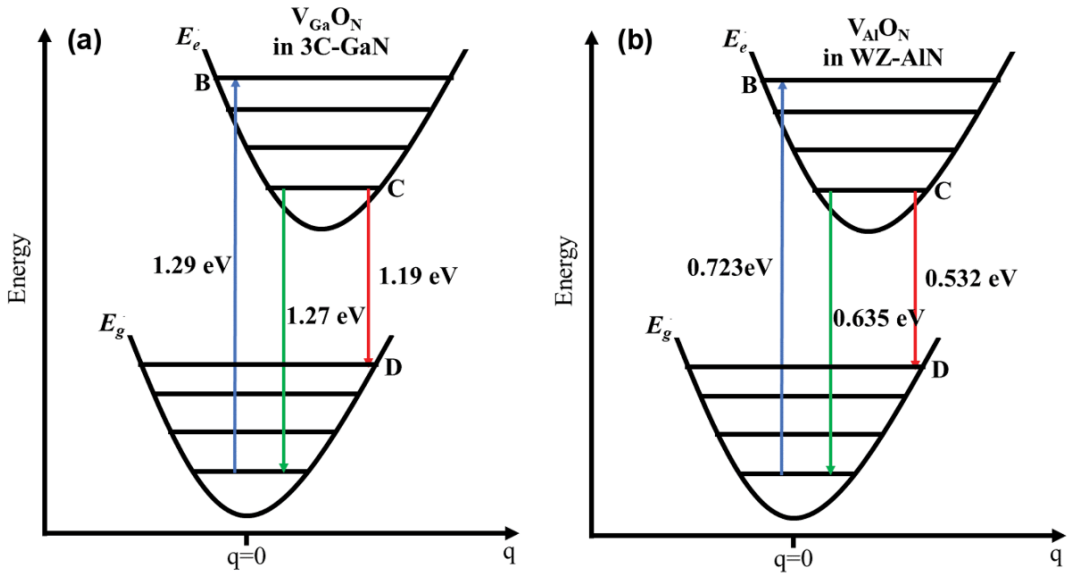

Figure 3.2: Configuration coordinate diagram of the neutral $V_{Ga}O_N$ in 3C-GaN (a) and the neutral $V_{Al}O_N$ in WZ AlN (b). The corresponding absorption, emission and ZPL transition are indicated for both systems with calculated energies.

Another defect type that plays an important role in the optical properties of semiconductors is stacking fault (SF). In the past, the study of SF related fluorescence was mainly focused on its role in the band to band transition of classical devices such as LEDs[136]. More recently, however, SF related single photon emitters are being reported in different materials. It is shown, for example, by controlled growth of Indium Phosphate (InP) nanowire with two interfacing crystal phases, an electronic transition that led to single photon emission can be generated[137]. Also, the recent report on single photon electroluminescence from SiC assigned the origin of the SPE to transitions between a point defect and localised SF[92].

The novel defect-related SPEs in GaN reported in this thesis are also strongly linked to electronic transitions that involve SFs based on experimental results as well as numerical calculation presented in Chapters 4. In the next subchapter, therefore, the structure and electronic properties of SF, mainly in GaN, will be reviewed in the framework of the SPE results discussed in Chapters 4, 5 & 6.

3.3 Optical properties of stacking faults

3.3.1 Formation of stacking faults (SFs)

Stacking faults (SF) are among the different structural defects forming during growth and processing of semiconductors [138-140]. This defect type commonly occurs due to agglomeration of point defects (vacancies or interstitials), affecting the preferred sequencing of crystal atoms in the lattice site [127]. To illustrate this further, let's consider a cross-sectional view of a hexagonal close-packed lattice (hcp), where each bonded (thin black lines) coloured circles represent a plane, labelled A and B in Figure 3.3.

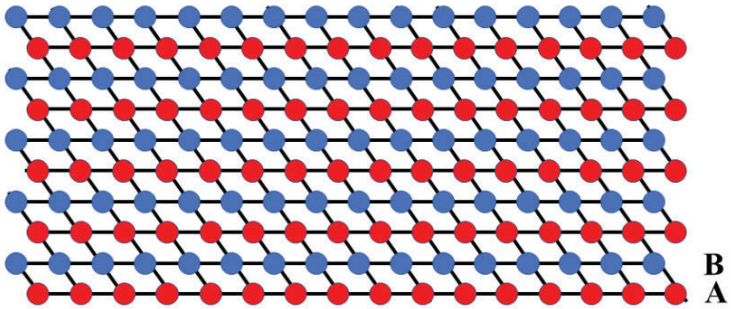

Figure 3.3: Illustration of a cross-sectional view on hexagonal sequencing of lattice atoms on two planes A and B.

Now if vacancies agglomerate by some removal mechanism of the plane **A** atoms, the sequencing will change from abababa to abaBBab as shown in Figure 3.4. That is, due to the agglomeration of vacancies in plane **A**, atoms in plane **B** relax and become neighbours forming the stacking faults. These are two-dimensional defects with corresponding formation energy. As can be seen, stacking faults terminate at dislocations, an essential property to the

determination of stacking faults via wet etching in semiconductors such as Silicon Carbide (SiC)[141-143].

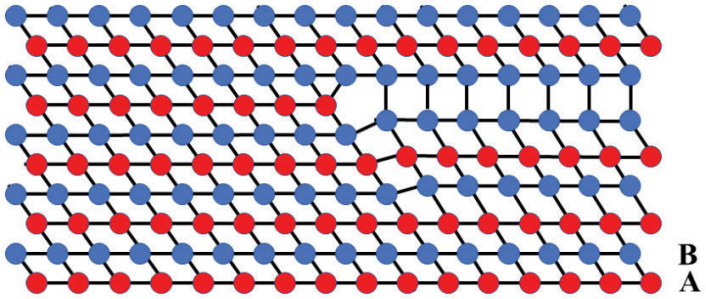

Figure 3.4: Illustration of stacking faults creation by agglomeration of vacancies in a hexagonal matrix.

Alternatively, stacking faults can form via agglomeration of interstitials as shown in Figure 3.5. That is, interstitials agglomerate on the plane of their own changing the sequencing from abababab to abABBaba creating the faulty plane. Once again, the boundary of this kind of SF is a dislocation. A stacking fault formed from an agglomeration of interstitials is commonly referred to as extrinsic SF. Whereas, the ones formed from an agglomeration of vacancies is known as intrinsic SF[127]. A stacking fault formation due to the insertion of the extra plane or agglomeration of vacancies could result in a cubic faulty plane surrounded by a hexagonal lattice. This is termed as cubic inclusion and may have different width depending on the number of agglomerated interstitials or vacancies [144-146]. In some semiconductors, such as gallium nitride (GaN), cubic inclusions modify the local electronic states of the hexagonal crystal in turn affecting optical behaviours as will be seen further below[52, 147, 148].

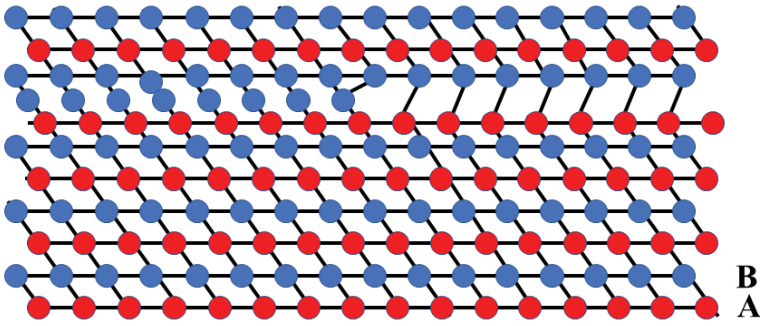

Figure 3.5: Illustration of stacking faults creation by agglomeration of interstitials in a hexagonal matrix.

3.3.2 Stacking faults in III-nitrides

While GaN grows in the wurtzite (WZ) phase at equilibrium having hcp crystal structure, it can also grow in the metastable zinc-blend (ZB) with cubic close packed (ccp) structure as shown in Figure 3.6 (a)&(b)[52]. Although both crystal structures have the same tetrahedral coordination, stacking sequence differs in the third-nearest configuration (Figure 3.6). Thus, the WZ exhibits ABABAB along the (0001) plane direction while the ZB exhibits ABCABC in the (111) plane direction. Stacking faults in WZ GaN is a result of the inclusion of localized ZB segments in WZ matrix.

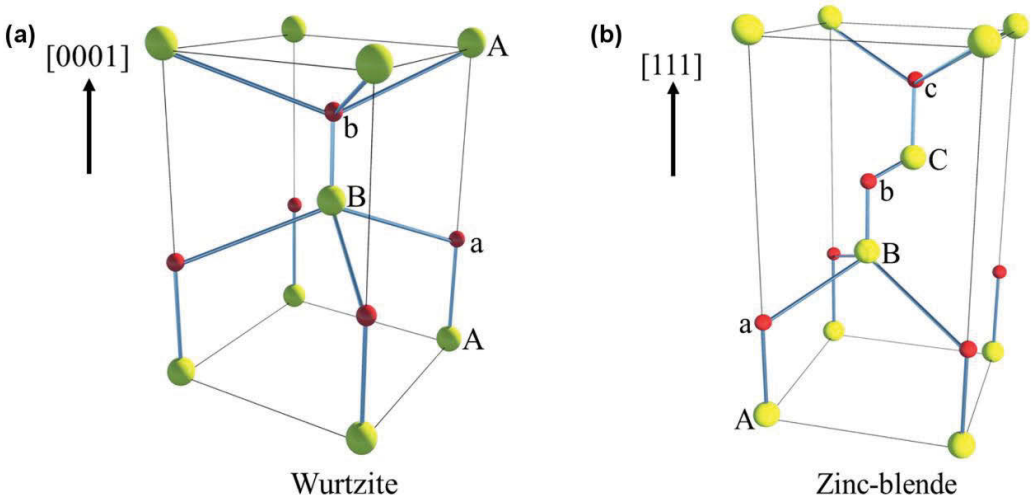

Figure 3.6: Wurtzite and Zinc-blende crystal phase stacking sequence.

There are three types of SFs identified in GaN as depicted in Figure 3.7[52].

a) Intrinsic I_1- could form due to agglomeration of vacancies which change the WZ sequencing such that all second bilayers will be the same. That is the WZ sequencing changes from ABABABAB to cubic inclusive ABABCBCB. This stacking only has one breach of the WZ sequence.

b) Intrinsic I_2- occurs due to agglomeration of vacancies at substrate interface causing atomic steps. In this case, the WZ has two breaches in its stacking changing to the sequencing of the form ABABCACA.

c) Extrinsic E- common in nanostructures, occurs due to agglomeration of interstitials with WZ now having three breaches in its stacking leading to the sequencing of the form ABABCABA.

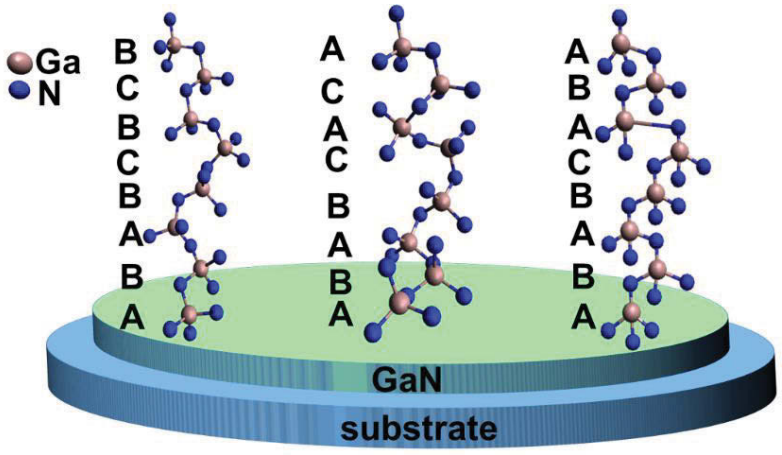

Figure 3.7: Schematics is showing the three main stacking faults, I_1, I_2 and I_3 in GaN.

Each of these cubic inclusions have distinct formation energies where I_1 requires the least and E the largest. Thus, the cubic inclusion of type I_1 is the most common to form during the growth of GaN crystals. The burgers vectors (b) of the partial dislocation in which the cubic inclusion I_1, I_2 and E terminate are, $b=\frac{1}{6}[2\,0\,\bar{2}\,3]$, $b=\frac{1}{3}[1\,0\,\bar{1}\,0]$ and $b=\frac{1}{2}[0\,0\,0\,1]$, respectively[52, 149].

3.3.3 Electronic states of stacking faults

Local discontinuity caused by the inclusion of stacking faults (cubic zinc blends (ZB)) in otherwise hexagonal matrix induces offsets in the band gap energy at the cubic inclusion site[145-147]. This will introduce local electronic states at the inclusions whose characteristics depend on the general properties of the materials in discussion. Here, electronic states induced by cubic inclusions in WZ GaN is considered. With near band edge

emission (NBE) energy of 3.478 eV for WZ GaN and 3.276 eV for ZB GaN, the offset in band gap energy at the cubic inclusion site is around 202 meV[52]. This step-in energy at the WZ/ZB interface induces quantum confinement to excitons (bound electron-hole pairs) at different localities of GaN. Thus, excitons are now confined in one-dimension where cubic inclusions act as 2- dimensional quantum wells (QWs)[145]. Furthermore, wurtzite phase of GaN exhibits spontaneous polarisation due to its singular polar axis while the zinc blend does not. This discontinuity in polarisation at the ZB/WZ interface results in electric field in the cubic inclusion. One of the manifestation of such field in the cubic inclusions is having QWs with triangular band profiles as depicted in Figure 3.8[150]. Also, the localised electric field is proved to be responsible for the experimentally observed red shift in luminescence as well as spectral diffusion by a mechanism known as a quantum confined stark effect (QCSE)[52].

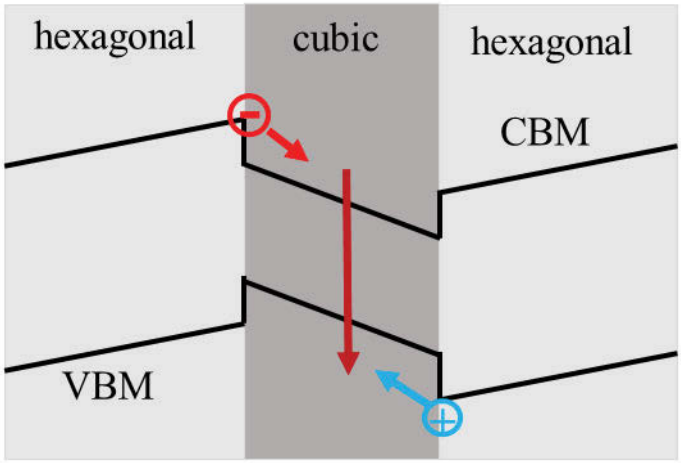

Figure 3.8: Schematics of a triangular band line up due to local cubic inclusion in otherwise hexagonal matrix.

An exciton within the QW can be treated like a hydrogen atom (Figure 3.8)[144]. Thus, using Bohr approximation of the atom, the Bohr-radius (the separation between the electron and hole) is given by

$$a_{ec} = \frac{\kappa \hbar^2}{\mu^* e^2} \tag{3.14}$$

where κ is the semiconductor permittivity, $\mu^* = 1/(1/m_e + 1/m_h)$ is the reduced mass of the electron-hole pair, $\hbar$ is the reduced Planck's constant and e is the charge of the electron. Typical values for the Bohr-radius of excitons are much smaller than the dimensions of the semiconductor, and they indicate the strength of the confinement. At the cubic inclusions where excitons are confined, the energy levels are quantised. The effective binding energy of the excitons in a quantised level is given by

$$\Delta E_{ex} = \frac{\mu^* e^4}{2\kappa^2 \hbar^2} \tag{3.15}$$

where for a fixed QW width and general parameter values for GaN, i.e., $m_h = 0.75m_0$, $m_e = 0.22m_0$ and $\kappa = 9.6$, exciton binding energy (ΔE_{ex}) of 25.1 meV and Bohr-radius (a_{ec}) of 29.9Å can be calculated. These values indicate that excitons bound in cubic inclusion in GaN are room temperature stable having ΔE_{ex} value slightly lower than κT (~ 25 meV).

The other important factor in calculating luminescence energy from cubic inclusion is the width (or thickness) of the stacking faults. One approach to determine the width of the inclusion is to count the number of breaches in the hexagonal sequencing as described in subsection 3.3.1[52]. Thus, for the three types of inclusions described before, the thickness corresponds to 1, 2 and 3 bilayers or $0.5C_0$, C_0 and $1.5C_0$ (where C_0 is the C -lattice constant). The second approach counts the number layers that follow the cubic sequencing of ABC[52]. As such, the three types of inclusions yield thicknesses of 3, 4 and 5 bilayers or $1.5C_0$, $2C_0$ and $2.5C_0$. The peak energy from each inclusion varies where from I_1, I_2 and I_3 yield 3.40-3.42 eV, 3.32-3.36 eV and 3.29 eV, respectively[52]. Also, the luminescence has narrow linewidth unless broadened by other mechanisms.

While luminescence peak energy shifts are ascribed to specific cubic inclusions, all the reported redshift so far have been in meV from the NBE of the WZ GaN as discussed before. In the next chapter, we report room-temperature, single photon emitters believed to be related

to cubic inclusion in GaN. The luminescence from these emitters ranges from the visible to the infrared spectral range. This is far from the cubic inclusion shifted emission, and a model is proposed to explain the substantial shift in luminescence peak as will be presented in Chapter 4. Below we focus on a reported list of mechanisms that cause small shifts from cubic inclusion emission to frame the further discussion on the topic.

Coupling with point defects: The presence of impurities in the vicinity of a cubic inclusion is proposed as a factor to influence the luminescence wavelength by affecting the localisation of the exciton as illustrated in Figure 3.9[52]. It is shown that donor impurities in GaN as far away as 10 nm couple with the cubic inclusion shifting the luminescence from SF of type I_1 by 9 meV. When the calculation is repeated by placing the donor impurities at the centre of the inclusion, the shift is pronounced yielding 53 meV. A similar conclusion was arrived by considering acceptor Mg-impurities in GaN located near cubic inclusions.

The range from which the cubic inclusion can couple to impurity atoms can reach up to 20nm[52]. Thus, for standard doping densities of up to $10^{17}cm^{-3}$, the cubic inclusion can couple to multiple impurities. Hence, upon excitation, multiple impurity states can be populated at a time. For low excitation density, narrow line widths of only a few meV are observed suggesting only the deepest donor-cubic inclusion states are excited. On the other hand, for high excitation density, the linewidth could reach 20 meV indicating that a large number of impurity states are excited[52].

One of the widely-reported indexes for the presence of cubic inclusion related luminescence in GaN is the S-shaped temperature dependence of the peak energy in the temperature range of 10 and 75K[52, 151-155]. The first red-shift occurs due to vibrational redistribution of charges within the localised states followed by blue shift due to deep-transitions as there are few phonon-coupled states at that temperature. Further heating activates more phonon states, thus red shifting the luminescence as in the case of free excitons. Such temperature dependent shift is among the most potent evidence considered in our discussion of the novel single

photon emitters in GaN. Also, this behaviour is reported for SF related luminescence in ZnO[156].

Strain-induced shifts: This refers to shifts in luminescence energy of the cubic inclusion due to relaxation and contraction of the host matrix[52, 157]. This is common in most semiconductors including GaN where compressive strain leads to blue shift while tensile strain leads to redshifts[158, 159]. Also, mechanical forces that induce a change in the band gap energy of the semiconductor will induce a change in the peak energy of the cubic inclusion, which is intuitive considering their identification as QW.

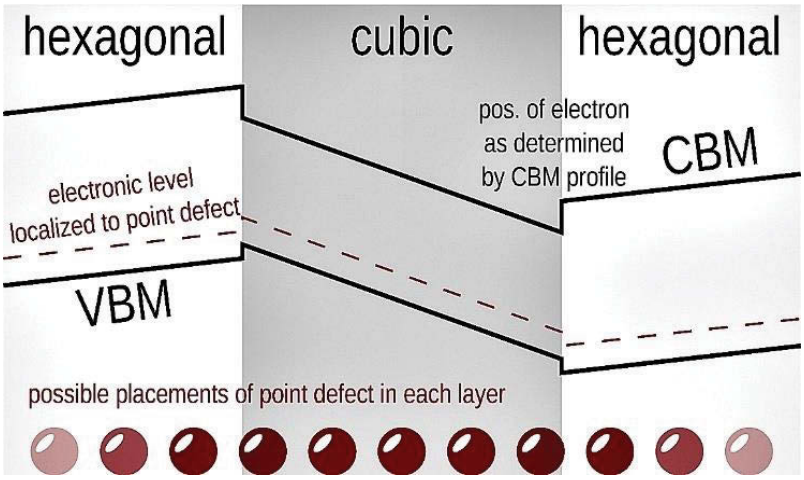

Figure 3.9: Schematics of triangular band line up of a cubic inclusion in a hexagonal matrix with point defects in the vicinity.

Stacking-fault bundling: as the name suggests, this refers to shift in peak energy and linewidth broadening of cubic inclusion related luminescence due to the closeness of SFs from one another[52, 155]. If the spacing between SFs is close enough, the electronic states of each QW will couple. Although the bundling of SFs is presented as a random occurrence, continuous InGaN QWs are artificially engineered to redshift the free exciton luminescence of GaN for light emitting diode (LED) applications. Calculations considering 3, type I_1 SF with inter-distance of less than 5 nm yield shifts in peak energy by up to 40 meV. Also, excitation of such bundled SFs leads to spectral broadening.

Intersections of SFs and QWs: The intersection of SFs and QWs leads to confinement in two-dimension forming 1-dimensional quantum wire[160, 161]. This is reported in non-polar direction grown AlGaN and InGaN QWs which leads to an additional peak that is redshifted from the QW emission line[154]. Polarization dependent measurements were used to demonstrate the one-dimensional characteristics of the emission.

3.4 Colour centres in diamond

Diamond, known to most for its high aesthetic value, have unique material properties that attract different industrial applications. For example, due to its extreme hardness with the highest Young's modulus of around 1 TPa, it can be used for machining of very hard, non-ferrous materials[72]. Furthermore, its high thermal conductivity of around $2x10^3$ W/mK coupled with high electric resistivity makes diamond useful for application as a heat sink. The wide bandgap (~5.5 eV) of diamond has made it a useful material in semiconductor electronics with applications ranging from UV-sensors to metal-semiconductor field effect transistors[72]. Although there are still challenges to reach desirable levels of n-type conductivity in diamond, good p-type conductivity can be achieved via boron doping[72, 162]. Different optical components are also made from diamond benefiting from its wide range of transmission (from UV to IR) and a high index of refraction (~2.4- the highest for visible light). The main advantage of using diamond for all these applications is that it allows operations under extreme conditions due to the materials hardness, chemical inertness, wear resistance and high thermal conductivity.

The sp^3 - hybridisation of carbon atoms with tetrahedral symmetry forms a diamond. The crystal unit cell, shown in Figure 3.10, is composed of two-face centred cubic lattices, offset by a vector $a/4$ in each direction where the lattice parameter a is around 3.57 Å[163]. The extreme hardness of diamond emanates from its very high density (~ 3.5 g/cm^3) and the high

strength of the covalent carbon-carbon bond. The heat transport in diamond is via phonons resulting in much higher thermal conductivity despite its very large band gap[72].

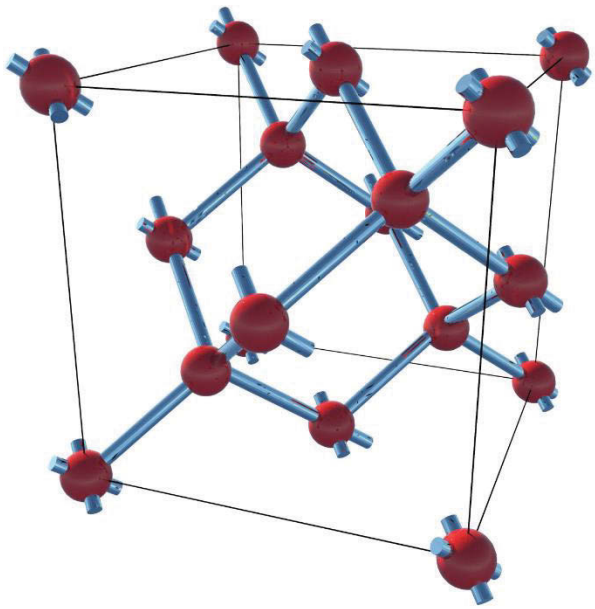

Figure 3.10: Schematic illustration of the diamond unit cell.

Putting the elegant material properties to different applications was hampered for a long time by the natural scarcity of diamond mineral, which can only be mined from few places on earth with lithospheric mantle possessing the necessary high-pressure high-temperature (HPHT) conditions[163]. In 1955 researchers converted the ambient condition stable allotrope of carbon, namely graphite, under the HPHT (hundreds of kbar of pressure and at ~ 2000 ^{o}C) condition to synthesise diamond in a laboratory for the first time[162, 163]. This synthetic diamond can have sizes of up to 1 mm and has all the mechanical attributes of the natural diamond[162]. Since then, cheaper alternatives of fabricating diamond such as chemical vapour deposition (CVD) and detonation nanodiamonds have been demonstrated[164]. Today, high quality, CVD grown, a free-standing polycrystalline diamond wafer of diameters reaching 120 mm - 140 mm, as well as a single crystalline diamond of size 8 x 8 x 2 mm, are commercially available[165, 166]. The gasses flowing into the CVD chamber are methane and hydrogen where the hydrogen terminates dangling carbon bonds from methane

preventing the formation of sp^2 - hybridised graphite at temperatures more than 2000 ^oC[9]. This growth technique also allows easy incorporation of impurity atoms during growth where they will be flown into the chamber as additional gasses.

Single crystalline diamond can be grown homoepitaxially on a diamond substrate. This growth results in natural properties of diamond but are slow and not suitable for growing large size wafers. On the other hand, heteroepitaxial growth on non-diamond substrates can give large size diamonds, but the growth will have a higher concentration of imperfection such as grain boundaries[72]. Imperfections in diamond crystal play an important role both in its mechanical and physical properties. For example, the presence of impurity atoms increases the hardness and wear resistance of diamond due to their contribution in restricting the motion of dislocation in the crystal[72, 162]. In addition, the high thermal conductivity is affected by the presence of dislocations in the diamond crystal because phonons scatter off the defect[72]. The presence of impurity defects also change the appearance of diamond by varying the colour [162]. For example, HPHT grown diamonds usually have yellow hue due to the high concentration of nitrogen impurity.

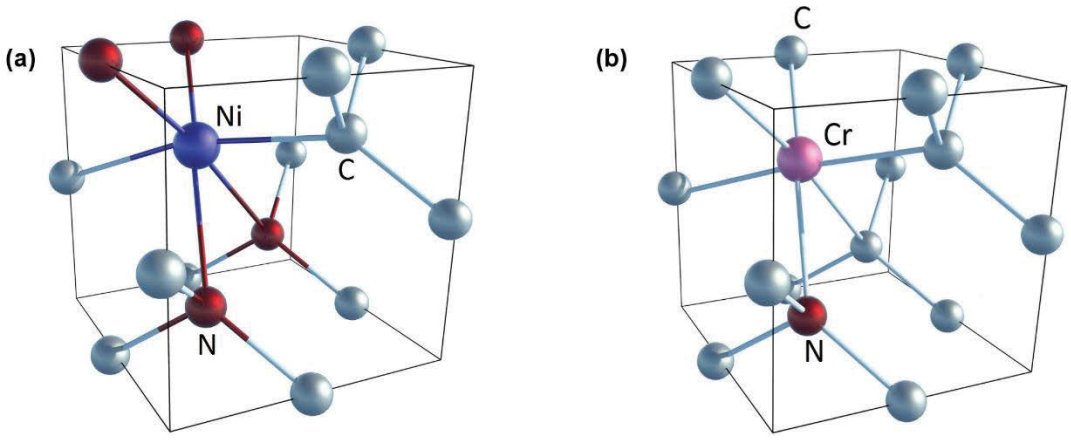

Figure 3.11: Atomic structure of (a) NE8-(b) Cr-related defects in diamond.

More importantly, the hundreds of optically active defects in the bulk of diamond affect the physical and other properties of the material depending on their type and concertation [10,

162]. Under laser excitation, a number of these point defects demonstrate single photon emission spanning a wide wavelength range[10, 16]. While the NV is the most prominent centre for quantum applications with attractive spin and optical properties as introduced in Chapter 1, several other defect-based SPEs are being discovered in diamond[162]. Also, extrinsic defects that are deliberately incorporated into the diamond lattice can serve as SPEs. For example, Nickel ions were successfully placed in the diamond lattice via ion implantation as well as incorporation during diamond growth[10, 167]. The incorporated Nickel forms different defect complexes in the diamond lattice, of which the Nickel-Nitrogen complex (NE8) is identified as SPE[10]. The atomic structure of the NE8 is shown in Figure 3.11 depicting a Nickel atom surrounded by four Nitrogen atoms and two vacancies. The centre of the ZPL for NE8 is reported to range between 782 to 802 nm. Another example of an ion species that is incorporated as defect-based SPE in diamond is Chromium (Cr). Although the atomic structure of Cr-center in diamond is not identified conclusively, a theoretical study indicates Cr atom strongly bonded to adjacent carbons and substitutional nitrogen (or sulfur) atom (shown in Figure 3.11 (b)) may be responsible for the emission[10, 80]. The ZPL for Cr related emission ranges from 740-790 nm. A summary of spectral properties of few defect-based SPE in diamond is shown in Figure 3.12.

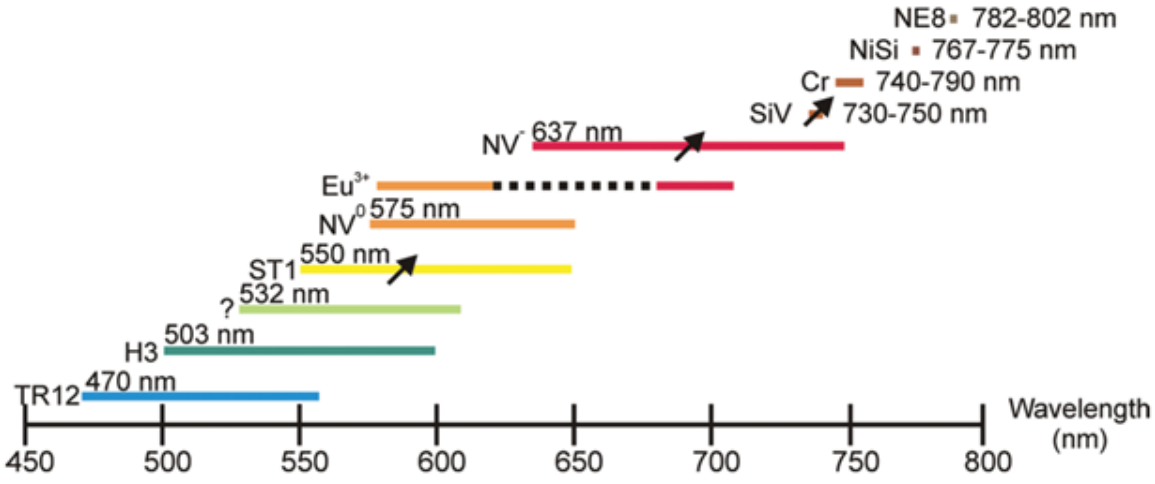

Figure 3.12: A map illustrating the spectral characteristics of a few of the identified SPE in diamond. The length of the lines corresponds to a range of emission from the respective SPE including the PSB. The

intrinsic carbon interstitials (TR12) emit with at ZPL of around 470 nm while the H3 centre consisted of two nitrogen atoms and a vacancy emits at 503 nm. At ZPLs of 532 nm and 734 nm, SPE with unidentified origin is reported. The so-called ST1 centre is also unidentified SPE from the diamond with ZPL at around 550 nm and allows optical manipulation of its spin as indicated by the arrow. By incorporating europium (Eu^{3+}) in the diamond lattice, fluorescence emission with two separate ZPLs corresponding to allowed radiative transitions in the impurity is reported. The NiSi is a Nickel-Silicon complex showing emission with ZPL between 767-775 nm[10].

The applicability of these single photon emitting defects for quantum technologies relies on the different criteria outlined in Chapter 1. One of the critical requirements stated is that an SPE should allow electrically triggered excitation. So far, however, RT stable single photon electroluminescence from diamond defects is only reported from NV-center making the centre among the most desirable together with its other valuable characteristics.

Silicon-Vacancy (SiV) centre is perhaps the second most investigated SPE in diamond [20, 168-170]. This is may be due to the centre's distinguishing photophysical characteristics at RT as well as its successful incorporation in both bulk and nanodiamonds [171-173]. Thus, symmetry and electronic structures of SiV is somehow understood. However, electrically excited single photon fluorescence from SiV was lacking in the literature. The first electrical excitation of the SiV ensemble will be presented in Chapter 7. In this subchapter, incorporation and electronic properties of SiV in a diamond diode will be discussed in light of the results in Chapter 7.

3.4.1 Incorporation of SiV center in diamond

Silicon (Si) atoms are unintentionally present in CVD grown diamonds; incorporated from the chamber window and wall which is left as residue after the use of silicon substrates[16]. This usually results in forming agglomerated SiV centres with low density which rarely shows single photon emission. Nevertheless, such incorporation can be used for proof-of-principle studies[174]. High-temperature heating (annealing) of the diamond sample can lessen the agglomeration effect by diffusing vacancies around. The linewidth of SiV narrows down to 0.03 nm after annealing at 1100 ^{o}C approaching the transform-limited linewidth[9].

However, for scalable nanophotonic applications, deterministic incorporation of the centre into the diamond matrix is vital. Delta doping of diamond with Silicon-atoms has been demonstrated to yield a controlled generation of SiV centre during homoepitaxial, microwave plasma CVD growth of ultrapure diamond film[9, 175]. The substrate used was a <001> oriented HPHT diamond on top of which a 60 µm film was grown. SiC substrate was placed underneath a molybdenum sample holder to serve as a source of the Si-atoms in addition to the quartz window. The concentration of Si introduced into the plasma and incorporated during growth is estimated to be < 1 ppb. The SiV centre generated this way produced stable SPEs that showed no spectral diffusion[175]. Also, with SiV centre approaching the transform-limited linewidth, spectral overlap from a randomly chosen centres of more than 91% is reported[175]. A successful coupling of the centre with a solid immersion lens is also demonstrated. Emission rates of up to 6 x 10^6 counts/s is reported for CVD incorporated SiV during nanodiamonds growth[9]. However, the spectrum showed diffusion with the ZPL ranging from 730 to 750 nm.

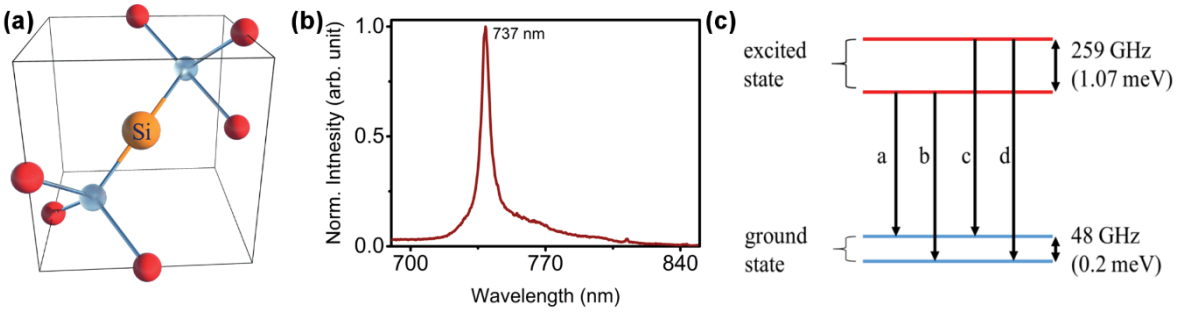

Figure 3.13: (a) Atomic structure of SiV centre in Diamond (b) Spectrum of SiV^- in diamond (c) electronic structure of SiV^- centre in diamond.

The other important approach to generating point defects is ion implantation, where ion species such as Cr, Si, Xe are accelerated into the diamond target[176-178]. An easy to use simulation- the stopping and range of ions in matter (SRIM) - has been developed to estimate ion penetration range. SRIM is also used to estimate the density of created defects for choices of implantation energy and ion species. The recipe for optimal latterly resolved Si^{2+} ion implantation has been developed and abundant single photon emitting SiV centres have been

generated[72]. To improve the lateral resolution, ion implantation can be carried out under mask[179]. The mask is developed using electron beam lithography. Ion implantation can also be used to dope wide variety of semiconductors including diamond. SiV centre from ion implantation usually has low emission rates of around several 1000 counts/s.

Ion implantation induces undesired damage to the target creating carbon interstitials and vacancies as the accelerated ion energies typically exceed the binding energies of the target. The damage changes the sp^3 - binding into the ambient stable sp^2 -binding of graphite[179]. If the damage results in the creation of vacancy concentration of more than about 10^{22} cm^{-3}, the diamond sample is said to have been graphitized. This threshold could be higher for ion implantation energy in the range of MeV where deeper ion localisation is accompanied by higher pressure from the undamaged surface prohibiting the expansion of damage to larger areas[179]. To recover the damage caused by ion implantation, the annihilation of interstitials and vacancies created during the damage is required. However, there is a significant discrepancy in the annealing temperature required to move carbon interstitials (50 K) and vacancies (700 K)[179]. Hence, extra carbon may be required during the annealing process. Also, annealing of diamond is usually carried out under vacuum to avoid oxidation of the diamond surface.

3.4.2 Structural and optical properties of SiV centre

This thesis will not discuss the details of this topic (see [180] for a detailed discussion). It, however, highlights essential points to frame results in Chapter 7. The fluorescence from the SiV centre was first identified in 1980 via CL spectroscopy of CVD grown diamond at around 738 nm, which later was assigned to silicon-related defect[181]. The assignment was carried out by implanting various ion species (~ 25) into a natural diamond where the signature luminescence (~738 nm) is only observed after Si ion implantation[162]. Further investigation, however, showed that ion implantation would also result in another, optically active, a damage-related defect known as General Radiance (GR1) line which emitted at

around 743 nm. However, upon annealing diamond above 800 ^{o}C, the GR1 line is observed to disappear[182]. To probe the actual source of the 738 emission, a Si impurity incorporated, CVD grown diamond was irradiated with electron beam[128]. After the irradiation, the sample showed both silicon-related luminescence at 738 nm as well as GR1 line emission at 743 nm. Annealing the sample above 800 ^{o}C, the GR1 line disappeared whereas the Si-related luminescence intensity increased dramatically[183]. This result was explained as, at elevated temperature the vacancy migrated to form more SiV centres, thus increasing the overall luminescence count. The same argument also explained the earlier observation of the quadratic relation between the implanted Si ion dosage and CL intensity [181]. This observation was used to prove the existence of a vacancy in the structure of the silicon-related defect.

The definitive structural description of SiV centre is mainly studied using theoretical models consolidated by experiments. The widely accepted structure of SiV now is: a Si impurity splits two vacancies forming the Si-divacancy as illustrated in Figure 3.13(a)[16]. The SiV centre has an accepted two charge states (see Chapter 2): The negative-charge state (SiV^{-}) with the ZPL at around 738 nm and the neutral-charge state (SiV^{0}) with luminescence peak around ~946 nm[169, 184]. This was first deducted from UV excitation of SiV centre, where the fluorescence from SiV^{-} disappears into a dark state[183]. This was explained as a charge transfer from SiV^{-} to a dark neutral charge state. The observation was further consolidated through electron paramagnetic resonance (EPR) measurement of a high purity diamond sample with SiV centre, where an emission at 946 nm is detected and assigned to SiV^{0} [184]. Furthermore, annealing the sample led to increased luminescence from SiV^{-} and reduced luminescence from SiV^{0}. This was explained as a charge transfer from neutral charge state to the negative charge. Exciting the sample with a UV laser yielded the inverse relation. In Chapter 7, we will present consistent results via electrical control of charges at the SiV^{-} ensemble where reduced intensity is observed when charges are withdrawn from the centre.

The SiV^- has been investigated at RT showing attractive spectral properties such as most of the fluorescence is concentrated in the ZPL with FWHM of 0.7 nm as shown in Figure 3.13(b)[78, 170]. The centre has weak phonon sideband that extends up to 750 nm with the HR-factor of ensembles ranging from 0.08 to 0.24. The excited lifetime of the centre is around 1 ns with relatively low quantum efficiency[16]. The transition kinetics of SiV^- centre was fully described considering a three-level model [78]. That is, there exists at least one shelving state (metastable state), for the excited state as a decay step to the ground state (see Chapter 2 for details). While the luminescence study of SiV centre so far was mainly carried out via excitations using electron beam (CL) or off-resonant light (laser of various wavelengths), Chapter 7 presents the first electrical excitation of the centre (EL).

Furthermore, polarisation and excitation photoluminescence (PLE) measurements at cryogenic temperature showed that the electronic structure of the centre is composed of split ground and excited state yielding (see Figure 3.13(c)) four distinct ZPL lines [175, 185, 186]. Indistinguishable photon generation from two distant SiV^- centres is demonstrated[187], indicating the capabilities of two-photon entanglement using the centre, which is a prerequisite for quantum computation using photons (see Chapter 1). Finally, spin-state manipulation via spin-photon interaction is demonstrated for both SiV^- and SiV^0 [188, 189].

So far, the background behind the study of single photons, excitation mechanisms, as well as defect-based single photon emission, is featured. We will now proceed to present the main contributions of this work by first disclosing novel single photon emitters from defects in GaN.

4 Spectroscopy of single photon emitting defects in GaN

Single photon emitters play a central role in many photonic quantum technologies some of which are discussed in Chapter 1[190, 191]. A promising class of single photon emitters consists of atomic colour centres in wide bandgap crystals, such as diamond[192, 193] silicon carbide[194] and hexagonal boron nitride[195]. However, it is currently not possible to grow these materials as sub-micron thick films on low-refractive index substrates, which is necessary for mature photonic integrated circuit technologies. Hence, there is great interest in identifying quantum emitters in technologically mature semiconductors that are compatible with suitable heteroepitaxy. Here, we demonstrate robust single photon emitters based on defects in GaN: a semiconductor that can emit light over the entire visible spectrum. We show that the emitters can be found in a variety of GaN wafers, thus providing easy access for further fundamental study and technological development. We propose a theoretical model to explain the origin of these emitters based on cubic inclusions in hexagonal gallium nitride.

In this chapter, we report room temperature (RT), bright, stable single photon emitters (SPEs) in GaN films that do not require any post-growth sample treatments. The emitters are defects that are optically active in the visible/near-infrared (NIR) spectral range, and the zero-phonon lines (ZPL) span a wide range of wavelengths. They were found in 5 GaN wafers that have different doping types, doping levels, and are grown on various substrates using Metal Organic Chemical Vapor Deposition (MOCVD).

4.1 Materials and structural analysis

To identify and characterize the SPEs, we analyzed 5 GaN samples grown on sapphire and silicon carbide (SiC). The wafers used in this work where grown by MOCVD, and have the following structures: Sample A: 2-μm-thick Mg-doped (Mg $>1x10^{20}$ cm^{-3})/ 2-μm-thick undoped GaN/ Sapphire (from Suzhou Nanowin Science and Technology Co., Ltd.); Sample

B: 2-µm-thick GaN/Sapphire; Sample C: 20-nm-thick p++ GaN:Mg ($1.5x10^{20}$ cm^{-3}) / 0.5-µm-thick p GaN:Mg ($1x10^{18}$ cm^{-3})/ 8-µm-thick n GaN:Si ($1.7x10^{16}$ cm^{-3})/ 0.2-µm-thick n++ GaN:Si ($2x10^{18}$ cm^{-3})/ 5-µm-thick n++ GaN:Si ($7x10^{18}$ cm^{-3})/ Sapphire; Sample D: standard LED structure; Sample E: 23-nm-thick AlGaN/ 1-nm-thick AlN/ 1.2-µm-thick GaN/ SiC.

Sample **(Sample size)**	**Optical microscope image** (scale bar is 20µm)	**AFM image**
A **(1 cm x 1 cm)**	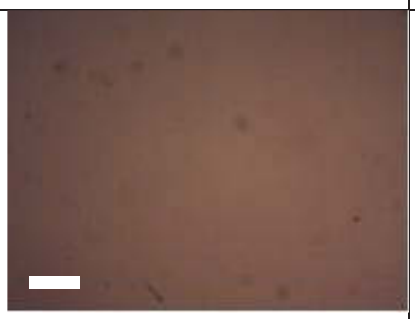	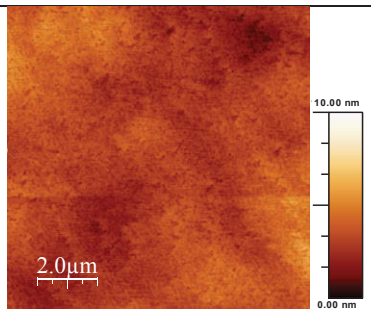
B **(1 cm x 1 cm)**	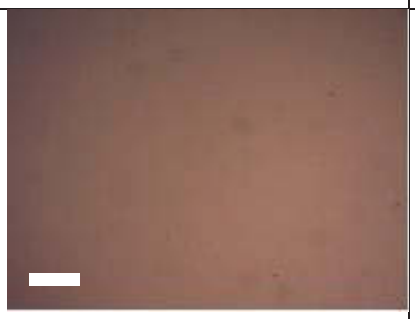	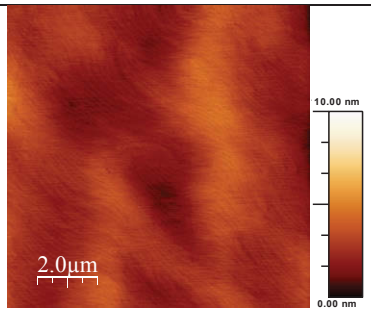
C **(1 cm x 1 cm)**	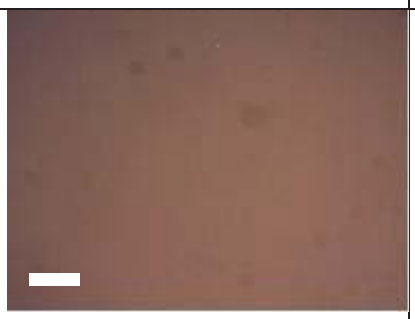	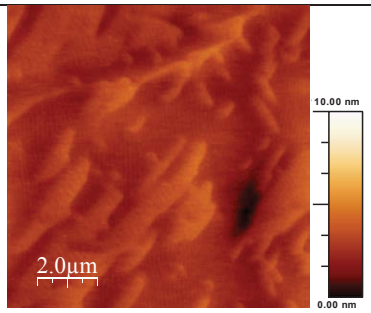

D **(1 cm x 1 cm)**	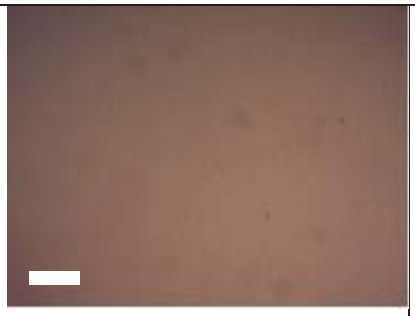	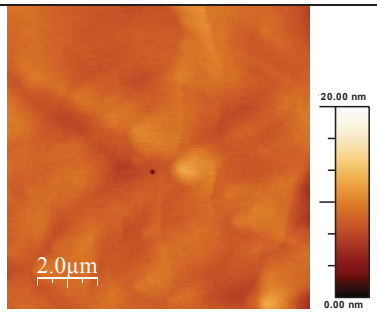
E **(1 cm x 1 cm)**		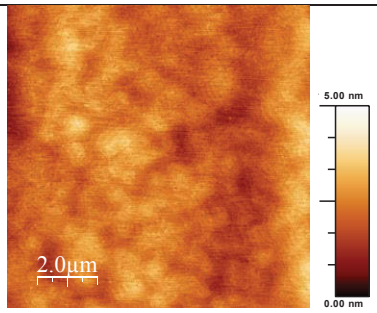

Table 4.1: Optical microscope and AFM images of Sample B – E.

Optical images and atomic force microscope (AFM) scans of the different samples is presented in Table 4.1. Also, the crystalline quality of the GaN samples was evaluated using X-ray diffraction (XRD) measurements. Summary of the measured structural parameters of the samples is provided in Table 4.2. For all samples, the surface roughness is below 1 nm (Table 4.2) indicating the single crystalline nature of the samples. This is consolidated by the FWHM values from the X-ray measurements shown in Table 4.2.

Sample	**XRD FWHM (0002)**		**AFM rms (nm)**
	degree	arcsec	
A	0.182	653.5	0.9
B	0.181	650.2	0.8
C	0.224	807.5	0.7
D	0.0640	230.3	0.8
E	0.118	426.1	0.5

Table 4.2: XRD data of the (0002) and AFM measurement of Sample A – E.

Additional structural analysis is conducted on sample A using Raman spectroscopy where backscattering from the *c*-plane of the sample is measured. Figure 4.1 shows the result where two known modes in WZ GaN: E_2 (E_2^L, E_2^H) phonon modes at 144 cm^{-1} and 569.6 cm^{-1}. Also, the longitudinal A1 (A_1 (LO)) is shown at 735.6 cm^{-1}. While the mode at 417 cm^{-1} is from sapphire, 1368 cm^{-1} and 1398 cm^{-1} are possibly from optical overtones and combination modes. As expected for a WZ GaN, the E_2^H mode has high intensity and narrower FWHM of 3.22 cm^{-1} further showing the quality and single crystal nature of the film.

The presence of morphological defects in sample A is investigated by etching it in molten KOH. The sample was etched for 15 mins in a crucible containing molten KOH and was kept on a hotplate at temperatures of around 350 ^oC as read from a thermocouple.

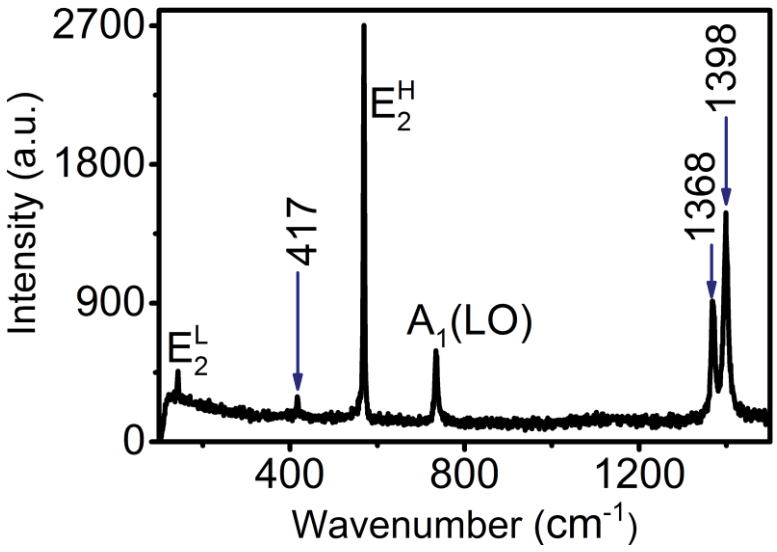

Figure 4.1: Raman spectroscopy of sample A showing known phonon modes for WZ GaN and sapphire.

The resulting topography of the sample is analysed using an optical microscope (OM) and scanning electron microscope (SEM) images as shown in Figure 4.2. After etching, the OM images show many dark stripes as shown in Figure 4.2(a). Further inspection of the dark stripes using SEM reveals visible surface morphologies which are agglomerated along a line (Figure 4.2(b)). A closer look on the morphologies with SEM (inset of Figure 4.2(b))) shows known structural defects such as threading dislocation agglomerates with different types of

etch pits. Although this morphology is known after KOH etching of MOCVD grown GaN, why the defects are agglomerated along a line is not yet clear.

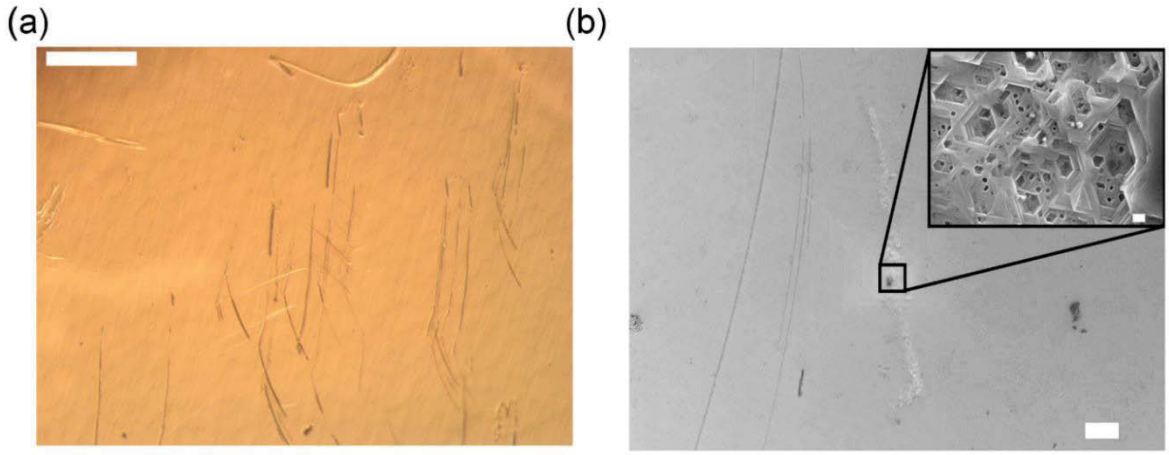

Figure 4.2: Post KOH sample topography analysis using (a) Optical microscope image with a scale bar of 100 µm (b) Scanning electron microscope (SEM) image with a scale bar of 10 µm with an inset magnifying the etched area with a scale bar of 100 nm.

4.2 Experimental setting

The spectroscopy measurements on all samples were performed using a scanning confocal microscope. The micro-photoluminescence set-up (µPL), illustrated in Figure 4.3, enables high spatial resolution scans resulting in intensity map. In this work, a cw-green laser of wavelength 532 nm (Gem 532™, Laser Quantum Ltd.) is used as the excitation (λ_{exc}) source. The laser beam is expanded to overfill the objective for optimum focusing. This is done by using two lenses, L1 (plano-convex) & L2 (spherical) in a Keplerian telescope arrangement as shown in Figure 4.3. Most of the measurements presented in this work are done with a filling factor of around 2. The beam then undergoes reflections at a Mirror (M1), a 532-nm dichroic mirror (532-nm laser BrightLine™, Semrock Inc.) and an X-Y piezo scanning mirror (FSM-300TM, Newport Corp.). Before it is focused onto a sample by a high-numerical-aperture (NA= 0.9, Nikon) objective lens, the beam passes through relay lenses (L3 & L4) to correct for aberration. High resolution scanning at the sample is carried out with the motorised X -Y piezo scanning mirror (SM).

To remedy the introduction of unwanted circular or cylindrical polarised light into λ_{exc} from different components on the set-up, a quarter waveplate ($\lambda/4$) is fixed after the first mirror (M1). The quarter waveplate is optimized to dampen counts arising from cylindrically polarized light. In addition, a half waveplate ($\lambda/2$) is placed after the quarter waveplate to rotate the polarization form of the excitation for absorption dependent analysis of SPEs.

The detected wavelength (λ_{det}) from the emitters is first filtered from excitation laser with the dichroic mirror (DM) and then by an additional 568 nm long-pass filter (SemrockTM) labelled as F1 in Figure 4.3. Finally, the detected signal is focused into a graded-index fibre with a core size of 62.5 μm, where confocality arises. Like the excitation hand, a quarter waveplate is fixed after the DM to dampen elliptically polarised components in the detected photons. In addition, a visible polariser (P1) is rotated to analyse emission polarisation of SPEs.

A fibre splitter then leads the coupled signal either to a spectrometer (Acton SpectraPro™, Princeton Instrument Inc.) for spectroscopic measurements or an integrated Hanbury-Brown and Twiss (HBT) interferometer for intensity fluctuation measurements (i.e., for proof of single photon emission). The CCD cooled spectrometer with a focal length of 300 mm is equipped with plane gratings of 300 g/mm, 600 g/mm and 1200 g/mm. At blaze wavelength of 500 nm, the 300 g/mm grating has a dispersion of 10.4 nm/mm with CCD spectral resolution 0.4 nm. The dispersion range and CCD spectral resolution for 600 g/mm are 5.1 nm/mm and 0.2 nm, respectively. For 1200 g/mm grating, the dispersion and resolution further refines to 2.38 nm/mm and 0.1 nm. The spectrometer comes with adjustable entrance slit which can be varied from 10 μm to 3 mm. In our case, the entrance slit is used to insert the other end of the collection fibre ferrule.

The HBT set up is composed of two avalanche photodiodes (Excelitas Technologies™) and a time-correlated single-photon-counting (TCSPC) module (PicoHarp300™, PicoQuant™) as shown in Figure 4.3. A delay line of 100 ns is introduced on the BNC leading to one of the APDs. TCSPC is used in a start-stop mode to collect short time correlation profiles

accumulating histograms up to 200 ns. For long autocorrelation times, the TCSPC is operated in T2-mode which allows, fast correlation of up to a few seconds.

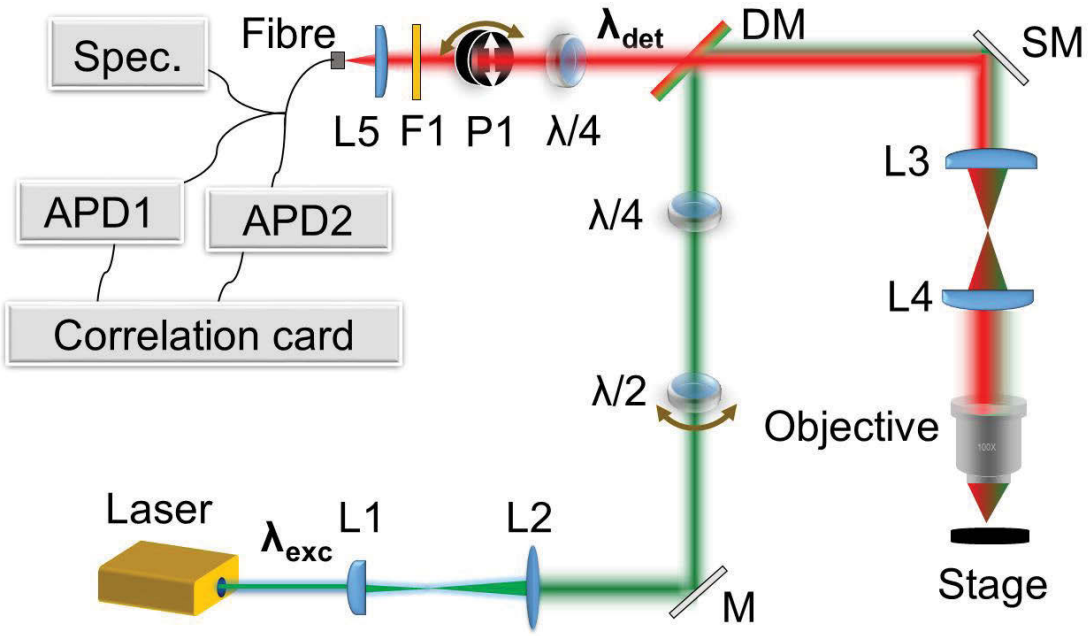

Figure 4.3: Schematics of confocal microscopy setup. The addition of two avalanche photodiodes and a time-correlation card illustrates the integrated HBT setup for single photon detection.

4.3 Spectroscopy of SPEs in GaN at room temperature

Figure 4.4 (b) shows a typical 60 µm X 60 µm fluorescence map with localised, bright spots labelled E1-E8, corresponding to isolated emission spots in Sample A. This map is obtained from a 1 cm^2 sample using an excitation power of 300 µW (measured before the microscope objective). Analysis of other regions of sample A indicates an average of 1 emitter per 25 μm^2.

Figure 4.4(c) summarises fluorescence scans of GaN Samples B-E, which consist of the layer structures shown in the insets. Sample B was grown directly on sapphire, C and D on sapphire overgrown with different GaN/InGaN epilayers, and Sample E was grown on SiC (see subchapter 4.1 for details). The circles in Figure 4.4 (c) indicate SPEs. Isolated bright spots

were found in each sample, though the density varied across the samples. We note that the samples were chosen randomly, with no specific growth requirements, to ascertain the widespread presence of SPEs in epitaxial GaN.

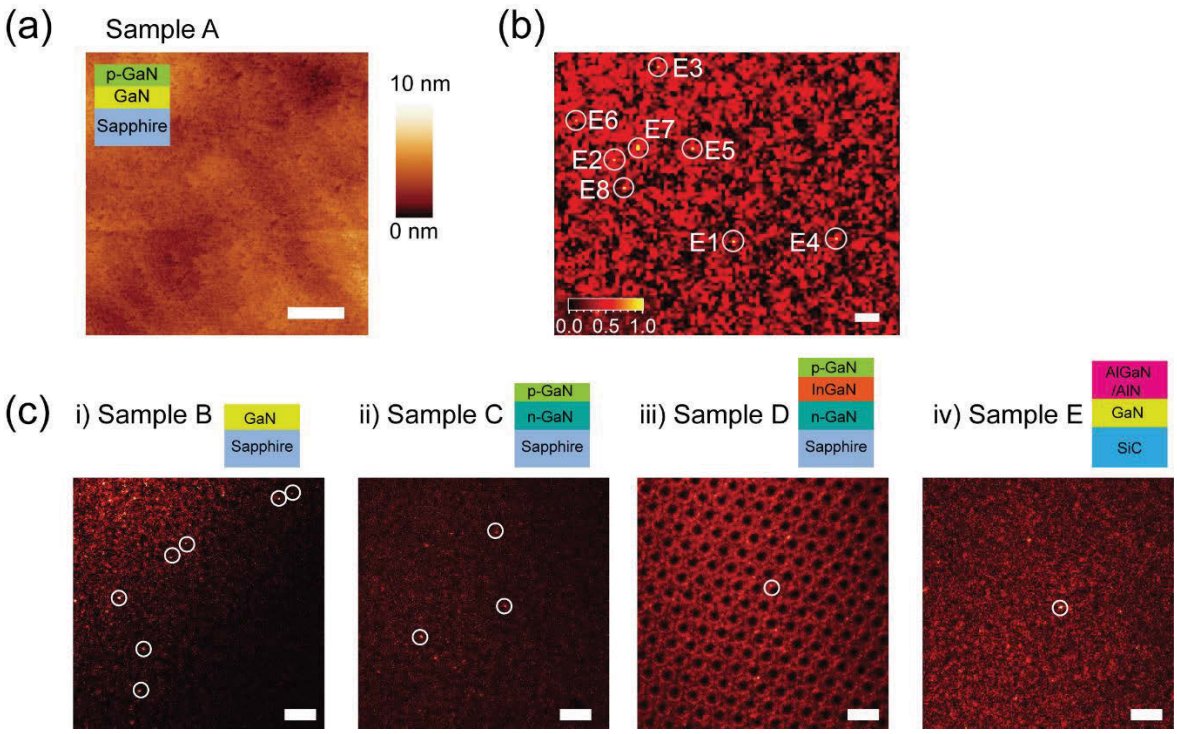

Figure 4.4: Defects in GaN wafers. a) 10 µm x 10 µm AFM image of Sample A. The surface roughness is < 1nm. The scale bar is 2 µm. Inset is the structure of Sample A depicting 2 µm Mg-doped GaN layer on 2 µm undoped GaN film grown on sapphire by MOCVD. b) 60 µm x 60 µm confocal fluorescence scan of Sample A obtained using a 300 µW excitation laser power. The scale bar is 5 µm. c) 40 µm x 40 µm confocal fluorescence scans of Samples B-E under 100 µW excitation power: i) 2 µm, undoped GaN, ii) 0.5 µm, Mg-doped GaN on 13.2 µm, Si-doped GaN, iii) GaN LED structure, iv) 1.2 µm, undoped GaN. Samples B-D are grown on sapphire. Sample E is grown on silicon carbide. The bright spots inside the white circles indicate localised emitters. Insets: schematic diagrams of Samples A-E.

Figure 4.5(a) shows RT photoluminescence (PL) spectra from emitters E1-E5 where distinct ZPL wavelengths of 640 nm, 657 nm, 681 nm, 703 nm and 736 nm are obtained. All spectra are measured under the same excitation power of 100 µW. The 696 nm luminescence peak corresponds to the ruby Cr_{Al}^{0} emission and is present in all spectra taken from the samples grown on sapphire. Additional representative RT spectra from emitters on Sample A

including E6-E8 are shown in Figure 4.6 further consolidating the variation in the peak ZPL wavelength.

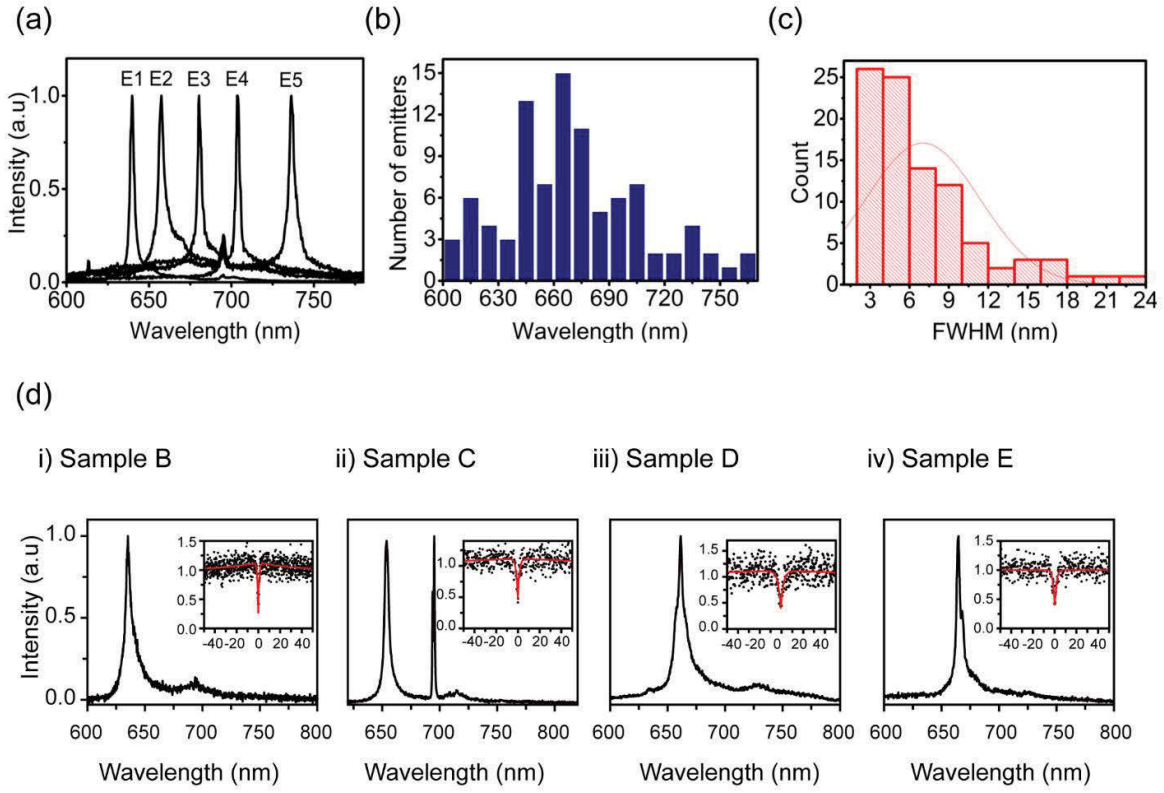

Figure 4.5: Single photon emitters in GaN. a) Room temperature spectra from emitters E1-E5 (shown in Figure 4.1b) reveal distinct ZPL wavelength of 640 nm, 657 nm, 681 nm, 703 nm and 736 nm. The peak at 696 nm is the Cr_{Al}^{0} emission from the sapphire substrate. b) Histogram of the zero-phonon line wavelength distribution and c) the corresponding FWHM distribution measured from emitters in sample A. d) Typical PL spectra and g^2 measured from emitters in Samples B-E.

The histogram in Figure 4.5(b) shows the ZPL wavelength distribution of 93 emitters with distinct spectra in Sample A. The bin width of the histogram is 10 nm as small differences in peak position can be caused by strain variations throughout the sample[170]. However, the ZPL wavelengths span more than 170 nm, suggesting a different primary mechanism for the broad distribution seen in Figure 4.5(b). A likely mechanism is proposed further below.

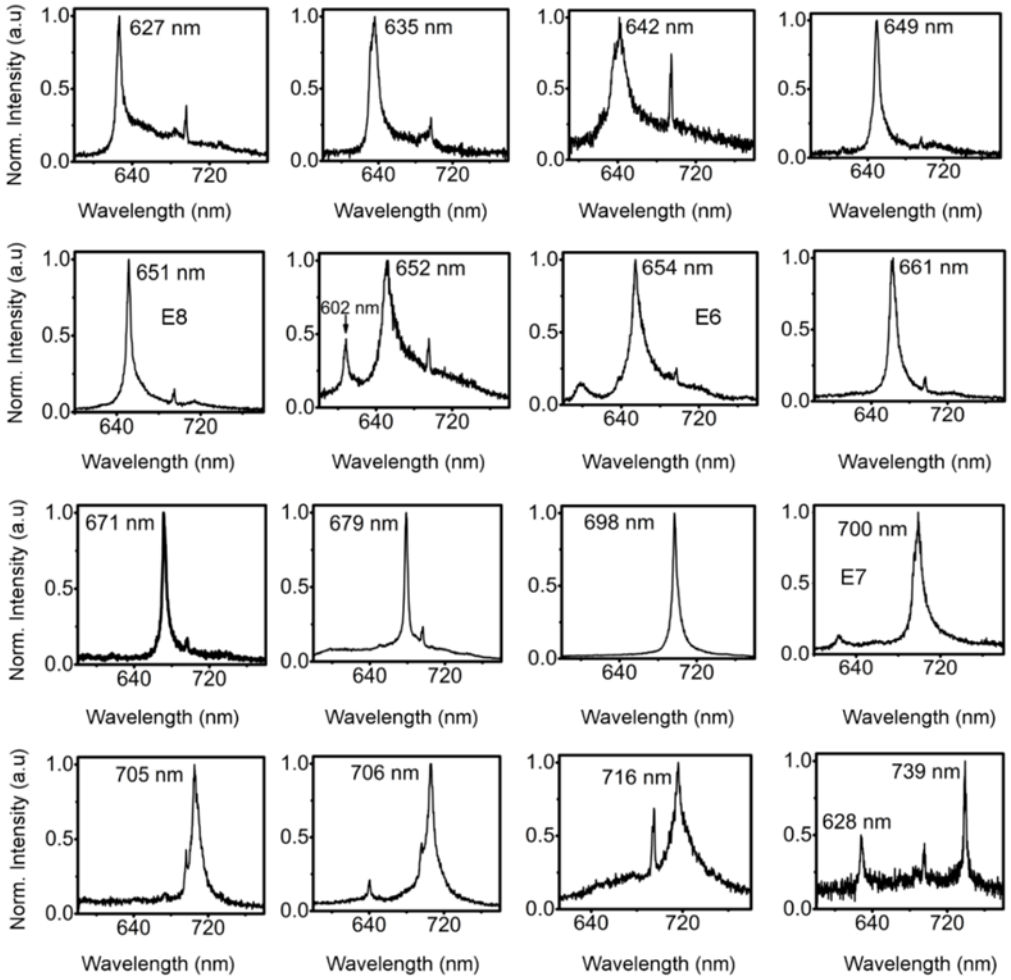

Figure 4.6: Room temperature spectra from emitters in GaN Sample A. Representative spectral characteristic of 16 different emitters collected from 5 different scans. 532 nm green excitation laser with a power of 100 µW - 250 µW was used, and each spectrum was integrated for 10 s. Spectra from emitters E6, E7 and E8 (see Figure 4.1b) are also included and labelled accordingly. The wavelength of each ZPL is specified (the emission at 696 nm corresponds to the ruby line in sapphire and is present in all the spectra).

The histogram in Figure 4.5(c) summarises RT ZPL line width distribution from 93 emitters in Sample A, with a median full width at half maximum (FWHM) of ~ 5 nm. Fits of the ZPL peak shape reveal an asymmetry caused by a low energy tail which may be caused by coupling to phonons. The ZPLs are narrower than the RT line width of the NV[196] centre in diamond and comparable to other defects in diamond (e.g. the SiV[197] and the Cr-related[176]).

Similar RT spectra are collected from SPEs in the other four samples to check if the observation is consistent across the different samples. As shown in Figure 4.5 (d)-(g), emission with narrow linewidth is observed from the respective samples. Distribution of both ZPL and FWHM of SPEs in Samples B, C, D & E are shown in Figure 4.7, indicating that similar spectral behaviours are observed as in Sample A. Therefore, it can be concluded that the underlying mechanism for single photon emission in the 5 GaN samples is the same regardless of inter-sample differences such as thickness, electronic grade as well as substrate used for growth.

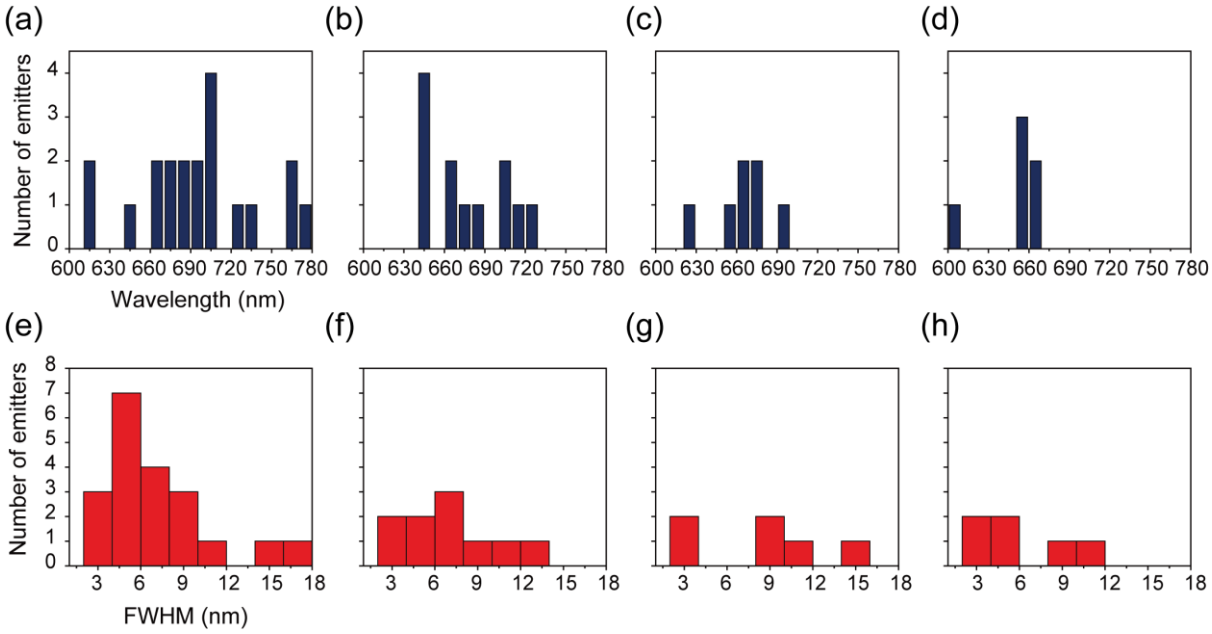

Figure 4.7: Histogram of the zero phonon line wavelength distribution and the corresponding FWHM distribution measured from emitters in samples B(a,e), C(b,f), D(c,g) and E(d,h). In 40 µm X 40 µm area, an average of 6~7 emitters (Sample B), 3~4 emitters (Sample C), 1~2 emitters (Sample D and E) are found.

While we are confident emission from all the samples have the same origins, it is not yet clear that the observed fluorescence is indeed from the GaN films. To confirm this, three pieces of Sample A were etched using chlorine reactive ion etching (RIE). The first sample was softly etched with ICP and RF powers of 1000 W & 30 W, respectively. The gasses flown were Chlorine (Cl), Hydrogen (H_2) and Argon (Ar) with rates of 20:4:4 sccm and DC bias of 62 V.

The etching was carried out in two steps under same parameters: The first round lasted for 2 min resulting in etch depth of ~100 nm followed by 4 min of soft etch giving total etch depth of around 300 nm. The pressure and temperature during this etching round were kept at 60 °C and 4 mT, respectively. The second piece was strongly etched in two rounds with ICP and RF powers of 1000 W & 200 W, and final round of soft etch at ICP/RF powers of 1000/30 W.

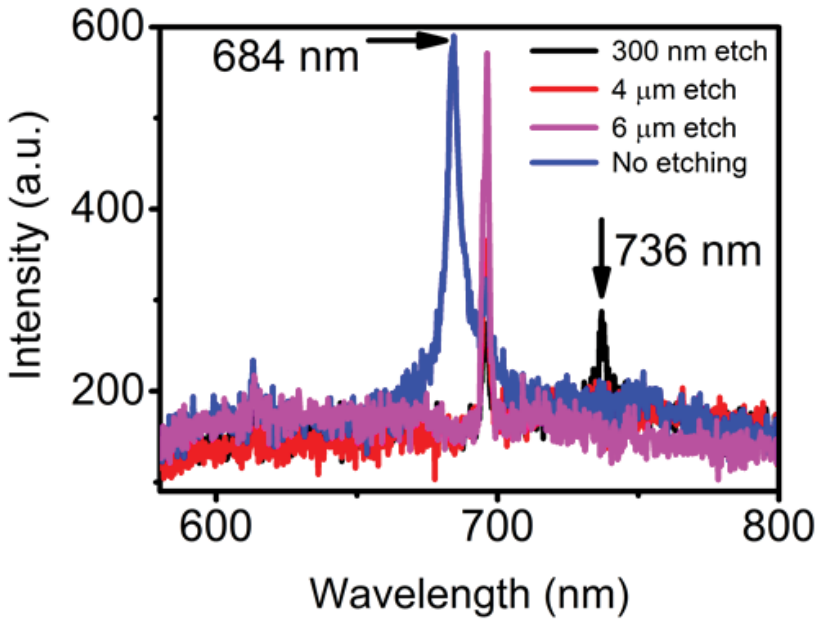

Figure 4.8: PL spectra from samples that were etched using chlorine reactive ion etching (RIE) to depths of 300 nm, 4 µm and 6 µm. As shown, after 300 nm etch, emitters were still resolved with representative fluorescence at 736 nm (black). However, after 4 µm (red) and 6 µm (pink) etching, no fluorescence can be observed except the chromium line in sapphire at 696 nm. PL from a sample that was not etched shows the familiar narrow line luminescence 684 nm (blue).

Under strong etch conditions, the etch rate was 400 nm/min where all other conditions were the same as during the etching of the first sample. After etching the sample for 10 min (4 µm deep) the sample looks mostly grey indicating the GaN layer was removed with very little patches of residual fringes. The third sample was strongly etched under the same conditions as the second sample for 15 min resulting in etch depth of around 6 µm deep where the sample now appear entirely grey indicating the underlying sapphire surface. Subsequent PL analyses show that the emitters were still present -after the 300 nm etch process, but no localised

fluorescence was observed if the 4 µm GaN epilayer was completely removed by the etch process as shown in Figure 4.8. This confirms that the emitters do indeed originate from GaN layer. Also, the ruby Cr-related luminescence at 693 nm strongly pronounced on the 6 µm etched sample.

4.4 Room temperature second-order autocorrelation measurements

Photon emission statistics of all emitters in the histograms were analysed using the HBT interferometer described in section 4.2 under excitation laser power of 50 µW (see Chapter 2 for details on HBT setup). Bright spots resolved with spectra in all the samples showed antibunching photon statistics, where the second-order autocorrelation measurement $(g^2(\tau))$ at zero delay time $(\tau = 0)$ shows that $g^2(0) < 1$ (see Chapter 2 for details). In particular, single photon emitting bright spots E1-E5 in Sample A (see Figure 4.4(a) and 4.5(a)) are identified with characteristics $g^2(0)$ <0.5 as shown Figure 4.9**.** Spots E6-E8 in sample A also exhibit antibunching but the $g^2(0)$ values exceed 0.5 (Figure 4.9). The second-order correlation measurement are fitted with the equation:

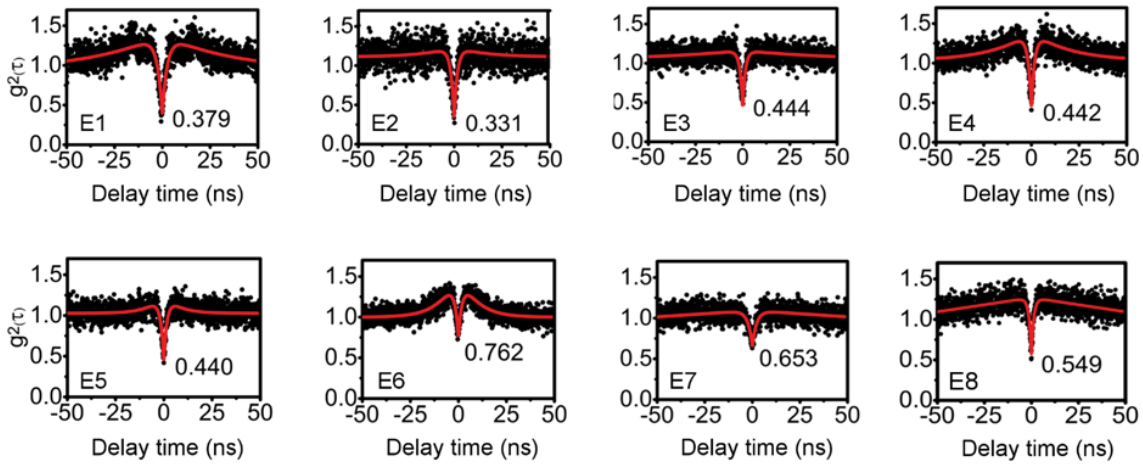

Figure 4.9: $g^2(\tau)$ characteristics of 8 emitters in Sample A. Emitters E1-E5 are single photon emitters with $g^2(0) < 0.5$, whereas E6-E8 show antibunching with $g^2(0) > 0.5$. All autocorrelation measurements were taken with a 50 µW, 532 nm laser and are not background corrected.

$$g^2(\tau) = 1 - (1+a)e^{|\tau|/|\tau_1|} + ae^{|\tau|/|\tau_2|} \quad (4.1)$$

where a, τ_1 and τ_2 are the scaling factor for bunching, excited state lifetime and metastable state lifetime, respectively. This expression is the same as equation (2.45) only re-written in terms of decay times.

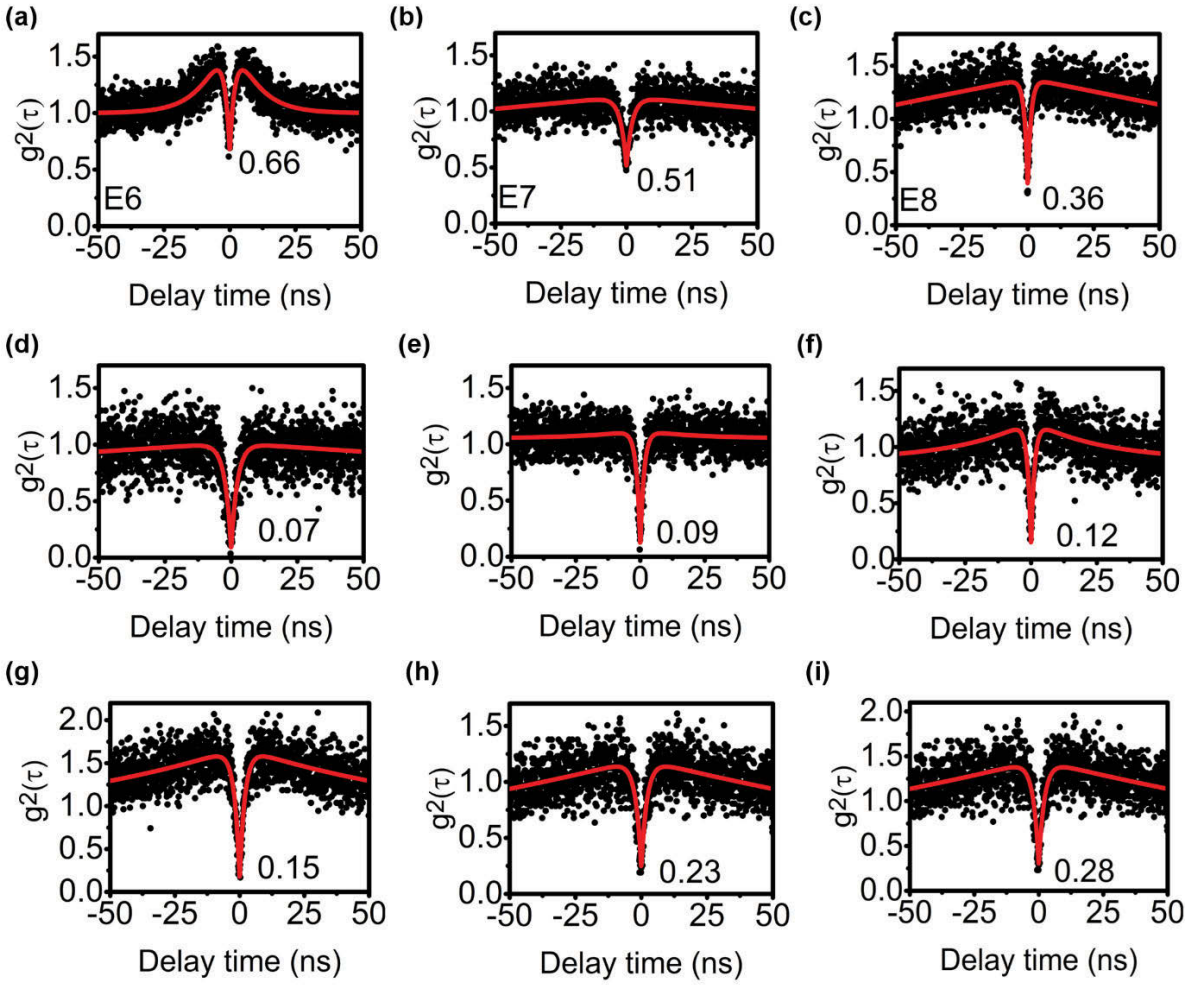

Figure 4.10: Background corrected $g^2(\tau)$ characteristics of emitters E6-E8 in Sample A are shown in (a) – (c). E6 have strong de-shelving state that results in a weak signal to noise ratio and consequently $g^2(0) > 0.5$. Additional background corrected $g^2(\tau)$ characteristics from six more single photon emitters in Sample A are provided through (d) - (i). All second-order correlation measurements are taken at excitation laser power of 50 µW.

After background correction, the $g^2(\tau)$- characteristics from E6-E8 improved as indicated by the reduced values of $g^2(0)$ in Figure 4.10. Additional background corrected $g^2(\tau)$-characteristics of SPEs from Sample A are included in Figure 4.10. Unlike defect related emitters in Diamond[186, 198, 199] where ensemble of emitters showed strong spectra but not antibunching, the bright spots resolved in the GaN films always show antibunching i.e., show $g^2(0) < 1$. This indicates that the system responsible for the emission single photons in GaN is strongly localized emitting only few photons.

Similarly, RT spectra and corresponding autocorrelation measurements from typical emitters in Samples B-E are shown in Figure 4.5 (d). Additional second-order correlation from multiple SPEs in each sample are provided in Figures 4.11-4.14. The pervasiveness of the SPEs in different GaN samples demonstrates that our findings are not limited to a rare defect found in select few ultrapure samples. While the abundance of SPEs in the different GaN samples without prerequisites for material preparation is ideal for proof-of-concept studies, controlled positioning of the centres is required for implantation of the centres for different applications. This, however, requires identification of the origin of SPEs where the structural and electronic properties will then be determined.

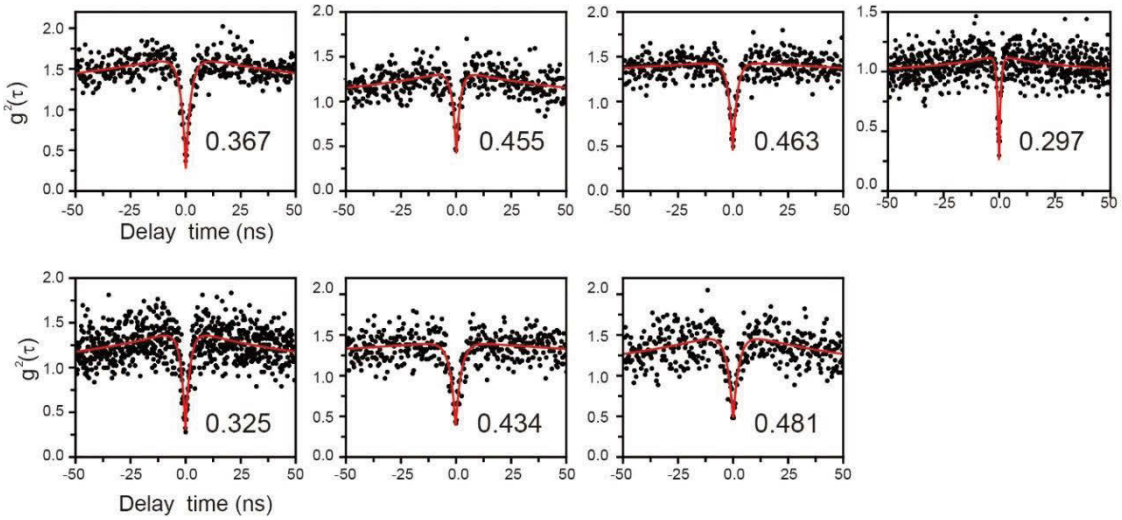

Figure 4.11: $g^2(\tau)$ characteristics of 7 emitters in Sample B. All 7 emitters are single photon emitters with $g^2(0) < 0.5$. Each antibunching characteristic correspond to the 7 circled bright spots in the confocal map shown in Fig. 1d (i).

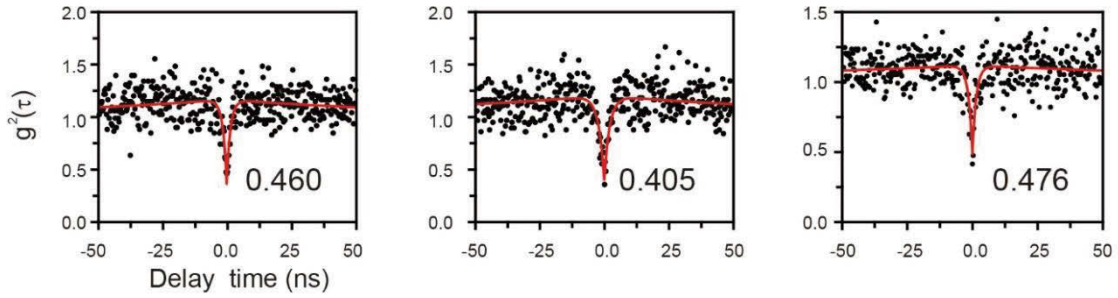

Figure 4.12: $g^2(\tau)$ characteristics of 3 emitters in Sample C. All 3 emitters are single photon emitters with $g^2(0) < 0.5$. They correspond to the 3 circled bright spots in Figure 4.1d (ii).

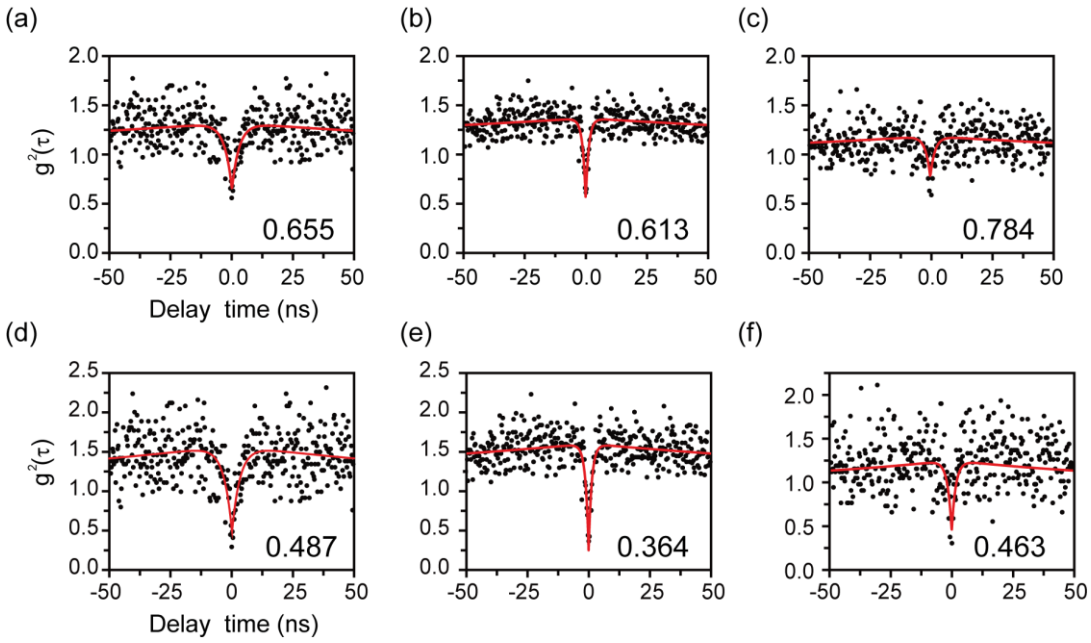

Figure 4.13: $g^2(\tau)$ characteristics of 3 emitters in Sample D without background correction (a-c) and after background correction (d-f).

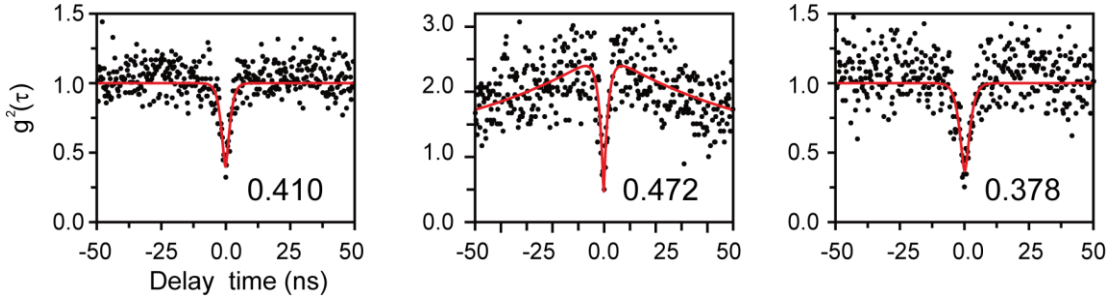

Figure 4.14: $g^2(\tau)$ characteristic of 3 emitters in Sample E. All 3 are single photon emitters with $g^2(0) < 0.5$.

4.5 Low-temperature Spectroscopy and second-order correlation measurements of SPEs in GaN

We now proceed to characterise the SPEs at cryogenic temperatures to learn more about their optical transitions and to gain insight into the microscopic origin of the emissions. We start by surveying single emitters at cryogenic temperatures in Sample A. In this subchapter, without loss of generality, luminescence wavelengths are converted to corresponding energy values for ease of visualising small shifts in ZPLs.

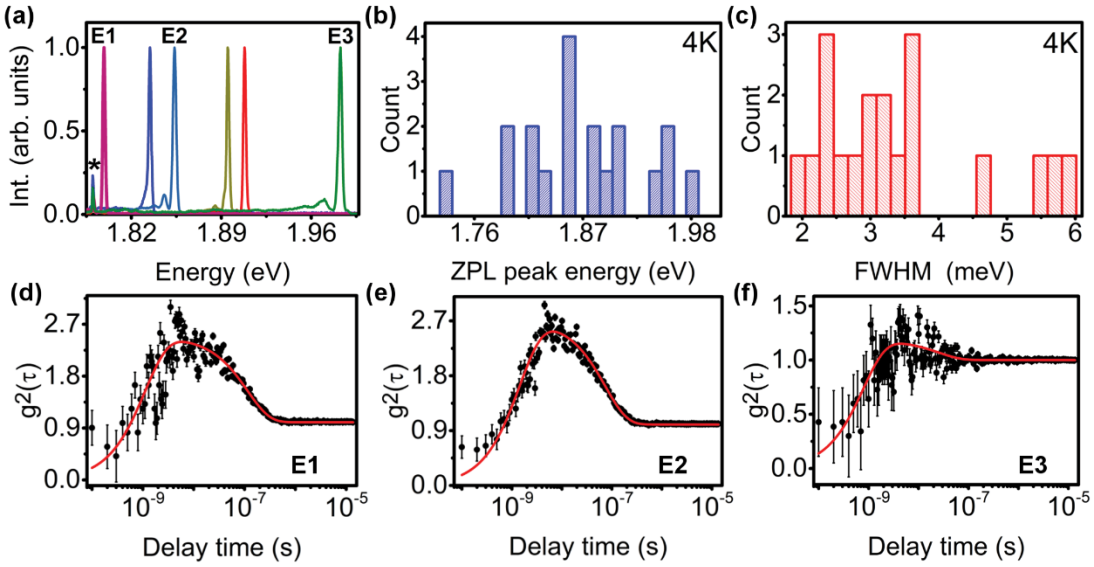

Figure 4.15: Low-temperature (4 K) spectroscopy and photon emission statistics of quantum emitters in GaN. a) Representative spectra from 6 emitters with ZPL peak energies of 1.796 eV (E1), 1.834, 1.852 eV (E2), 1.895 eV, 1.908 eV and 1.981 eV (E3). b) ZPL peak energy distribution of 19 emitters with a mean value of (1.869±0.064) eV. c) Histogram showing the FWHM distribution of the emitters in (b) with mean linewidth value of (3.39±1.12) meV. All measurements were taken with an excitation laser power of 100 µW. d-f) Second-order autocorrelation measurements for the three emitters labelled E1-E3 in (a) under an excitation power of 50 µW. The curves are fitted with three-level, second-order autocorrelation functions and show that the emitters E1-E3 are single photon emitters with $g^2(\tau=0)$ values of 0.30, 0.27 and 0.18, respectively.

Figure 4.15(a) shows spectra from 6 emitters selected at random using an excitation laser power of 100 µW, at 4 K. Distinct ZPLs are obtained for each of the emitters. The distribution of ZPL peak energy from 19 more emitters is shown in Figure 4.15(b). The ZPL position

ranges from 1.736 eV to 1.983 eV with a mean of ~ (1.869±0.064) eV. The histogram is similar to the one discussed above for spectroscopy of SPEs at RT (which has a mean of ~1.824 eV), illustrating that the mechanism responsible for the observed ZPL energy range is unaffected by temperature changes. A histogram of the FWHM of the 19 emitters at 4K is also shown in Figure 4.15(c) with the mean linewidth of ~(3.39±1.12) meV, which is approximately 7 times smaller than the calculated mean linewidth at RT. The additional narrow peak from Cr impurity in the sapphire substrate is shown at 1.789 eV. We did not observe spectrometer-limited linewidths, and the broadening is most likely caused by coupling to phonons or ultrafast spectral diffusion (see Chapter 5 for more details).

To further characterize the SPEs, we focus on emitters E1, E2, and E3 shown in Figure 4.15(a), with ZPLs (FWHM) of 1.796 eV (1.6 meV), 1.852 eV (2.4 meV) and 1.981 eV (2.3 meV), respectively. Figure 4.15 (d)-(e) shows $g^2(\tau)$- characteristics for long correlation times of up to 15 μs. The single-photon nature of the light emitted from E1-E3 is revealed by $g^2(\tau=0)$ values of 0.30, 0.27 and 0.18, respectively. The deviations from zero are due to background fluorescence and detector jitter. The data can be fitted optimally with equation (4.1)/ (2.45) which is the three-level model with a long-lived metastable state (see Chapter 2). The scaling factor for bunching (a), excited state lifetime (τ_1) and metastable state lifetime (τ_2) are calculated as fitting parameters of $g^2(\tau)$- curves. These values are summarized in Table 4.3.

	E1	E2	E3
a	1.44	1.71	0.12
τ_1 (ns)	1.29	1.55	0.76
τ_2 (ns)	118	73.2	35.3

Table 4.3: Parametric values a, τ_1 and τ_2 obtained by fitting the second-order autocorrelation functions of E1, E2 and E3, assuming the three-level system dynamics.

Although the bunching behaviour is different for each one of the emitters, it is clear that a shelving state observed at RT in section 4.10 persists at cryogenic temperatures. More extended second-order photon correlation measurements of up to 0.1 s from E1-E3 (shown in

Figure 4.16) confirm the absence of additional, long-lived metastable states, with the $g^2(\tau)$ profiles remaining constant along the normal up to 0.1 seconds.

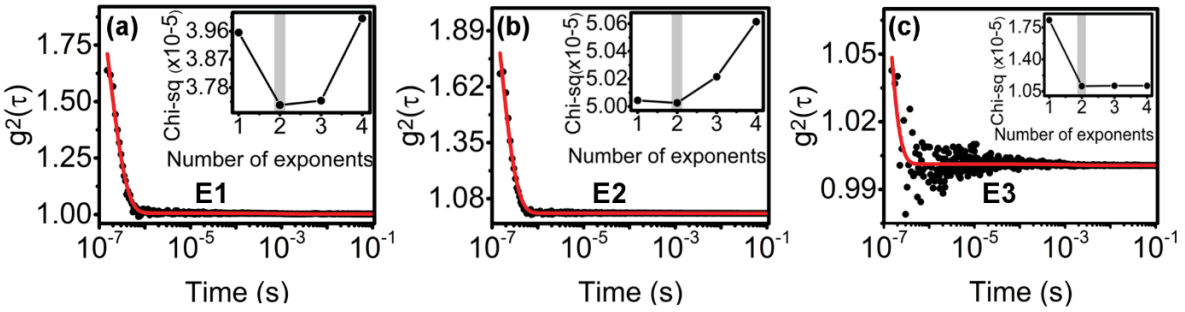

Figure 4.16: (a-c) Long time fluorescence correlation measurements for E1, E2 and E3 under an excitation power of 50 µW. The fit (red) for all the three $g^2(\tau)$ characteristics is a double exponential decay function giving the least chi-square value indicated by the respective inset figures. $g^2(\tau)$ starts with the bunching height corresponding to an ns-shelving state in each of the emitters, but drops to normal and remains constant for the measurement times scale range of up to 0.1 seconds. This is consistent with previous observation of stable SPEs in GaN.

Figures 4.17-4.19 show spectral properties of E1-E3 as a function of the change in the temperature range of 4K to RT. Strikingly, the ZPL energy of emitters in GaN exhibit an unusual S-shape (inverted S-shape) dependence on temperature which is unlike most known solid-state emitters. To investigate this unusual behaviour, in detail, the temperature resolved spectra of E1-E3 were first fitted with a Gaussian curve of the form:

$$I(E) \approx \frac{A}{w\sqrt{\pi/2}} e^{-2*\left(\frac{E-E_{ZPL}}{w}\right)^2} \tag{4.2}$$

where w is the width and A is a fitting parameter. The FWHM is calculated as $1.178*w$. The fitting yields the minimum χ^2 values where peak ZPL energy, as well as FWHM of the three emitters, are extracted at different temperatures.

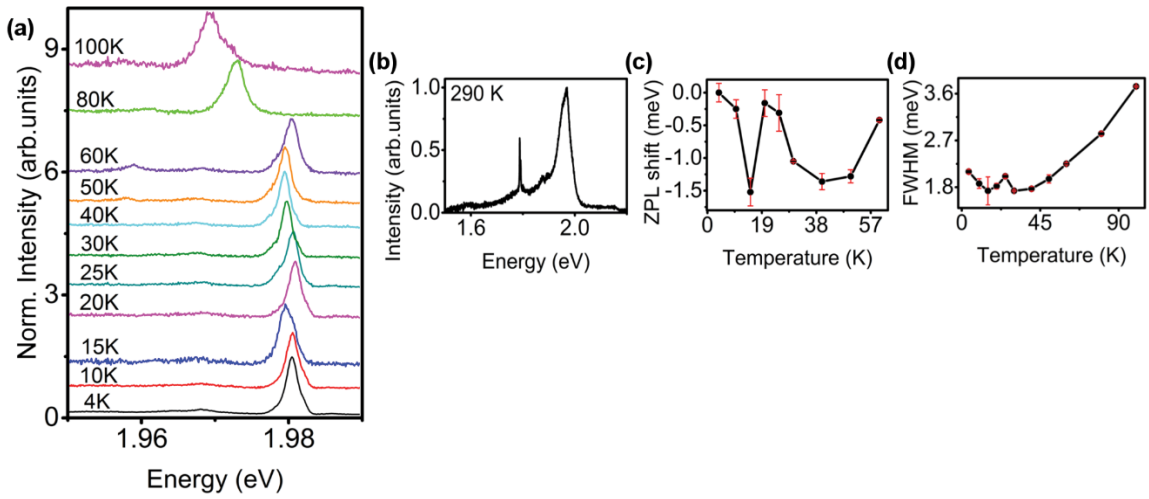

Figure 4.17: (a) Temperature-dependent spectroscopy of E1 showing both ZPL peak shift and linewidth broadening. There is a visible phonon mode 3.1meV away from ZPL up to temperature of 80K (b) Spectrum at 290 K of E1 plotted in a separate panel for better visualisation. (c) ZPL peak shift at low temperature showing the usual S-shaped temperature dependence for E1. (d) Corresponding linewidth broadening as a function temperature shown only up to 100 K for E1.

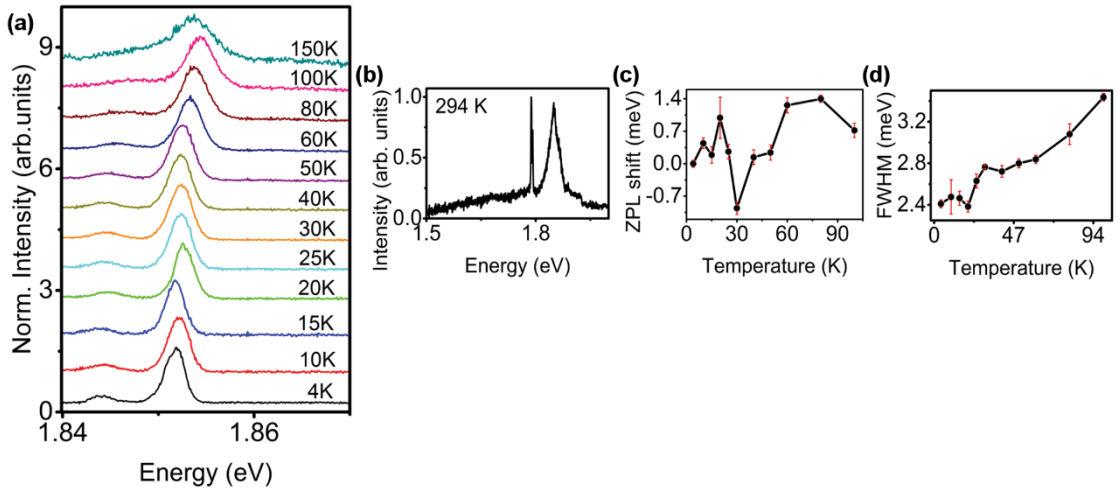

Figure 4.18: (a) Temperature-dependent spectroscopy of E2 showing both ZPL peak shift and linewidth broadening. A phonon mode is also shown here around 8 meV away from the ZPL up to 60K (b) Spectrum at 290 K of E2 plotted in a separate panel for better visualisation. (c) ZPL peak shift at low temperature showing the usual S-shaped temperature dependence for E2. (d) Corresponding linewidth broadening as a function temperature shown only up to 100 K for E2.

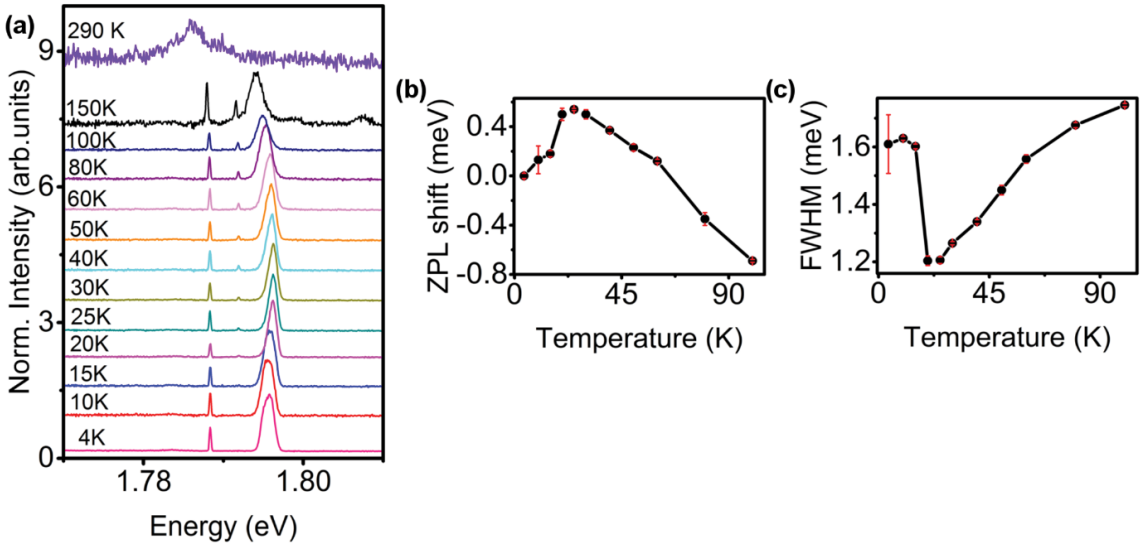

Figure 4.19: (a) Temperature-dependent spectroscopy of E3 showing both ZPL peak shift and linewidth broadening. A phonon mode is activated beginning 20K around 3meV away from the ZPL (b) ZPL peak shift at low temperature showing the usual S-shaped like temperature dependence for E3. (c) Corresponding linewidth broadening as a function temperature shown only up to 100 K for E3.

The extracted peak values from the fit are used to plot the temperature resolved ZPL shift ($\Delta E_{ZPL}(T)$) for E1-E3 as shown in Figure 4.20 (a-c). The shift is calculated simply by $\Delta E_{ZPL}(T) = E_{ZPL}(T) - E_{ZPL}(4K)$, where $E_{ZPL}(T)$ and $E_{ZPL}(4)$ are peak ZPL energy values at given temperature and 4K, respectively. Now, we want to compare the unique ZPL shift observed in GaN emitters to other customary mechanisms in solid-state emitters such as the NV defect in diamond.

- **Lattice contraction**: This is the most common cause of instability in peak energy in atomic defects such as SiV and NV centres in diamond, where strain field shifts the ZPL peak energy. $\Delta E_{ZPL}(T)$ shift due to lattice contraction shows temperature dependence proportional to T^4. However, the temperature dependence of the ZPL shifts of E1-E3 are poorly fitted with T^4 (blue line) showing divergence both at low and high temperature. This indicates that lattice contraction could not be the dominant factor causing ZPL shifts in GaN emitters.

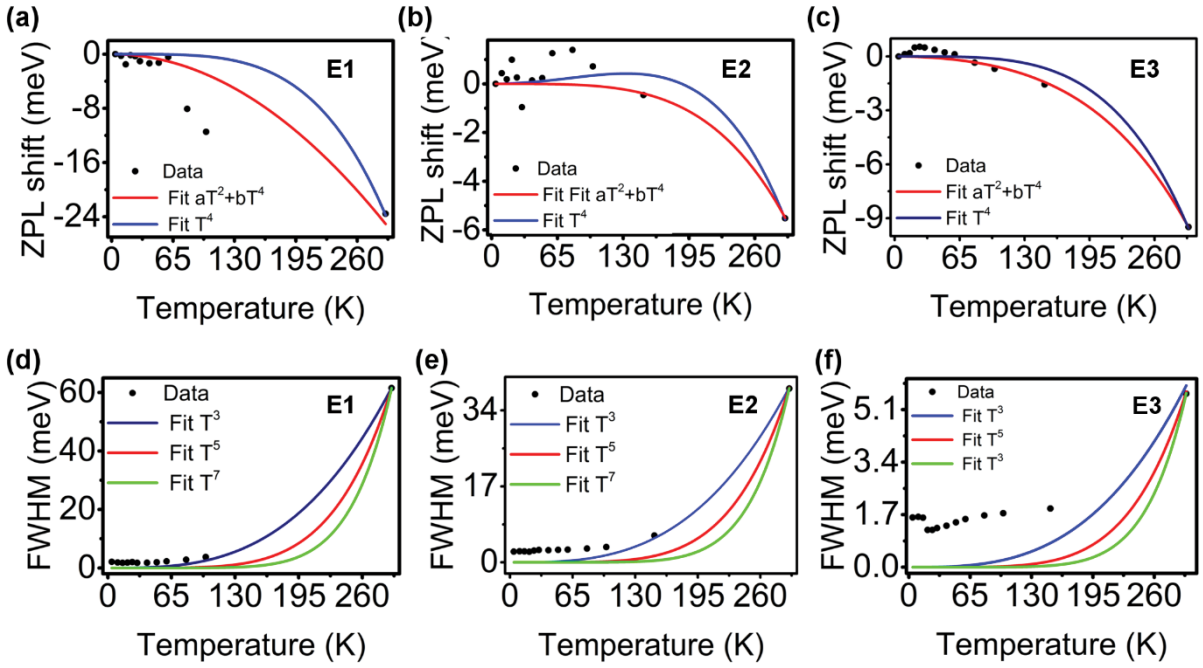

Figure 4.20: ZPL shift and linewidth broadening in GaN emitters (a-c) ZPL peak shift of emitters E1-E3 as a function of temperature where the shift showed S-shaped temperature dependence (Figure 4.17-4.19). The data is fitted with polynomial functions of the form T^4 (blue) and $aT^2 + bT^4$ (red) where the later yield better fits at high temperature. (e-f) Shows the corresponding linewidth broadening of E1-E3 with increasing temperature. These trends are fitted with functions of the form T^3 (blue), T^5 (red) and T^7 (green) with T^3 yields reasonable fits for E1&E2.

- **Phonon coupling:** The other probable factor shifting ZPLs is phonon coupling of the electronic transition in addition to the lattice contraction. Such ZPL shifts are shown to follow a polynomial temperature dependence of the form $aT^2 + bT^4$. This model produces better fits (red line) for ZPL shifts of E2&E3 at higher temperature values (> 100 K) as shown in Figures 4.20 (b&c). This indicates that while phonon coupling plays a role in the demonstrated blue shift of the mean ZPL peaks of GaN SPEs with decreasing temperature, the primary cause of the S-shape (inverse S-shape) dependence at lower temperatures is still unclear.

The S-shaped shift in the ZPL wavelength peak is also observed regardless of GaN film structure (Sample A & B) as shown Figure 4.21.

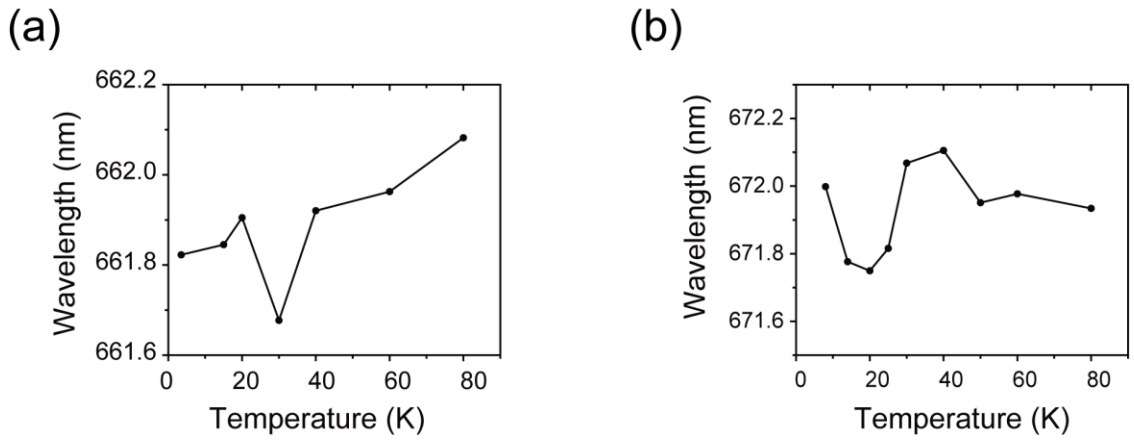

Figure 4.21: (a) Temperature dependence of the ZPL position of other emitters in Sample A and sample (B). ZPL wavelength shows 'S-shaped' dependence.

Turning our discussion to the linewidths of E1-E3, it is already stated none of the SPEs are spectrally limited at temperature value of 4K. This may already indicate the existence of a broadening mechanism other than the homogenous, phonon scattering (see Chapter 3). This is further consolidated by the temperature resolved FWHM results of E1-E3 shown in Figure 4.20 (e-f) where the data deviates from known phonon scattering models (shown by the solid coloured lines). The data were fitted with monotonic temperature dependence functions of the form T^3 (red line), T^5 (blue line) and T^7 (green line). For E1, T^3 dependence produced a fit with least χ^2 value showing more divergence at low-temperature values. This indicates that the dominating linewidth broadening mechanism is not homogenous. Furthermore, E1 showed the most substantial broadening of the three emitters with increasing temperature where phonon modes disappear into the broadened ZPL as shown in Figure 4.20 (a&b). E2 showed similar broadening as E1, depicted in Figure 4.20 (a,b&d) where T^3 fitting yield the least χ^2 value. On the other hand, E3 showed the least linewidth broadening of the emitters where all of the monotonic fits showed the largest deviation from the temperature dependence data. The temperature dependent linewidth measurements of E1-E3 strongly indicate that spectra in GaN SPEs are mainly determined by a mechanism that causes inhomogeneous broadening.

The emitters in GaN exhibit an unusual 'S-shaped' dependence, suggesting that the emitters are not simple atomic defect centres, but have an alternate origin. Furthermore, the broad spectral spread of ZPL wavelengths across individual wafers and between the same wafers suggests that the emitters are associated with growth defects rather than a particular impurity (such as the NV defect in diamond).

4.6 The role of stacking faults in the single photon emission from GaN films

Point defect agglomeration during growth of wurtzite GaN can lead to the formation of stacking faults (SF) with varying widths spanning a few angstrom to 10 nm (see Chapter 3 for details)[200, 201]. Figure 4.23 (a) is a schematic illustration of a 5-bilayer cubic inclusion in a 12-bilayer slab of wurtzite GaN, forming stacking faults. Consequently, localised cubic inclusions introduce a quantum well for conduction band electron due to the narrower band gap of cubic GaN relative to wurtzite GaN. The cubic inclusion is surrounded by the spontaneously polarised wurtzite matrix, resulting in electronic states with a localised electric field[145, 202]. These electronic states with a strong electric field act as effective triangular quantum well structures, altering the local optical properties of GaN [145, 203, 204]. The presence of SFs in the GaN films investigated here is observed using CL spectra.

Low-temperature depth-resolved CL spectra is measured at 80 K from two spots on sample A. The CL spectra from spot 1 & 2 are shown in Figure 4.22 (a) and (b), respectively. The insets show penetration depth as a function of electron beam energy calculated by Monte Carlo simulation. As depicted, the band edge luminescence from Sample A shows peak energy of 3.3 eV with shoulder peak of around 3.2 eV indicating a shift from the literature value for wurtzite GaN by 0.1 eV. While the shifted spectra with the shoulder are indicative of the presence of stacking faults in the GaN films[52, 149], the peak energy is lower than reported before[52]. This may be due to the luminescent defect localisation in the valence band which further red shifted the band-edge emission peak-energy.

Furthermore, CL intensity from spot 1 increased with penetration depth as shown in Figure 4.22 (a). This is due to the large interaction volume at higher beam energies. However, the spectral intensity from Spot 2 at a penetration depth of 465 nm (15 keV) is lower than it is at 241 nm (10 keV) as shown in Figure 4.22(b) with the shoulder peak missing at a depth of around 465 nm. This may be because at depths of around 241 nm (10 keV) luminescent SF with a peak energy of 3.2 eV is present. On the other hand, the luminescent SF is absent at depth values of around 465 nm (15 keV), hence lower CL intensity regardless of the large interaction volume.

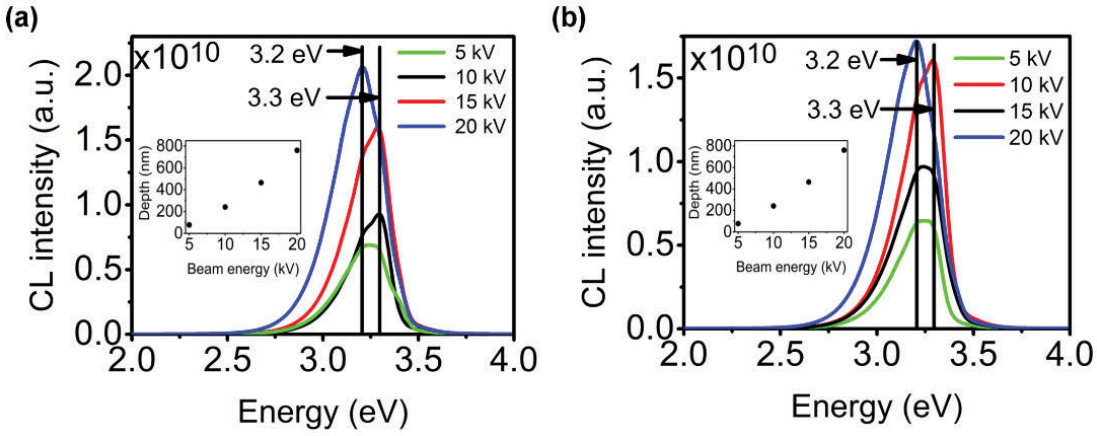

Figure 4.22: Depth-resolved cathodoluminescence (CL) from two spots on sample A at 80 K: (a) CL spectra using different beam energies to obtained depth-resolved CL from spot 1. In depths between around 78 nm to 465 nm, CL peak of 3.3 eV dominates while at 761 nm deeper into the sample CL peak of 3.2 eV dominates. Same electron beam power of around 60.5 µW is used at the different depths. The inset shows depth estimation using Monte Carlo simulations for the different beam energies. (b) A similar measurement as in the case of (a) but on the spot 2. This measurement has also yielded a similar result with 3.3 eV peak dominating till depths of around 465 nm where 3.2 eV dominates at depths around 761 nm.

Also, the presence of SFs and their role in the observed quantum emissions is supported by the observed "S-shaped" temperature dependence of the ZPL wavelength seen in Figures 4.20 &4.21. The ZPL blue-shifts as T is increased from 10 K to 30 K, and red-shifts as T is increased beyond 30 K. This has been reported previously for band-edge excitons in *c*- and *a*-plane grown GaN[205-207], where the blue shift is explained by an exciton transition from a shallower energy level of conduction band quantum wells to holes in the valence band. It

can occur due to carrier reshuffling within the stacking faults by lattice strain or location of extrinsic atoms in the vicinity of a stacking fault[205]. The redshift at temperatures greater than 30 K can arise from thermal activation of additional bilayers, allowing deeper quantum-well-potential-bound exciton transitions[208, 209]. An alternative explanation for the redshift is a delocalisation of holes in the valence band and recombination with stacking-fault-bound electrons [205, 210]. The temperature dependent ZPL shift between Sample A and Sample B is shown in Figure 4.20 & 4.21 may be caused by a different strain field around carriers leading to a reshuffling that leads to shallower (sample A) or deeper (Sample B) radiative transitions.

4.7 A numerical model of the origin of SPE in GaN

Based on the experimental results presented in preceding chapters, we attribute the antibunched photon emissions reported here to the radiative recombination of an exciton bound to a point defect that resides inside or next to a stacking fault. In our model, the hole is tightly localised to the defect site whereas the electron is loosely bound by a Coulomb interaction introduced by the localised hole in the optically allowed lowest-energy excited state of the point defect. This localisation modifies the stacking fault's triangular potential profile acting on the electron as illustrated in Figure 4.23(b). We solve a quasi-one-dimensional Hamiltonian of this potential [92] where we applied fundamental material parameters of wurtzite and cubic GaN such as the band gaps, band alignments, effective masses of the hole and electron, dielectric constants, and steepness of the triangular well caused by spontaneous polarisation. The resulting calculated energy of the exciton is assumed to be the ZPL energy of the emitter.

4.7.1 Modelling parameters

The energy of the excited states is calculated in a quasi-one-dimensional potential line-up determined by the properties of cubic inclusions in wurtzite GaN. Most importantly, the electric field change at the cubic-hexagonal boundary for GaN is $\Delta\varepsilon$=2.9 MV/cm [184].

General material properties of GaN (effective masses of electrons and holes, as well as dielectric constant) are taken from literature. When the point defect is positioned at the side and nearly halfway between the middle plane of the cubic inclusions, the binding energy (E_b) between the electron and hole of the exciton exhibits a maximum of 35 meV[195]. This arrangement of defects in relation to the cubic inclusions results in the most attractive potential for the electron. However, it decreases to considerably lower values than that corresponds to room temperature (ca. T_r=26 meV) if the point defect is outside the cubic part. In the lowest energy excited state, the hole is strongly bound whereas the electron is loosely bound by the Coulomb-potential introduced by the hole. Thermal excitations of this lowest energy excited state may break the bound exciton by promoting the electron to the conduction band. If this effect occurs, then the defect will be charged and will not be optically active anymore. By assuming an instantaneous ionisation process of the conduction band electron, the thermal stability of the bound exciton may be calculated following Boltzmann law of the form $\exp(\frac{E_b}{T_r})$. We calculated this Boltzmann-factor for each defect site that provides a statistical weight, i.e., the relative concentration of the optically active centers that can be detected in the experiments at room temperature. By combining the afore-mentioned trend in the calculated binding energies and the weight of the point defects as a function of their location, the point defects located far from the cubic inclusions can be excluded from the family of optically active centers operating at room temperature.

4.7.2 Modelling results

By fixing the thickness of the cubic inclusion to 5 bilayers and setting the localisation potential of the hole so that the latter yields a ZPL wavelength of 680 nm for the point defect in pure wurtzite GaN. The simulation gives rise to the spectral spreading between 600 nm and 705 nm (see Figure 4.23(c)) if point defects are distributed uniformly between -4 nm to 4 nm with respect to the middle of the cubic inclusion. The calculated binding energy, i.e., the Coulomb-coupling in the corresponding exciton depends on the actual location of the point defects and goes up to 35 meV. The relative signal intensities are weighted according to the

thermal stability of the excitons at room temperature for each defect location that leads to the final ZPL distribution of the emitters in Figure 4.23(c). The modelling results are in good agreement with the experimental data, both in terms of ZPL energies and ZPL distribution. More information about the modelling is given in the supporting information. While strong experimental and numerical evidence indicate that radiative recombination of an exciton bound to a point defect in GaN is responsible for the single emitters, further investigations are required to confirm this hypothesis. It is also important to note that the observed emitters are different from GaN or InGaN quantum dots, which have been isolated and shown to exhibit quantum emissions [54, 55]. These sources operate at room temperatures and originate from crystal size confinement of the QDs.

4.8 Conclusion

To conclude, we showed that GaN is a promising host of bright SPEs in the visible and near-infrared spectral ranges. In particular, we demonstrated that these emitters are prevalent in broad range GaN films grown on sapphire and SiC substrates. Low-temperature studies and subsequent Hamiltonian parametrised calculations suggest that the quantum emitters are defects localised near an extended stacking fault formed due to a cubic inclusion. The model suggests that generation and, potentially, control of the emitter wavelengths may be possible by the intentional introduction of cubic layers in the GaN growth process. A dedicated growth technique can also be used to precisely control the lateral position of each emitter.

This chapter featured the first report of single photon emitting defect in GaN as well as provided evidence of defect system that might be responsible for the emission. To evaluate the potential of the newly found emitters for different applications, detailed study on the photophysics is required. The following chapter provides a detailed study of the photophysics of SPEs in GaN both at cryogenic and room temperatures.

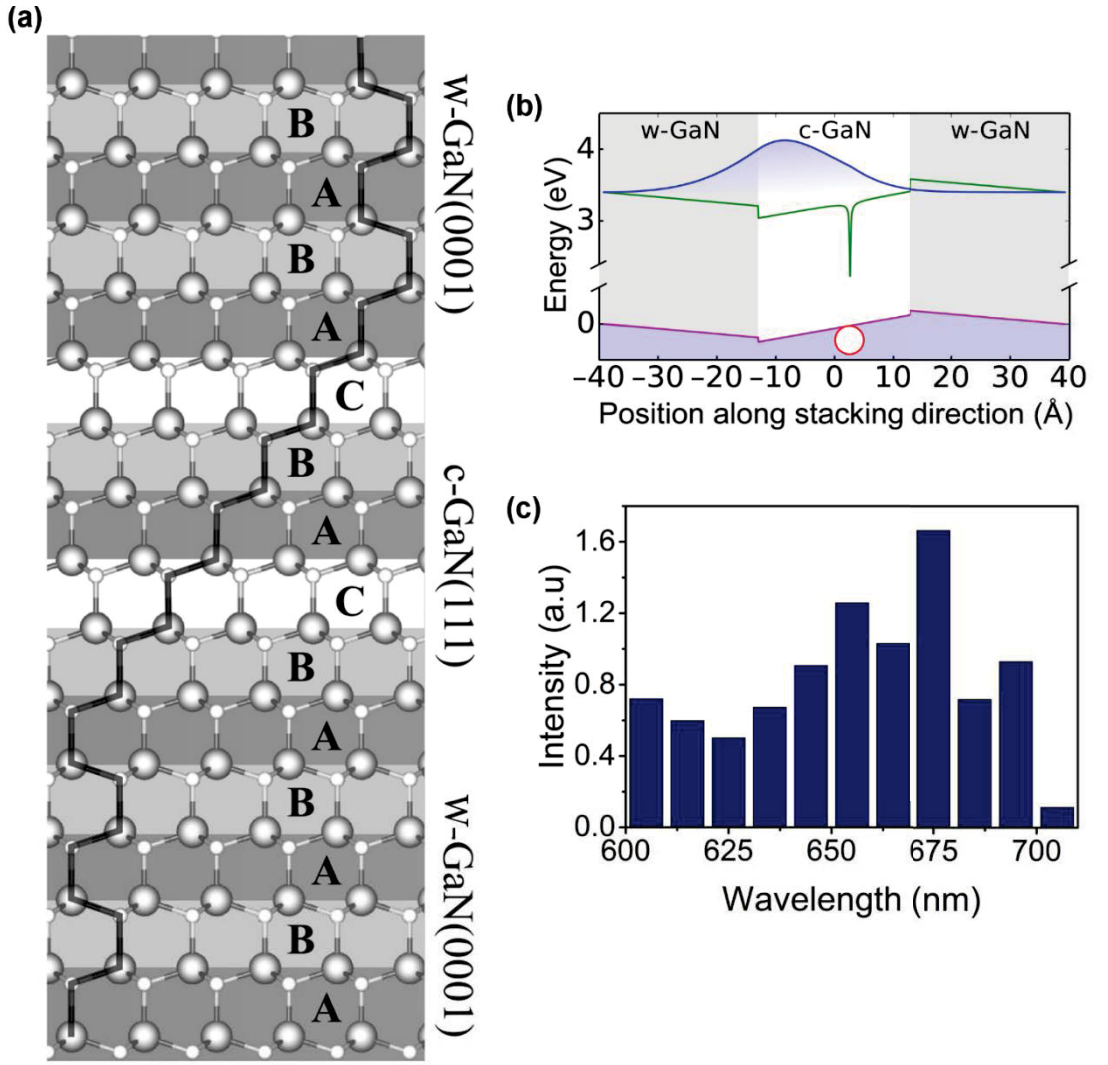

Figure 4.23: Numerical wavelength calculations: a) Schematic illustration of stacking faults generated by a cubic inclusion in wurtzite GaN. b) Location of the exciton in the cubic inclusion which spans 5 bilayers and is shown in a total slab of 12-bilayers of GaN. The potentials applied to the electron, and the hole is the conduction band minimum (green curve) and valence band maximum (purple curve), respectively. The hole (red circle on the valence band maximum) is pinned by a point defect, while the electron is delocalized across the inclusion according to the density profile shown in blue. c) Wavelength distribution, spanning 600 to 705 nm, based on model Hamiltonian GaN parameterised calculations for a defect arrangement along the cubic inclusion shown in Figure 4.23(b).

5 Photophysics of single photon emitters in GaN

In this chapter, we present photophysical analysis from several SPEs in GaN at cryogenic and room temperatures. First, RT fluorescence trace of emitters from Samples A-E is presented to determine stability under different laser power. This is followed by saturation behaviour study of the SPEs in different GaN samples to compare count rate dependence on excitation power. Also, RT maximum average brightness of ~(427±215) kCounts/s is measured from the saturation measurement of several emitters in Sample A. Based on second-order correlation measurements at different fractions of the saturation power, the transition kinetics of SPEs in GaN is determined. The transition kinetics is studied both by considering a shelving state that depends linearly as well as non-linearly on excitation power. The rate analysis of the transition is used to determine radiative and nonradiative lifetimes of 6 emitters in Sample A. Polarization measurements on 14 emitters are used to determine visibility as well as relative orientations of the emission and absorption polarisation. The preferred orientation of absorption dipole of the SPEs in GaN crystal is also estimated.

The low-temperature study focuses on the three emitters (E1-E3) in sample A whose spectroscopy is already presented in subchapter 4.5. Time-resolved PL measurements from E1-E3 reveal that the FWHM at 4 K determined before is three orders of magnitude broader than the transform-limited widths. The SPEs are further investigated using time-resolved spectroscopy at 4K to determine the role of spectral diffusion on the inhomogeneous broadening observed before. The results underpin some of the fundamental properties of SPE in GaN both at cryogenic and RT and define the benchmark for future work in GaN-based single photon emission.

5.1 RT fluorescence time-trace and saturation behaviours of SPEs in GaN

5.1.1 Florescence intensity trajectory of SPEs in GaN

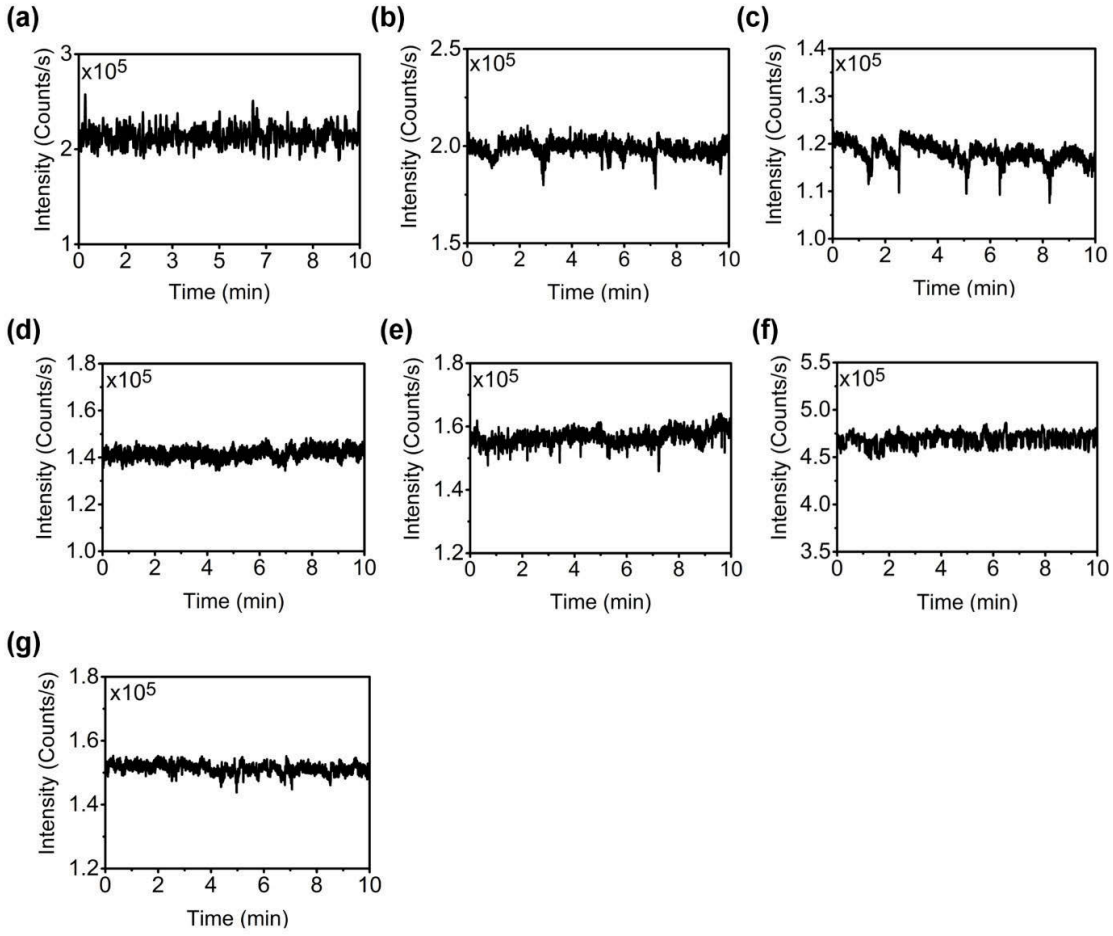

Figure 5.1: Long-time fluorescence stability of emitters from sample A (a,b,c), B(d),C(e), D(f) and E(g). The emission intensity was measured using excitation laser power of 3 mW (much higher than saturation powers) and a time bin of 50 ms.

Photostability of the SPEs is studied by recording PL intensity versus time under cw laser excitation. This is referred to as fluorescence time trace of intensity or fluorescence intensity trajectory. Here, the measurement was carried out under excitation power of 3 mW over 10 minutes of continuous acquisition using detector time bin of 50 ms. Figure 5.1 (a)-(g) shows fluorescence time trace obtained from 3 SPEs in sample A (Figure (a)-(c)) and one from each of the 4 other samples (Samples B-E) discussed in Chapter 4. Most of the emitters studied in

this work were stable with few showing blinking (see Chapter 6 for details). However, no bleaching was observed under our experimental conditions.

5.1.2 Saturation behaviour of SPEs in GaN

RT power dependent brightness of SPEs is investigated in Samples A-E via saturation measurements where background subtracted, average count rates are determined as a function of excitation power. First, the brightness properties of 3 SPEs from sample A with corresponding emission line and $g^2(\tau)$ - characteristics are shown in Figure 5.2. The power-dependent emission intensities are fitted using the relationship:

$$I = I_{\infty} \frac{P}{P + P_{sat}} \tag{5.1}$$

where I_{∞} is the maximum intensity, and P_{sat} is the saturation power yielding 503, 703, 474 kCounts/s at 613 μW, 1.3 mW, 1.6 mW, respectively. These intensity values are comparable with other single emitters in bulk materials[176, 194]. Furthermore, it shows brightness as well as saturation power variation between SPEs in the sample. To investigate the variation in the saturation behaviours of SPEs in Samples B-E, four more measurements are conducted as shown in Figure 5.3. After fitting the background corrected, saturation behaviour using the same equation, maximum brightness of 160, 200, 300 and 150 kCounts/s at saturation powers of 660, 1200, 410 and 910 are measured for the SPEs in Samples B-E, respectively. The result demonstrates that the saturation behaviour between SPEs in GaN is comparable indicating that the absorption and emission mechanism in these family of emitters is similar.

While the background corrected, brightness values of SPEs in the different samples presented so far give an idea of the maximum intensity, estimation of lower bound in intensity via g^2 – corrected data is important[211]. This is because by considering the ideal case of $g^{(2)}(0) = 0$, the effect of uncorrelated background on the total count rate can be corrected. In this manner, a relative intensity can be estimated for the single photon emitters at different excitation

powers. The two approaches of saturation behaviour determination are compared for an emitter in Sample A with ZPL wavelength of 657 nm.

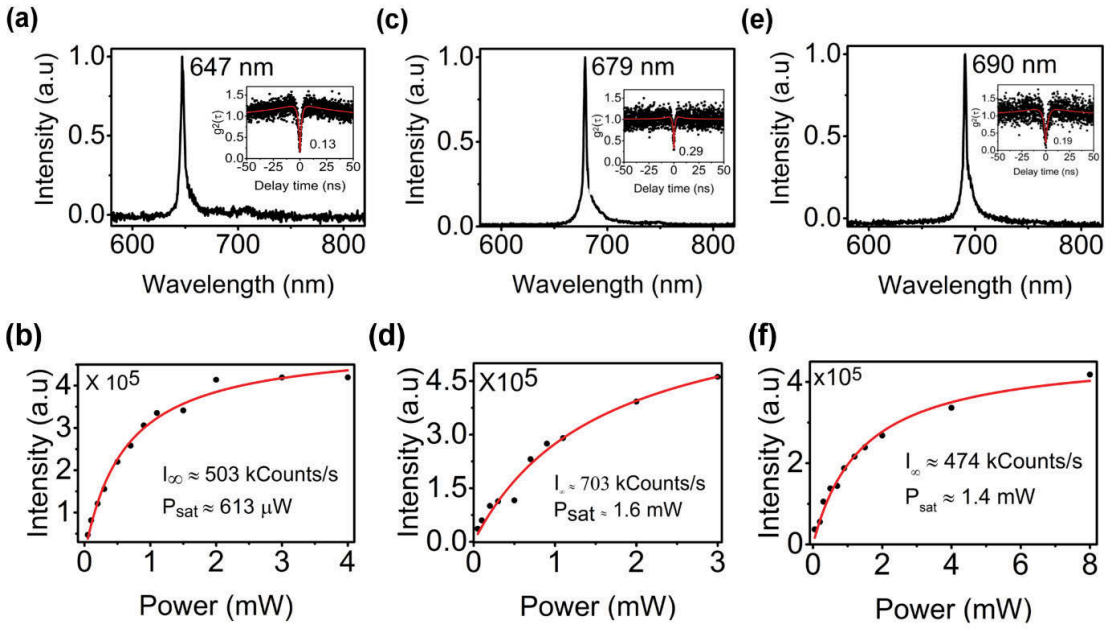

Figure 5.2: Spectral characteristics of 3 emitters in Sample A. All 3 are single photon emitters with $g^2(0) < 0.5$ as shown in the insets of each spectra. The power dependent brightness behavior of emitter with spectra shown in (a) is given in (b). Similarly, brightness behavior of emitter whose spectra is shown in (c) is provided in (d) and of (e) is shown in (f). Maximum intensity and saturation power of (b), (d) and (f) is given in the inset of their respective figures.

Figure 5.4 shows the saturation behaviour of the emitter obtained using two different approaches[211]. In the first approach, the saturation data are corrected for background and fitted (red points and line) with equation (5.1), which yield a maximum intensity I_∞ of 501 kcounts/s at a saturation power of 930 µW.

Alternatively, the single photon emission rate can be estimated using g^2 – corrected data as described above[211]. At an excitation power of 50 µW, the emitter yields antibunching dip at zero-delay time ($g^2_{exp}(\tau = 0)$) of 0.331. The normalized $g^2_{exp}(\tau)$ can be corrected for background [211]:

$$g^2_{exp}(\tau) = g^2_i(\tau)\rho^2 + 1 - \rho^2 \qquad (5.2)$$

where $g_i^2(\tau)$ is the pure antibunching function and ρ is the ratio of single photon emission rate (R) to total count rate (T) (cf. equation (2.46)).

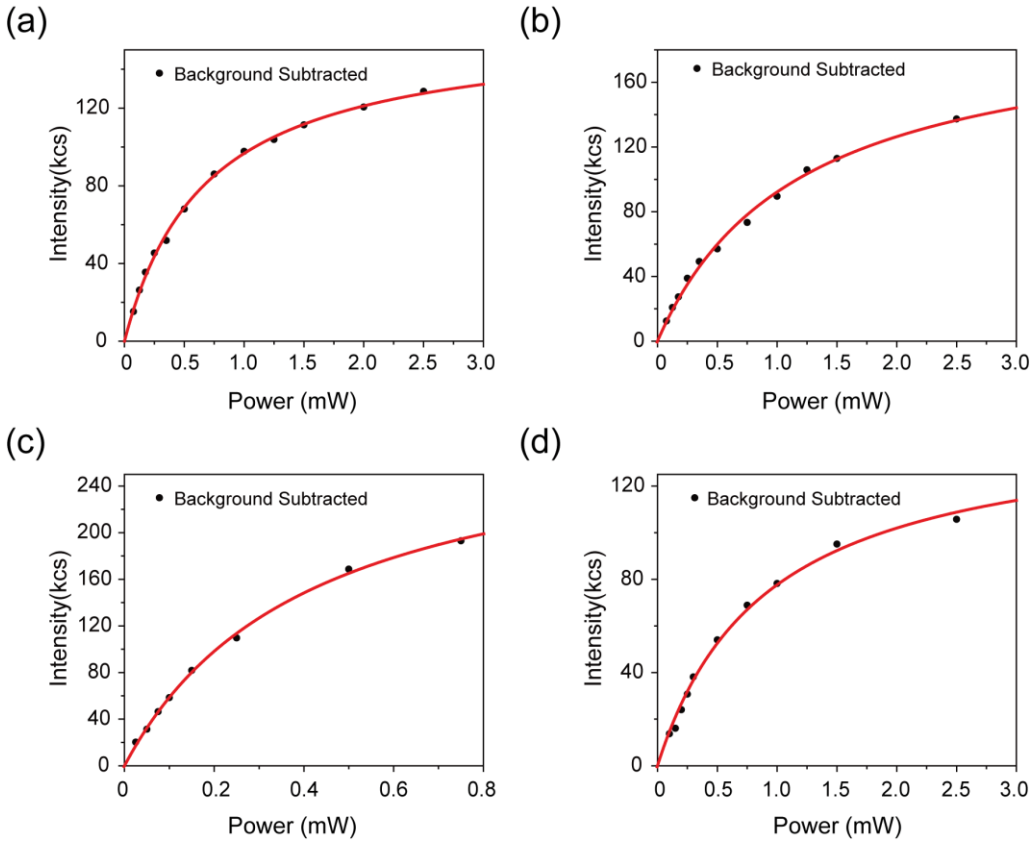

Figure 5.3: Saturation characteristics of the emitter from Sample B-E. Fluorescence intensity of emitters from sample B (a), C (b), D(c) and E (d) as a function of excitation power. The background-subtracted saturation curve (red) yields a maximum intensity of 160, 200, 300 and 150 kCounts/s at a saturation power of 660, 1200, 410 and 910 µW, respectively.

Ideally, antibunching of an SPE satisfies the condition $g_i^2(\tau = 0) = 0$, and the expression $R = T(1 - g_{exp}^2(\tau = 0))^{1/2}$ follows from Equation (5.2). Substituting experimental values for T and $g_{exp}^2(\tau = 0)$ at different excitation powers, the single photon emission rate (R) is determined for the emitter.

In Figure 5.4, the blue dots show single photon emission rate of the emitter versus excitation power. Fitting this curve with the power model defined by Equation (5.1), a single photon

emission rate of 203 kcounts/s is obtained at saturation power of 313 µW (solid blue lines). Both methods independently confirm the high brightness of these emitters.

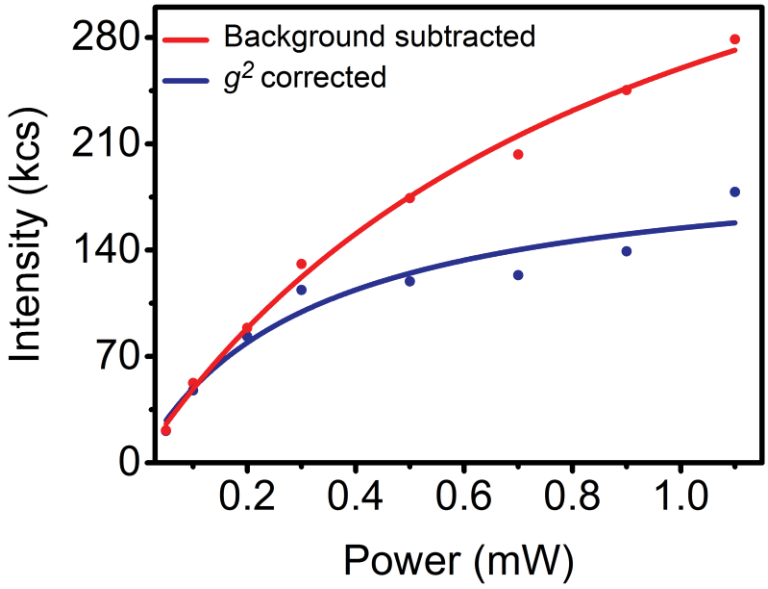

Figure 5.4: Fluorescence intensity of emitter E2 as a function of excitation power. The background-corrected saturation curve (red) yields a maximum intensity of 501 kCounts/s at a saturation power of 930 µW. The g^2-corrected saturation curve (blue) yields a lower bound on the maximum single photon emission rate of 203 kCounts/s at a saturation power of 313 µW.

To understand the variation in P_{sat} and I_∞ values among different SPEs between the same sample and among different samples in detail, the saturation behavior is studied for 9 more emitters in GaN. We measured the brightness of 9 SPEs and extracted the maximum fluorescence intensity of each emitter. Figure 5.5 (a) shows an example of background-corrected, power-dependent saturation behavior for a representative emitter in Sample A as fitted with equation (5.1). The emitter has a RT ZPL at 1.818 eV with I_∞ and P_{sat} yielding ~105 kCounts/s and ~558 µW, respectively.

The histograms in Figure 5.5(b) summarises the maximum intensity and saturation power for 8 additional emitters. The mean value of maximum intensity, I_∞, is ~(427±215) kCounts/s, where all emitters are excited using a 532-nm cw laser. This is comparable to other emitters

in 3D crystals and can be further improved by employing solid immersion lenses or nanoscale pillars [212-215]. The significant standard deviation observed in the mean fluorescence intensity, as well as the saturation power, ~(1270±735) μW, may arise from discrepancies in the effective absorption of the off-resonant excitation by the different emitters due to their multiple orientations in the film, as will discussed in detail below[78].

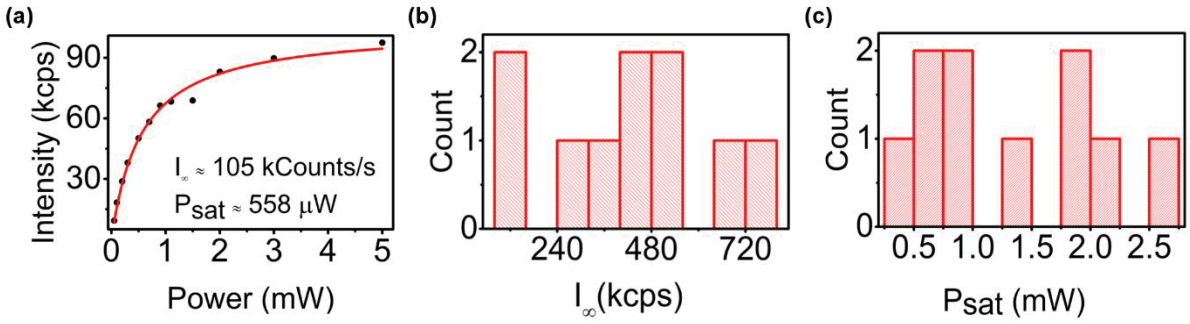

Figure 5.5: Saturation behaviours of emitters in GaN at room temperature. a) Background-corrected fluorescence intensity versus power from a representative emitter with a ZPL at 1.818 eV, and a maximum intensity of ~105 kCounnts/s at a saturation power of 558 μW. b, c) Statistical distribution of the maximum intensity and saturation power from 8 emitters, with a mean value of ~(427±215) kCounts/s and ~(1270±735) μW, respectively.

5.2 RT transition kinetics analysis of SPEs in GaN

Optical transitions in the GaN defects that exhibit single photon emission have all shown strong power dependent bunching behaviour (See Figure 5.6 & 5.9). This indicates that radiative luminescence in these SPEs results from at least a three-level relaxation process that involves a metastable state. A quick recap of the three-level (blue box in Figure 5.7) system is provided here (see Chapter 2 for details). Upon photon absorption, ground state, 1, is coupled to excited state, 2, via excitation rate coefficient, κ_{12}. In a two-level system, photon emission results when the excited particle relaxes to the ground state, with a relaxation coefficient κ_{21}. In the case of a three-level transition, photon emission results, when the excited particle undergoes radiative relaxation to ground state from excited state, 2, with rate coefficient κ_{21}. Relaxation rate coefficient, κ_{23}, is the non-radiative channel where no photon

will be emitted as long as the particle remains in the metastable state, 3. Thus, optical transition systems involving at least one metastable state should show power dependent characteristic as depopulation of particles from the metastable state changes with excitation power.

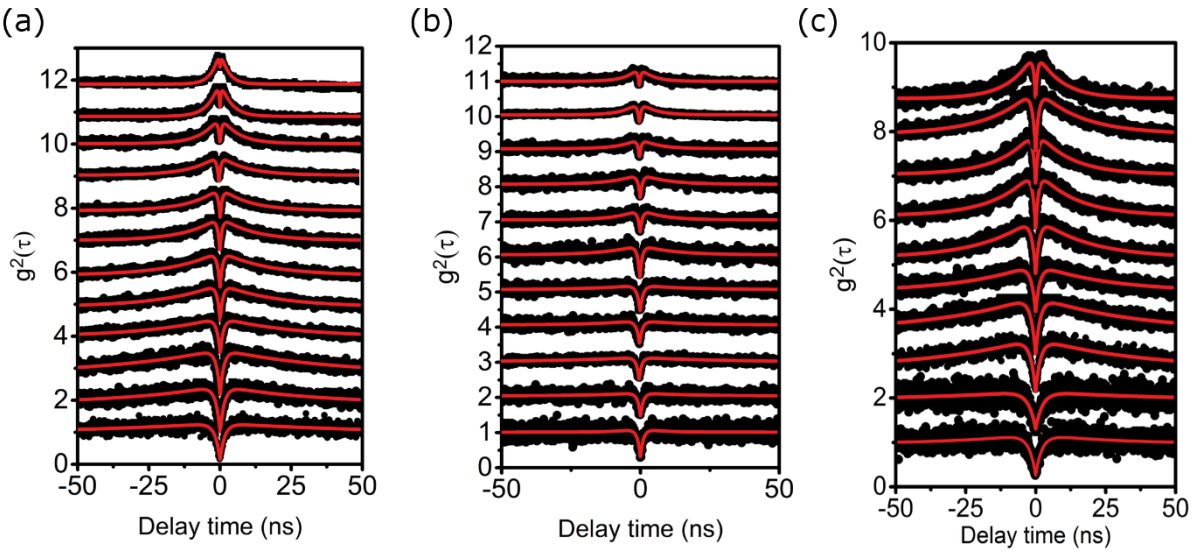

Figure 5.6: Power dependent antibunching characteristics of the three emitters presented in Figure 5.2 with spectral peak at 647 nm, 679 nm and 690 nm is provided in (a) (c) & (e) respectively. As shown, emitters show power dependent bunching characteristics in the three emitters.

First, power dependent antibunching characteristics of an emitter from sample A will be measured to calculate rate coefficients and elucidate particle population dynamics. Figure 5.8 displays power dependent second-order autocorrelation data with fits generated using the three-level model equation of $g^2(\tau)$ (Equation (4.1)/(2.45)). All data set are normalized to 1 assuming that at very long-time photon statistics would follow Poissonian distribution. The lifetimes τ_1, τ_2 and scaling factor a are obtained as parameters from the power dependent antibunching fits. The values for different pumping powers are shown in Figure 5.8 (b), (c) & (d). In addition, lifetimes and scaling factor at zero and infinitely high powers are obtained after fitting data points with single and double decay exponents, respectively. The values are $\tau_1{}^0$= 4.74 ns, $\tau_1{}^\infty$= 1.04 ns; $\tau_2{}^0$= 53.28 ns, $\tau_2{}^\infty$= 12.47 ns; a^0 = 0.035, a^∞=0.66; where

superscripts 0 and ∞ designate power at zero and infinitely high-power values. Parametric values are related to rate coefficients as[78]:

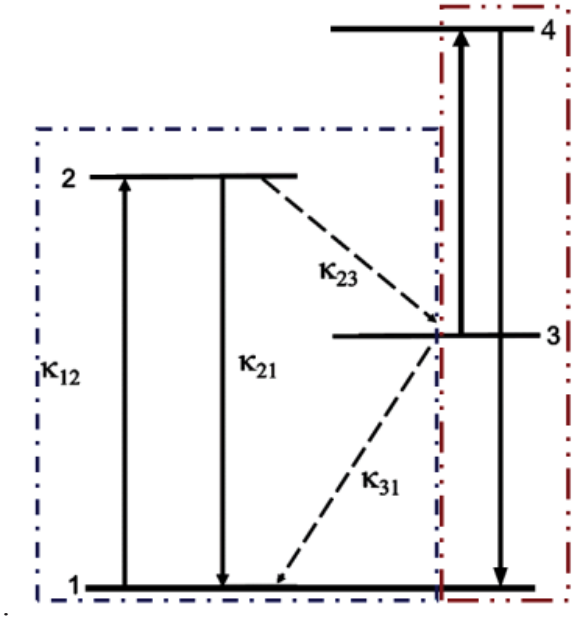

Figure 5.7: Schematic diagram illustrating three-level optical transitions. κ_{12} denotes transition coefficient from ground state, 1, to excited state, 2. Relaxation coefficient κ_{21} represent spontaneous emission, whereas κ_{23} is the metastable state, 3, populating rate coefficient and κ_{31} is de-shelving from metastable state to ground state. The red box further illustrates an alternate pathway for intensity dependent de-shelving from state 3 to a new excited state, 4.

$$\tau_{1,2} = {}^{2}/_{A \pm \sqrt{A^2 + B}} \tag{5.3}$$

where

$$A = \kappa_{12} + \kappa_{21} + \kappa_{23} + \kappa_{31} \; ; \; B = \kappa_{12}\kappa_{23} + \kappa_{12}\kappa_{31} + \kappa_{23}\kappa_{31} + \kappa_{23}\kappa_{31}$$

$$\mathrm{a} = \frac{1-\tau_2\kappa_{31}}{\kappa_{31}(\tau_2-\tau_1)} \tag{5.4}$$

Considering a metastable state that is constant (no dependence on pumping powers), κ_{12}, κ_{21}, κ_{23} and κ_{31} are calculated using relations of lifetimes and scaling factor at zero and infinitely high powers[69]. Accordingly, κ_{21}= 162.6 MHz, κ_{23}= 162.6 MHz, and κ_{31}= 48.5 MHz. Using this relation $\kappa_{12} = \sigma P$; where σ is the absorption cross-section and is constant

in three-level system[78, 216]. Hence, using σ= 0.12 MHz/ μW, equations (5.3) & (5.4), power dependent characteristics of τ_1, τ_2 and a are plotted as blue dashed-line in Figure 5.8. Clearly, three-level consideration with a constant metastable state does not properly fit the power dependent trends that the parametric values showed in this emitter. Alternatively, power-dependent de-shelving, where transitions from the metastable state to a new state, 4, is considered as indicated by red-box in Figure 5.7. Thus, κ_{31} is no longer constant and is given by a sub-linear relation of[78]:

$$\kappa_{31} = \frac{\mathrm{d.p}}{P+c} + \kappa_{31}^{0} \tag{5.5}$$

where κ_{31}^{0} is power independent. In this case, rate coefficients are given by:

$$\kappa_{31}^{0} = \frac{1}{\tau_2^{0}}; \quad \mathrm{d} = \frac{\frac{1}{\tau_2^{\infty}} - (1+\mathrm{a}^{\infty})\frac{1}{\tau_2^{0}}}{1+\mathrm{a}^{\infty}}$$

$$; \kappa_{23} = \frac{1}{\tau_2^{\infty}} - \kappa_{31}^{0} - d; \kappa_{21} = \frac{1}{\tau_1^{0}} - \kappa_{23}$$

Similar to the three-level consideration, the rate coefficients are calculated for lifetimes and scaling factor at vanishing powers. Results yield κ_{31}^{0}= 18.9 MHz, d = 49.2 MHz, κ_{23}= 12.3 MHz and κ_{21}= 198.8 MHz. While κ_{12} still linearly depends on power, σ can no longer be determined from saturation power[78]. Therefore, c and σ are unknowns that will be determined via fitting the power dependent data of τ_1, τ_2 and a. The fit calculated this way is shown in Figure 5.8 with the bold red lines. As can be seen, the extended model generates better fit for power dependent parametric values of the lifetimes, where $\boldsymbol{\sigma}$= 1.07 MHz/μW and c= 7.43 mW. Furthermore, these values, although prone to error, clearly depict the existence of metastable states in the optical transition of the emitter. The value of κ_{31}^{0} is comparatively higher than reported for SiV defect in diamond showing shorter time in metastable transition [78]. In addition, the large discrepancy between c and P_{sat} in this emitter indicate maximum intensity may not depend on the saturation of the metastable state.

Rate coefficients generated using this model can be used to calculate the quantum efficiency of this particular emitter. The quantum efficiency (η_{qe}) is related to the maximum intensity count of the emitter (I_∞) as:

$$I_\infty = \eta_{det}\eta_{qe}\frac{\kappa_{21}}{1+\frac{\kappa_{23}}{(\kappa_{31}^0+d)}} \tag{5.6}$$

where detection efficiency (η_{det}) for our set-up is approximated to be around 20%[195]. Rearranging equation (5.6) and plugging the values, the quantum efficiency of 9 % is calculated for this emitter.

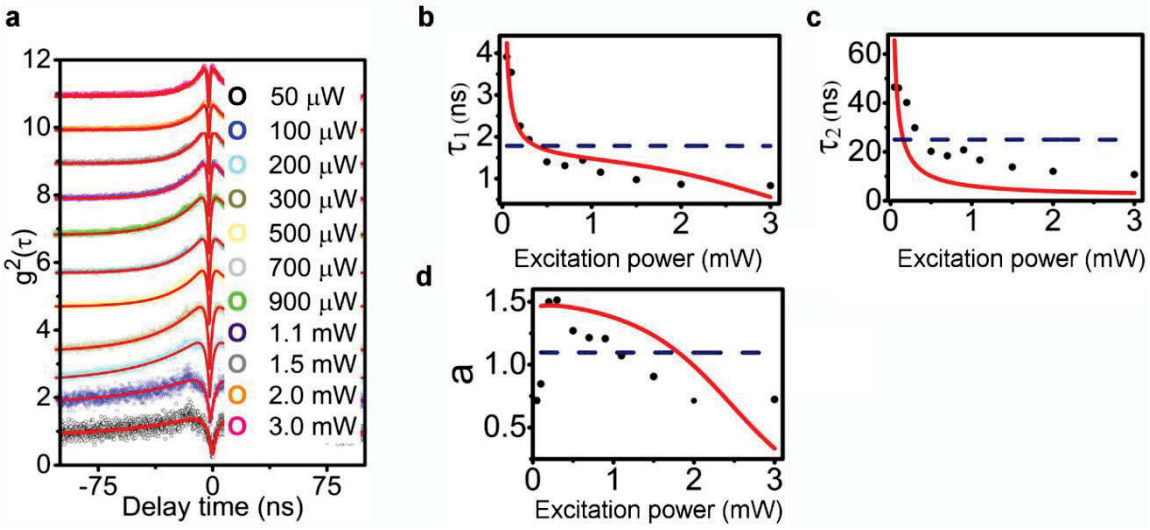

Figure 5.8: Power dependent single photon behaviour of the emitter. a) Measured $g^2(\tau)$ with different powers b), c) and d) show that radiative lifetime, τ_1, metastable non-radiative lifetime, τ_2, and scaling factor for bunching, a, extracted from fitting the $g^2(\tau)$ function for different powers in (a).

Considering the similarities in the power dependent antibunching characteristics as well as maximum intensity in all emitters investigated, similar quantum efficiency is expected for all emitters. However, this value deviates from the true internal quantum efficiency of the emitter, first due to the approximate estimation of rate coefficients. More importantly, factors such as calculation of I_∞ only based on ZPL (without considering the percentage of emission

from phonon sidebands) and background luminescence are discussed in literatures to offset the value of quantum efficiency determination using such approach [78].

Although the extended model generates fits that describe transition dynamics in GaN emitters, improved model that describe the power dependent nature of parameters is still required. One widely used model that yields a better description of the transition kinetics in GaN emitters is described in Subchapter 2.2.1. For the quantitative analysis of the transition kinetics using this model, power dependent second-order correlation measurements are taken from 6 emitters E1-E6 as shown in Figure 5.9. The measurements reveal bunching statistics at intermediate time scales for increasing excitation powers, further confirming the involvement of shelving states in the transition kinetics of SPEs at RT. The strength of the bunching behaviour at different values of P_{sat} varies between emitters, as expected from the substantial differences in saturation behaviours discussed above.

The data is well fitted using a second-order autocorrelation equation (2.45)(red line)[69] with a, λ_1, and λ_2 are the scaling factor for bunching, radiative and non-radiative decay rates, respectively. After extracting a, λ_1, and λ_2 as fit parameters for each emitter in Figure 5.9, the power dependence is plotted. Figure 5.10 is the power dependence of a, λ_1, and λ_2 for E1-E6. By finding the best fit for the power dependent behaviours of the parameters, insight is obtained into the transition kinetics of SPE.

The parameters λ_1, λ_2 and a are expressed as (See chapter 2 for details)[81, 217]:

$$\lambda_1 = \kappa_{12} + \kappa_{21} \tag{5.7}$$

$$\lambda_2 = \kappa_{31} + \frac{\kappa_{23}\kappa_{12}}{(\kappa_{12} + \kappa_{21})} \tag{5.8}$$

$$a = \frac{\kappa_{12}\kappa_{23}}{\kappa_{31}(\kappa_{12} + \kappa_{21})} \tag{5.9}$$

where κ_{12}, κ_{21}, κ_{23} and κ_{31}, are the rate coefficients for the transitions between coupled states $|1> \rightarrow |2>$, $|2> \rightarrow |1>$, $|2> \rightarrow |3>$ and $|3> \rightarrow |1>$, respectively. The expressions $|1>$, $|2>$ and $|3>$

represent the ground, excited and shelving states, respectively. The linear relationship between excitation power, P, and κ_{12} is given by $\kappa_{12} = \alpha\kappa_{21}P = \sigma\frac{I}{h\upsilon}$ where α is the fitting parameter, σ is the absorption cross-section and $\frac{I}{h\upsilon}$ is the photon flux with I being the intensity of excitation, h is Planck's constant and υ the excitation frequency. In the case κ_{31} depends linearly on P, the relation $\kappa_{31} = \kappa_{31}^{0}(1+\beta P)$ holds. κ_{31}^{0} is a constant rate coefficient when the system is not absorbing power and β is the fitting parameter signifying the magnitude of dependence of the shelving state on the excitation power.

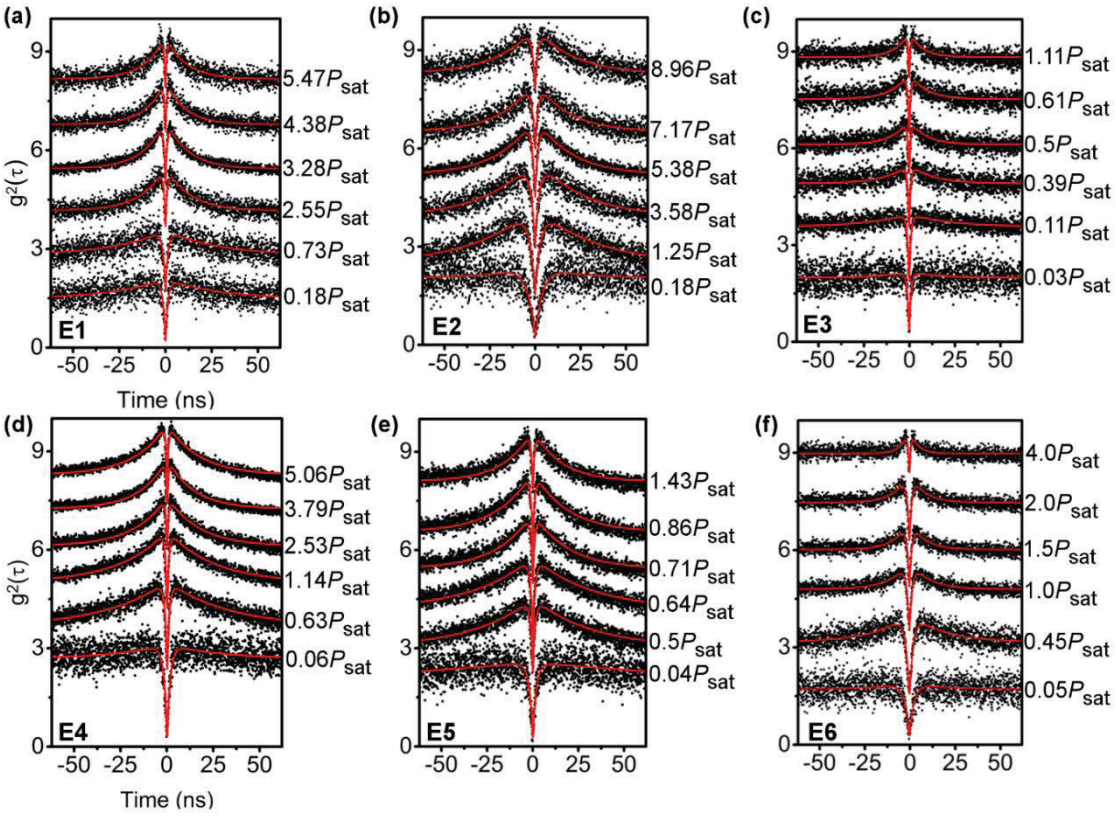

Figure 5.9: Power-dependent antibunching characteristics of the six emitters E1-E6. While all emitters showed power-dependent bunching behaviour, the strength of bunching at intermediate time scales occurs at different fractions of the excitation power. The antibunching behaviours are well fitted (red curve) using second-order autocorrelation function for three-level systems.

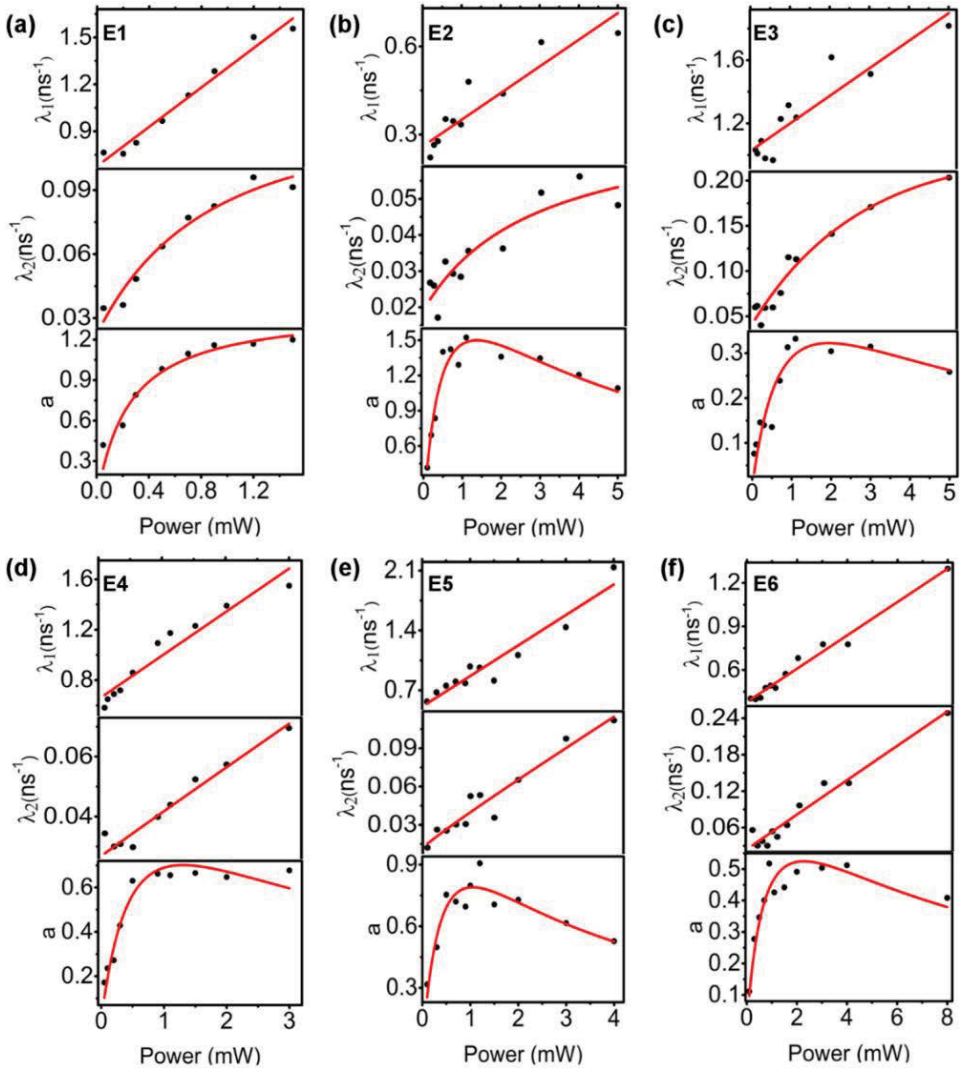

Figure 5.10: Power-dependent properties of the decay rates λ_1, λ_2 and the scaling factor a for the 3 emitters E1-E6 measured at room temperature. The data points (black dots) are fitted well (red lines) by considering three-level transition kinetics.

Fitting the power-dependent behaviours of λ_1, λ_2 and a for each emitter in Figure 5.9 via the three-level transition kinetics model, we determine the characteristic rate-coefficients and relevant parameters. Table 5.1 summarises these values for each emitter together with their corresponding ZPL energy. The non-radiative decay in E2 and E3 occurs via a power-dependent shelving mechanism with a positive value for β. On the other hand, the non-radiative decay in E1 occurs via a power-independent shelving state where $\beta = 0$. The

difference in the value of β indicates a different dependence of absorption cross-section for the individual shelving state, with varying excitation power.

The excited state lifetime, $\tau_{|2\rangle}$, is calculated for the 6 emitters using the expression $\tau_{|2\rangle} = (\kappa_{21} + \kappa_{23})^{-1}$ [218]. As shown in Table 5.2, emitters in GaN have short lifetimes with moderate variation between them. Also, κ_{21} is ~2–40 times larger than κ_{23}, indicating the strong propensity of the excited state to decay radiatively to the ground state, rather than via the 'dark' shelving state. One of the advantages of the rate analysis, using this approach, is that it allows us to estimate the metastable lifetime ($\tau_{|3\rangle}$) separately from the excited state lifetime. The quantity $\tau_{|3\rangle}$ is given by $1/\kappa_{31}$ or $1/\kappa_{31}^{0}$ in the case of a power-dependent shelving state[218].

SPE	ZPL (eV)	κ_{21} (ns^{-1})	κ_{23} (ns^{-1})	κ_{31} (ns^{-1})	κ_{31}^{0} (ns^{-1})	α (μW^{-1})	β (μW^{-1})
E1	1.934	0.678	0.127	0.024	-	9.27×10^{-4}	0
E2	1.818	0.268	0.046	-	0.021	3.31×10^{-4}	3.29×10^{-5}
E3	1.826	1.039	0.521	-	0.043	1.65×10^{-4}	3.49×10^{-4}
E4	1.787	0.665	0.015	-	0.027	5.10×10^{-4}	5.33×10^{-4}
E5	1.797	0.510	0.088	-	0.012	6.99×10^{-4}	1.95×10^{-3}
E6	1.839	0.385	0.026	-	0.028	2.96×10^{-4}	9.88×10^{-4}

Table 5.1: Rate coefficients extracted for the selected three SPEs by fitting their power-dependent parameters in Figure 5.10. The quantities κ_{12}, κ_{21}, κ_{23} and κ_{31} are the rate coefficients for transitions between coupled states $|1\rangle \rightarrow |2\rangle$, $|2\rangle \rightarrow |1\rangle$, $|2\rangle \rightarrow |3\rangle$ and $|3\rangle \rightarrow |1\rangle$, respectively. All emitters except E1 show a power-dependent shelving state. α and β are linear fitting parameters for the power dependence of κ_{12} and κ_{31}, respectively.

	E1	E2	E3	E4	E5	E6
$\tau_{\|2\rangle}$ (ns)	1.2	3.2	0.6	1.5	1.7	2.4
$\tau_{\|3\rangle}$ (ns)	41.7	47.6	23.3	37.0	83.3	35.7

Table 5.2: Calculated values of the excited state ($\tau_{|2\rangle}$) and metastable state lifetime ($\tau_{|3\rangle}$) for the 6 emitters

5.3 Polarisation properties of SPEs in GaN

In this subchapter, we focus on the polarisation analysis of the SPE in GaN at RT. Polar plots of polarization data from the three SPEs presented in Figure 5.2 (a), (c) &(e) are shown in Figure 5.11 (a) (b) & (c), respectively**.** The absorption (excitation) polarisation profiles shown in each plot [green] are measured by first placing a half-wave plate on the excitation path of the confocal set-up (See Figure 4.3). Then, spectra are taken by rotating the half waveplate to change the angle which in turn changes polarisation form of the excitation laser. This is because the angle is subtended between the polarisation direction of the original excitation laser and the axis of the polariser, where each rotation results in a different polarisation form. Thus, each of the green data points in Figure 5.11 corresponds to the maximum intensity of the spectrum at the corresponding rotation angle of the half-wave plate. In this way, the excitation polarisation dependence of the SPE is analysed.

To analyse the polarisation direction of the emitted photon, first, the half-wave plate was fixed at an angle where maximum absorption intensity occurs for each emitter. Then, by rotating a visible polariser mounted in the collection path of the set-up, the spectrum is collected at each rotation angles (see Figure 4.3). As a result, we obtain the emission polarisation profile for the representative emitters [red] in Figure 5.11 by plotting the maximum emission spectra intensity as a function of rotation angles. As shown, intensity variations of the 3 emitters are recorded as a function of rotating excitation [green] or emission [red] polarisation direction.

In this polarisation analysis set-up, under a cross-polarized condition where all linear polarisation forms should be dampened, residual intensity counts were still detected. This residual count is due to unwanted optical ellipticity introduced by birefringent components such as the dichroic mirror, the sample (GaN) as well as the high-NA objective. This is corrected by introducing quarter waveplates on both excitation and detection pathways (See Figure 4.3). That is, quarter waveplates on the excitation and emission end will be rotated and fixed to minimise residual intensity count on detectors under cross-polarised condition. Thus, all polarisation measurements afterwards are ride off unwanted residual intensity.

The polarisation data are fitted with the function $I(\phi) = a + b\cos^2(\phi)$ where a, b and ϕ are offset parameter, initial intensity amplitude and angle between excitation and dipole orientation, respectively[132]. Fitting the emission polarisation of the 3 emitters with this function, we determine the minimum ($I_{min} = I(\phi = 90^\circ) = a$) and maximum ($I_{max} = I(\phi = 0) = a + b$) of the emission (absorption) polarisation to be at ~135° (60°) and ~40° (140°), respectively. Such analysis of polar plots is useful as it allows for easy determination of the dipole polarisation visibility, as well as the relative orientations of the absorption and emission polarisation for individual emitters [219-221]. The polarisation visibility is given by the intensity contrast equation:

$$I = \frac{I_{max} - I_{min}}{I_{max} + I_{min}} \tag{5.10}$$

which, with regard to the emitter shown in Figure 5.11, yields excellent emission polarisation visibility of 99 %, 99 % and 94 %.

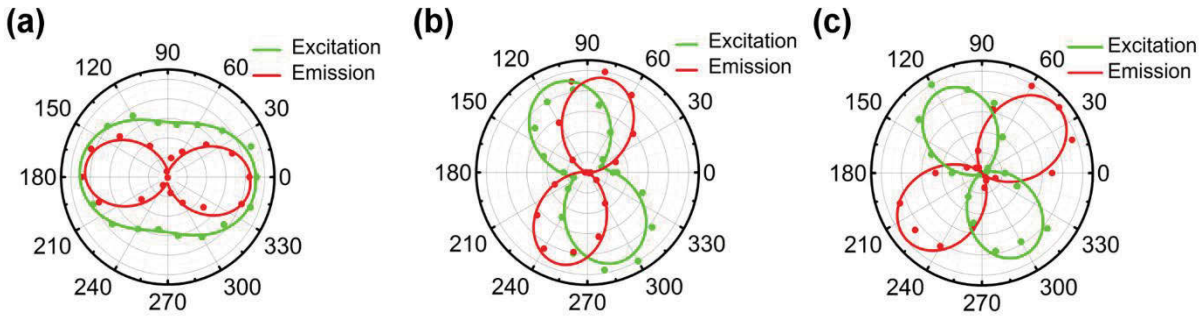

Figure 5.11: Polarization characteristics of the 3 emitters in Sample A. The polarisation measurement for emitters whose spectral characteristic is presented in Figure 5.2 (a), (c) & (e) is shown here as (a), (b) and (c) respectively. Green curves represent excitation polarisation while red represents emission polarisation.

To further consolidate the observed polarisation behaviours, we carried out similar measurements on 14 additional emitters. Figure 5.12(a) shows a polar plot from the additional representative emitter with an RT ZPL at 1.818 eV. The emission (absorption) polarisation direction for the representative emitter occurs at ~135° (60°) and ~40° (140°), respectively. The absorption and emission polarisation visibility of 34% and 79% are calculated. Notably, the absorption is not fully polarised, while the emission is. We carried out similar

measurements for the 14 additional emitters. Figure 5.12(b) shows the histogram of their percentile visibility in absorption (green) and emission (red). Interestingly, we observe a significant discrepancy in absorption polarisation visibility, which ranges between 26% and 94% with the mean value at~(57±26)%. The rather broad distribution of absorption dipole visibility results in the large distribution of laser power required to saturate the emitters, as discussed before. This significant difference in excitation visibility, as well as saturation behaviour, indicates that the orientation of the dipole varies from emitter to emitter, with weak absorption polarisation visibility being likely the result of the dipole having significant out-of-plane components in the 3D crystal[132, 221].

On the other hand, a mean emission polarisation visibility of ~(91±11)% is obtained for the same emitters. This visibility is a reliable indicator that these emitters in GaN are linearly polarised (ideal case ~100% for a single dipole). We attribute the deviation from the ideal value of the visibility to fluorescence aberrations arising from residual birefringence and imaging through a high-NA (0.9) objective [131, 132].

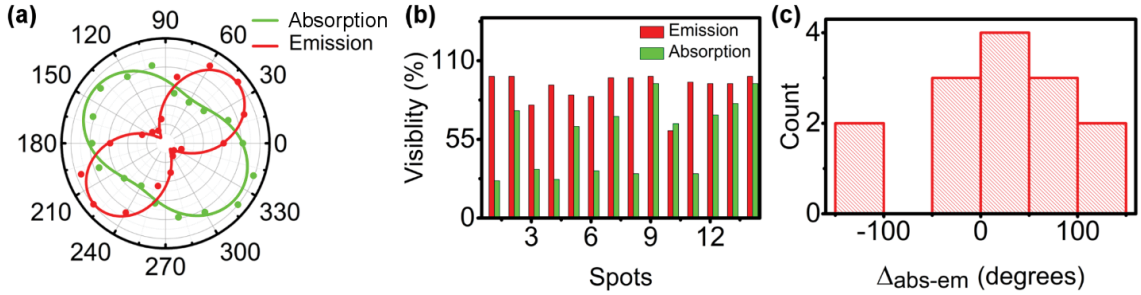

Figure 5.12: Room-temperature polarisation spectroscopy of emitters in GaN. a) Absorption (green) and emission (red) polarisation profiles from an emitter with a ZPL at 1.818 eV, exhibiting polarisation visibilities of 34% and 79%, respectively. b) Polarization visibilities of 14 emitters showing that while the emitters are strongly polarised in emission, they show variable degrees of absorption polarisation. c) Histogram of the difference in orientation between absorption and emission polarisation.

The relative orientation between the absorption and the emission dipoles is further analysed for the 14 emitters showing a misalignment ranging from -110º to 120º as shown by the histogram in Figure 5.12(c). This is expected, considering that the emitters are believed to be point defects located in cubic inclusions. Consequently, for off-resonant excitation, absorption may involve a transition to an excited state of the inclusion. The emission

transition, however, involves only the highly localised levels of the defect thus, giving a more distinct radial emission direction compared to that of absorption.

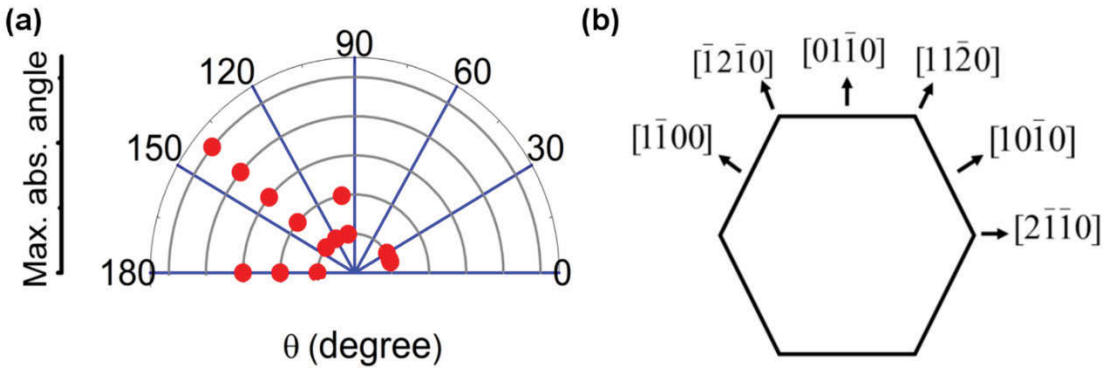

Figure 5.13: Maximum absorption angles for the 14 emitters shown in Figure 5.6. a) Scatter plot of the maximum absorption axis of the 14 emitters. b) Fundamental lattice directions of the wurtzite unit cell, showing that the maximum in angular distribution in (a) corresponds to the $[1\,\bar{1}\,00]$ lattice direction of wurtzite GaN.

To elucidate the nature of the preferential excitation axis, the maximum absorption polarisation angle is measured for the 14 emitters and is compared to the wurtzite crystal plane directions in Figure 5.13(a). The angle spans all directions, with a maximum occurrence at ~140°, which corresponds to the $[1\,\bar{1}\,00]$ lattice direction of the (0001) wurtzite GaN, as shown in Figure 5.13(b). The rotational orientation of the sample was deduced by considering that the sample is mounted with the unit cell along the (0001) plane almost parallel to the excitation field. In this arrangement, rotating the excitation polarisation through 180° sweeps all planes of the hexagonal unit cell. Hence, the highest occurrence angle of 140° which corresponds to the lattice plane direction $[1\,\bar{1}\,00]$ is believed to contain the highest density of cubic inclusions. Furthermore, the highest absorption visibility of 94%, is observed from an emitter with an orientation angle of ~16°, which corresponds to a minimal out-of-plane orientation. This is expected since confined exciton separation occurs along the c axis, where the excitation is aligned parallel to the c axis[92].

5.4 Low-temperature photophysics of SPE in GaN

The SPEs E1-E3 whose low-temperature spectroscopy is presented in Chapter 4 will be further investigated here. The photostability of these emitters was first checked using the fluorescence time trace measurement as shown in Figure 5.14. First, time-resolved PL measurements were carried out on the SPEs using a 532-nm pulsed excitation laser with a pulse width of 32 ps (Figure 5.15). Double-exponential fits (red lines) of the experimental data yielded lifetimes of 1.6 ns, 2.7 ns and 2.0 ns (where the fast decay component of each fit corresponds to the system response). Based on the measured lifetimes, the calculated Fourier transform limited linewidths, Γ, of emitters E1, E2 and E3 are 0.4, 0.2 and 0.3 μeV, respectively. These values are roughly three orders of magnitude lower than the measured linewidths presented in chapter 4 for E1-E3.

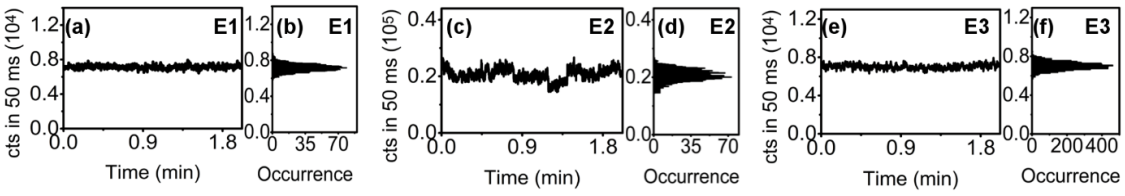

Figure 5.14: Fluorescence time trace measurements and corresponding photon statistics of the three emitters E1, E2 and E3 from in Figure 5.1 (main text) under an excitation power of 100 μW. All three emitters are stable with single-photon statistics. The higher noise level observed on the time trace of E2 is due to sample drift during measurement.

A similar, significant deviation in the natural linewidth has been reported previously in off-resonantly excited single GaN and InGaN quantum dots (QDs), and it is associated with spectral diffusion [25, 26]. The primary cause for spectral diffusion in QDs is charge fluctuations, which are likely exacerbated in GaN by the large in-built electric field caused by the spontaneous and piezoelectric polarisation of GaN [25, 27]. Hence, we attribute the ZPL broadening seen in Figure 4.15 to ultrafast spectral diffusion (at μs- or ns-time scales). Ultrafast spectral diffusion has been reported as a mechanism for broadening in other materials such as SiC and diamond [12, 28].

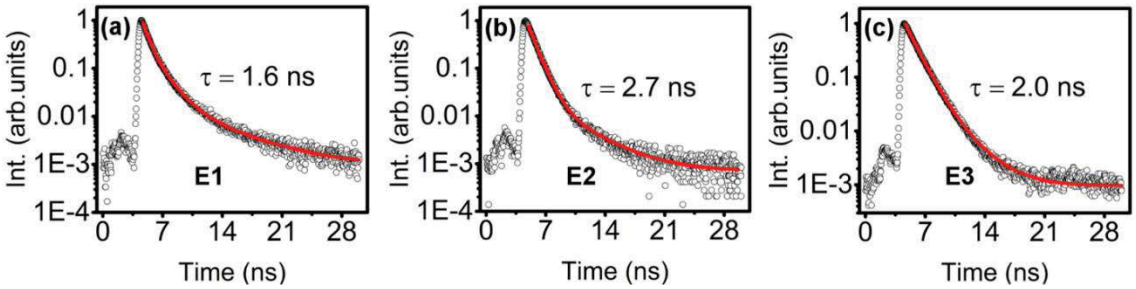

Figure 5.15: PL decay time measurements of quantum emitters in GaN obtained at 4 K using a 532-nm pulsed excitation laser. a-c). Double exponential fits (red line) of the background-corrected measurements yield excited state lifetimes of 1.6, 2.7 and 2.0 ns for emitters E1, E2 and E3, respectively.

To gain more information on ZPL stability, we performed time-resolved spectroscopy (Figure 5.16). The mean ZPL peak position for emitters E1-E3, at an excitation power of 50 μW, is (1.796±0.0002) eV, (1.852±0.0005) eV and (1.981±0.0002) eV, showing that the ZPLs are stable and there is no substantial spectral diffusion at a time-scale of seconds. Thus, faster (μs to ns) measurements are required to probe the aforementioned ultrafast spectral kinetics.

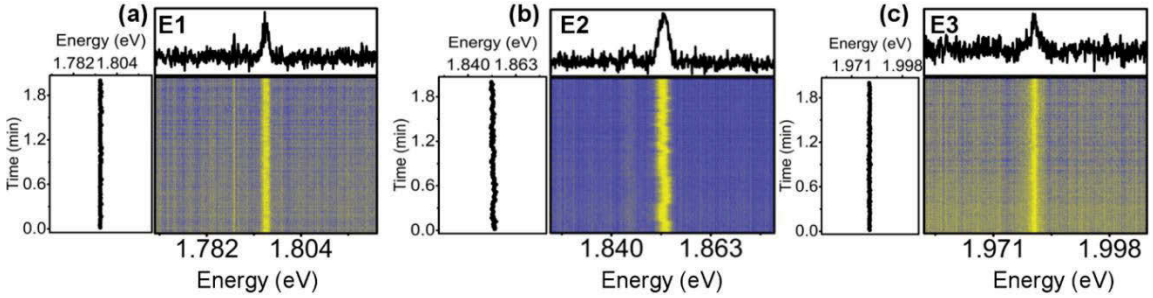

Figure 5.16: Time-resolved PL spectra of the emitters E1-E3 obtained at 4 K using an excitation power of 50μW. a-c) ZPL peak energy (left) measured every second for 2 minutes. The spectral maps show the bright yellow points as the peaks of the ZPL corresponding to the integrated spectrum (top) for each emitter. A stable mean ZPL peak energy of (1.796±0.0002) eV, (1.852±0.0005) eV and (1.981±0.0002) eV is observed for E1, E2 and E3, respectively.

5.5 Conclusion

To conclude, we carried out detailed photophysical analysis of SPEs in GaN at cryogenic and room temperatures. It is shown that most emitters are photostable under excitation powers much higher than the saturation. Some emitters showed unique blinking behaviours motivating the work covered in Chapter 6. Saturation behaviour of SPEs was measured,

showing brightness difference among emitters with an average saturation count rate of ~(427±215) kCounts/s. The emitters transition kinetics was also described well using a three-level system. Polarization measurements from multiple emitters show high mean emission visibility of more than 90% and varying strength in the absorption cross-section under excitation with a linearly polarised, off-resonant laser.

While the FWHM of GaN emitters is significantly narrower at 4 K than at RT, the FWHM does not approach the Fourier Transform-limited linewidths. Ultrafast spectral diffusion is the most likely explanation for the line broadening where future experimental investigation using approaches such as correlation interferometry should confirm this hypothesis[222]. This work evaluates SPEs in GaN highlighting the bottlenecks that might hinder their immediate implementation for quantum applications. The following chapter focuses on a peculiar blinking behaviour observed in some of the SPEs in GaN.

6 Photo-induced blinking in a solid-state quantum system

In this chapter, we report on an unusual, photo-induced blinking phenomenon of SPEs in gallium nitride (GaN). This is shown to be due to modification in the transition kinetics of the emitter, via the introduction of additional laser-activated states. We investigate and characterise blinking effect on the brightness of the source and statistics of the emitted photons. Combining second-order correlation and fluorescence trajectory measurements, we determine the photo-dynamics of the trap states and characterise power dependent decay rates and characteristic "off"-time blinking. These results shed lights on understanding solid-state quantum system dynamics and, specifically, power-induced blinking phenomena in SPEs.

Fluorescence blinking also referred as fluorescence intermittency, is usually an undesired but ubiquitous phenomenon in most quantum light sources, including quantum dots (QDs)[102, 113, 223], defects in wide-bandgap semiconductors [24, 78, 99] and single molecules [112, 224, 225]. Blinking arises when, upon laser excitation, a fluorescent centre undergoes sporadic jumps between "dark" and "bright" states in the photo-emission[223] (see Chapter 2 for details). This phenomenon is identified by the random fall ("off"/"dark" state) and rise ("on"/"bright" state) in photon counts during a long time (milliseconds to hours) fluorescence photostability measurements. Although the cause of the "dark" state has been rigorously studied in various fluorescent systems, a universal physical mechanism that explains blinking has not yet been pinned down [102, 106, 111, 226-228].

The clear majority of the new family of single-photon emitters (SPEs) in Gallium Nitride (GaN) display photo-stable fluorescent emission with single-state photon statistics as described in Chapter 5. Interestingly, however, approximately 5% of the emitters start showing blinking once the power of the excitation laser rises over a certain threshold.

Here, we investigate the nature of this excitation-induced blinking behaviour of SPEs in GaN, at room temperature. Unlike most known SPEs where blinking occurs across all excitation powers without altering its photodynamics, in the present work we report on a previously unexplored behaviour where blinking only occurs above a particular excitation threshold and the emitter's photodynamics is permanently altered without bleaching. By combining transition kinetics analysis and fluorescence correlation measurements at short (nanoseconds) and long (millisecond) time scales, we gather new insights into the blinking mechanism. Furthermore, we propose a mechanism to explain this behaviour in the attempt to generalise the phenomenon and extend the description of such laser-induced blinking to another solid state SPEs.

6.1 Excitation power dependent blinking of SPEs in GaN

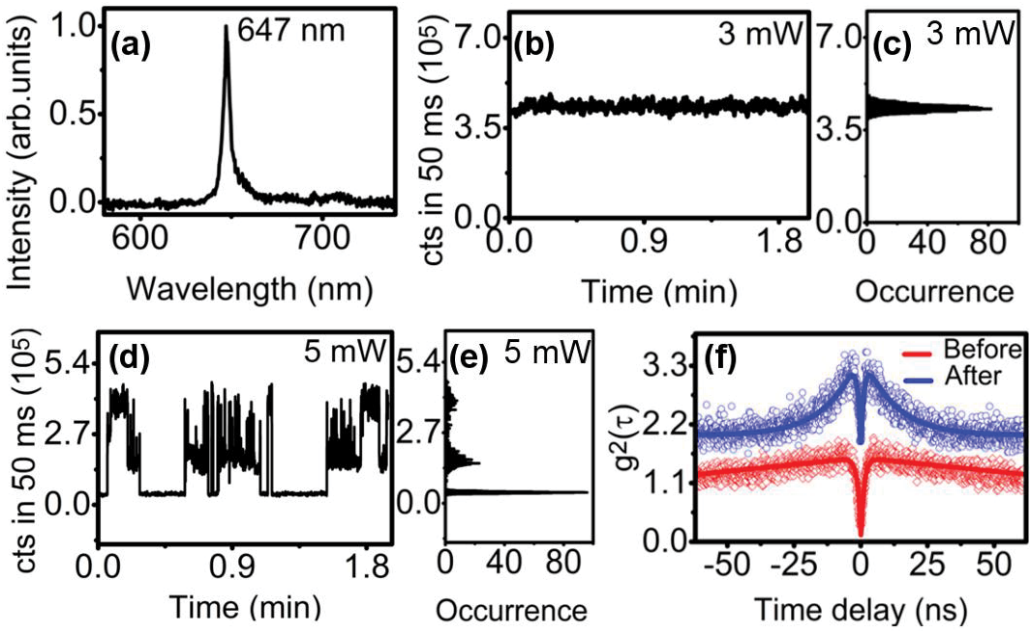

Figure 6.1: Excitation power-induced blinking of an SPE in GaN. a) RT spectra of the SPE taken under 200-µW power excitation; the ZPL lies at 647 nm with an FWHM of ~4 nm. b) Fluorescence trajectory of the same emitter. The time trace is collected from the ZPL with 630 ± 30 nm bandpass filter for 2 minutes. c) Occurrence statistics of the number of photon counts in (b) over a time of 2 minutes. The emitter shows stable emission d) Fluorescence trajectory of the same emitter excited with 5 mW. The time trace is collected from the ZPL using the same BP filter. e) Photon occurrence statistics of (d) at the same excitation power of 5 mW, with notable blinking. Time binning in (a-e) is 50 ms. f) The $g^2(\tau)$ measured for the same emitter before (red), and after (blue) the blinking was induced with high-power excitation; the

$g^2(\tau)$ curves in (f) are taken with 100 µW excitation power. The blue curve is offset vertically by 1 for clarity (see Figure 6.4). The same emitter yield two different values of g2(0)≈ 0.24 vs $g^2(0)$≈0.65 for before and after the high-power-excitation blinking was induced, respectively.

SPEs in Sample A (i.e. 2-µm thick Magnesium-doped GaN layer on 2-µm undoped GaN grown on sapphire) are used for this study. The SPEs were isolated at RT using a custom-made confocal microscope which is equipped with the HBT interferometer for second-order autocorrelation ($g^2(\tau)$) measurements (see subchapter 4.2 for details). A 532-nm, cw laser was used for excitation by focusing it to spot size of ~ 450 nm using a 0.9 NA objective, and the laser power was measured at the entrance pupil of the objective (filling factor ~ 2).

Figure 6.1(a) shows PL spectrum of an isolated SPE excited with 200 µW of laser power, at room temperature. The emitter displays a characteristic emission with ZPL at 647 nm and FWHM of ~4 nm. Figure 6.1(b) shows the emitter's fluorescence stability, measured at 3 mW. The corresponding occurrence statistics of the emission intensity is shown in Figure 6.1(c). The photon distribution follows a single state photon statistics at an excitation power of 3 mW[229].

For this particular centre, a 5-mW excitation induces a sudden change in the photon statistics, which starts displaying a marked blinking behaviour as illustrated in Figure 6.1(d). The photon statistics of the emitter at 5 mW (Figure 6.1(e)), shows three distinct states, in contrast to the single state photon statistics of the same emitter at 3 mW (Figure 6.1(c)). We note that this blinking did not result in bleaching of the emitter during the time frame of this characterisation. The fluorescence trajectories – before and after the blinking is induced – for different excitation powers as shown in Figure 6.2. The average value of intensity for each excitation power is tabulated in Table 6.1.

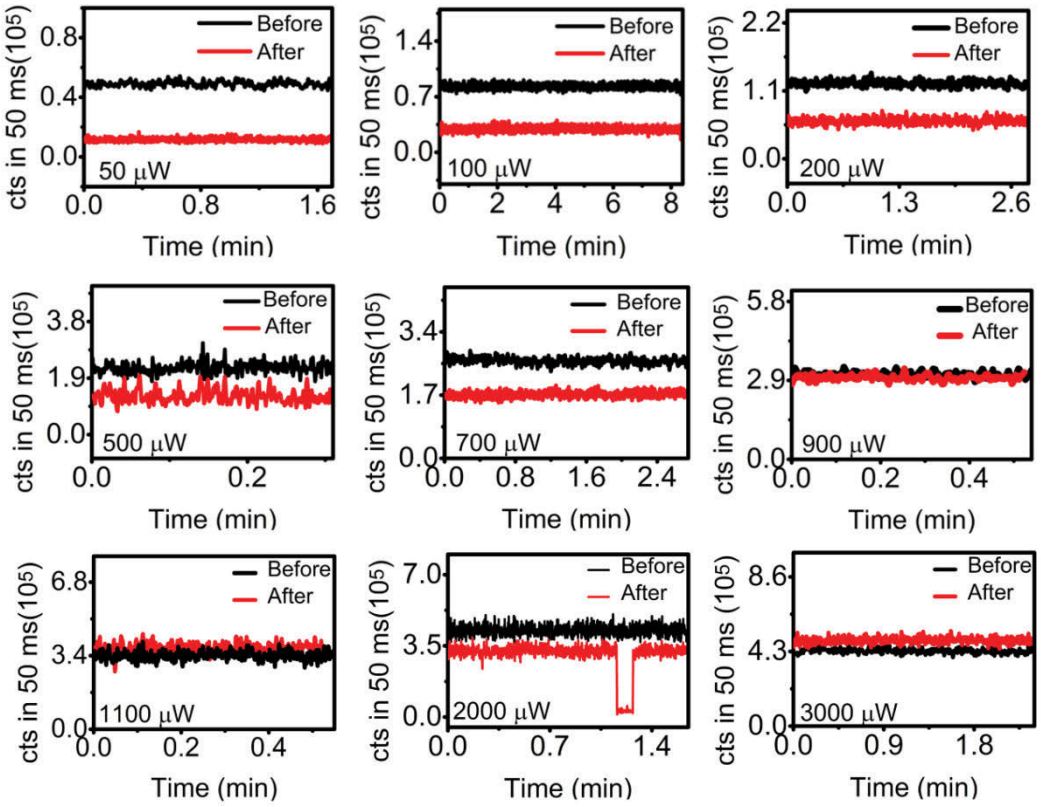

Figure 6.2: Comparison of fluorescence trajectories of the same SPE before (black) and after (red) high-power-excitation blinking was induced: [black] and [red] curves are measured at the same excitation powers. Note how at lower excitation powers (50–700 μW) the emitter shows reduced fluorescence intensity after blinking (a random blinking event is shown in the graph for 2000-μW excitation).

Excitation Power (μW)	Average Intensity Before blinking [x10^5] (counts/s)	Average Intensity After blinking [x10^5] (counts/s)
50	0.472	0.123
100	0.815	0.295
200	1.209	0.613
500	2.199	1.307
700	2.582	1.727
900	3.059	2.817
1100	3.354	3.639
2000	4.139	2.939
3000	4.194	4.943

Table 6.1: Background-corrected intensity values at different excitation powers before and after blinking.

Prompted by the unusual blinking characteristics of the SPEs, the $g^2(\tau)$ measurements were taken at different excitation powers before and after blinking, using the HBT interferometer. Figure 6.1(f) shows two $g^2(\tau)$ curves of the same SPE taken at an excitation power of 100 μW before (red) and after (blue) blinking was induced. The sequence diagram shown in Figure 6.3 illustrates how the measurement was carried out.

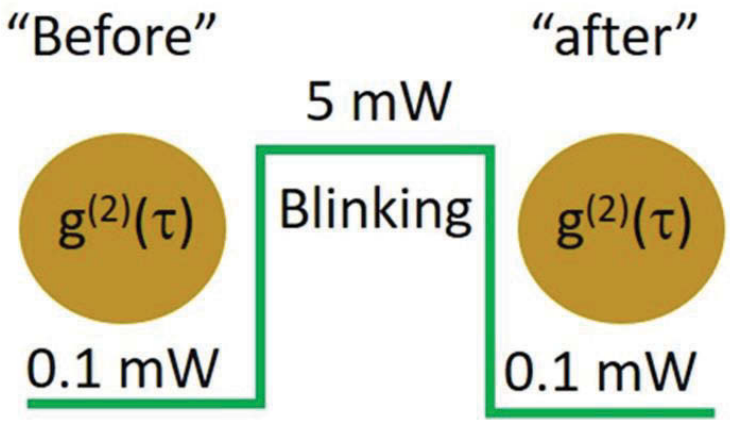

Figure 6.3: Sequence diagram of how the second-order autocorrelation function $g^{(2)}(0)$ and trajectory measurements were measured. First, the data is collected at low power of 0.1 mW ("before"), then the laser power is increased to induce blinking, and the same optical measurements are repeated at lower powers ("after").

The autocorrelation curves in Figure 6.1(f) are re-plotted in two separate panels and are presented in Figure 6.4 (b&c) for better visibility of the change in the absolute antibunching characteristics. Remarkably, the photon statistics before and after the induced blinking are different, with the emitter showing – beyond the expected bunching at intermediate time scales due to the high excitation power – a reduction in the contrast of the $g^2(0)$ function ($g^2(0)$ = 0.65 after, vs 0.24 before). This indicates that the transition dynamics of the emitter is permanently modified.

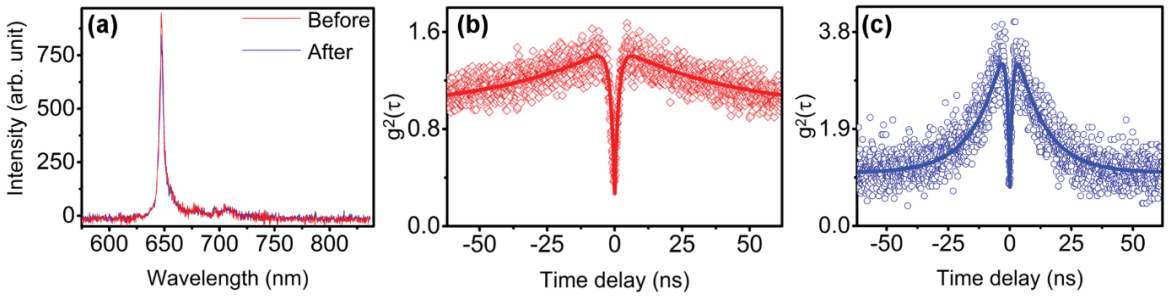

Figure 6.4: (a) RT spectra of the SPE taken under 200-μW power excitation before (red) and blue (after blinking). (b)&(c) are replots of autocorrelation curves in Figure 6.1(f) on two separate panels for better visualization of the absolute change in the antibunching dip as well as bunching curves before and after blinking.

We argue that the change is caused by the activation of a trap state which provides an additional, nonradiative transition pathway to the ground state before the system can be re-excited. This is illustrated in the level diagram in Figure 6.5[230, 231]. Note that this behaviour is dramatically different from that of other solid-state emitters – e.g. the NV centre in diamond – where high excitation simply results in an increased population of its metastable state, and the photo-dynamics is preserved[232-234].

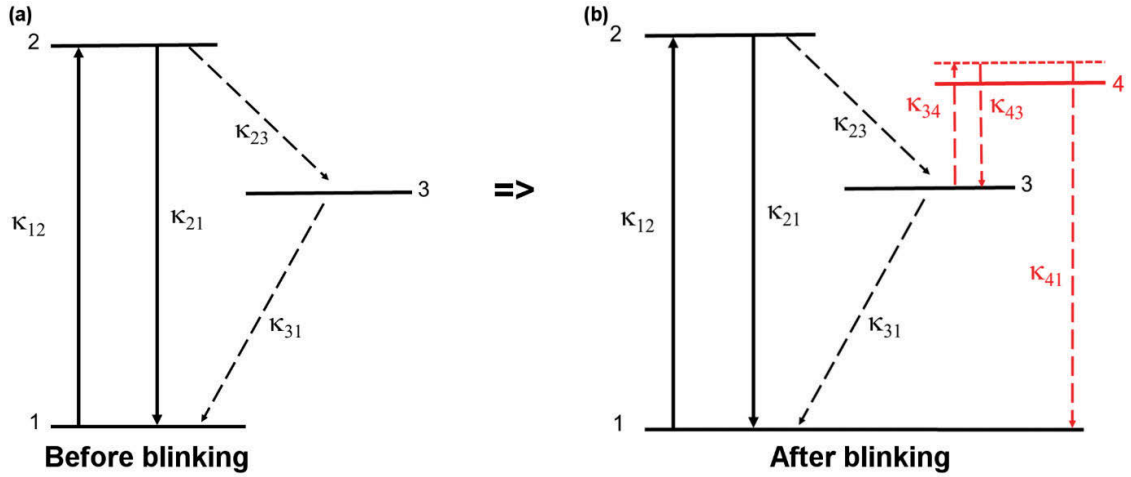

Figure 6.5: Schematics of the transition kinetics before (a) and after (b) power-induced blinking. After blinking, a new trap state (red) is formed as shown in (b). Transition rates are indicated with κ_{ij} where *i,j* = 1,2,3,4 indicate the ground, first electronic excited state, metastable and induced trap state, respectively. Continuous and dashed arrows indicate radiative and non-radiative transitions, respectively.

While the presence of a newly photon-activated state is revealed via reduced average intensity and $g^2(0)$ value after blinking, the three states blinking observed in Figure 6.1(b)&(c) can no longer be resolved via the 50 ms fluorescence trajectory measurement shown in Figure 6.2. This is due to fast decay from the state, 4, to the ground state via strongly coupled decay coefficient κ_{41} making the "off"-state duration much shorter to be detected by 50 ms bin. One mechanism that facilitates fast depopulation from a trap state is auger-assisted decay process, where the subsequent addition of a charge state knocks the former to the ground state (see subchapter 2.3 for details)[109, 235, 236]. This is consolidated by the three distinct photon states shown Figure 6.1(d,e) where multi-level blinking is due to the power-law distribution as a result of fluctuating non-radiative process.

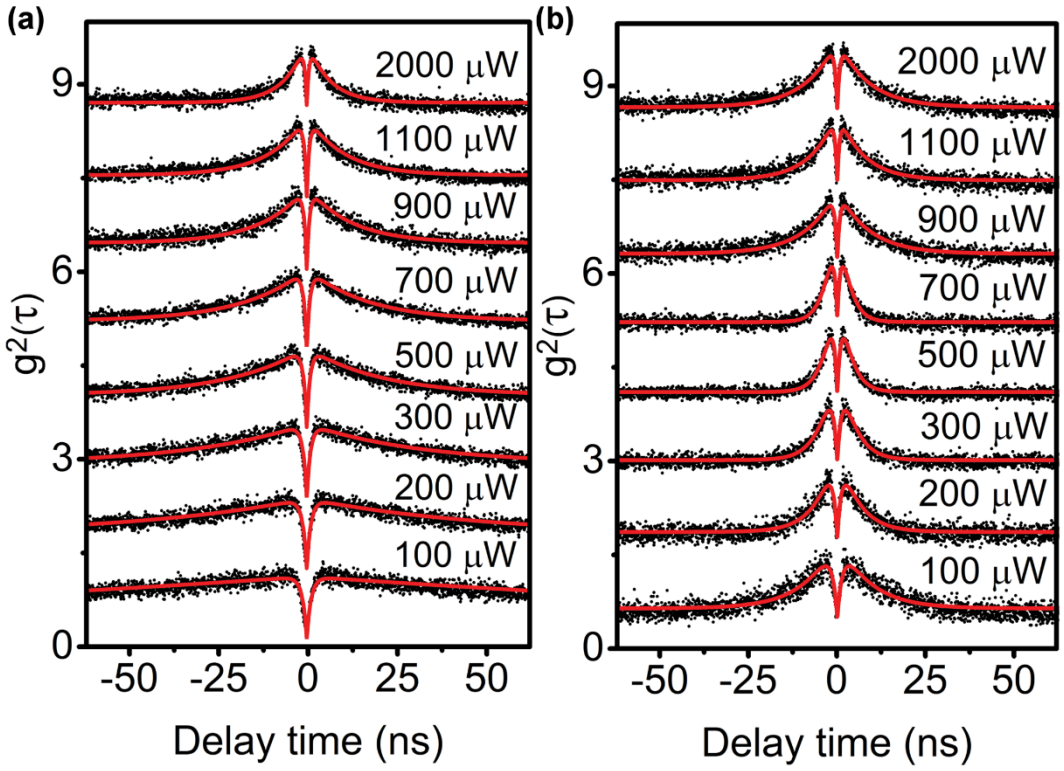

Figure 6.6: $g^2(0)$ measured from the SPE before and after blinking at increasing powers. Individual curves are shifted vertically for comparison purposes. For powers, 50–700 μW, the bunching effect at intermediate time scales is more pronounced in the 'after blinking' case than the 'before blinking' one. See main text.

The power dependent second-order correlation measurement before and after blinking are background corrected and fitted with the three-level model given in equation (2.45). λ_1 and λ_2 are fitting parameters for radiative and non-radiative decay rates while a is a scaling factor for bunching as defined before. At this excitation power, $g^2(0) = 0.24$ and 0.65 'before' and 'after' blinking, respectively. The deviation from zero is due to background fluorescence which is relatively strong in GaN. While the contrast in $g^2(0)$ is reduced after the power-induced blinking has occurred, it is still the same SPE, only with a much lower signal to noise ratio (i.e. reduced brightness as per the additional dark shelving state). This confirmed by the spectral characteristics before and after blinking depicted in figure 6.4(a) where the peak energy did not show a shift. Additional power-dependent $g^2(\tau)$ -curves before and after blinking are shown in Figure 6.6 indicating the same behaviour of enhanced bunching after the emitter starts blinking.

6.2 Transition kinetics and saturation analysis of SPE in GaN before and after blinking

To study further the changes in transition kinetics of the emitter, we analyze brightness and transition kinetic before and after blinking. Figure 6.7 shows plots of power-dependent intensity values for the SPE before and after the blinking was induced. The plots are fitted with a three-level saturation model given in equation (5.1). Before blinking, I_∞ is ~527 kcounts/s at P_{sat}~660 μW. The same center showed two different saturation behaviours before and after blinking. After the blinking is induced, the emission intensity at excitation powers <900 μW is slightly lower than it was before blinking (for the same powers). This is consistent with the model we propose of a laser-activated trap state compounding the non-radiative transition. At excitation powers ≥900 μW, the effect of the additional trap state on emission intensity is overall reduced due to rapid depopulation to the ground state [77, 216].

The transition kinetics analysis is carried out by extracting λ_1, λ_2 and a as fit parameters from the background-corrected, power-dependent $g^2(\tau)$ measurements before and after blinking as

shown in Figures 6.6 (a)&(b). Figures 6.7 (b)-(d) display the extracted λ_1, λ_2 and a as a function of excitation powers, before and after blinking was induced. The power dependence of λ_1, λ_2 and a is fitted by assuming a three-level model with a shelving state that depends linearly on the excitation power for both 'before' and 'after' blinking which is described in detail in Chapters 2&4[69, 81, 237].

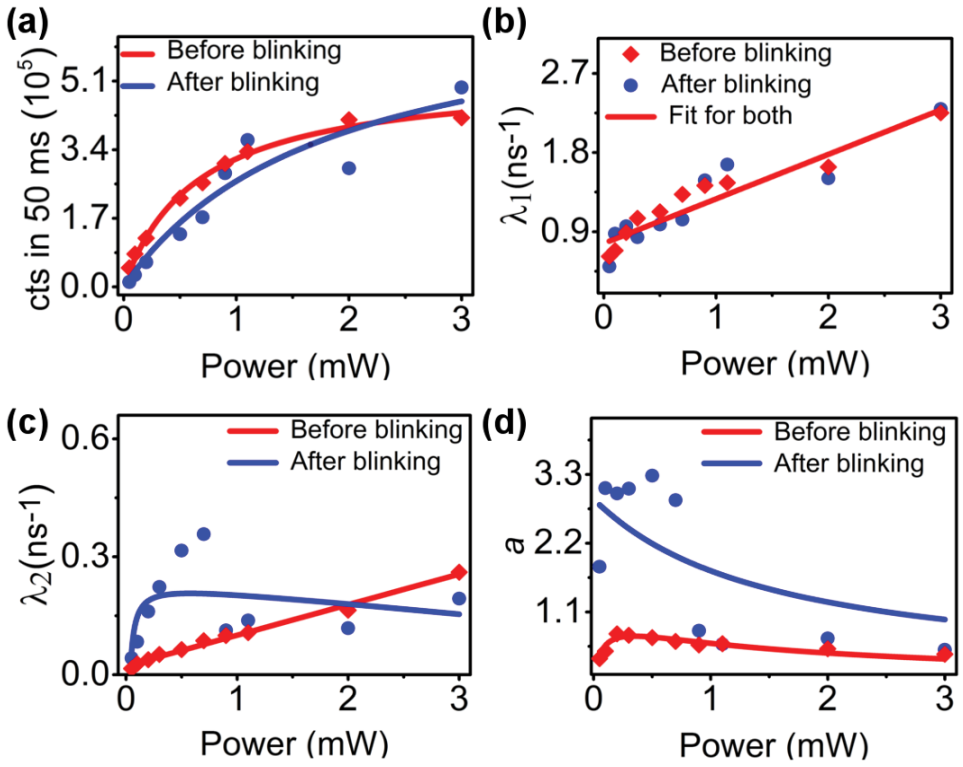

Figure 6.7: Excitation-power dependent parameters of the emitter. a) The brightness of the emitter before (red) and after (blue) blinking is shown as the average photon counts at different powers. Before blinking, at saturation power (P_{sat}) ~660 µW, the highest intensity of 527 kcounts/s is obtained. After blinking, the saturation behaviour is fitted with a three-level model showing a remarkably different curve. b–d) Power-dependent characteristics for the fit parameters τ_1 , τ_2 , a, respectively, for the $g^2(\tau)$ function. These values are extracted as parameters from the $g^2(\tau)$ function fitting (Figure 6.6). A three-level model with linear power dependence for the shelving state described the transition kinetics before blinking (red fitting lines) accurately. After blinking, however, the same model fails to fit λ_2 and a as highlighted by the blue lines in (c) and (d).

Using the relations in equations 5.7-5.9 and accounting for the excitation-power-dependent κ_{31}, values for λ_1, λ_2 and a (Figures 6.7(a)-(c)) are fitted both for the before and after blinking

case. The model worked well before the emitter blinked for all the three parameters giving rate coefficient values of κ_{21} = 736.1 MHz, κ_{23} = 412.7 MHz, κ^0_{31} = 6.8 MHz and fitting parameters α = 67.9 mW^{-1} and β = 12.4 mW^{-1}. The high value for κ_{23} is common in GaN SPEs and explains the propensity of the excited state to decay non-radiatively via a shelving state, as well as the bunching behaviour at intermediate time scales, observed even at low excitation powers. Also, the ratio κ_{23}/κ_{31} decreases with increasing excitation power showing fast depopulation of the shelving state. After the emitter blinked, the model fitted λ_1 with same fitting parameter α = 67.9 mW^{-1}, showing that the radiative decay pathway remained unaltered even after the emitter blinked.

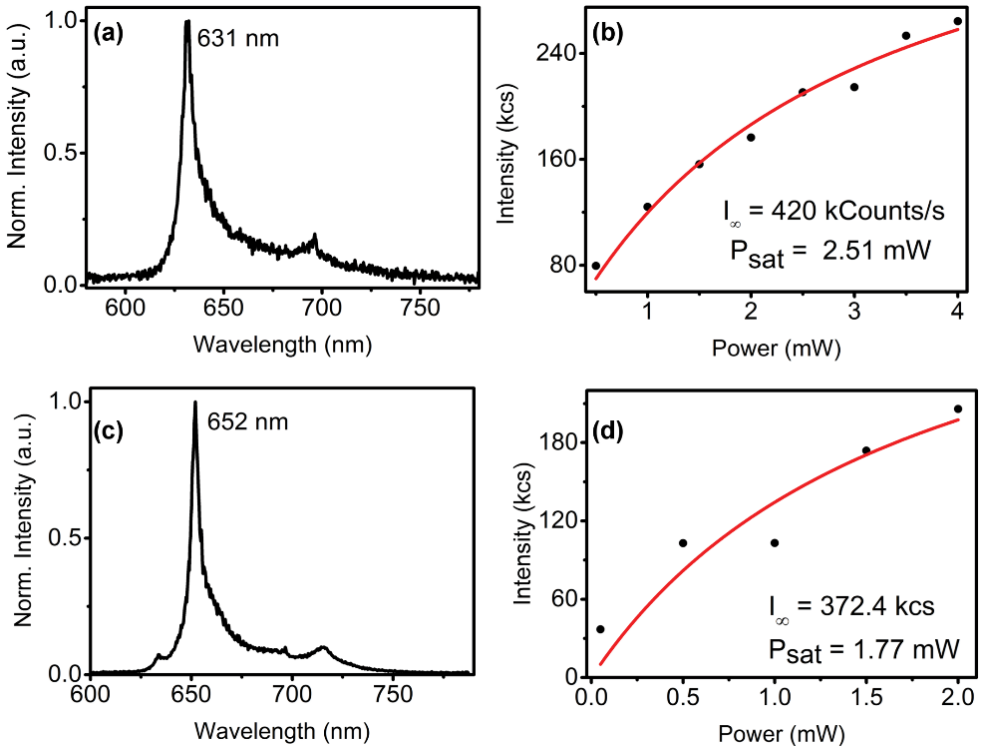

Figure 6.8: Spectroscopy and power-saturation analysis of stable and blinking emitters analysed in the study. a) Photoluminescence spectrum of the stable emitter with ZPL at 631 nm and FWHM ~8 nm. b) Saturation behaviour of the stable emitter collected using excitation power of up to 4 mW. c) Photoluminescence spectrum of an emitter that showed power induced blinking with ZPL at 652 nm and FWHM ~6 nm. d) Saturation behaviour of the blinking emitter fitted with a three-level model. The radiative transition is unaffected by the blinking behaviour.

These results suggest that whatever the nature of the laser-induced change in the emitter might be, such change does not alter, in a detectable manner, the first excited electronic state. In contrast, the consideration of a shelving state that linearly depends on excitation power fails to fit the power dependent behaviours of λ_2 and a after the emitter blinked, showing a more complex behaviour. This is also in accord with the pronounced bunching behaviour at intermediate time scales observed for the emitter at low powers after the induced blinking. Therefore, the laser power has induced a permanent change in the transition kinetics of emitter by introducing a shelving state.

6.3 Long correlation time $g^2(\tau)$-measurements of a blinking SPE in GaN

While rate analysis and brightness characterisation hint to a permanent change in the photo-dynamics of the emitter, more direct evidence for the power-induced trap state is required. We, therefore, recorded long time-fluorescence correlation behaviours for two different emitters in the time range of a few microseconds to 0.1 seconds – one that exhibits absolute photostability and another one that exhibits blinking at higher excitation powers (similar to the one characterised earlier). The spectra and saturation behaviours of the two SPEs is shown in Figure 6.8.

Figure 6.9(a) shows power-dependent, long-time-scale correlated $g^2(\tau)$ from the photostable SPEs. Each measurement is fitted with exponential decay function that holds the least chi-square value, where the decay rate determines the bunching behaviour [239]. In this case, no significant (compared to noise level) decay rates can be observed at the microsecond-to-millisecond time scale. The $g^2(\tau)$ is fitted with the single exponential of the form, $g^2(\tau)=1+A\, e^{-[\lambda_2\tau]}$ to extract the decay rate, λ_2, from the shelving state in the ns range at different powers. Note that the radiative decay rate, λ_1, is not shown in this measurement as correlation starts from a few microseconds. As shown, the $g^2(\tau)$ remains constant along the normal line during the measurement time for all excitation powers. Thus, the stable emitter is fully described by a three-level model showing no additional trap state at long correlation time.

The same set of measurement and analysis is carried out for an emitter that exhibited excitation-dependent blinking. In this case, $g^2(\tau)$ measurement at long time scales shows a strong dependence on the excitation power as evident from Figure 6.9(b), where an extra decay channel appears at the ms scale. A qualitative difference can also be spotted with increasing power. At 100 µW, $g^2(\tau)$ remains constant along the normal at the ms scale – much like the stable emitter at all excitation powers. At higher excitation powers, starting from 500 µW, $g^2(\tau)$ shows additional bunching decay in the ms range[229].

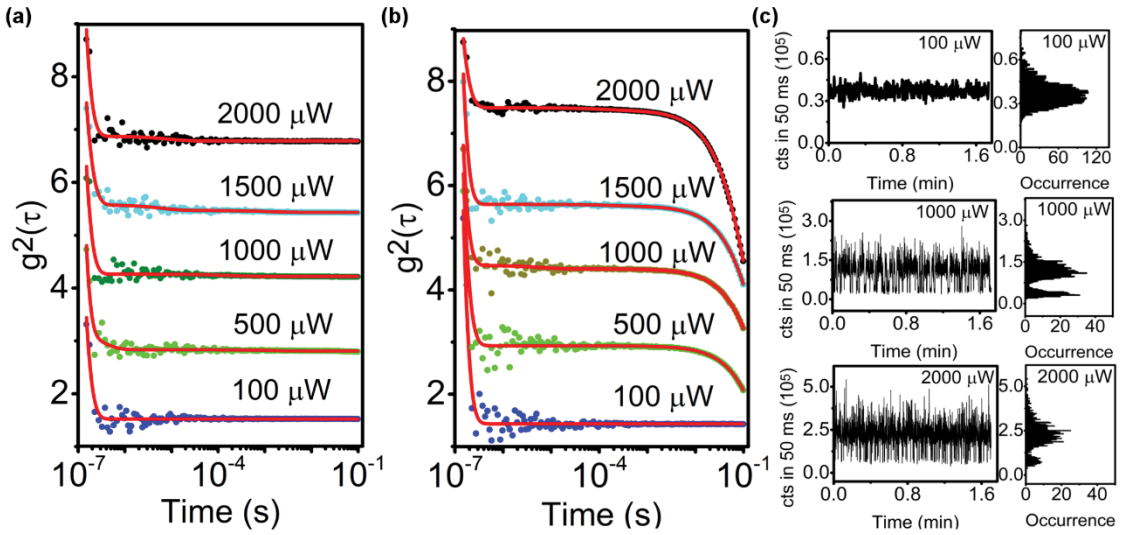

Figure 6.9: Power-dependent long lifetime fluorescence of a stable and a blinking emitter. a) Long time scale, excitation-power-dependent $g^2(\tau)$ characteristics of a stable emitter. The best fit is determined using a single and double exponential decay function with the least chi-square value. $g^2(\tau)$ starts with monotonic decay that corresponds to ns shelving state but remains constant for the measurement time scale range of microseconds to 0.1 seconds. b) Long time scale $g^2(\tau)$ characteristics of a power-induced blinking emitter at different excitation powers. Fitting the $g^2(\tau)$ characteristics at excitation powers of 100 µW is done using single exponential decay function where $g^2(\tau)$ remained constant along the normal; whereas, for excitation power of 500–2000 µW, the emitter showed an additional bunching curve in the ms range with the height increasing with power. c) Fluorescence photostability and photon occurrence statistics under 50-ms binning for the emitter in (b) with increasing excitation power. The emitter, initially stable with near-Poissonian statistics, starts blinking for excitation powers ≥500 µW.

This is direct evidence for a power-induced change in the emitters photodynamics with an activation of the fourth state. Note that using a standard autocorrelation function at short delay times, this decay at ms timescales cannot be noticed, and will simply be manifested in a higher bunching (see Figure 6.1(f)). However, to describe this system precisely, an additional state

in the system should be introduced. Using the $g^2(\tau)$ with double decay functions for excitation power in the range 500–2000 μW, we determined characteristic decay times for the longer decay channel of 371 ms, 222.4 ms, 181.8 ms and 110.4 ms at 500 μW, 1000 μW, 1500 μW and 2000 μW, respectively. The decay time of the induced trap state decreases with increasing excitation power, showing rapid depopulation from the newly activated trap state at higher excitation powers. This is consistent with the observed reduction of blinking events with increasing power and similar intensity after blinking was induced (as per in Figure 6.9(c)).

6.4 Probability density distribution of blinking SPE in GaN

Figure 6.9(c) shows the fluorescence photostability analysis corresponding to the blinking emitter displayed in Figure 6.9(b): binning time is 50 ms and excitation powers are 100 μW, 1000 μW and 2000 μW. As per before, to the right of each photostability time trace, the corresponding photon statistics is displayed, with 1000 photon binning. At 100 μW, the emitter showed stable emission with the intensity trace displaying no "dark" state interruptions as well as minimal photon statistics deviation from single state photon statistics. Upon further increase of the excitation power from 500 μW to 2000 μW, long timescale blinking set in with the fluorescence photostability showing clear "on" and "off" times. The alternating "on" and "off" events are observed on the photon statistics, with the occurrence of the "off" states decreasing with increasing excitation power.

To quantify the "on" and "off" times at different excitation powers, the probability density distribution $P[\tau_{on}]$ and $P[\tau_{off}]$ were plotted by setting a threshold intensity on the fluorescence trajectories of the blinking (Figure 6.9(c))[101]. In the fluorescence time-trace, above and below the set threshold the emitter is considered to be "on" (τ_{on}) or rather "off" (τ_{off}), respectively.

$$P(\tau_{on}, \tau_{off}) \approx \exp\left(\frac{-\tau}{(\tau_{on}, \tau_{off})}\right) \tag{6.1}$$

This relation shows a linear distribution on log-linear plots as displayed in Figure 6.10 for different excitation powers. Unlike the widely-reported power-law dependence of the

probability density distribution on the τ_{on} and τ_{off} [101, 109, 240, 241], the single exponential decay of the form shown in equation (6.1) is observed for both "on" and "off" times in the emitters we analysed [24, 105]. From these plots, the characteristic decay times for τ_{on} and τ_{off} are determined for the excitation-dependent blinking, discussed above.

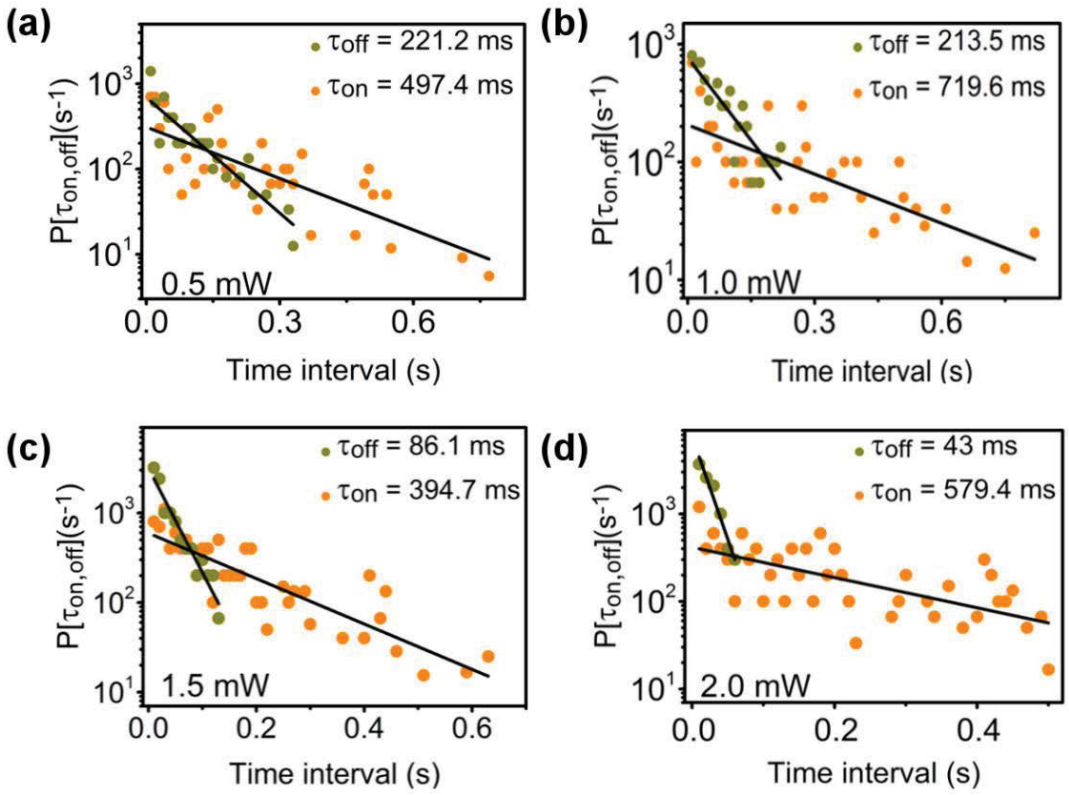

Figure 6.10: Probability distribution of "on" (orange) and "off" (dark yellow) states of the blinking emitter at different excitation powers. a–d) Semi-log plots of the "on" and "off" time distributions of the fluorescence trajectories shown in Figure 6.9(c). The probability distributions of both the "on" and "off" times at all excitation powers show exponential decay, as indicated by the linear trend on the semi-log plots. The "off" probability distributions hold characteristic decay time (τ_{off}) that drop with increasing excitation power starting at 221.2 ms, 213.5 ms, 86.1 ms and 43.1 ms for power excitation in the range 50–2000 μW. Conversely, the "on" time distribution did not show dependence on excitation power and gave a mean characteristic decay time (τ_{on}) of (548±137) ms.

For excitation powers in the range of 500–2000 μW, characteristic "off"-time, τ_{off}, were measured to be ~221.2 ms, 213.5 ms, 86.1 ms and 43.1 ms, respectively. The decline in the "off" times with increasing power is consistent with the fitting at the long time scale of $g^2(\tau)$

and with the reduced blinking at high powers due to faster depopulation from the activated trap state.

Conversely, the probability distribution of "on" times did not show a significant dependence on the excitation power, yielding a mean "on" time (τ_{on}) of (548±137) ms. The weak dependence was also observed in the fluorescence statistics, where the "on" event occurrence remained the same while the "off" event decreased. This suggests that the depopulation of the new trap state possibly leads to a population of another shelving state. This is indicated by the rate coefficient, $\kappa_{43,}$ in Figure 6.5. However, because the original shelving state and the induced trap state are weakly coupled in time, as demonstrated already via the second-order autocorrelation function analysis of the transition kinetics, the effective increase in "on" times are not significant.

6.5 Conclusion

In conclusion, this chapter covered a comprehensive investigation of excitation, power-dependent blinking of SPEs in GaN. It is demonstrated that the excitation power permanently activates trapping states which act as additional shelving states associated with blinking. This is in contrast to known emitters in solids that, upon higher excitation power, populate the same shelving/metastable state, and remain stable. Unlike quantum dots and single molecules which bleach under high excitation laser powers, SPEs in GaN only showed blinking. Overall, this chapter helps to shed more light onto a rather complicated phenomenon – blinking in solid state SPEs – and emphasises that standard three-level models may not always be ideal to describe the photo-dynamics of such systems.

This chapter concludes part of the thesis that covered optical excitation and study of novel SPEs in GaN. Next chapter features electrical excitation of SiV centres in diamond PIN diode. This is a first such demonstration and gives insight into the charge dynamics behind the SiV fluorescence.

7 Electrical excitation of silicon-vacancy in single crystal diamond

The study of SPEs in GaN presented in Chapters 4-6 was mainly conducted using lasers in a PL set-up. One of the primary future objectives is to achieve electrical excitation of these new family of emitters in GaN. This has been achieved on the matured defect in diamond- the NV centre [19]. In this chapter, we demonstrate electrical excitation from ensembles of the other well-established centre in diamond, namely Silicon-Vacancy (SiV). The results and discussion presented here motivate further work on electrically driven single photon emission both in GaN and diamond.

While SiV centres have been studied in detail under optical excitation, electroluminescence (EL) properties of this centre in a single crystal diamond remain unexplored. Electrical excitation is crucial since it opens pathways to engineer scalable devices employing electrically driven emitters and realise efficient packaging on a single chip[19, 242, 243]. Furthermore, it enables studying charge injection and dynamics between various charge states of a particular defect[19, 56, 244, 245]. In this chapter, we report on electrical excitation of engineered SiV ensembles in a single crystal diamond. In particular, we show that the same emission is obtained using optical and electrical excitation—a unique feature that has not been demonstrated in single crystalline diamond yet[246].

The SiV centres were incorporated using ion implantation into an intrinsic (i) region of a p-i-n single crystal diamond diode. By comparing the typical PL spectroscopy to electrically stimulated emissions from the same SiV centre, direct evidence of electrically driven emission from the ensembles is provided. The capability of electrically exciting SiV ensembles in diamond allows us to the study charge state switching in the defect directly by injecting and withdrawing excess charge carriers. The results are consistent with previous charge state switching reports in SiV ensembles via UV excitation[183] and annealing of the centres [184].

Therefore, the realisation of the first EL from SiV^- ensembles assists in understanding the electronic properties of the defect as well as serve as a step towards electrically driven SPEs from the centre, which is not achieved yet.

7.1 Ion implantation of Si^{2+} in diamond PIN diode

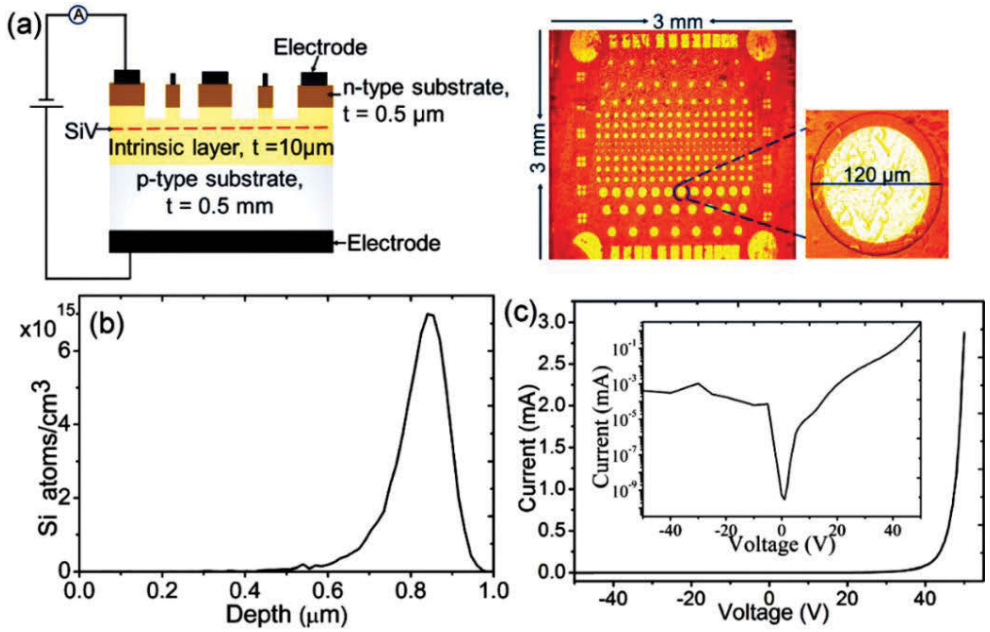

Figure 7.1: (a) Schematic illustration of a single crystal PIN diode with implanted Si-atoms and an optical image of the device. The diameters of the n-type diamond mesa are 120 µm, and the metallic contacts on top are 100 µm. (b) Monte Carlo depth profile of ion-implanted Si-atoms into diamond obtained using SRIM calculations. The end of range is estimated at 820 nm. (c) I-V-characteristic plot is showing diode rectification at a forward threshold voltage of 43V at room temperature. The inset shows Log-Linear curve of the same data set.

The starting material is a single crystal diamond PIN diode[19, 56]. The diode structure consists of a p-type diamond substrate layer of thickness 0.5 mm, an intrinsic diamond layer of 10 µm, and 0.5 µm n-type diamond mesas. Detailed growth conditions were described elsewhere[19]. As a contact electrode, 30 nm Ti/100 nm Pt/200 nm Au was deposited on both the n- and p-type sides of the device. Figure 7.1(a) shows the schematic of the device (left) and the optical microscope image of an array of devices on the chip where a row of 120 µm diameter circular mesas are primarily investigated in this study (right). The reason for the

choice of these row of mesas is twofold: appropriateness for probe electrodes used for the experiment and efficient devices with less heat loss compared to larger mesas. The dark circle around the n-type layer is a two-dimensional image depth resolution depiction of the pillar height.

To introduce the silicon ions (Si^{2+}) into the diamond, ion implantation is employed. Monte Carlo simulation is used to estimate the implantation energy so that the silicon atoms will predominantly reside within the i-region of the device. Figure 7.1(b) shows the SRIM simulation under 1.5 MeV acceleration energy, which results in approximately 820 nm end of range. A small dose of $1x10^{11}$ atoms/cm^2 is implanted over the whole area of the sample. The diode property of the device is then characterised via *I-V* rectification curve under forward bias, and the result is shown in Figure 7.1(c). The threshold forward current of 0.89 mA at room temperature corresponds to the current density of 7.9 A/cm^2 at the specific device showing rectification at the threshold voltage of 43 V. The devices probed here have lower rectification ratio of ~10^4[19]. The high threshold voltage driving a relatively low current density into the device is attributed to the high specific contact resistance between phosphorous doped n-type diamond mesas and top side contacts[247].

7.2 EL and PL excitation of SiV ensembles in diamond diode

EL from the fabricated SiV ensembles is carried out using an external voltage source to inject carriers and scanning confocal microscope (described in subchapter 4.2) with a high numerical aperture objective (0.7, Nikon, x100). The collected light is passed through a dichroic mirror and focused onto a graded-index fibre with a core size of 62.5 μm that acts as a confocal aperture. The collected emission splits into an avalanche photodetector and a spectrometer. PL measurements were carried out on the same set-up using a continuous wave 532 nm excitation laser.

Figure 7.2(a) and (b) show the EL confocal map as well as corresponding spectra from bright centres identified at the edges of the mesas under a current of 2.9 mA. The EL map indicates

the recombination zone with lower carrier concentration in the i-layer of the device. The bright circular luminescence observed around the pillar agrees with EL studies from ion implanted NV-centres in similar diamond samples[19]. The EL spectrum in Figure 7.2 (b) corresponds to bright spot circled on the map as shown in Figure 7.2(a). This spectrum shows a ZPL at 738 nm which corresponds to the ZPL of the SiV^- ensemble in diamond.

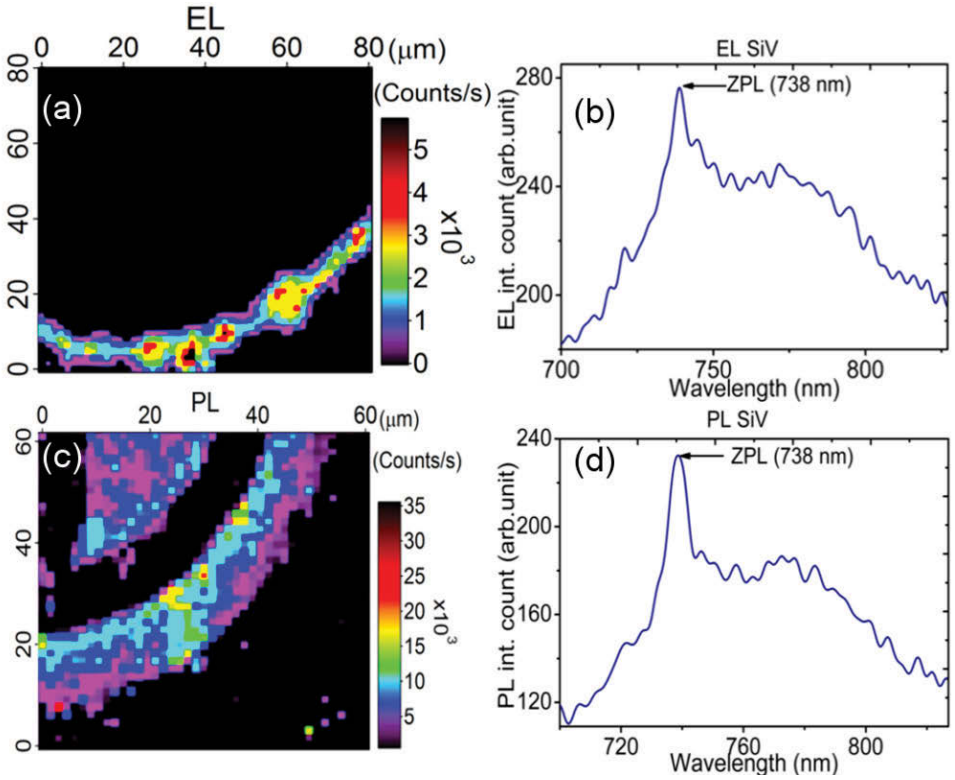

Figure 7.2: (a) Electroluminescence map of an 80 µm x 80 µm area showing luminescence from the edge of the pillar. (b) EL spectrum from the circled bright spot of the EL map. The EL spectrum is collected at a forward bias of 50V used to inject current of 2.9 mA into the device. (c) Photoluminescence map of a 60 µm x 60 µm area, exhibiting comparable emission from around the edge of the pillar (d) PL spectrum from the circled bright spot of the PL map. The excitation is performed using a 532 nm cw-laser at 867 µW.

Figures 7.2(c) and (d) show the confocal PL map and corresponding spectra of the devices under optical excitation using a 532-nm laser at 867 µW. Like in the case of the EL measurement, bright spots are observed at the edges of the mesa. The measured PL spectrum exhibits a similar peak at 738 nm. This is direct evidence that an ensemble of SiV^- color center

is excited both optically and electrically in a single crystal diamond. The broad signal in the range of 750–800 nm is attributed to the phonon sideband of the SiV. All the EL and PL measurements were recorded from the same device. All the devices showed similar characteristic behaviour in both EL and PL. The observation of the same centre with the same charge state both optically and electrically in diamond is important for practical device engineering and is an advantageous feature of the SiV^- defect. Indeed, while NV centres were excited electrically, only the NV^0 charge state is visible under electrical excitation while the NV^- defect can be triggered optically [19, 245, 247]. Second-order autocorrelation measurements were attempted from several scans to identify single photon emitting SiV centres both using PL and EL. However, we could not find isolated SiV centre under this ion-implantation conditions. Nevertheless, the proof-of-concept that SiV centre can be excited electrically is established.

7.3 Saturation and stability behaviours of SiV ensembles under excess carrier injection

Figure 7.3 shows the saturation measurement of SiV^- ensembles plotted as a function of applied current. The fitting equation is given by $r = r_{sat}\frac{I}{I_{sat}+I}$, where r is arbitrary EL count rate for injection current (I), r_{sat} is the maximum electrically driven luminescence count rate that can be attained in this device at saturation current of I_{sat}: the electrical equivalent formulation of the PL saturation behaviour discussed in Chapters 4-6. The results suggest that r_{sat} is ~6.8 kCounts/s. The emission intensity is not strong which is expected considering fluorescence of SiV centres prepared via ion implantation are dim [171, 177, 248].

Electrical stability of the SiV^- centre under forward bias is also studied, to ensure a constant emission of photons is generated. Figure 7.3 (b) shows that EL count rates as a function of time for fixed injection of 2.5 mA current. The emitters remain stable for the duration of the

measurement (minutes), with no blinking or bleaching being observed. The stable emission is useful for studying the SiV^- ensemble for longer periods under excess carrier injection.

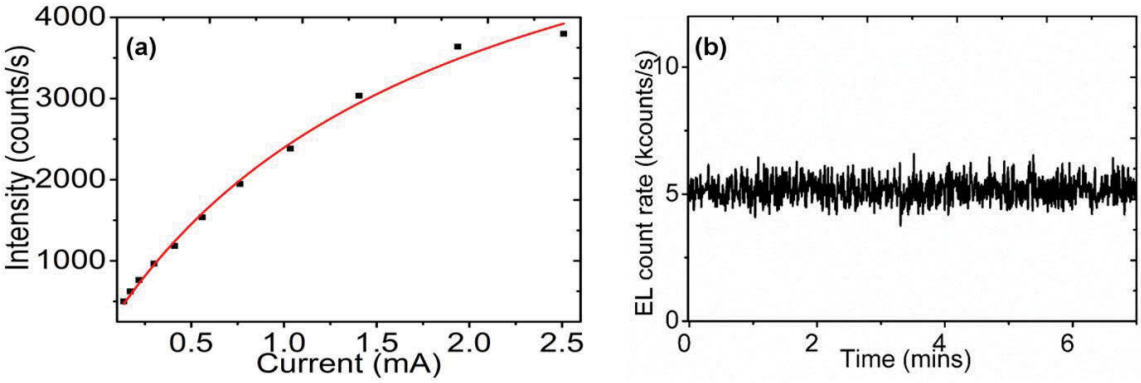

Figure 7.3: (a) Electrical driven luminescence saturation measurement of the stable SiV vacancy together with fitting curve indicated by the solid red line. (b) Shows stability measurement from the negative charge state of SiV centre when 2.5 mA of current is injected into the device. The colour centre showed stable emission for more than 6 min.

7.4 Charge switching between ensembles of SiV^- and SiV^0

We studied the behaviour of the SiV ensemble under forward and reverse biased PL measurements. These studies were fruitful to understand the switching dynamics of the NV defect in diamond[56, 244]. For the case of the NV centre, applying negative bias under constant green excitation resulted in switching the NV state from the negatively charged to the neutral state. Figure 7.4 shows intensity varying emission from SiV centres as a result of forward and reverse biasing under 532 nm excitation laser. The bias voltage is varied between 52 V and -100 V injecting a different amount of forward and reverse current to the sample. As expected, under forward bias PL, the intensity of the SiV^- ZPL decreases with a decreased bias voltage. Under an increased reversed bias, the SiV^- ZPL intensity further decreases—likely due to injection of holes into the defect. As shown, however, no clear evidence of SiV^0 emission at ~946 nm was observed under these conditions[249]. This can be explained by the relatively low quantum efficiency of this defect. Similar results are reported via photochromes of diamond under UV excitation [183] where intensity in SiV^- ensembles became dim

suggesting charge migration into the neutral charge state. Under annealing, the reverse is observed, where the intensity in SiV^0 ensemble decreased whereas SiV^- ensembles increased[184].

Finally, CL of SiV ensembles was measured from the same sample at different electron beam fluences as shown in Figure 7.4 (b). Two primary observation are deducted: First, we are indeed probing ensembles of SiV centres where upon decreasing the beam energy, the CL intensity falls as well. This indicates that the smaller interaction volume means fewer centres to be excited resulting in low CL intensity. In addition, CL spectra only showed signatures of SiV^- centres. This is consistent with charge state studies of NV, where under EL and CL measurement only the neutral charge state is observed while the negative charge state remained in the dark. As discussed in Chapter 2, this may be due to the prohibition of certain charge states to fluoresce under excess charge recombination.

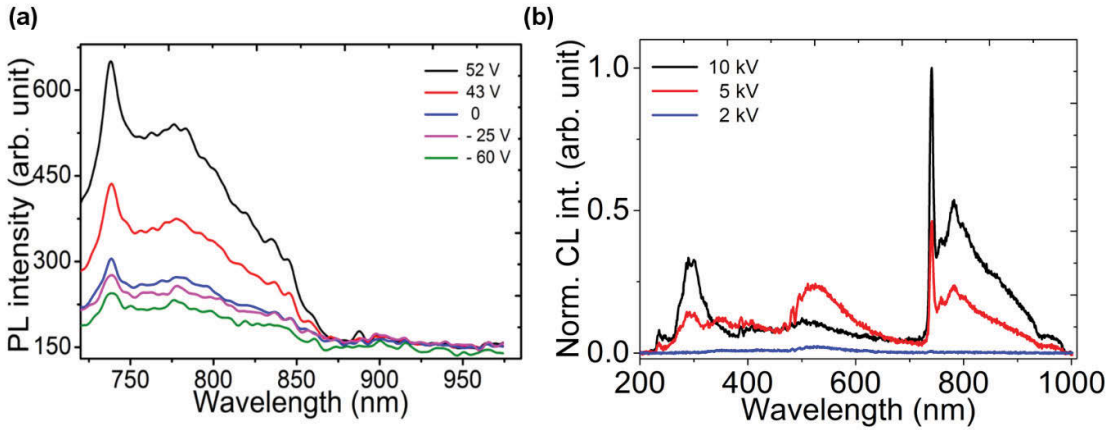

Figure 7.4: (a) Forward and reverse biased PL measurement show reduction in the intensity of the SiV^- ZPL. The bias voltage is varied between 52 V and -60 V. In forward bias, higher injection of carriers excites more centres resulting in higher luminescence intensity from SiV^- centre. As the reverse current increases, intensity from SiV^- decreases due to injection of holes into the centre. Charge switching to SiV^0, however, is not observed with emission around 946 nm. (b) CL spectra from SiV ensemble at different electron beam fluence.

7.5 Conclusion

To summarise, electrical excitation of ensembles of SiV^- centres in a single crystal diamond is demonstrated. The electrically driven emission is stable at room temperature and can be detected under current density injection of 7.9 A/cm^2. Forward and reverse biased PL measurement combined with EL measurements have provided insight into the excitation mechanisms of the SiV^- colour centres. However, the SiV^0 was not observed. Similarly, electrically driven single photon emission from single SiV centres was not also achieved. Further work is, therefore, required to understand the dynamics of this defect under electrical excitation. Also, investigation of ways to improve the creation efficiency of the SiV emitters using ion implantation is also required to achieve electrical excitation of a single SiV centre.

8 Summary and outlook

This work featured spectroscopic study of defect based single photon emission from GaN and diamond. As such, it is separated into two main parts: The first part reports on a new family of defect based SPE in GaN studied mainly by using PL spectroscopy. Various photophysical properties of the SPEs are investigated both at cryogenic and room temperatures elucidating major attributes as well as bottlenecks for applications. The second part of the thesis focuses on RT electroluminescence study of SiV ensembles in the diamond device. This previously unreported observation is also used to study charge state dynamics at the defect centre. In this chapter, we summarise relevant findings and results in the two main topics. Finally, the outlook is provided to motivate further work on the topic as well as point future directions for possible applications.

8.1 Defect-based single photon emitters in GaN

The primary finding in this work is the new, room temperature stable SPEs in GaN. These emitters are resolved abundantly in different GaN wafers regardless of the choice of substrate for growth or the electronic grades of the films. Structural analysis of the different wafers shows that all films are single crystalline, wurtzite GaN. The emitters are also readily resolved in excess from commercially obtained wafers without post-processing requirements showing the extent of robustness in these family of emitters. The ease of accessing the room temperature stable SPE in the commercially available material (GaN) makes them ideal for proof of concept studies.

In this work, the SPEs were resolved on 5 different pieces of GaN films cut from wafers with different structures and electronic properties including a PN and PIN diodes. Four of the wafers were grown on sapphire while the other is grown on SiC substrate. To confirm emission was indeed from the GaN layer, one of the samples was etched, stripping it off the

GaN film. Post-etching spectroscopy confirms that no SPE can be found from the underlying sapphire substrate. This is a direct proof that the emitters indeed are from the GaN film.

Properties of the SPEs in GaN were investigated using spectroscopic as well as second-order autocorrelation measurements. Time-dependent intensity behaviour of the emission is also studied. Both cryogenic and room temperature spectral characteristics from several of the SPEs on the 5 GaN films indicate that these emitters have narrow ZPL with weak phonon sidebands. The average FWHM is around 5 nm at RT and 0.3 nm at 4 K. As indicated by the average linewidth values at 4 K, however, none of the emitters showed spectrally limited linewidth. The result hints the presence of an underlying broadening mechanism. This property hampers the applicability of the new family of SPEs for quantum technologies. Possible workarounds for this problem are suggested as an outlook.

Furthermore, the distribution of ZPL peak energies (wavelengths) from several SPEs in GaN shows a wide range - extending from the visible to NIR. This is observed within a sample and across all the samples. Similar behaviour was observed at cryogenic temperatures where the mean ZPL peak value in energy showed a slight blue shift. Although multiple emitters with the same peak wavelengths can be found on the sample, locating them before the second-order correlation measurement is not currently possible. Thus, excitation of any two centres has a high probability of resulting in two distinct peak wavelengths. This further hinders applicability, for example, in quantum computation where indistinguishable photon sources are required.

Quantum nature of the SPEs in GaN are studied by measuring second-order correlation functions from isolated bright spots in a confocal scan at cryogenic and room temperature. Several emitters across the 5 samples have shown strong antibunching giving direct evidence of single photon emission. The SPEs studied are efficiently excited using off-resonant (532 nm), low excitation powers (50 μW). The strength of the antibunching varies from emitter to emitter due to strong background contribution from the GaN matrix. Interestingly, all emitters

resolved showed antibunching. That is, we could not find a bright spot with distinct spectra that didn't show antibunching. This is contrary to other atomic SPEs where ensemble in the centres would result in bright spectra and show no antibunching due to the multiple photon emission. This indicates that the origin of the quantum light source in GaN can only allow electronic transition that results in at most a few photon emission. While the ability to excite bright, SPEs with low laser power is attractive, the strong background contribution dampens the single photon purity.

Another peculiarity in the spectroscopy of SPEs in GaN was revealed using temperature-resolved PL. The ZPL peak energy shift was recorded at different sample temperatures showing a non-monotonic change that is best described as "S-shaped" (inverted "S-shaped"). Similar studies in other defect based SPEs such NV and SiV in diamond showed monotonic dependence on the temperature. In fact, S-shaped temperature dependence in III-nitrides and other semiconductors is associated with stacking fault related luminescence. It is, therefore, believed that the electronic transition resulting in single photon emission from GaN films involves SFs. The presence of SFs in at least one of the GaN samples is experimentally confirmed using low-temperature CL spectroscopy, where a red shift in band edge luminescence is observed indicating the presence of a cubic inclusion.

Numerical model Hamiltonian calculations, parametrised with GaN material properties were performed to further elucidate the involvement of cubic inclusions (SFs) in the electronic transitions of the SPEs. For a choice of cubic inclusion width in WZ GaN matrix, the ZPL of an optically active defect can be fixed. In our case, it was 680 nm which is consistent with the average ZPL peak observed experimentally. As the defect moves relative to the centre of the cubic inclusion, the ZPL peak energies also change. This is also consistent with the experimental observation where broad span in peak energies are observed. Therefore, the origin of the SPEs in GaN is tentatively assigned to exciton transition involving optically active point defects located within variable distances from the centre of localised cubic inclusion in the vicinity.

Following the first report of SPEs in GaN, a detailed study of the photophysical behaviour is conducted. First, RT fluorescence stability of the SPEs under different excitation powers was studied. Majority of the SPEs across the 5 samples showed absolute photostability while a few showed blinking. None of the emitters in the samples studied showed photobleaching. The average photon count at different power was also used to investigate the brightness of the emitters in the different samples. The average maximum intensity of ~(427±215) kCounts/s is calculated making the SPE in GaN among the brightest bulk emitters recorded. The saturation power showed considerable variation between different emitters with an average value of ~(1270±735) μW. The stability and brightness of the SPEs are attractive for room temperature applications.

Power dependent second-order autocorrelation measurements were also conducted to study the bunching behaviours of the SPEs. The results reveal that transition kinetics of the stable, emitters in GaN involves at least one shelving state as depicted by increased bunching with increasing power. The power dependent bunching parameters where successfully described by using three-level kinetic transition model. The kinetics is described both by considering linear, and sublinear shelving (metastable) states power dependence, where the later yield better results. Based on the kinetics analysis, excited state and metastable lifetimes were also calculated allowing insight into intra-energy level dynamics.

Another essential photophysical characteristics for SPEs is sensitivity to light direction. Polarisation-resolved spectroscopy measurement carried out on multiple SPEs in GaN shows linear polarisation with a very high degree of emission polarisation visibility (~ (91±11) %). The absorption polarisation, on the other hand, showed little visibility of ~ (57±26) % with substantial variation between emitters. This is consistent with the observed variation in the saturation power among the different emitters. The relative orientations of absorption and emission polarisation direction were analyzed showing a significant misalignment. This is believed to be due to the off-resonant excitation where absorption to a much higher state than

the state from which radiative decay occurs is allowed. Absorption polarisation orientation relative to crystal axis is also determined where most of the SPEs seem to gravitate towards $[1\bar{1}00]$ lattice plane direction of the hexagonal GaN unit cell. The high degree of emission polarisation is attractive for quantum cryptographic applications.

To understand the cause of spectral broadening, time-resolved PL was studied on three, stable SPEs. The results yield that the transform limited linewidths of 0.4, 0.2 and 0.3 μeV. The values are three-orders of magnitude narrower than determined with the grating, resolution of the spectrometer. This further consolidates the presence of strong broadening mechanism. One such mechanism is spectral diffusion, which we checked for the SPEs in GaN using time-resolved spectroscopy. However, emitters showed little or no spectral diffusion in the ms timescale. Thus, the broadening is strongly suspected to be due to ultrafast (μs to ns) spectral diffusion. This is determinant making these family of SPEs hard to use for quantum technology application at this stage.

Finally, some of the emitters in GaN showed unusual photo-induced blinking behaviours. That is, the photon statistics from these emitters vary from single state photon statistics to multiphoton statistics with increasing power. This abnormal behaviour in defect based SPEs was studied in detail in this work. The transition kinetics from one emitter shows distinct behaviours before and after blinking with a substantial difference in the non-radiative decay rate behaviours. This was coupled with reduced brightness in emission after blinking. By combining power dependent fluorescence projectile and second-order autocorrelation measurements, characteristic decay rates, as well as blinking times, are determined as a function of excitation power. This vital insight indicates that the transition kinetics of some of the emitters can be permanently altered using excitation power above a certain threshold. This may be due to photothermal activation of dangling bonds which then act as a shelving state.

The first part of the thesis focuses on the discovery and comprehensive characteristic of emitters in GaN film. Now, we move to summarising the second part of the thesis which is to characterise an already known defect in diamond using electroluminescence.

8.2 Electroluminescence from Silicon-Vacancy in diamond

This part of the work focused on incorporating SIV centres in diamond and demonstrate the first electrically excited fluorescence from the centre. The starting device was as-prepared PIN single crystalline diamond. The SiV centres were incorporated by ion implanting Si atoms into the intrinsic layer of the device based on simulation. The *IV*-characteristics of the device was measured after ion implantation yielding a current density of around 7.9 A/cm^2 at the threshold voltage of ~ 43 V. This corresponds to rectification ratio of around 10^4 which is small compared to *IV*-characteristics of a similar device used in a different study (~10^9). This is believed to be due to the quality of contacts used which in our case was worsened by ion implantation.

After annealing to mitigate implantation damage, the device was scanned first under laser excitation using the confocal set-up. After identifying the defect luminescence as SiV^- by taking spectra, the laser is then blocked. At this stage, the same device is scanned under excess carrier injection using external voltage source. Going to the same bright spot where the PL was taken, we measure the EL. This way direct evidence of RT electroluminescence from SiV^- ensembles were obtained. Nevertheless, we were unable to demonstrate electroluminescence from an isolated SiV^- centre, which is a well-known single photon emitter. This could be due to a few reasons. First, the ion implantation recipe may not have been the right one to create isolated defects, where implanted species form agglomerates. It may also be that we did not trigger our excess carrier injection as a result exciting several SiV centres within a wide area. Finally, our detection efficiency of the count rate from a single, ion implanted SiV centre is expected to be very low.

The stability and saturation behaviours of the SiV ensemble were further investigated under excess carrier injection. The ensemble remained stable showing no sign of blinking or bleaching under current injection of 2.5 mA. The maximum brightness measured around the same current injection is 6.8 kCounts/s. This is expected considering that ion implanted SiV centres are dim.

Finally, charge state switching between the neutral and negatively charged states of the SiV ensemble is investigated using short-circuited PL. That is, while the SiV ensemble is under the green laser excitation, the device was reverse biased, enabling withdrawal of carriers from the ensemble. An increase in the reverse bias resulted in reduced PL intensity showing excess carriers are being taken away from the centre. This result is consistent with earlier charge state switching studies using annealing and UV excitation centres. However, the neutral charge state remained in the dark state in our measurement.

In summary, we reported the first defect related, RT stable SPE in GaN. We further investigated the spectroscopic behaviours of the SPE both at cryogenic and room temperature. This was followed by the photophysical studies of the emitters where both attributes, as well as bottlenecks, are identified by evaluating the emitters for quantum technology applications. Population dynamics analysis is used to understand the transition kinetics in the emitter as well as investigate unique photothermal induced blinking behaviours. The emitters show great potential for quantum applications pending more work to improve the spectral properties. The second part of the thesis reported the first electroluminescence from SiV ensembles. Next, we present future directions that we believe will take the present work to the next step based on our cumulative observation during the study.

8.3 Outlook

While the new emitters in GaN show promising potentials for different cutting-edge technologies, major bottlenecks that need to be addressed are identified. First, it is already stated that these emitters span a wide wavelength range and are spectrally broadened where the cause is assigned to fast spectral diffusion. If the fast-spectral diffusion is indeed caused by internal local electric field, it might be possible to twin it by applying external electric field as well as mechanical strain [250-252]. The second approach is cavity coupling of emission to improve the linewidth broadening [253, 254]. For appropriate cavity design, however, knowledge of luminescence peak and absorption polarisation are minimal requirements, which currently are both hard to determine before measurement. Thus, fundamental work to determine the exact nature of the SPE, as well as its absorption mechanism, is vital. Excitation photoluminescence is also believed to reveal more properties of the emitters, especially on the absorption polarisation mechanisms.

The other problem, which might also have a contribution on the previous ones, is background fluorescence from the GaN matrix. This is a common problem in other bulk wide bandgap semiconductors as well due to the large transparency window where the usual approach to alleviate it is to fabricate nanostructure that contains the emitters [211, 255].

One interesting direction to pursue is optically detected magnetic resonance (ODMR) study of the emitters to evaluate whether the transition in these defects can be manipulated for spin qubit applications [256, 257]. More importantly, it will be interesting to see if emitters in GaN can serve as a capable single photon emitting diodes (SPEDs) by attempting electrical excitation. This demonstration will have made GaN as vital material for quantum LEDs (QLEDs) as it is for classical LED[136].

Another significant result in this work is laser power induced blinking in some of the GaN emitters. While exciting insight is gained in the possible mechanism causing the blinking via

power dependent measurements, many more questions remain unanswered in this regard. For example, if the photothermal process is indeed the cause of blinking at above threshold excitation powers, then heating the sample even at a higher temperature will exasperate the process. Even more deterministic is to identify stable emitters and irradiate them with an electron beam to see if the photo-dynamics changes. Other factors known to affect blinking in systems like QDs and single molecules are surface states, size of the systems or the matrix in which the QD or single molecules reside[102, 113]. The absence of these factors in solid-state emitters such as the ones studied here may be manifested in the distinct probability distribution of blinking times. For instance, while probability distribution of "on"- and "off"-times in systems like QDs usually follows a power-law distribution, reports of blinking from NV[99] in diamond, $C_{Si}V_C$ in SiC[24] and now defects in GaN show exponential probability distribution with characteristic times. Therefore, comparative study of blinking from various single photon emitters may be the way forward in finding a universal mechanism of photon intermittency.

Finally, while electrical excitation from SiV ensembles in diamond is demonstrated, single photon electroluminescence from the centre is still lacking. Thus, a primary direction here would be to trigger SiV centres in diamond to generate electrically driven single photons[19]. Upon achieving this primary goal, electrically driven SPEs from arrays of the diamond device can be pursued.

As hinted in Chapters 2&7, the other exciting aspect of the study of excess carrier recombination at single photon emitting defects is the relation between CL and EL. Both techniques rely on carrier trapping at the defect site and seem to show consistent spectral results regardless of the way the excess carrier is generated. For example, charge states whose spectra are readily resolved when using CL are also revealed when using EL. Conversely as well, charge states that don't show fluorescence under CL also don't show it under EL. This is the case both for NV and SiV defects in diamond in our observation. Although theoretical report expresses this as expected[93], there are few reports that contradict such

conclusion[19]. Thus, comparative study of the charge state switching using EL and CL in single photon emitters is required for clarity.

Reference

1. J. F. Clauser, Physical Review D **9**, 853 (1974).
2. R. Kidd, J. Ardini, and A. Anton, American Journal of Physics **57**, 27-35 (1989).
3. H. J. Kimble, M. Dagenais, and L. Mandel, Physical Review Letters **39**, 691 (1977).
4. D. C. Burnham, and D. L. Weinberg, Physical Review Letters **25**, 84 (1970).
5. R. Loudon, *The quantum theory of light* (OUP Oxford, 2000).
6. C. Cohen-Tannoudji, J. Dupont-Roc, and G. Grynberg, *Photons and atoms: Introduction to quantum electrodynamics* (Wiley Online Library, 1989).
7. A. Arons, and M. Peppard, American Journal of Physics **33**, 367-374 (1965).
8. M. Eisaman, J. Fan, A. Migdall, and S. V. Polyakov, Review of scientific instruments **82**, 071101 (2011).
9. T. Schröder, S. L. Mouradian, J. Zheng, M. E. Trusheim, M. Walsh, E. H. Chen, L. Li, I. Bayn, and D. Englund, JOSA B **33**, B65-B83 (2016).
10. I. Aharonovich, and E. Neu, Advanced Optical Materials **2**, 911-928 (2014).
11. E. Knill, nature **463**, 441-443 (2010).
12. K. Kieling, T. Rudolph, and J. Eisert, Physical Review Letters **99**, 130501 (2007).
13. E. Klarreich, Nature **418**, 270-272 (2002).
14. J. W. Silverstone, R. Santagati, D. Bonneau, M. J. Strain, M. Sorel, J. L. O'Brien, and M. G. Thompson, Nature communications **6** (2015).
15. J. L. O'brien, A. Furusawa, and J. Vučković, Nature Photonics **3**, 687-695 (2009).
16. I. Aharonovich, S. Castelletto, D. Simpson, C. Su, A. Greentree, and S. Prawer, Reports on progress in Physics **74**, 076501 (2011).
17. I. Aharonovich, D. Englund, and M. Toth, Nature Photonics **10**, 631-641 (2016).
18. L. Childress, and R. Hanson, MRS bulletin **38**, 134-138 (2013).
19. N. Mizuochi, T. Makino, H. Kato, D. Takeuchi, M. Ogura, H. Okushi, M. Nothaft, P. Neumann, A. Gali, and F. Jelezko, Nature photonics **6**, 299-303 (2012).
20. H. Bernien, L. Childress, L. Robledo, M. Markham, D. Twitchen, and R. Hanson, Physical Review Letters **108**, 043604 (2012).
21. E. Rittweger, K. Y. Han, S. E. Irvine, C. Eggeling, and S. W. Hell, Nature Photonics **3**, 144-147 (2009).
22. P. Maurer, J. Maze, P. Stanwix, L. Jiang, A. V. Gorshkov, A. A. Zibrov, B. Harke, J. Hodges, A. S. Zibrov, and A. Yacoby, Nature Physics **6**, 912 (2010).
23. G. Balasubramanian, I. Chan, R. Kolesov, M. Al-Hmoud, J. Tisler, C. Shin, C. Kim, A. Wojcik, P. R. Hemmer, and A. Krueger, Nature **455**, 648 (2008).
24. S. Castelletto, B. Johnson, V. Ivády, N. Stavrias, T. Umeda, A. Gali, and T. Ohshima, Nature materials **13**, 151-156 (2014).
25. O. Neitzke, A. Morfa, J. Wolters, A. W. Schell, G. Kewes, and O. Benson, Nano Lett **15**, 3024-3029 (2015).
26. M. R. Krames, O. B. Shchekin, R. Mueller-Mach, G. O. Mueller, L. Zhou, G. Harbers, and M. G. Craford, Journal of display technology **3**, 160-175 (2007).

27. N. Ikeda, Y. Niiyama, H. Kambayashi, Y. Sato, T. Nomura, S. Kato, and S. Yoshida, Proceedings of the IEEE **98**, 1151-1161 (2010).
28. K. Matocha, T. P. Chow, and R. J. Gutmann, IEEE Transactions on Electron Devices **52**, 6-10 (2005).
29. S. Nakamura, M. Senoh, S.-i. Nagahama, N. Iwasa, T. Yamada, T. Matsushita, H. Kiyoku, Y. Sugimoto, T. Kozaki, and H. Umemoto, Japanese journal of applied physics **37**, L309 (1998).
30. V. Kirilyuk, *Optical characterization of gallium nitride* ([Sl: sn], 2002).
31. W. Angerer, N. Yang, A. Yodh, M. Khan, and C. Sun, Physical Review B **59**, 2932 (1999).
32. S. A. Jewett, M. S. Makowski, B. Andrews, M. J. Manfra, and A. Ivanisevic, Acta biomaterialia **8**, 728-733 (2012).
33. S. N. Mohammad, A. A. Salvador, and H. Morkoc, Proceedings of the IEEE **83**, 1306-1355 (1995).
34. S. Strite, and H. Morkoç, Journal of Vacuum Science & Technology B **10**, 1237-1266 (1992).
35. C. Xiong, W. Pernice, K. K. Ryu, C. Schuck, K. Y. Fong, T. Palacios, and H. X. Tang, Opt. Express **19**, 10462-10470 (2011).
36. N. V. Trivino, U. Dharanipathy, J.-F. Carlin, Z. Diao, R. Houdre, and N. Grandjean, Applied Physics Letters **102**, 081120 (2013).
37. H. Matsubara, S. Yoshimoto, H. Saito, Y. Jianglin, Y. Tanaka, and S. Noda, Science **319**, 445-447 (2008).
38. T. Tawara, H. Gotoh, T. Akasaka, N. Kobayashi, and T. Saitoh, Physical review letters **92**, 256402 (2004).
39. D. Simeonov, E. Feltin, A. Altoukhov, A. Castiglia, J.-F. Carlin, R. Butté, and N. Grandjean, Applied Physics Letters **92**, 171102 (2008).
40. I. Aharonovich, A. Woolf, K. J. Russell, T. Zhu, N. Niu, M. J. Kappers, R. A. Oliver, and E. L. Hu, Applied Physics Letters **103**, 021112 (2013).
41. K. McGroddy, A. David, E. Matioli, M. Iza, S. Nakamura, S. DenBaars, J. Speck, C. Weisbuch, and E. Hu, Applied physics letters **93**, 103502 (2008).
42. T. Oder, J. Shakya, J. Lin, and H. Jiang, Applied Physics Letters **83**, 1231-1233 (2003).
43. M. Arita, S. Kako, S. Iwamoto, and Y. Arakawa, Applied Physics Express **5**, 126502 (2012).
44. H.-S. Lee, K. Ryu, M. Sun, and T. Palacios, IEEE Electron Device Letters **33**, 200-202 (2012).
45. J. Chung, J. Lee, E. Piner, and T. Palacios, "Seamless on-wafer integration of gan hemts and si (100) mosfets," in *Device Research Conference, 2009. DRC 2009*(IEEE2009), pp. 155-156.
46. F. Bernardini, V. Fiorentini, and D. Vanderbilt, Physical Review B **56**, R10024 (1997).
47. J. Weyher, A. Zauner, P. Brown, F. Karouta, A. Barcz, M. Wojdak, and S. Porowski, PHYSICA STATUS SOLIDI A APPLIED RESEARCH **176**, 573-578 (1999).
48. http://www-opto.e-technik.uni-ulm.de/lehre/cs/III_V_map_a.jpg.
49. H. Manasevit, F. Erdmann, and W. Simpson, Journal of the Electrochemical Society **118**, 1864-1868 (1971).
50. H. A. Isamu Akasaki, Masahiro Kito and Kazumasa Hiramatsu, Journal of Luminescence **48-49**, 666-670 (1991).
51. M. A. Reshchikov, and H. Morkoç, Journal of Applied Physics **97**, 061301 (2005).

52. J. Lähnemann, U. Jahn, O. Brandt, T. Flissikowski, P. Dogan, and H. T. Grahn, Journal of Physics D: Applied Physics **47**, 423001 (2014).
53. B. Demory, T. A. Hill, C.-H. Teng, L. Zhang, H. Deng, and P.-C. Ku, ACS Photonics **2**, 1065-1070 (2015).
54. M. J. Holmes, K. Choi, S. Kako, M. Arita, and Y. Arakawa, Nano Lett **14**, 982-986 (2014).
55. S. Deshpande, T. Frost, A. Hazari, and P. Bhattacharya, Applied Physics Letters **105**, 141109 (2014).
56. H. Kato, M. Wolfer, C. Schreyvogel, M. Kunzer, W. Müller-Sebert, H. Obloh, S. Yamasaki, and C. Nebel, Applied Physics Letters **102**, 151101 (2013).
57. J. Thorn, M. Neel, V. Donato, G. Bergreen, R. E. Davies, and M. Beck, American journal of physics **72**, 1210-1219 (2004).
58. P. Grangier, G. Roger, and A. Aspect, EPL (Europhysics Letters) **1**, 173 (1986).
59. R. H. Brown, and R. Q. Twiss, Nature **177**, 27-29 (1956).
60. R. Twiss, A. Little, and R. H. Brown, Nature **180**, 324-326 (1957).
61. G. Greenstein, and A. Zajonc, *The quantum challenge: Modern research on the foundations of quantum mechanics* (Jones & Bartlett Learning, 1997).
62. L. Mandel, and E. Wolf, *Optical coherence and quantum optics* (Cambridge university press, 1995).
63. M. O. Scully, and M. S. Zubairy, "Quantum optics," (AAPT, 1999).
64. https://www.physik.hu-berlin.de/de/nano/lehre.
65. F. Arecchi, E. Gatti, and A. Sona, Physics Letters **20**, 27-29 (1966).
66. P. Kelley, and W. Kleiner, Physical Review **136**, A316 (1964).
67. R. J. Glauber, Quantum Theory of Optical Coherence: Selected Papers and Lectures, 23-182 (1965).
68. S. Felekyan, R. Kühnemuth, V. Kudryavtsev, C. Sandhagen, W. Becker, and C. Seidel, Review of scientific instruments **76**, 083104 (2005).
69. S. Kitson, P. Jonsson, J. Rarity, and P. Tapster, Physical Review A **58**, 620 (1998).
70. L. J. Bissell, *Experimental realization of efficient, room temperature single-photon sources with definite circular and linear polarizations* (University of Rochester, 2011).
71. T. Basché, W. Moerner, M. Orrit, and H. Talon, Physical review letters **69**, 1516 (1992).
72. C. Wang, "A solid-state single photon source based on color centers in diamond," (lmu, 2007).
73. L. Yao-Yi, C. Mu-Tian, Z. Hui-Jun, L. Shao-Ding, and W. Qu-Quan, Chinese Physics Letters **22**, 2960 (2005).
74. C. Brunel, B. Lounis, P. Tamarat, and M. Orrit, Physical Review Letters **83**, 2722 (1999).
75. S. Kako, C. Santori, K. Hoshino, S. Götzinger, Y. Yamamoto, and Y. Arakawa, Nature materials **5**, 887 (2006).
76. P. Michler, A. Kiraz, C. Becher, W. Schoenfeld, P. Petroff, L. Zhang, E. Hu, and A. Imamoglu, science **290**, 2282-2285 (2000).
77. C. Kurtsiefer, S. Mayer, P. Zarda, and H. Weinfurter, Physical review letters **85**, 290 (2000).
78. E. Neu, M. Agio, and C. Becher, Opt. Express **20**, 19956-19971 (2012).
79. A. M. Berhane, K.-Y. Jeong, Z. Bodrog, S. Fiedler, T. Schröder, N. V. Triviño, T. Palacios, A. Gali, M. Toth, D. Englund, and I. Aharonovich, Advanced Materials, 1605092-n/a (2017).

80. I. Aharonovich, S. Castelletto, D. Simpson, A. Greentree, and S. Prawer, Physical Review A **81**, 043813 (2010).
81. E. Wu, V. Jacques, H. Zeng, P. Grangier, F. Treussart, and J.-F. Roch, Opt. Express **14**, 1296-1303 (2006).
82. R. Brouri, A. Beveratos, J.-P. Poizat, and P. Grangier, Optics letters **25**, 1294-1296 (2000).
83. L. Fleury, J.-M. Segura, G. Zumofen, B. Hecht, and U. Wild, Physical review letters **84**, 1148 (2000).
84. Z. Yuan, B. E. Kardynal, R. M. Stevenson, A. J. Shields, C. J. Lobo, K. Cooper, N. S. Beattie, D. A. Ritchie, and M. Pepper, science **295**, 102-105 (2002).
85. S. Deshpande, J. Heo, A. Das, and P. Bhattacharya, Nature communications **4**, 1675 (2013).
86. A. M. Berhane, S. Choi, H. Kato, T. Makino, N. Mizuochi, S. Yamasaki, and I. Aharonovich, Applied Physics Letters **106**, 171102 (2015).
87. S. Choi, A. M. Berhane, A. Gentle, C. Ton-That, M. R. Phillips, and I. Aharonovich, ACS applied materials & interfaces **7**, 5619-5623 (2015).
88. S. P. Murarka, and M. C. Peckerar, Academic Press, Inc, 1250 Sixth Avenue, San Diego, California 92101, USA, 1989. (1989).
89. S. M. Sze, and K. K. Ng, *Physics of semiconductor devices* (John wiley & sons, 2006).
90. J. I. Pankove, *Optical processes in semiconductors* (Courier Corporation, 2012).
91. B. Tuck, and C. Christopoulos, *Physical electronics* (Arnold London, 1986).
92. A. Lohrmann, N. Iwamoto, Z. Bodrog, S. Castelletto, T. Ohshima, T. J. Karle, A. Gali, S. Prawer, J. C. McCallum, and B. C. Johnson, Nat Commun **6**, 7783 (2015).
93. D. Y. Fedyanin, and M. Agio, New Journal of Physics **18**, 073012 (2016).
94. A. J. Shields, Nature photonics **1**, 215-223 (2007).
95. W. M. Jubadi, and S. N. M. Noor, "Simulations of variable i-layer thickness effects on silicon pin diode iv characteristics," in *Industrial Electronics & Applications (ISIEA), 2010 IEEE Symposium on*(IEEE2010), pp. 428-432.
96. B. Doherty, MicroNote Series **701**, 1-2 (2006).
97. F. J. Heremans, C. G. Yale, and D. D. Awschalom, Proceedings of the IEEE **104**, 2009-2023 (2016).
98. M. Yu, and A. Van Orden, Physical review letters **97**, 237402 (2006).
99. C. Bradac, T. Gaebel, N. Naidoo, M. J. Sellars, J. Twamley, L. J. Brown, A. S. Barnard, T. Plakhotnik, A. V. Zvyagin, and J. R. Rabeau, Nat Nanotechnol **5**, 345-349 (2010).
100. A. M. Berhane, C. Bradac, and I. Aharonovich, Physical Review B **96**, 041203 (2017).
101. M. Kuno, D. P. Fromm, H. F. Hamann, A. Gallagher, and D. J. Nesbitt, The journal of chemical physics **112**, 3117-3120 (2000).
102. P. Frantsuzov, M. Kuno, B. Janko, and R. A. Marcus, Nature Physics **4**, 519-522 (2008).
103. M. Kuno, D. Fromm, H. Hamann, A. Gallagher, and D. J. Nesbitt, The Journal of chemical physics **115**, 1028-1040 (2001).
104. T. Basché, S. Kummer, and C. Bräuchle, Nature **373**, 132-134 (1995).
105. A. L. Efros, and M. Rosen, Physical Review Letters **78**, 1110 (1997).
106. K. T. Shimizu, R. G. Neuhauser, C. A. Leatherdale, S. A. Empedocles, W. Woo, and M. G. Bawendi, Physical Review B **63**, 205316 (2001).
107. M. Nirmal, B. O. Dabbousi, M. G. Bawendi, and J. Macklin, Nature **383**, 802 (1996).

108. G. Margolin, V. Protasenko, M. Kuno, and E. Barkai, arXiv preprint cond-mat/0506512 (2005).
109. P. A. Frantsuzov, and R. A. Marcus, Physical Review B **72**, 155321 (2005).
110. M. Yu, Colorado State University (2008).
111. G. Messin, J.-P. Hermier, E. Giacobino, P. Desbiolles, and M. Dahan, Optics Letters **26**, 1891-1893 (2001).
112. T. Gensch, M. Böhmer, and P. F. Aramendía, The Journal of Physical Chemistry A **109**, 6652-6658 (2005).
113. A. L. Efros, and D. J. Nesbitt, Nat Nanotechnol **11**, 661-671 (2016).
114. R. Neuhauser, K. Shimizu, W. Woo, S. Empedocles, and M. Bawendi, Physical Review Letters **85**, 3301 (2000).
115. V. Türck, S. Rodt, O. Stier, R. Heitz, R. Engelhardt, U. Pohl, D. Bimberg, and R. Steingrüber, Physical Review B **61**, 9944 (2000).
116. S. A. Empedocles, and M. G. Bawendi, Science **278**, 2114-2117 (1997).
117. V. Türck, S. Rodt, R. Heitz, O. Stier, M. Straßburg, U. Pohl, and D. Bimberg, Physica E: Low-dimensional Systems and Nanostructures **13**, 269-272 (2002).
118. J. Müller, J. M. Lupton, A. L. Rogach, J. Feldmann, D. V. Talapin, and H. Weller, Physical Review B **72**, 205339 (2005).
119. P. Michler, A. Imamoglu, M. Mason, and P. Carlson, Nature **406**, 968 (2000).
120. S. Buckley, K. Rivoire, and J. Vučković, Reports on Progress in Physics **75**, 126503 (2012).
121. S. Deshpande, J. Heo, A. Das, and P. Bhattacharya, Nat Commun **4**, 1675 (2013).
122. F. Pisanello, G. Leménager, L. Martiradonna, L. Carbone, S. Vezzoli, P. Desfonds, P. D. Cozzoli, J. P. Hermier, E. Giacobino, and R. Cingolani, Advanced Materials **25**, 1974-1980 (2013).
123. B. Lounis, and W. E. Moerner, Nature **407**, 491 (2000).
124. M. Keller, B. Lange, K. Hayasaka, W. Lange, and H. Walther, Nature **431**, 1075 (2004).
125. P. Maunz, D. Moehring, M. Madsen, R. Kohn Jr, K. Younge, and C. Monroe, arXiv preprint quant-ph/0608047 (2006).
126. J. Bourgoin, *Point defects in semiconductors ii: Experimental aspects* (Springer Science & Business Media, 2012).
127. http://www.tf.uni-kiel.de/matwis/amat/def_en/.
128. J. Walker, Reports on Progress in Physics **42**, 1605 (1979).
129. K.-M. Fu, C. Santori, P. E. Barclay, L. J. Rogers, N. B. Manson, and R. G. Beausoleil, "Observation of the dynamic jahn-teller effect in the excited states of nitrogen-vacancy centers in diamond," in *OPTO*(International Society for Optics and Photonics2010), pp. 761108-761108-761108.
130. G. Davies, Reports on Progress in Physics **44**, 787 (1981).
131. J. T. Fourkas, Optics letters **26**, 211-213 (2001).
132. N. R. Jungwirth, H.-S. Chang, M. Jiang, and G. D. Fuchs, ACS nano **10**, 1210-1215 (2015).
133. N. R. Jungwirth, and G. D. Fuchs, arXiv preprint arXiv:1704.05536 (2017).
134. X. Wang, M. Zhao, Z. Wang, X. He, Y. Xi, and S. Yan, Applied Physics Letters **100**, 192401 (2012).

135. T. Muller, C. Hepp, B. Pingault, E. Neu, S. Gsell, M. Schreck, H. Sternschulte, D. Steinmüller-Nethl, C. Becher, and M. Atature, arXiv preprint arXiv:1312.2997 (2013).
136. I. Akasaki, H. Amano, M. Kito, and K. Hiramatsu, Journal of luminescence **48**, 666-670 (1991).
137. N. Akopian, G. Patriarche, L. Liu, J.-C. Harmand, and V. Zwiller, Nano letters **10**, 1198-1201 (2010).
138. P. Bogusl, E. Briggs, and J. Bernholc, Physical Review B **51**, 17255 (1995).
139. G. Feng, J. Suda, and T. Kimoto, Applied Physics Letters **92**, 221906 (2008).
140. A. F. Wright, Journal of Applied Physics **82**, 5259 (1997).
141. S. Izumi, H. Tsuchida, I. Kamata, and T. Tawara, Applied Physics Letters **86**, 202108 (2005).
142. D. Zhuang, and J. Edgar, Materials Science and Engineering: R: Reports **48**, 1-46 (2005).
143. F. Semendy, and U. Lee, "Observation and study of dislocation etch pits in molecular beam epitaxy grown gallium nitride with the use of phosphoric acid and molten potassium hydroxide," (ARMY RESEARCH LAB ADELPHI MD, 2007).
144. M. Suffczyński, R. Stępniewski, and J. Baranowski, Acta Physica Polonica A **92**, 993-996 (1997).
145. Y. G. S. Y. T. Rebane, M. Albrecht, phys. stat. sol. **164**, 141 (1997).
146. J. A. Majewski, and P. Vogl, MRS Internet Journal of Nitride Semiconductor Research **3**, e21 (1998).
147. T. C. M. Z. Z. Bandic, Z. Ikonic, Physical Review B **56**, 7 (1997).
148. R. Liu, A. Bell, F. A. Ponce, C. Q. Chen, J. W. Yang, and M. A. Khan, Applied Physics Letters **86**, 021908 (2005).
149. G. Schmidt, P. Veit, M. Wieneke, F. Bertram, A. Dadgar, A. Krost, and J. Christen, physica status solidi (b) **253**, 73-77 (2016).
150. J. A. Majewski, and P. Vogl, Materials Research Society Internet Journal of Nitride Semiconductor Research **3** (1998).
151. P. Paskov, R. Schifano, B. Monemar, T. Paskova, S. Figge, and D. Hommel, Journal of Applied Physics **98**, 093519 (2005).
152. T. Paskova, R. Kroeger, P. Paskov, S. Figge, D. Hommel, B. Monemar, B. Haskell, P. Fini, J. Speck, and S. Nakamura, "Microscopic emission properties of nonpolar a-plane gan grown by hvpe," in *Proc. SPIE*(2006), p. 612106.
153. K. Korona, A. Reszka, M. Sobanska, P. Perkowska, A. Wysmołek, K. Klosek, and Z. Zytkiewicz, Journal of Luminescence **155**, 293-297 (2014).
154. P. Corfdir, P. Lefebvre, J. Levrat, A. Dussaigne, J.-D. Ganière, D. Martin, J. Ristić, T. Zhu, N. Grandjean, and B. Deveaud-Plédran, Journal of Applied Physics **105**, 043102 (2009).
155. P. Paskov, R. Schifano, T. Malinauskas, T. Paskova, J. Bergman, B. Monemar, S. Figge, D. Hommel, B. Haskell, and P. Fini, physica status solidi (c) **3**, 1499-1502 (2006).
156. S. Yang, C. Kuo, W.-R. Liu, B. Lin, H.-C. Hsu, C.-H. Hsu, and W. Hsieh, Applied Physics Letters **100**, 101907 (2012).
157. M. Häberlen, T. Badcock, M. Moram, J. Hollander, M. Kappers, P. Dawson, C. Humphreys, and R. Oliver, Journal of Applied Physics **108**, 033523 (2010).
158. P. Perlin, I. Gorczyca, N. Christensen, I. Grzegory, H. Teisseyre, and T. Suski, Physical Review B **45**, 13307 (1992).

159. W. Shan, R. Hauenstein, A. Fischer, J. Song, W. Perry, M. Bremser, R. Davis, and B. Goldenberg, Physical Review B **54**, 13460 (1996).
160. T. Badcock, P. Dawson, M. Kappers, C. McAleese, J. Hollander, C. Johnston, D. S. Rao, A. M. Sanchez, and C. Humphreys, Applied Physics Letters **93**, 101901 (2008).
161. P. Corfdir, P. Lefebvre, L. Balet, S. Sonderegger, A. Dussaigne, T. Zhu, D. Martin, J.-D. Ganière, N. Grandjean, and B. Deveaud-Plédran, Journal of Applied Physics **107**, 043524 (2010).
162. A. M. Zaitsev, *Optical properties of diamond: A data handbook* (Springer Science & Business Media, 2013).
163. I. Aharonovich, *Novel single photon emitters based on color centers in diamond* (University of Melbourne, School of Physics, 2010).
164. M. Schwander, and K. Partes, Diamond and related materials **20**, 1287-1301 (2011).
165. R. Balmer, J. Brandon, S. Clewes, H. Dhillon, J. Dodson, I. Friel, P. Inglis, T. Madgwick, M. Markham, and T. Mollart, Journal of Physics: Condensed Matter **21**, 364221 (2009).
166. J. C. Angus, Diamond and Related Materials **49**, 77-86 (2014).
167. J. Rabeau, Y. Chin, S. Prawer, F. Jelezko, T. Gaebel, and J. Wrachtrup, Applied Physics Letters **86**, 131926 (2005).
168. J. Jeske, D. W. Lau, X. Vidal, L. P. McGuinness, P. Reineck, B. C. Johnson, M. W. Doherty, J. C. McCallum, S. Onoda, and F. Jelezko, Nature Communications **8**, 14000 (2017).
169. T. Müller, C. Hepp, B. Pingault, E. Neu, S. Gsell, M. Schreck, H. Sternschulte, D. Steinmüller-Nethl, C. Becher, and M. Atatüre, Nature communications **5** (2014).
170. K. D. Jahnke, A. Sipahigil, J. M. Binder, M. W. Doherty, M. Metsch, L. J. Rogers, N. B. Manson, M. D. Lukin, and F. Jelezko, New Journal of Physics **17**, 043011 (2015).
171. C. Wang, C. Kurtsiefer, H. Weinfurter, and B. Burchard, Journal of Physics B: Atomic, Molecular and Optical Physics **39**, 37 (2005).
172. T. Schröder, M. Walsh, J. Zheng, S. Mouradian, L. Li, G. Malladi, H. Bakhru, M. Lu, A. Stein, M. Heuck, and D. Englund, Opt. Mater. Express **7**, 1514-1524 (2017).
173. L. J. Rogers, K. D. Jahnke, M. W. Doherty, A. Dietrich, L. P. McGuinness, C. Müller, T. Teraji, H. Sumiya, J. Isoya, N. B. Manson, and F. Jelezko, Physical Review B **89** (2014).
174. E. K. Neu, (2012).
175. L. J. Rogers, K. D. Jahnke, T. Teraji, L. Marseglia, C. Muller, B. Naydenov, H. Schauffert, C. Kranz, J. Isoya, L. P. McGuinness, and F. Jelezko, Nat Commun **5**, 4739 (2014).
176. I. Aharonovich, S. Castelletto, B. C. Johnson, J. C. McCallum, D. A. Simpson, A. D. Greentree, and S. Prawer, Physical Review B **81**, 121201 (2010).
177. S. Tamura, G. Koike, A. Komatsubara, T. Teraji, S. Onoda, L. P. McGuinness, L. Rogers, B. Naydenov, E. Wu, and L. Yan, Applied Physics Express **7**, 115201 (2014).
178. R. Sandstrom, L. Ke, A. Martin, Z. Wang, M. Kianinia, B. Green, W. Gao, and I. Aharonovich, arXiv preprint arXiv:1704.01636 (2017).
179. K. Beha, H. Fedder, M. Wolfer, M. C. Becker, P. Siyushev, M. Jamali, A. Batalov, C. Hinz, J. Hees, and L. Kirste, Beilstein journal of nanotechnology **3**, 895 (2012).
180. C. Hepp, T. Müller, V. Waselowski, J. N. Becker, B. Pingault, H. Sternschulte, D. Steinmüller-Nethl, A. Gali, J. R. Maze, and M. Atatüre, Physical Review Letters **112**, 036405 (2014).

181. V. Vavilov, and A. Gippius, Sov. Phys. Semicond. **14**, 1078-1079 (1980).
182. C. Clark, and C. Dickerson, Surface and Coatings Technology **47**, 336-343 (1991).
183. K. Iakoubovskii, G. Adriaenssens, M. Nesládek, and L. Stals, Diamond and related materials **8**, 717-720 (1999).
184. U. F. S. D'Haenens-Johansson, A. M. Edmonds, B. L. Green, M. E. Newton, G. Davies, P. M. Martineau, R. U. A. Khan, and D. J. Twitchen, Physical Review B **84** (2011).
185. E. Neu, M. Fischer, S. Gsell, M. Schreck, and C. Becher, Physical Review B **84** (2011).
186. U. Jantzen, A. B. Kurz, D. S. Rudnicki, C. Schäfermeier, K. D. Jahnke, U. L. Andersen, V. A. Davydov, V. N. Agafonov, A. Kubanek, and L. J. Rogers, New Journal of Physics **18**, 073036 (2016).
187. A. Sipahigil, K. D. Jahnke, L. J. Rogers, T. Teraji, J. Isoya, A. S. Zibrov, F. Jelezko, and M. D. Lukin, Physical review letters **113**, 113602 (2014).
188. T. Müller, C. Hepp, B. Pingault, E. Neu, S. Gsell, M. Schreck, H. Sternschulte, D. Steinmüller-Nethl, C. Becher, and M. Atatüre, Nature communications **5**, 3328 (2014).
189. B. Green, S. Mottishaw, B. Breeze, A. Edmonds, U. D'Haenens-Johansson, M. Doherty, S. Williams, D. Twitchen, and M. Newton, arXiv preprint arXiv:1705.10205 (2017).
190. M. G. Thompson, A. Politi, J. C. Matthews, and J. L. O'Brien, IET circuits, devices & systems **5**, 94-102 (2011).
191. O. Gazzano, S. M. de Vasconcellos, C. Arnold, A. Nowak, E. Galopin, I. Sagnes, L. Lanco, A. Lemaître, and P. Senellart, Nature communications **4**, 1425 (2013).
192. A. Batalov, C. Zierl, T. Gaebel, P. Neumann, I. Y. Chan, G. Balasubramanian, P. R. Hemmer, F. Jelezko, and J. Wrachtrup, Phys Rev Lett **100**, 077401 (2008).
193. A. Batalov, V. Jacques, F. Kaiser, P. Siyushev, P. Neumann, L. J. Rogers, R. L. McMurtrie, N. B. Manson, F. Jelezko, and J. Wrachtrup, Phys Rev Lett **102**, 195506 (2009).
194. S. Castelletto, B. C. Johnson, V. Ivády, N. Stavrias, T. Umeda, A. Gali, and T. Ohshima, Nat Mater **13**, 151-156 (2014).
195. T. T. Tran, K. Bray, M. J. Ford, M. Toth, and I. Aharonovich, Nature nanotechnology **11**, 37-41 (2016).
196. N. Manson, J. Harrison, and M. Sellars, Physical Review B **74**, 104303 (2006).
197. L. J. Rogers, K. D. Jahnke, T. Teraji, L. Marseglia, C. Müller, B. Naydenov, H. Schauffert, C. Kranz, J. Isoya, and L. P. McGuinness, Nature communications **5** (2014).
198. K. Li, Y. Zhou, A. Rasmita, I. Aharonovich, and W. Gao, Physical Review Applied **6**, 024010 (2016).
199. A. Tallaire, A. Collins, D. Charles, J. Achard, R. Sussmann, A. Gicquel, M. Newton, A. Edmonds, and R. Cruddace, Diamond and related materials **15**, 1700-1707 (2006).
200. A. Belabbes, L. de Carvalho, A. Schleife, and F. Bechstedt, Physical Review B **84**, 125108 (2011).
201. M. Suffczyński, R. Stępniewski, and J. Baranowski, Acta Physica Polonica A **5**, 993-996 (1997).
202. K. P. Korona, Physical Review B **65** (2002).
203. H. P. Iwata, U. Lindefelt, S. Öberg, and P. R. Briddon, Physical Review B **68** (2003).

204. L. J. Brillson, T. M. Levin, G. H. Jessen, A. P. Young, C. Tu, Y. Naoi, F. A. Ponce, Y. Yang, G. J. Lapeyre, J. D. MacKenzie, and C. R. Abernathy, Physica B: Condensed Matter **273-274**, 70-74 (1999).
205. P. Corfdir, P. Lefebvre, J. Levrat, A. Dussaigne, J.-D. Ganière, D. Martin, J. Ristic, T. Zhu, N. Grandjean, and B. Deveaud-Plédran, Journal of Applied Physics **105**, 043102 (2009).
206. S. Fischer, G. Steude, D. Hofmann, F. Kurth, F. Anders, M. Topf, B. Meyer, F. Bertram, M. Schmidt, and J. Christen, Journal of crystal growth **189**, 556-560 (1998).
207. P. Paskov, R. Schifano, T. Paskova, T. Malinauskas, J. Bergman, B. Monemar, S. Figge, and D. Hommel, Physica B: Condensed Matter **376**, 473-476 (2006).
208. Y.-H. Cho, G. Gainer, A. Fischer, J. Song, S. Keller, U. Mishra, and S. DenBaars, Applied Physics Letters **73**, 1370-1372 (1998).
209. M. Dinu, J. Cunningham, F. Quochi, and J. Shah, Journal of applied physics **94**, 1506-1512 (2003).
210. P. Paskov, R. Schifano, B. Monemar, T. Paskova, S. Figge, and D. Hommel, Journal of Applied Physics **98**, 93519-93519 (2005).
211. L. Li, E. H. Chen, J. Zheng, S. L. Mouradian, F. Dolde, T. Schröder, S. Karaveli, M. L. Markham, D. J. Twitchen, and D. Englund, Nano letters **15**, 1493-1497 (2015).
212. M. Widmann, S. Y. Lee, T. Rendler, N. T. Son, H. Fedder, S. Paik, L. P. Yang, N. Zhao, S. Yang, I. Booker, A. Denisenko, M. Jamali, S. A. Momenzadeh, I. Gerhardt, T. Ohshima, A. Gali, E. Janzen, and J. Wrachtrup, Nat Mater **14**, 164-168 (2015).
213. J. Hadden, J. Harrison, A. Stanley-Clarke, L. Marseglia, Y.-L. Ho, B. Patton, J. O'Brien, and J. Rarity, Applied Physics Letters **97**, 241901 (2010).
214. B. J. Hausmann, T. M. Babinec, J. T. Choy, J. S. Hodges, S. Hong, I. Bulu, A. Yacoby, M. D. Lukin, and M. Lončar, New Journal of Physics **13**, 045004 (2011).
215. T. T. Tran, C. Zachreson, A. M. Berhane, K. Bray, R. G. Sandstrom, L. H. Li, T. Taniguchi, K. Watanabe, I. Aharonovich, and M. Toth, Physical Review Applied **5**, 034005 (2016).
216. E. Neu, D. Steinmetz, J. Riedrich-Möller, S. Gsell, M. Fischer, M. Schreck, and C. Becher, New Journal of Physics **13**, 025012 (2011).
217. I. Aharonovich, S. Castelletto, D. Simpson, A. Greentree, and S. Prawer, Phys Rev A 2010.
218. N. Jungwirth, Y. Pai, H. Chang, E. MacQuarrie, K. Nguyen, and G. Fuchs, Journal of Applied Physics **116**, 043509 (2014).
219. E. Neu, M. Fischer, S. Gsell, M. Schreck, and C. Becher, Physical Review B **84**, 205211 (2011).
220. I. Aharonovich, S. Castelletto, B. C. Johnson, J. C. McCallum, D. A. Simpson, A. D. Greentree, and S. Prawer, Physical Review B **81** (2010).
221. A. L. Exarhos, D. A. Hopper, R. R. Grote, A. Alkauskas, and L. C. Bassett, ACS nano **11**, 3328-3336 (2017).
222. J. Wolters, N. Sadzak, A. W. Schell, T. Schröder, and O. Benson, Physical Review Letters **110**, 027401 (2013).
223. F. D. Stefani, J. P. Hoogenboom, and E. Barkai, Physics Today **62**, 34-39 (2009).
224. E. Barkai, Y. Jung, and R. Silbey, Annu. Rev. Phys. Chem. **55**, 457-507 (2004).
225. V. Rombach-Riegraf, P. Oswald, R. Bienert, J. Petersen, M. Domingo, J. Pardo, P. Gräber, and E. Galvez, Biochemical and biophysical research communications **430**, 260-264 (2013).

226. B. Mahler, P. Spinicelli, S. Buil, X. Quelin, J.-P. Hermier, and B. Dubertret, Nature materials **7**, 659-664 (2008).
227. J. N. Clifford, T. D. Bell, P. Tinnefeld, M. Heilemann, S. M. Melnikov, J.-i. Hotta, M. Sliwa, P. Dedecker, M. Sauer, and J. Hofkens, The Journal of Physical Chemistry B **111**, 6987-6991 (2007).
228. W.-T. Yip, D. Hu, J. Yu, D. A. Vanden Bout, and P. F. Barbara, The Journal of Physical Chemistry A **102**, 7564-7575 (1998).
229. O. Neitzke, A. Morfa, J. Wolters, A. W. Schell, G. n. Kewes, and O. Benson, Nano letters **15**, 3024-3029 (2015).
230. B. Szûcs, A. Gali, Z. Hajnal, P. Deák, and C. G. Van de Walle, Physical Review B **68**, 085202 (2003).
231. C. G. Van de Walle, Physical Review B **56**, R10020 (1997).
232. K. Han, D. Wildanger, E. Rittweger, J. Meijer, S. Pezzagna, S. Hell, and C. Eggeling, New Journal of Physics **14**, 123002 (2012).
233. E. Rittweger, D. Wildanger, and S. Hell, EPL (Europhysics Letters) **86**, 14001 (2009).
234. T. Plakhotnik, and R. Chapman, New Journal of Physics **13**, 045001 (2011).
235. N. I. Hammer, K. T. Early, K. Sill, M. Y. Odoi, T. Emrick, and M. D. Barnes, The Journal of Physical Chemistry B **110**, 14167-14171 (2006).
236. S.-J. Park, S. Link, W. L. Miller, A. Gesquiere, and P. F. Barbara, Chemical Physics **341**, 169-174 (2007).
237. I. Aharonovich, S. Castelletto, D. A. Simpson, A. D. Greentree, and S. Prawer, Physical Review A **81**, 043813 (2010).
238. S. S. M. a. U. f. a. t. e. d. a. a. o. t. kinetics.
239. T. T. Tran, C. Elbadawi, D. Totonjian, C. J. Lobo, G. Grosso, H. Moon, D. R. Englund, M. J. Ford, I. Aharonovich, and M. Toth, ACS nano **10**, 7331-7338 (2016).
240. J. Tang, and R. A. Marcus, Physical review letters **95**, 107401 (2005).
241. R. Verberk, A. M. van Oijen, and M. Orrit, Physical Review B **66**, 233202 (2002).
242. B. Ellis, M. A. Mayer, G. Shambat, T. Sarmiento, J. Harris, E. E. Haller, and J. Vučković, Nature photonics **5**, 297-300 (2011).
243. R. Stevenson, C. Salter, J. Nilsson, A. Bennett, M. Ward, I. Farrer, D. Ritchie, and A. Shields, Physical review letters **108**, 040503 (2012).
244. Y. Doi, T. Makino, H. Kato, D. Takeuchi, M. Ogura, H. Okushi, H. Morishita, T. Tashima, S. Miwa, and S. Yamasaki, Physical Review X **4**, 011057 (2014).
245. A. Lohrmann, S. Pezzagna, I. Dobrinets, P. Spinicelli, V. Jacques, J.-F. Roch, J. Meijer, and A. Zaitsev, Applied Physics Letters **99**, 251106 (2011).
246. X. Liang, L. Wang, X. Ma, D. Li, P. Cheng, D. Yang, J. Chen, and T. Sekiguchi, Applied physics letters **90**, 161123 (2007).
247. H. Kato, H. Umezawa, N. Tokuda, D. Takeuchi, H. Okushi, and S. Yamasaki, Applied Physics Letters **93**, 202103 (2008).
248. S. Pezzagna, D. Rogalla, D. Wildanger, J. Meijer, and A. Zaitsev, New Journal of Physics **13**, 035024 (2011).
249. U. D'Haenens-Johansson, A. Edmonds, B. Green, M. Newton, G. Davies, P. Martineau, R. Khan, and D. Twitchen, Physical Review B **84**, 245208 (2011).

250. N. Akopian, N. Lindner, E. Poem, Y. Berlatzky, J. Avron, D. Gershoni, B. Gerardot, and P. Petroff, Physical Review Letters **96**, 130501 (2006).
251. R. Trotta, E. Zallo, C. Ortix, P. Atkinson, J. Plumhof, J. Van den Brink, A. Rastelli, and O. Schmidt, Physical review letters **109**, 147401 (2012).
252. C. E. Kuklewicz, R. N. Malein, P. M. Petroff, and B. D. Gerardot, Nano letters **12**, 3761-3765 (2012).
253. A. Faraon, C. Santori, Z. Huang, V. M. Acosta, and R. G. Beausoleil, Physical review letters **109**, 033604 (2012).
254. J. Wolters, A. W. Schell, G. Kewes, N. Nüsse, M. Schoengen, H. Döscher, T. Hannappel, B. Löchel, M. Barth, and O. Benson, Applied Physics Letters **97**, 141108 (2010).
255. B. J. M. Hausmann, T. M. Babinec, J. T. Choy, J. S. Hodges, S. Hong, I. Bulu, A. Yacoby, M. D. Lukin, and M. Lončar, New Journal of Physics **13**, 045004 (2011).
256. E. R. Glaser, W. E. Carlos, G. C. B. Braga, J. A. Freitas, W. J. Moore, B. V. Shanabrook, R. L. Henry, A. E. Wickenden, D. D. Koleske, H. Obloh, P. Kozodoy, S. P. DenBaars, and U. K. Mishra, Physical Review B **65** (2002).
257. M. Bayerl, M. Brandt, T. Suski, I. Grzegory, S. Porowski, and M. Stutzmann, Physica B: Condensed Matter **273**, 120-123 (1999).